CERN / LHCC 2000–12
ALICE TDR 8
16 February 2000

A L I C E

Technical Design Report

of the

Time of Flight System (TOF)

Cover design by Fabienne Marcastel

Printed at CERN
February 2000

ISBN 92-9083-159-6

ALICE Collaboration

Alessandria, Italy, Facoltà di Scienze dell'Università:
G. Dellacasa, L. Ramello, E. Scalas and M. Sitta.

Aligarh, India, Physics Department, Aligarh Muslim University:
N. Ahmad, S. Ahmad, T. Ahmad, W. Bari, M. Irfan and M. Zafar.

Athens, Greece, Nuclear and Particle Physics Division, University of Athens:
A.L.S. Angelis1), G. Mavromanolakis and A.D. Panagiotou.

Athens, Greece, Institute of Nuclear Physics, NRC Demokritos:
K. Kalfas.

Bari, Italy, Dipartimento di Fisica dell'Università and Sezione INFN:
R. Caliandro, D. Cozza, G. De Cataldo, D. Di Bari, D. Elia, R.A. Fini, B. Ghidini, V. Lenti, V. Manzari, E. Nappi1), F. Navach and F. Posa.

Bari, Italy, Politecnico and Sezione INFN:
F. Corsi, D. De Venuto, R. Dinapoli, G. Lisco, C. Marzocca and E. Monno.

Beijing, China, China Institute of Atomic Energy:
X. Li, S. Lu, Z. Lu, B. Sa, J. Yuan, J. Zhou, S. Zhou and X. Zhu.

Bergen, Norway, Department of Physics, University of Bergen:
E. Andersen, K. Fanebust, H. Helstrup, A. Klovning, O.A. Maeland, O.H. Odland, D. Röhrich, R. Rongved and A.S. Vestbøe.

Bhubaneswar, India, Institute of Physics:
A.K. Dubey, D.P. Mahapatra, B. Mohanty and S.C. Phatak.

Birmingham, United Kingdom, School of Physics and Space Research, University of Birmingham:
I.J. Bloodworth, D. Evans, G.T. Jones, P. Jovanović, J.B. Kinson, A. Kirk, O. Villalobos Baillie and M.F. Votruba.

Bologna, Italy, University/INFN:
F. Anselmo, P. Antonioli, G. Bari, M. Basile, L. Bellagamba, D. Boscherini, A. Bruni, G. Bruni, G. Cara Romeo, E. Cerron-Zeballos, F. Cindolo, N. Coppola, M. Corradi, S. De Pasquale, D. Falchieri, A. Gabrielli, E. Gandolfi, P. Giusti, D. Hatzifotiadou, N.Y. Kim, G. Laurenti, M.L. Luvisetto, A. Margotti, M. Masetti, R. Nania, F. Palmonari, A. Pesci, F. Pierella, A. Polini, G. Sartorelli, A. Semak, G. Valenti, M.C.S. Williams and A. Zichichi.

Bratislava, Slovakia, Faculty of Mathematics and Physics, Comenius University:
J. Braciník, V. Černý, J. Ftáčnik, V. Hlinka, R. Janik, R. Lietava, M. Pikna, J. Pišút, N. Pišútová, P. Rosinsky, B. Sitar, P. Strmeň, I. Szarka and M. Zagiba.

Bucharest, Romania, National Institute for Physics and Nuclear Engineering:
A. Andronic, V. Catanescu, M. Ciobanu, M. Duma, C.I. Legrand, D. Moisa, M. Petrovici, V. Simion and G. Stoicea.

Budapest, Hungary, KFKI Research Institute for Particle and Nuclear Physics, Hungarian Academy of Sciences:
E. Denes, B. Eged, Z. Fodor, G. Harangozo, Z. Meggyesi, G. Palla, G. Rubin, J. Sulyan, J. Sziklai, B.N. Vissy and J. Zimanyi.

Cagliari, Italy, Dipartimento di Fisica dell’Università and Sezione INFN:
C. Cicalo, A. De Falco, M.P. Macciotta-Serpi, A. Masoni, A. Pataki, G. Puddu, P. Randaccio, S. Serci, E. Siddi and G. Usai.

Calcutta, India, Saha Institute of Nuclear Physics:
P. Bhattacharya, S. Bose, Sukalyan Chattopadhyay, N. Majumdar, S. Mukhopadhyay, A. Sanyal, S. Sarkar, P. Sen, S.K. Sen, B.C. Sinha and T. Sinha.

Calcutta, India, Variable Energy Cyclotron Centre:
Subhasis Chattopadhyay, M.R. Dutta Majumdar, M.S. Ganti, T.K. Nayak, S. Pal, R.N. Singaraju, Bikash Sinha, M.D. Trivedi and Y.P. Viyogi.

Catania, Italy, Dipartimento di Fisica dell’Università and Sezione INFN:
A. Badalà, R. Barbera, M. Gulino, S. Ingrassia, A. Insolia, L. Lo Nigro, D. Lo Presti, A. Palmeri, G.S. Pappalardo, L. Pappalardo, C. Petta, N. Randazzo, S. Reito, F. Riggi, G.V. Russo and S. Vanadia.

CERN, Switzerland, European Organization for Nuclear Research:
Y. Andres, J. Bächler, J.A. Belikov2), V. Berejnoi3), J.-C. Berset, R. Brun, M. Campbell, W. Carena, F. Carminati, S. Chapeland, P. Chochula4), V. Colin de Verdière, J. Cruz de Sousa Barbosa, M. Davenport, J. de Groot, A. Di Mauro, R. Divià, C. Eisenberg, C. Engster, J. Espirito Santo, R. Esteve Bosch, M. Flammier, F. Formenti, D. Fraissard, E. Futo5), B. Goret, T. Grassi6), C. Gregory, M. Hoch, P.G. Innocenti, W. Klempt, A. Kluge, X. Lagrue, G. Lecoeur, J.C. Legrand, L. Leistam, B. Lenkeit, P. Lenoir, Y. Lesenechal, C. Lourenço, P. Martinengo, M. Mast, T. Meyer, A. Morsch, M. Mota, L. Musa, B. Perrin, F. Piuz, E. Quercigh, J. Raynaud, A. Rivetti, K. Šafařík, J.-C. Santiard, K. Schossmaier, J. Schukraft, E. Schyns, W. Snoeys, P. Sonderegger, M. Spegel, D. Swoboda, P. Szymanski, G. Tabary, P. Vande Vyvre, A. Vascotto, S. Wenig, P. Wertelaers and J. Zalipska.

Chandigarh, India, Physics Department, Panjab University:
M.M. Aggarwal, A.K. Bhatia, V.S. Bhatia and G. Sood.

Clermont-Ferrand, France, Laboratoire de Physique Corpusculaire (LPC), IN2P3-CNRS and Université Blaise Pascal:
IN2P3: A. Baldit, V. Barret, N. Bastid, G. Blanchard, J. Castor, T. Chambon, P. Crochet, F. Daudon, A. Devaux, P. Dupieux, B. Espagnon, P. Force, L. Lamoine, J. Lecoq, L. Royer, P. Saturnini and G. Savinel.

A. Genoux-Lubain7), F. Manso7) and P. Rosnet7).

Coimbra, Portugal, Departamento de Física, Faculdade de Ciências e Tecnologia:
R. Ferreira Marques, P. Fonte, J. Pinhao and A. Policarpo.

Columbus, U.S.A., Department of Physics, Ohio State University:
H.L. Caines, H.M. Dyke, T.J. Humanic, M. Lisa, B.S. Nilsen, G. Paić and E. Sugarbaker.

Copenhagen, Denmark, Niels Bohr Institute:
I. Bearden, H. Bøggild, P. Christiansen, J.J. Gaardhøje, O. Hansen, A. Holm, B.S. Nielsen and D. Ouerdane.

Cracow, Poland, Henryk Niewodniczanski Institute of Nuclear Physics, High Energy Physics Department:
J. Bartke, E. Gładysz-Dziaduś, E. Górnicki, M. Kowalski, A. Rybicki, P. Stefański and Z. Wlodarczyk(8).

Darmstadt, Germany, Gesellschaft für Schwerionenforschung (GSI):
R. Averbeck, E. Badura, C. Blume, P. Braun-Munzinger, H.W. Daues, A. Deusser, A. Devismes, C. Finck, P. Foka, U. Frankenfeld, C. Garabatos, G. Hering, M. Ivanov(4), J. Lühning, P. Malzacher, C. Markert, A. Mischke, D. Miśkowiec, W.F.J. Müller, F. Rademakers, H. Sako, A. Sandoval, H. Sann, H.R. Schmidt, S. Sedykh, A. Sharma(1), H. Stelzer, R. Veenhof and D. Vranic.

Darmstadt, Germany, Institut für Kernphysik, Technische Universität(*):
A. Förster, H. Oeschler and F. Uhlig.

Frankfurt, Germany, Institut für Kernphysik, Johann Wolfgang Goethe-Universität:
C. Adler, W. Amend, J. Berger, J. Berschin, A. Billmeier, P. Buncic, D. Flierl, M. Gaździcki, J. Hehner, S. Lange, R. Renfordt, H. Rheinfels-Immans, C. Roland, G. Roland, R. Stock, H. Ströbele and C. Struck.

Gatchina, Russia, St. Petersburg Nuclear Physics Institute:
K. Egorov, B. Komkov, V. Kozlov, N. Miftakhov, V. Nikouline, V. Samsonov, O. Tarasenkova, V. Vishnevskii, S. Volkov and A. Vorobiev.

Heidelberg, Germany, Kirchhoff Institute for Physics:
R. Achenbach, O. Braun, M. Keller, F.O. Lesser, V. Lindenstruth, R. Schneider, M. Schulz, T. Steinbeck and L. Voerg.

Heidelberg, Germany, Physikalisches Institut, Ruprecht-Karls Universität:
H. Appelshäuser, S. Damjanovic, T. Dietel, S.I. Esumi, K. Filimonov, P. Glässel, N. Herrmann, A. Marin, V. Petráček, J. Rak, A. Reischl, M.J. Richter, E. Schäfer, W. Schmitz, W. Seipp, J. Slivova, H.C. Soltveit, H.J. Specht, J. Stachel, H. Tilsner, J.P. Wessels, T. Wienold, B. Windelband and S. Yurevich.

Ioannina, Greece, University of Ioannina, Department of Physics:
X. Aslanoglou and N.G. Nicolis.

Jaipur, India, Physics Department, University of Rajasthan:
A. Bharti, S.K. Gupta, R. Raniwala and S. Raniwala.

Jammu, India, Physics Department, Jammu University:
S.K. Badyal, A. Bhasin, A. Gupta, V.K. Gupta, S. Mahajan, L.K. Mangotra, B.V.K.S. Potukuchi, N.K. Rao and S.S. Sambyal.

JINR, Russia, Joint Institute for Nuclear Research:
P.G. Akichine, V.A. Arefiev, V.I. Astakhov, A.A. Baldine, A.M. Baldine, V.D. Bartenev, B.V. Batiounia, I.V. Boguslavsky, Z.V. Borissovskaia, P. Bylinkine, A.V. Chabounov, G.S. Chabratova, I.A. Chichov, V. Danilov, V.I. Datskov, V.K. Dodokhov, L.G. Efimov, A.G. Fedounov, O.A. Golubitsky, B.N. Guouskov, O.I. Iouldachev, V.G. Kadychevsky, I.E. Karpunina, E.K. Koshurnikov, A.D. Kovalenko, A. Lioubimtsev, V.L. Lioubochits, V.I. Lobanov, G.I. Lykasov, E.A. Matiouchevski, K.V. Mikhailov, I. Minaev, P.V. Nomokonov, I.V. Pouzynin, I. Roufanov, I.A. Shelaev, A.V. Sidorov, M.K. Suleimanov, G.P. Tsvineva and A.S. Vodopianov.

V. Kuznetsov9) and V. Shestakov9).

Ts. Baatar10), B. Khurelbaatar10) and R. Togoo10).

K.G. Akhobadze11), A.K. Djavrishvili11), T. Grigalashvili11), E.S. Ioramashvili11), A.V. Kharadze11), L. Khizanishvili11), T.V. Khuskivadze11), L.V. Shalamberidze11) and N. Shubitidze11).

N. Grigalashvili12), M. Nioradze12), M. Tabidze12) and Y. Tevzadze12).

D. Felea13), A. Gheata13), M. Gheata13), M. Haiduc13), D. Hasegan13), R. Marginean13), R.I. Nanciu13) and S.I. Zgura13).

Jyväskylä, Finland, Department of Physics, University of Jyväskylä and Helsinki Institute of Physics:
J. Aysto, M. Bondila, M. Komogorov, V. Lyapin, V. Ruuskanen and W. Trzaska.

Kharkov, Ukraine, National Scientific Centre ‘Kharkov Institute of Physics and Technology’:
G.L. Bochek, V.F. Boldyshev, A.N. Dovbnya, V.I. Kulibaba, N.I. Maslov, S.V. Naumov, S.M. Potin, I.M. Prokhorets and A.F. Starodubtsev.

Kharkov, Ukraine, Scientific and Technological Research Institute of Instrument Engineering:
V.N. Borshchov, S.K. Kiprich, O.M. Listratenko, G. Protsay, A.N. Reznik, A.N. Ryabukhin and V.E. Starkov.

Kiev, Ukraine, Department of High Energy Density Physics, Bogolyubov Institute for Theoretical Physics, National Academy of Sciences of Ukraine:
T. Hryn’ova, D.E. Kharzeev, O.P. Pavlenko, A. Velytsky and G. Zinovjev.

Košice, Slovakia, Institute of Experimental Physics, Slovak Academy of Sciences and Faculty of Science P.J. Šafárik University:
J. Bán, J. Fedorišin, M. Hnatič, A. Jusko, I. Králik, A. Kravčáková, F. Kriváň, I. Kuľková, M. Lupták, G. Martinská, B. Pastirčák1), L. Šándor, J. Urbán, S. Vokál and J. Vrláková.

Lausanne, Switzerland, Integrated System Laboratory (ISL), Ecole Polytechnique Fédérale de Lausanne (EPFL)*):
A. Aizza, F.A. Cherigui, M. Mattavelli and D. Mlynek.

Legnaro, Italy, Laboratori Nazionali di Legnaro:
A. Bologna, M. Lombardi, R.A. Ricci and L. Vannucci.

Lisbon, Portugal, Departamento de Física, Instituto Superior Técnico:
P. Branco, R. Carvalho, J. Seixas and R. Vilela Mendes.

Lund, Sweden, Division of Cosmic and Subatomic Physics, University of Lund:
L. Carlen, S.I.A. Garpman, H.-A. Gustafsson, P. Nilsson, A. Oskarsson, L. Osterman, I. Otterlund, D. Silvermyr and E.A. Stenlund.

Lyon, France, Institut de Physique Nucléaire de Lyon (IPNL), IN2P3-CNRS and Université Claude Bernard Lyon-I:
M.Y. Chartoire, M. Chevallier, B. Cheynis, L. Ducroux, E. Gangler, M. Goyot, J.Y. Grossiord, R. Guernane, A. Guichard, D. Guinet, G. Jacquet, P. Lautesse and S. Tissot.

Marburg, Germany, Fachbereich Physik, Philipps Universität:
V. Friese, C. Höhne and F. Pühlhofer.

Mexico City, Mexico, Centro de Investigación y de Estudios Avanzados:
R. Hernández Montoya, G. Herrera Corral and L.M. Montaño.

Moscow, Russia, Institute for Nuclear Research, Academy of Science:
K.A. Chileev, M.B. Goloubeva, F.F. Gouber, T.L. Karavitcheva, A.B. Kourepin, A.I. Maevskaia, V.I. Razine, A.I. Rechetine and N.S. Topilskaia.

Moscow, Russia, Institute for Theoretical and Experimental Physics:
A.N. Akindinov, V. Golovine, A.B. Kaidalov, M.M. Kats, I.T. Kiselev, S.M. Kisselev, E. Lioublev, M. Martemianov, A.N. Martemiyanov, P.A. Polozov, V.S. Serov, A.V. Smirnitski, M.M. Tchoumakov, I.A. Vetlitski, K.G. Volochine, L.S. Vorobiev and B.V. Zagreev.

Moscow, Russia, Russian Research Center 'Kurchatov Institute':
V. Antonenko, S. Beliaev, I. Doubovik, S. Fokine, M. Ippolitov, K. Karadjev, A.L. Lebedev, V. Lebedev, V.I. Manko, T. Moukhanova, A. Nianine, S. Nikolaev, S. Nikouline, O. Patarakine, D. Peressounko, I. Sibiriak, A. Vasiliev, A. Vinogradov and M. Volkov.

Moscow, Russia, Moscow Engineering Physics Institute:
V.A. Grigoriev, V.A. Kapline and V.A. Loguinov.

Münster, Germany, Institut für Kernphysik, Westfälische Wilhelms Universität:
D. Bucher, R. Glasow, N. Heine, T. Peitzmann, K. Reygers, R. Santo, H. Schlagheck, W. Verhoeven and M. Wahn.

Nantes, France, Laboratoire de Physique Subatomique et des Technologies Associées (SUBATECH), Ecole des Mines de Nantes, IN2P3-CNRS and Université de Nantes:
L. Aphecetche, A. Boucham, S. Bouvier, J. Castillo, L. Conin, J.P. Cussonneau, H. Delagrange, D. D'Enterria, M. Dialinas, C. Drancourt, B. Erazmus, G. Guilloux, H.H. Gutbrod, M.S. Labalme, P. Lautridou, F. Lefèvre, M. Le Guay, L. Luquin, L. Martin, G. Martinez, V. Métivier, M.J. Mora, W. Pinganaud, G. Puil, O. Ravel, F. Retiere, C.S. Roy, D. Roy, Y. Schutz and A. Tournaire.

NIKHEF, The Netherlands, National Institute for Nuclear and High Energy Physics:
M. Botje14), A. Buijs15), J.J.F. Buskop14), A.P. De Haas15), P.K.A. De Witt Huberts14,15), R. Kamermans14,15), P.G. Kuijer14,15), D. Muigg15), G. Nooren14), C.J. Oskamp15), A. Van Den Brink15) and N. Van Eijndhoven15).

Novosibirsk, Russia, Budker Institute for Nuclear Physics:
A.R. Frolov and I.N. Pestov.

Oak Ridge, U.S.A., Instrumentation and Controls Division, Oak Ridge National Laboratory:
T. Awes, C.L. Britton, W.L. Bryan, J.W. Walker and A.L. Wintenberg.

Orsay, France, Institut de Physique Nucléaire (IPNO), IN2P3-CNRS and Université de Paris-Sud:
L. Bimbot, P.F. Courtat, R. Douet, P. Edelbruck, D. Jouan, Y. Le Bornec, M. Mac Cormick, J. Peyré, J. Pouthas and N. Willis.

Oslo, Norway, Department of Physics, University of Oslo:
A.K. Holme, G. Løvhøiden, B. Skaali, T.S. Tveter and D. Wormald.

Padua, Italy, Dipartimento di Fisica dell'Università and Sezione INFN:
F. Antinori, N. Carrer, M. Morando, A. Pepato, F. Scarlassara, G. Segato, F. Soramel and R. Turrisi.

Prague, Czech Republic, Institute of Physics, Academy of Science:
A. Beitlerova, J. Mareš, E. Mihoková, M. Nikl, K. Píška, K. Polák and P. Závada.

Protvino, Russia, Institute for High Energy Physics:
A.M. Blik, M. Bogolyubsky, G. Britvitch, S. Erine, G.V. Khaoustov, I.V. Kharlov, V. Lichine, M. Lobanov, N. Minaev, S.A. Sadovski, V.D. Samoilenko, P.A. Semenov, V.I. Suzdalev and V. Tikhonov.

Řež u Prahy, Czech Republic, Academy of Sciences of Czech Republic, Nuclear Physics Institute:
V. Hanzal, J. Hošek, I. Hřivnáčová1), S. Kouchpil, V. Kouchpil, A. Kugler, M. Šumbera, P. Tlustý, V. Wagner and D. Zákoucký.

Rome, Italy, Dipartimento di Fisica dell'Università 'La Sapienza' and Sezione INFN:
S. Di Liberto, M.A. Mazzoni, F. Meddi, D. Prosperi and G. Rosa.

Saclay, France, Centre d'Etudes Nucléaires, DAPNIA:
P. Ageron, A. Baldisseri, H. Borel, D. Cacaut, I. Chevrot, P. De Girolamo, J. Gosset, L. Gosset, P. Hardy, D. Jourde, J.C. Lugol and F.M. Staley.

Salerno, Italy, Dipartimento di Scienze Fisiche 'E.R.Caianiello' dell'Universitá and INFN:
L. Cifarelli, B. Cozzoni, G. Grella, M. Guida, J. Quartieri, G. Romano, A. Seganti, D. Vicinanza and T. Virgili.

Sarov, Russia, Russian Federal Nuclear Center (VNIIEF):
V. Basmanov, D. Budnikov, V. Ianowski, R. Ilkaev, L. Ilkaeva, A. Ivanov, A. Khlebnikov, E. Kolokolnikov, S. Nazarenko, V. Punin, S. Poutevskoi, I. Selin, I. Vinogradov, S. Zhelezov and A. Zhitnik.

Shanghai, China, Shanghai Institute of Ceramics (SICCAS):
Q. Deng, P. Li, J. Liao and D. Yan.

St. Petersburg, Russia, Institute for Physics of St. Petersburg State University, Mendeleev Institute for Metrology and Meson Scientific Association:
L.Y. Abramova, V.S. Alexandrov, P. Bolokhov, A.A. Bolonine, M.A. Braun, V.M. Dobulevitch, G.A. Feofilov, S. Guerassimov, S.N. Igolkine, M.I. Ioudkine, A.A. Kolojvari, V. Kondratiev, I.A. Novikov, S.V. Potapov, O.I. Stolyarov, A.M. Switchev, T.A. Toulina, F.A. Tsimbal, F.F. Valiev, V.V. Vetchernine and L.I. Vinogradov.

Strasbourg, France, Institut de Recherches Subatomiques (IReS), IN2P3-CNRS and Université Louis Pasteur:
L. Arnold, J. Baudot, D. Bonnet, J.P. Coffin, M. Germain, C. Gojak, B. Hippolyte, C. Kuhn, J. Lutz and A. Tarchini.

Trieste, Italy, Dipartimento di Fisica dell'Università and Sezione INFN:
V. Bonvicini, L. Bosisio, P. Camerini, E. Fragiacomo, A. Gregorio, N. Grion, G. Margagliotti, C. Piemonte, A. Rachevski, R. Rui and A. Vacchi.

Turin, Italy, Dipartimenti di Fisica dell'Università and INFN:
G. Alberici, B. Alessandro, R. Arnaldi, P. Barberis, S. Beolé, E. Botta, P.G. Cerello, E. Chiavassa, P. Cortese, E. Crescio, F. Daudo, N. De Marco, A. Ferretti, L. Gaido, M. Gallio, G. Giraudo, P. Giubellino, A. Marzari-Chiesa, M. Masera, G. Mazza, P. Mereu, B. Minetti, M. Monteno, O. Morra, A. Musso, D. Nouais, C. Oppedisano, A. Piccotti, G. Piragino, L. Riccati, E. Scomparin, F. Tosello, E. Vercellin, A. Werbrouck and R. Wheadon.

Warsaw, Poland, Soltan Institute for Nuclear Studies:
D. Czerwinski, A. Deloff, K. Karpio, S. Kozak, M. Kozlowski, L. Lukaszek, H. Malinowski, T. Siemiarczuk, G. Stefanek, L. Tykarski and G. Wilk.

Warsaw, Poland, University of Technology, Institute of Physics:
J. Grabski, P. Leszczynski, T.J. Pawlak, W.S. Peryt, J. Pluta and M. Przewlocki.

Wuhan, China, Institute of Particle Physics, Huazhong Normal University:
X. Cai, S.Q. Feng, Y. Hu, W. Li, F. Liu, F.M. Liu, H. Liu, L.S. Liu, Y. Liu, W.Y. Qian, X.R. Wang, S.Q. Wu, T. Wu, C.C. Xu, C.B. Yang, Z.B. Yin, D.C. Zhou and D.M. Zhou.

Yerevan, Armenia, Yerevan Physics Institute:
M. Atayan, V. Danielyan, A. Grigorian, S. Grigoryan, H. Gulkanyan, V. Kakoyan, Yu. Margaryan, S. Mehrabyan, L. Parlakyan, R. Shahoyan and H. Vardanyan.

Zagreb, Croatia, Ruder Bošković Institute:
T. Anticic, K. Kadija and T.Susa.

---

[*] Applying to join ALICE.
[1] Also at CERN, Geneva, Switzerland.
[2] On leave from JINR, Dubna, Russia.
[3] On leave from IHEP, Protvino, Russia.
[4] On leave from Comenius University, Bratislava, Slovakia.
[5] On leave from Budapest University, Hungary.
[6] On leave from Dipartimento di Fisica dell'Universitá and Sezione INFN, Padua, Italy.
[7] Institut Universitaire de Technologie de Monluçon, Allier, France.
[8] Institute of Physics, Pedagogical University, Kielce, Poland.
[9] Research Centre for Applied Nuclear Physics (RCANP), Dubna, Russia.
[10] Institute of Physics and Technology, Mongolian Academy of Sciences, Ulaanbaatar, Mongolia.
[11] Institute of Physics, Georgian Academy of Sciences, Tbilisi, Georgia.
[12] High Energy Physics Institute, Tbilisi State University, Tbilisi, Georgia.
[13] Institute of Space Sciences, Bucharest, Romania.
[14] Foundation of Fundamental Research of Matter in The Netherlands.
[15] Utrecht University, Utrecht, The Netherlands.

Acknowledgements

The Collaboration wishes to thank all the technical and administrative staff (in particular S. Barras, S. Maridor and S. Stappers) involved during the preparation of this TDR. The editorial board, M. Basile, L. Cifarelli, F. Cindolo, G. Laurenti, G. Valenti (chair), C. Williams and A. Zichichi, wishes to thank J. Engster-Montgomery and C. Manoli for proofreading the TDR. We also thank the Desktop Publishing Service, for their professional help with the editing.

Contents

1 Introduction

1.1 The ALICE experiment

ALICE (A Large Ion Collider Experiment) [1] is an experiment at the Large Hadron Collider (LHC), optimized for the study of heavy-ion collisions, at a centre-of-mass energy ~ 5.5 TeV per nucleon. The prime aim of the experiment is to study, in detail, the behaviour of nuclear matter at high densities and temperatures, in view of probing deconfinement and chiral symmetry restoration.

Essentially, the detector consists of two main components. The central part, which covers $\pm 45^\circ$ ($|\eta| < 0.9$) over the full azimuth, is embedded in the L3 magnet with a weak solenoidal field of 0.2 T. Outside the Inner Tracking System (ITS) [2], there is a cylindrical TPC [3] and a large time-of-flight (TOF) array. In addition, there are two small-area detectors: an electromagnetic calorimeter (Photon Spectrometer, PHOS) [4] and an array of RICH counters optimized for high-momentum inclusive particle identification (HMPID) [5]. These detectors are mainly devoted to the study of hadronic signals and photons. The other components ($|\eta| > 2.$) consist of the forward muon spectrometer [6] ($|\eta| \approx 2.5 - 4.0$), devoted to the study of quarkonia behaviour in dense matter and a set of forward multiplicity detectors and calorimeters (PMD [7], ZDC [8]). The layout of the ALICE experiment is shown in Fig. I.
A major technical challenge is presented by the large number of particles produced in the collisions of lead ions. There is a considerable spread in the currently available predictions for the multiplicity of charged particles produced in a central Pb–Pb collision. The design of ALICE is based on the highest value at midrapidity: 8000 charged particles per unit of rapidity. This multiplicity dictates the granularity of the detectors and their optimal distance from the colliding beams.

1.2 Particle Identification in ALICE

Particle identification (PID) over a large part of the phase space, and for many different particles, is an important design feature. ALICE has two detector systems dedicated exclusively to PID; a TOF array optimized for large acceptance and average momenta below 2.5 GeV/c, and a small system [HMPID] specialized in higher momenta. Track finding in heavy-ion collisions at the LHC presents a big challenge, due to the extremely high track density. In order to achieve a high granularity and a good two-track separation, three-dimensional hit information is used, wherever feasible, with many points on each track and a weak magnetic field. The ionization density of each track is measured for particle identification at low momentum below 0.5 GeV/c.

The need for a large number of points on each track has led to the choice of a TPC as the main tracking system. In spite of its drawbacks, related to speed and data volume, it is the only device which can provide reliable performance for a large volume of up to 8000 charged particles per unit of rapidity. The minimum possible inner radius of the TPC ($r_{\text{in}} \approx 85$ cm) is given by the maximum acceptable hit density. The outer radius ($r_{\text{out}} \approx 250$ cm) is determined by the minimum length required for a $\mathrm{d}E/\mathrm{d}x$ resolution better than 10%. At smaller radii (and larger track densities), tracking is taken over by the ITS.

The event-by-event (E-by-E) hadron identification will give the opportunity to measure, with high statistics, on a single event basis the shape of the p_t distribution of pions, kaons and protons, their average p_t (i.e. their individual temperature) and the π/K/p ratios. Consequently, it will provide information in terms of QCD thermodynamics, separately for different particle species, on possible thermodynamical instabilities during phase transitions resulting in temperature fluctuations, on the degree of thermal equilibrium, on collective flow phenomena and on expansion dynamics, In addition, kaon identification will provide information on flavour composition to probe the level of s-quark density, which is expected to be large from partial chiral symmetry restoration in a QGP. Identified kaons are also particularly important for the identification of $\phi \rightarrow K^+K^-$ decays (production rate and particle decay width), while the measurement of the ϕ yield sets more stringent constraints on the origin of the observed flavour composition, as compared to the K/π ratio.

Finally, identified kaons are essential, coupled with secondary vertex detection, to identify open charm decays such as, for instance, $D^0 \rightarrow K^-\pi^+$ and $D^+ \rightarrow K^-\pi^+\pi^+$. Owing to its large mass, charm can only be produced in the early stage of the heavy ion collision and it probably ends up in the final state, mostly in the form of open charm hadrons, due to its very low annihilation probability. The degree of open charm enhancement is expected to be sensitive to the parton kinematics at the primordial stage. Additionally, the detection of open charm will be essential for cross-section normalization, necessary in the detection of the well known J/Ψ suppression that probes the QGP formation.

All the basic physics goals, briefly recalled above, demand a TOF detector with outstanding intrinsic characteristics. The TOF rapidity acceptance has to be large enough to cover the full central acceptance of ALICE, in order to allow a significant study of the observables of interest on an E-by-E basis. This implies that a large number of hadrons of average momenta $\sim$ 1 GeV/c should be measured.

More precisely, the TOF detector should cover the hadron momentum range from about 0.5 GeV/c (upper limit for dE/dx measurements in both the ITS and TPC detectors for K/π separation) to about 2.5 GeV/c (statistics limit in single events). The momentum region above this value will be covered by a smaller detector, the HMPID, complementing the TOF for inclusive measurements only. In addition to the excellent intrinsic resolution of the detector itself, an overall time resolution of 150 *ps* is achievable in our TOF system, i.e.: including all other sources of timing errors. This resolution would guarantee a 3σ K/π separation up to $p_{3\sigma} = 1.7\ GeV/c$, whereas 200 *ps* or worse would leave a substantial fraction of the momentum spectrum unmeasured.

1.3 Required time resolution for the TOF PID

The performance of a TOF system for particle ID depends on the intrinsic timing resolution of the detectors as well as the system's resolution.

To evaluate the influence of different parameters of the TOF system on the PID quality, let us consider the following expressions:

$$m = p \cdot \sqrt{\frac{t^2}{l^2} - 1} \tag{1.1}$$

where m is the mass of the particle, p the momentum, E the energy, t the time-of-flight and l the track length. It is simple to show that the $\partial m/m$ resolution has three main contributions:

$$\frac{\partial m}{m} = \frac{\partial p}{p}$$

$$\frac{\partial m}{m} = \left(\frac{E}{m}\right)^2 \frac{\partial t}{t}$$

$$\frac{\partial m}{m} = \left(\frac{E}{m}\right)^2 \frac{\partial l}{l}$$

and that, at relatively high momenta, it is driven much more by the errors on the time-of-flight and track length measurements than by the error on the momentum determination. The technique proposed for the TOF of ALICE should reach an intrinsic resolution better than $\sim$ 90 ps. Including the other sources of timing errors (see Chapt.4), a resolution of about 150 ps is expected. The nominal performance of a TOF array with a system resolution from 80 to 150 ps, located at R = 3.70 m from the vertex, is shown in Fig. 1.1 for particles emitted at 90 degrees.

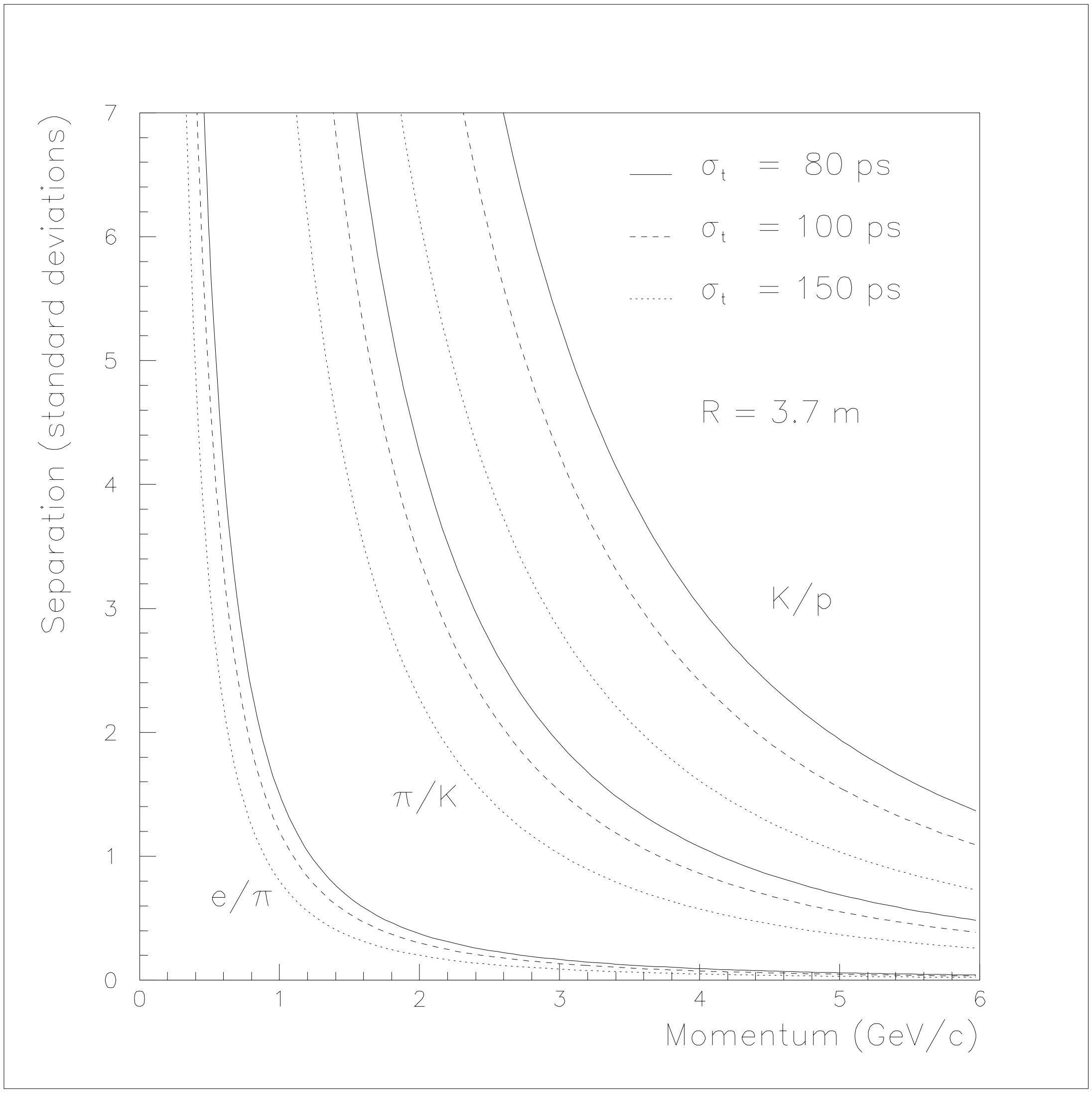

Figure 1.1: Particle separation with a TOF detector.

2 R&D program, prototype test results

2.1 Introduction

Our goal is to build a TOF array that covers ~ 176 m^2, with 160 000 cells of $3{\times}3$ cm^2, with a time resolution of ~ 100 ps. Many smaller arrays were built in the past, using scintillators and good phototubes. However, the cost of a system of the size we envisage is prohibitive if it was to be based on this scintillator/phototube technology. Gaseous detectors are obvious candidates when large area coverage is needed. For the TOF detector, a part of the ALICE R&D program, three gaseous type detectors have been considered. These are the Pestov counter, the parallel plate chamber (PPC) and the multigap resistive plate chamber (MRPC).

All three of these gaseous type detectors are of the parallel plate chambers design. The key aspect of parallel plate chambers is that the electric field is high and uniform over the whole sensitive gaseous volume of the detector. Any ionisation produced by a through-going charged particle will immediately start a gas avalanche process which will eventually generate the observed signals on the pick-up electrodes. There is no time drift associated with the movement of the electrons to a region of high electric field. Thus the time jitter of these devices is caused by the fluctuations in the growth of the avalanche. In the case of the Pestov counter, one also has additional fluctuations related to the transition from an avalanche to a streamer. First we will review the Pestov counter and the PPC and present the latest R&D results. Since the multigap RPC is the baseline option, this device will be discussed in detail.

2.2 History of R&D for the TOF in ALICE

2.2.1 The Pestov spark counter

The use of the Pestov spark counter offers high time resolution (up to 25 ps) and good position resolution (~ 300 μm) [1]. The detection efficiency is close to 100%, and the counting rate capability is sufficient for typical heavy-ion experiments.

The idea of a spark counter with a localised discharge was proposed and realised at INP, Novosibirsk in 1971 [2]. The first application of these counters in a physics experiment was the pion form factor measurement, near the threshold, at the electron-positron VEPP- 2 collider, Novosibirsk in 1978-1985 [3]. In 1986-1991 the R&D work for e^+e^- colliders was continued within a SLAC-Novosibirsk collaboration.

In this section we shall review the R&D results obtained within the framework of the PesTOF collaboration [1] for the ALICE experiment, as well as the outcome of ongoing research and first applications in the GSI-FOPI and the CERN-NA49 experiments. The present R&D work was driven by potential large-scale applications, which require a detector design suitable for mass production, as well as by the wish to reduce the timing tails to an absolute minimum. The latter task is of particular importance for the low energy GSI FOPI-experiment, where the K/π ratio is an order of magnitude lower than for ALICE-type collisions and hence the disturbance by late timing signals is most severe.

2.2.1.1 Working principle of the Pestov spark counter

A big advantage of gas-filled parallel-plate detectors for timing measurements is the homogeneous electric field in the gas gap. In this case, every primary ionisation gives immediate input to the timing signal,

---

[1] The PesTOF collaboration includes the following institutions: GSI Darmstadt, BINP Novosibirsk, JINR Dubna, MEPHI Moscow, RMKI Budapest.

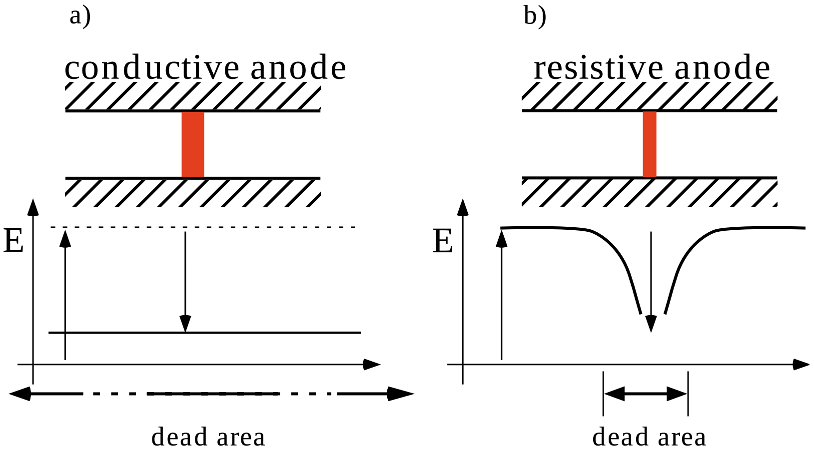

Figure 2.1: a) Spark and associated breakdown of the electric field and the corresponding dead area for a normal conducting anode; b) same for spark gap with a semiconductive anode.

independently of its position in the gas gap. The initial ionisation appears during the crossing of the gas gap by an ionising particle. Hence, the crossing time puts a lower limit on the best possible time resolution value, which is approximately 10 ps for relativistic particles for a gap size of a few mm.

It is important to recall the basic physics principles of a standard parallel plate spark counter. The spark counter works in a streamer discharge mode, which can be realised in a gas mixture with good photon absorption properties. The spark development starts from a free electron, which produces a Townsend avalanche in a high electric field:

$$N_e = exp(\alpha v_{drift} \cdot t)$$
$$\alpha = Ap \cdot exp(-Bp/E)$$

where α is the first Townsend coefficient, A, B are constants, p the pressure, E the electric field, and v_{drift} the electron drift velocity. When the number of electrons in the head of the avalanche reaches 10^8 (Meek's criterion), a new, very fast streamer mechanism of ionisation propagation appears. The streamers produce a conducting plasma channel between the electrodes. The discharge current through this channel increases and finally a spark appears. An important feature, the delay time of the discharge development from an electron to a spark is mainly determined by the first Townsend avalanche, i.e. by the first ionisation which occurs in the gap. The fluctuation of this delay time is the sum of the fluctuations of the avalanche development and, dominantly, the occurrence of the streamer. The time resolution is given by the fluctuation of the delay time, i.e. by

$$\delta\tau \sim \tau \sim 1/(\alpha v_{drift})$$
$$1/pv_{drift} \cdot exp(Bp/E) \sim 1/E \cdot exp(Bp/E)$$

where $v_{drift} \sim E/p$.

A *standard* spark counter (with metallic anode and cathode) has an area in the order of a few cm^2 because as the area increases, the discharge energy in a spark becomes so large that it will damage the counter electrodes. The counting rate of this type of counter is also limited by a dead time of more than 1 ms, which is needed to remove ions from the gap (this value depends on the gas mixture). To reduce these problems, a new version of the spark counter was proposed [2]. The main modifications were the introduction of a resistive electrode (semiconducting glass) and a special gas mixture for photon absorption. With these modifications the performance of spark counters changes dramatically. Now, only a small local area of electrode is discharged by a spark. The high voltage drops only around each

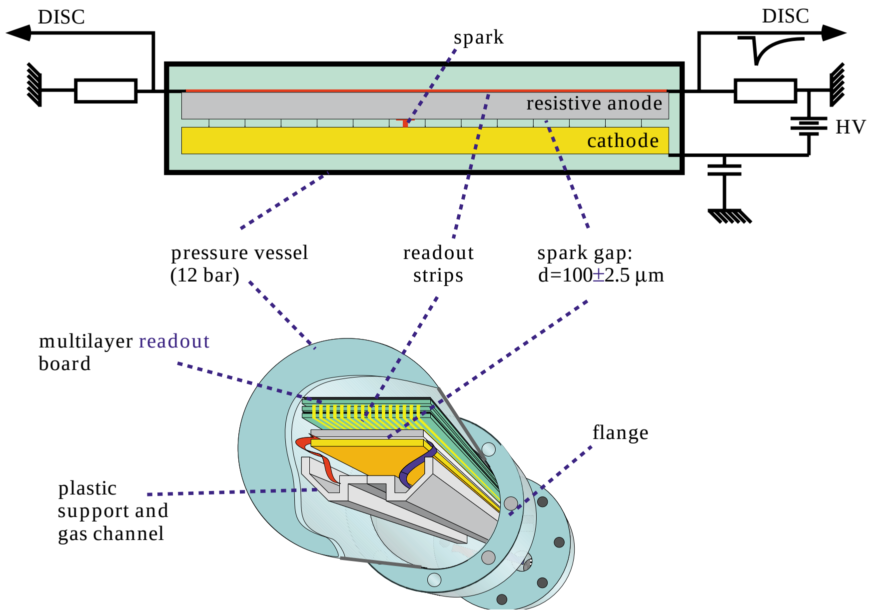

Figure 2.2: Layout of the Pestov spark counter. The top figure shows a schematic view of the main components of the counter, i.e., the electrodes, the 100 μm spark gap, the pressurized gas and the indication of the readout scheme via strip lines. The bottom figure shows a more realistic view with additional components, i.e. the 50 Ω multi-layer readout board and the extruded plastic support structure which serves also as gas channel.

discharge, while the remaining counter area is still sensitive to particles. The overall rate capability of the spark counter improves significantly. The problem associated with the high energy of the spark also disappears due to the smaller area of each discharge (see Fig. 2.1). Fig. 2.2 shows the layout of the Pestov counter.

A constant high voltage, of up to twice the threshold value for particle detection, is applied to the counter electrodes. The counter is read out via strip lines positioned on the outer side of the resistive electrode. The impedance of each strip line is equal to 50 Ω. Signals from sparks are detected by fast discriminators at both ends of each strip. The following design criteria ensure satisfactory performance of the counter:

1) Time resolution being proportional to the gap size, a small gap size of 100 μm is adopted.

2) A gas pressure of 12 bars yields about 96 % counter efficiency.

3) The bulk resistivity of the anode exceeds 10^9 Ωcm, to provide enough time to remove ions from the gap. The thickness of the anode (2 mm in this case) determines the size of the dead area. The dead area should be large enough to ensure complete photon absorption by the quencher gases in the region of the breakdown thus avoiding the initiation of secondary sparks by Compton electrons.

4) The quencher gases provide photon absorption from the energy corresponding to the cathode work function, to prevent secondary sparks initiated by photon feed back. Fig. 2.3 shows the absorption spectrum of the standard gas mixture consisting of 0.07(bar) C_4H_6 + 0.3 C_2H_4 + 2.4 $C_4H_1 0$ + 9.23 Ar = 12 bar. Each gas component absorbs photons at a different photon energy range.

In many previous experiments conducted with various gas compositions (but without freons) and cathode materials [4], a strong influence of the photon feedback on the discharge localization was observed. Fig. 2.4 shows an example of this effect. The average signal from the counter was used to estimate the level of the discharge localization. For the standard gas mixture, but without 1,3-Butadiene (C_4H_6),

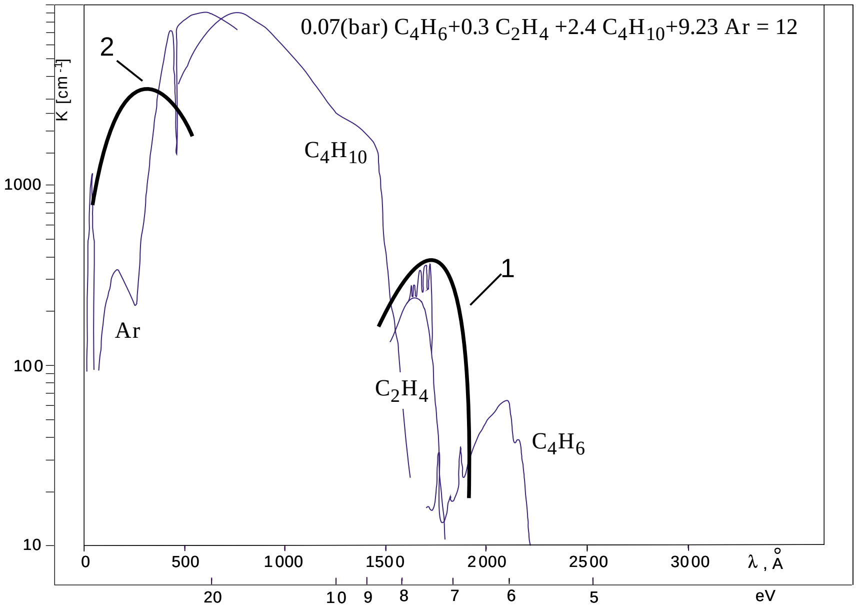

Figure 2.3: Absorption spectra of the gas components corresponding to their quantity in the gas mixtures used. 1) Propylene (C_3H_6); 2) Neon.

the localization worsens considerably (Fig. 2.4, curve 2). After replacing Ethylene (C_2H_4) with the same quantity of Propylene (C_3H_6), the localization of the gas composition with 1,3-Butadiene (C_4H_6) was almost restored (Fig. 2.4, curve 3) since the absorption characteristic of this new component covered partially the absorption region of 1,3-Butadiene (see Fig 2.3, curve 1). Note that a gas mixture without 1,3-Butadiene, which poses a health hazard, has been identified.

The pressure of each component of this gas mixture has been optimised with respect to time resolution, discharge localisation, stability of operation and counter lifetime. However, the absorption efficiency of this gas mixture is very low around the work function of typical cathode materials, e.g. aluminium or copper. The "gap" between the work function of the cathode material and the region where the photo-absorption cross section is sufficiently high is closed during a process called conditioning: the counter is operated with a γ-source in order to produce a thin polymeric layer on the surface of the cathode that shifts the work function to higher energies. After recording 10^5-10^6 sparks/cm^2, the counter characteristics stabilise with time.

To avoid conditioning with a γ-source, a new R&D program is in progress, using a cathode material with a sufficiently high work function. Measurements with spark counters using tungsten cathodes demonstrated good performance without conditioning [5] but the counter life-time with the standard gas mixture became worse due to the Malter effect. Therefore, both a new gas mixture with low polymerisation and a cathode material, with a high enough electron work function without the need of a polymeric layer are sought. A potential candidate is a mixture with DME, which has low polymerisation [6], in combination with an aluminium nitride cathode, which has a work function of about 8 eV [7]. The localisation properties of this spark counter have recently been investigated [8] with positive result.

2.2.1.2 Main counter and electronics characteristics

The pulse shape and its discrimination Using the "standard" gas mixture (see Fig. 2.3) the threshold for particle detection is about 3 kV. The output pulses (cf. Fig. 2.10) have a rise time better than 200 ps. The trailing part of the signal varies due to after-pulses which appear in the range of a few nanoseconds. The fast rise time and the variable overall pulse exclude standard methods of slew com-

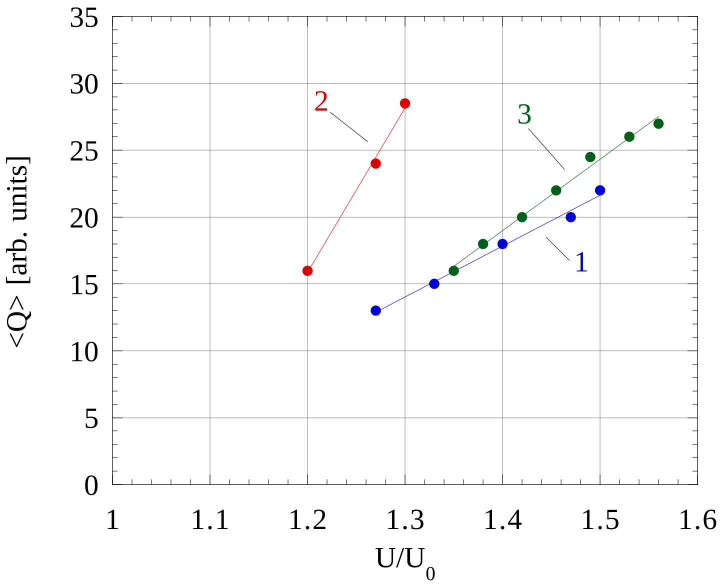

Figure 2.4: Average charge from the spark counter as a function of overvoltage: 1) the standard gas mixture; 2) the standard gas mixture but without 1.3-Butadiene (C_4H_6); 3) the previous gas mixture with replacement of Ethylene (C_2H_4) by Propylene (C_3H_6).

pensation, e.g. using the measured charge or using a constant fraction discriminator. A fast leading edge discriminator would be desirable. However, measurements [9] have shown that standard leading edge discriminators limit the time resolution to about 70 ps. Therefore a novel type of discriminator is used to match the intrinsic response time of the counter and to provide slew compensation. This discrimination is based on the simultaneous time measurement by two identical leading-edge discriminators with different thresholds [10] and provides hardware extrapolation to time t_0. The principal circuit diagram and the extrapolation method are depicted in Fig. 2.5. One can show that the proper choice of resistors and capacitors in Fig. 2.5 a) yields a crossing time of the two internally generated voltages, independently from the rise time of the input pulse. The experimental accuracy of the slew compensation turns out to be 10-20 ps [9, 10]. A chip version of the DTD is under development [11].

Efficiency Fig. 2.6a depicts the measurements of the counter efficiency obtained at different high voltages. The solid curve corresponds to calculations based on the streamer theory [12]. Fig. 2.6b) shows the plateau curve obtained with a ^{60}Co γ-source (closed circles). It shows the onset of the detection threshold at about 3.2 kV. The plateau is reached at 4 kV. A comfortable operating voltage, in the middle of the plateau curve (4.5 kV), yields a corresponding time resolution which is sufficient for typical heavy-ion experiments. The background is shown as the open circles when the source is shielded. This counting rate compares favourably with typical rates of a few 10 Hz/cm^2 in heavy-ion experiments.

Long-term stability test In total, 8 counters have been operated satisfactorily over a period of more than 6 months. The integrated dose rate was equivalent to about 5 years LHC Pb running in the projected ALICE environment [11].

Space resolution The gap size of 0.1 mm determines the accuracy of the coordinate measurement in the direction perpendicular to the electrode plane. The counter, read out via strip lines (Fig. 2.2), provides a two-dimensional reconstruction of the spark location in the electrode plane [9]. The position

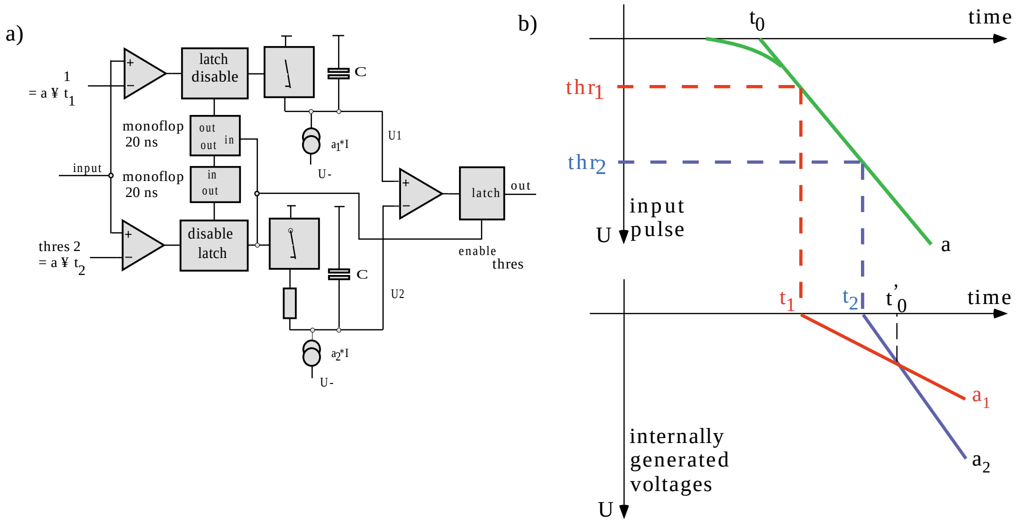

Figure 2.5: a) Principal circuit diagram of the Double Threshold Discriminator; b) Schematic diagram of the walk compensation by extrapolation to t_0.

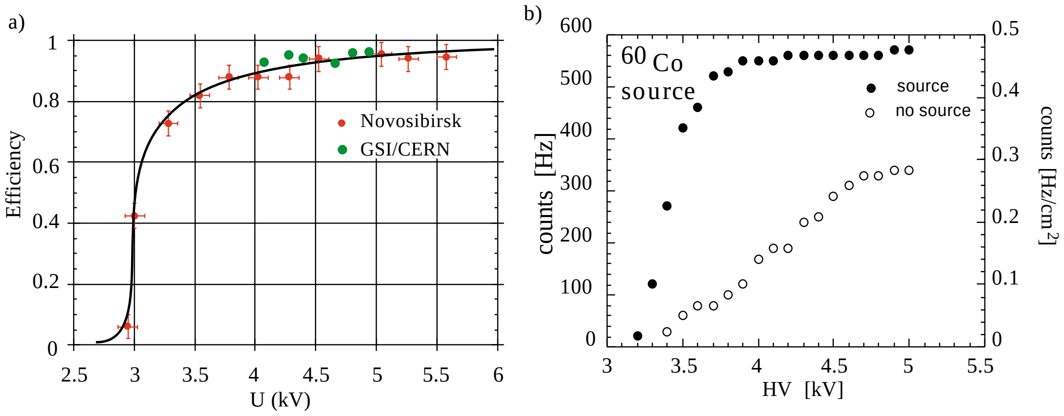

Figure 2.6: a) Efficiency for the detection of a minimum ionising particle; b) plateau curve from the irradiation of the counter with photons from a ^{60}Co source (closed circles) and with source shielded (open circles).

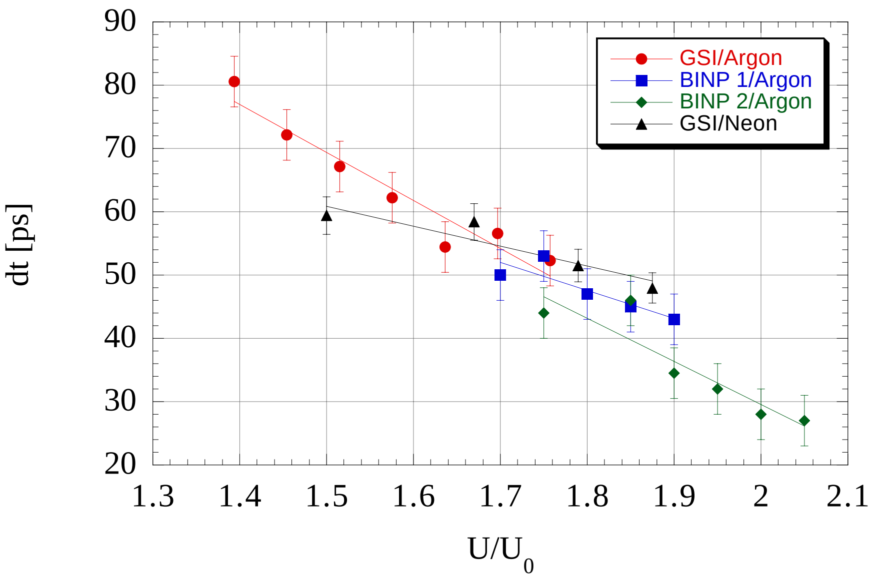

Figure 2.7: Time resolution (FWHM/2.35) as a function of overvoltage applied to the counter. The graph compares experiments done at GSI and at BINP. At BINP gas mixtures with different fractions of butadiene were used.

determination, transverse to the strip direction, is based on the measurement of the distribution of the charge on several strips. From experimental data, the transverse coordinate resolution has been measured to be 0.3 mm . The position of a spark in strip direction is measured by the time difference of the signal arriving at opposite ends of the strip. The longitudinal position resolution is limited by the resolution of the electronics, mainly by the binning of the time digitizer, and is 2.5 mm for a binning of 50 ps.

Time resolution Fig. 2.7 shows the time resolution as a function of overvoltage applied to the counter. The measurements, based on the FWHM of experimental distributions, show that the time resolution (FWHM/2.35) of 25 ps is possible with spark counters [1]. The time resolution scales, in the range considered, linearly with the overvoltage applied.

2.2.1.3 Timing tails and photon feedback

The experimental timing distributions have “tails” which extend beyond a Gaussian curve. A typical experimental distribution is shown in Fig. 2.8.

The experimental setup for the cosmic tests consisted of two spark counters, which were placed on top of each other at a distance of 50 mm. The timing spectra between these counters were taken, using as a trigger the coincidence signal of both counters. The features of these experiments were:

a) the full area of 40×300 mm^2 of each counter was under test;

b) about 1-2 days were needed to accumulate a timing spectrum;

c) stability and reproducibility of the results during more than one month of operation were demonstrated.

To estimate quantitatively the percentage of the timing tail events, two characteristics were calculated for each experimental distribution: the “non-Gaussian tail”, i.e., the part of the distribution which extends beyond the Gaussian curve, and the “timing tail $>$ 500 ps”, i.e., the fraction of events with a delay time

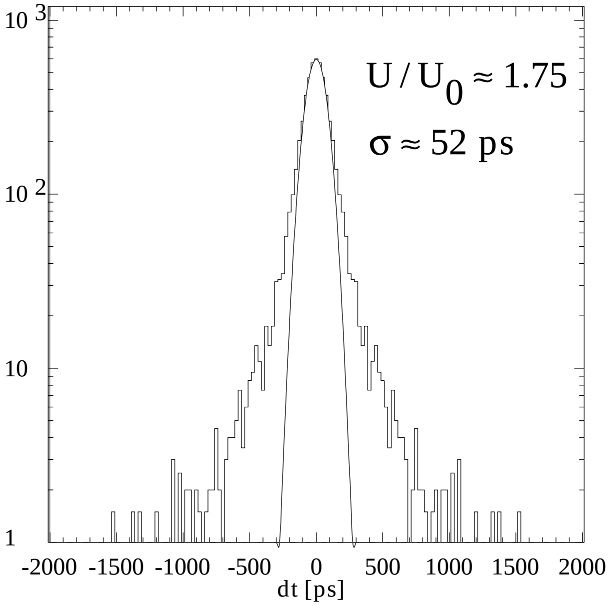

Figure 2.8: Time resolution obtained between two Pestov counters with cosmic rays and the standard gas mixture.

exceeding 500 ps. Fig. 2.9 shows the dependence of these two characteristics on the overvoltage for the counters with the standard gas mixture (standard organic + Argon) and with a new gas mixture (standard organic + Neon).

The experimental setup for the spark counter tests at the GSI heavy ion beam facility is described in [13]. During these experiments a comparative test of the spark counter performance was made with different gas compositions, based on the organic part from the standard gas mixture in combination with a noble gas (Helium, Neon, Argon, Krypton or Xenon). The correlation between the timing tail and the type of noble gas in the gas mixture was determined. The tail values were at a minimum with the Neon-based gas mixture and strongly increased with heavier noble gases.

Employing a ^{60}Co γ-source, a precursor signal from the spark counter was observed. A fast 5 GS/s oscilloscope was used to obtain the pulse shape directly from two neighbouring strips of the spark counter. A spark counter with the standard gas mixture was used. Measurements were carried out at three differ-

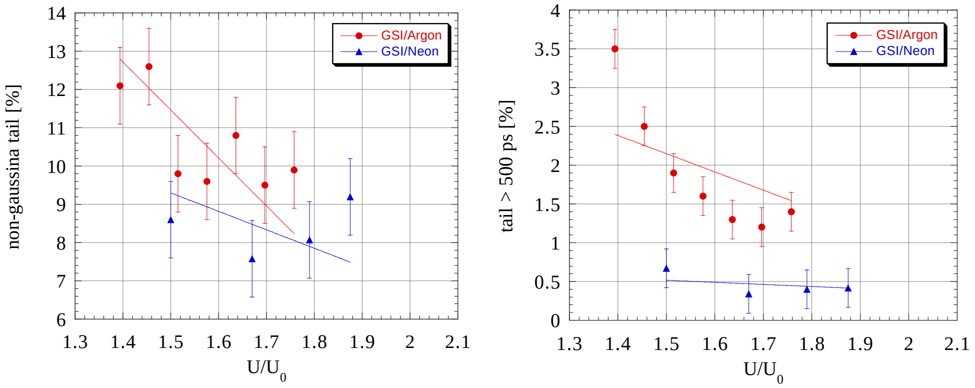

Figure 2.9: "Non-gaussian tail" (left) and "timing tail >500 ps" (right). The lines are the model prediction based on the assumption that the timing tail is proportional to the time resolution (Fig. 2.7).

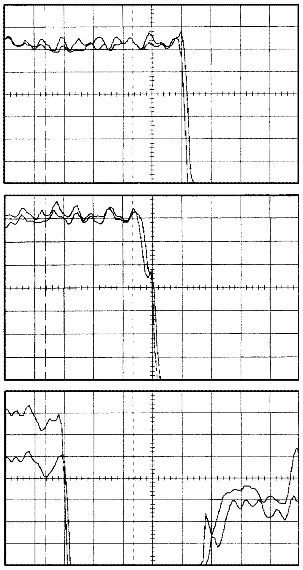

Figure 2.10: Leading edge of signals from two neighbouring strips at the standard gas mixture, HV=3.6 kV. The oscilloscope settings were 2 mV/div and 2 ns/div. The rise time shown in the graphs is limited by the bandwidth of the oscilloscope.

ent HV settings: a) near the counter threshold at 3 kV; b) at the beginning of the plateau at 3.6 kV and c) at 4.0 kV. Typical signal pulses at HV=3.6 kV are presented here because the time resolution of the oscilloscope in this case is well adapted to the counter time characteristics. The average signal amplitude from the spark counter was $\approx$100 mV on 50 Ω load at HV=3.6 kV. Fig. 2.10 shows the beginning of the signal formation in the case where a primary ionization appears just between the two strips studied. Most signals had a sharp front (Fig. 2.10 top). However, more than 12% of events had a small precursor signal. The average amplitude of these signals was only about 2 mV but was observed with a significance S/B$\approx$5. The appearance of precursor signals was, in many cases, very close in time to the leading edge of the main pulse (Fig. 2.10 middle). Fig. 2.10 bottom shows another example of a precursor signal, which was separated from the main signal by $\approx$1 ns.

Nature of delayed signals (model) It is important for further understanding, to recall the physical principle of the standard parallel plate counter discussed previously. The delay time of the discharge development from an electron to a spark is mainly determined by the first Townsend avalanche and equal to $20/\alpha v_- \equiv X_0/v_-$, where α and v_- are the first Townsend coefficient and the electron drift velocity, respectively. The fluctuation of the delay time is the sum of the fluctuation of the avalanche development and the occurrence of the streamer. As it was shown experimentally, the counter time resolution is roughly proportional to the delay time [12].

However, in some cases the anode stops the development of some avalanches before they reach the “critical” charge. This happens in the cases when a primary ionization is created near the anode, in a gas layer closer than $X_0=20/\alpha$ to the anode. Two mechanisms of delayed streamer creation are conceivable, based on photon feedback from this avalanche:

1) The initial avalanche continues to grow due to secondary avalanches initiated by the feedback photons and finally reaches the “critical” charge. The additional delay time in the occurrence of the streamer depends on the additional charge, ΔQ, needed for streamer creation and the ionization property of the gas mixture. In the case of a small ΔQ this delay time is very short. An increase

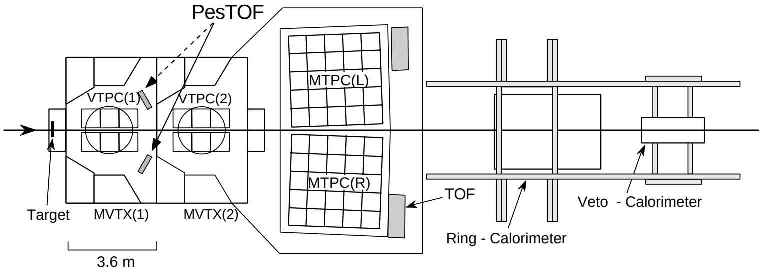

Figure 2.11: Set-up of the NA49 experiment. The dashed arrow points to the foreseen installation of the second tower in 2000.

in the gas ionization cross section reduces the timing tail due to secondary electrons being created by photons, close to the initial avalanche.

2) An avalanche (or a chain of avalanches) initiated by feedback photons grows, without interference, with the initial avalanche. In this case the additional delay time of the streamer is equal to or exceeds the standard streamer delay time. It is important to be aware that streamers initiated by photoelectrons from the cathode belong to this group of events.

The model predicts an improvement of the timing tail with increasing HV, since the gas layer thickness ($X_0=20/\alpha$) is reduced. The experimental data (Fig. 2.9) confirm this model's prediction.

The spark counter time resolution is proportional to X_0/v_- and the timing tail (for a small X_0) is, according to the model, also proportional to X_0. The experimental data confirm a correlation in the behaviour of the time resolution and timing tail curves when changing HV (Fig. 2.7, 2.9).

For the gas mixture studied, the "tail $>$ 500 ps" is a small fraction of the "non-Gaussian" tail (Fig. 2.9). In the framework of the model, this experimental result means that the delayed streamers were created mainly by a continuous increase of the initial avalanche (first mechanism, see above) and that the ionization property of the gas mixture is important. Only Isobutane and Argon, in the standard gas mixture, provide photon absorption by gas ionization, but the argon cross section rapidly decreases for photon energies above 30 eV. The model predicts an improvement of the timing tail with the replacement of Argon by Neon since Neon has the best absorption characteristics among noble gases at this photon energy range (Fig. 2.3, curve 2). The experimental results confirmed this prediction.

The direct observation of a precursor signal has an obvious explanation in the framework of the model: a precursor signal is a low gain primary avalanche, which initiates a delayed spark (timing signal).

It is important to be aware that, at present, the model predictions are qualitative only and many additional effects were not taken into account (for example, the dependence of the emission spectrum on the HV applied as well as on the gas composition, and so on).

2.2.1.4 Application of Pestov spark counters in experiments

Arrays of Pestov spark counters have been used in the 1997-1999 runs of the NA49 experiment. Fig. 2.11 shows the experimental set-up of the NA49 experiment, indicating the position of the Pestov spark counters array.

Fig. 2.12 shows a particle identification spectrum obtained with an array of 12 counters during the 1997 p-Pb run. The separation of kaons from pions was limited by the existence of timing tails as discussed above. The time resolution obtained for the *total* area of the array was $\approx$ 80 ps, which is very close to the nominal resolution obtainable at the overvoltage applied (U/U_0=1.5) (cf. Fig. 2.7) . The influence of the timing tails can be reduced by using Neon as the main gas, or by providing a larger

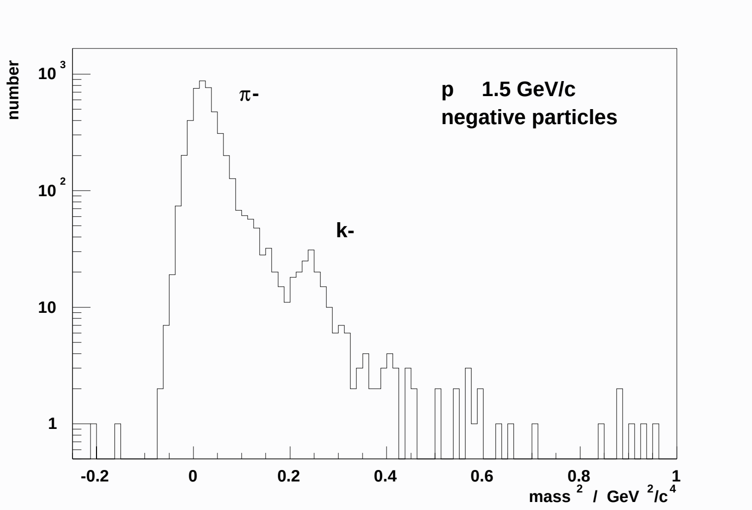

Figure 2.12: Particle identification spectrum obtained in NA49 p-Pb collisions.

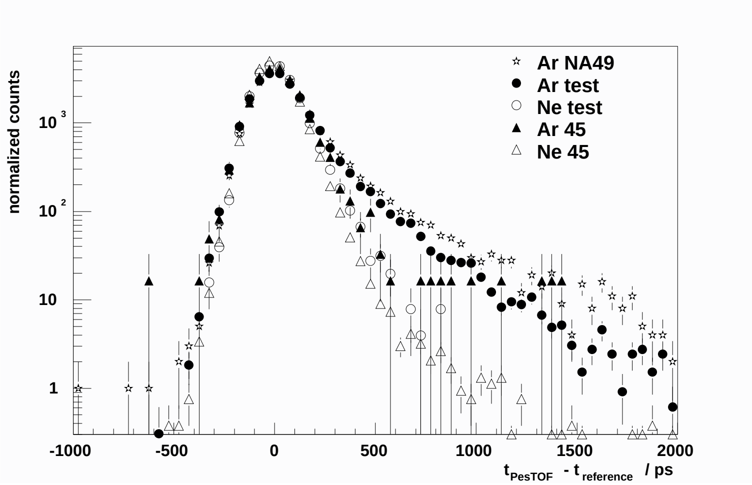

Figure 2.13: Timing spectrum for different gases and geometries.

effective gap (e.g. 45° particle incidence). This is demonstrated in Fig. 2.13, which scales the time resolution spectrum for Ar-based gas mixtures with parameters obtained in various test runs employing other gases or geometries [13].

During the lead beam time in November 1999, a "tower" of Pestov counters consisting of 20 Pestov counters, which were mounted on a common flange, was employed. The counters were staggered in two rows to provide full geometric coverage. This multiflange allowed an equal distribution of gas to all counters. The total surface of the PesTOF wall (taking into account the counter overlapping regions) was about 0.22 m^2, where each of the counters had a sensitive area of 40 × 300 mm^2. To improve on the timing tail, a gas mixture with Neon as the main gas was used in this run.

The time and charge signals of the 20 Pestov detectors were read out with a new, very compact electronic system. Each detector had 32 timing TDCs and 16 QDCs. As in previous experiments [14], the discriminators and QDCs were mounted directly on the detectors. A new development was that the time converters also were mounted directly on the detectors, so that the whole system of 640 TDCs and 320 QDCs, apart from the necessary power lines, was connected by only 5 twisted-pair cables to a VME-crate. Equally important, for the first time, a new technique for high-precision timing measurements with a large detector was used, where time-stamps and not time differences were measured. This led to a significant simplification of the experiment. The new TDC-system made use of 4-channel High Resolution TDC chips, developed at CERN by J.Christiansen and M.Mota [15]. The necessary logic and the layout of the different boards, including the VME-units, were developed, tested and built by the group of J.Biri at the KFKI in Budapest.

The readout of the PesTOF tower electronics was incorporated into the NA49 data acquisition. About 200k lead-lead events at 40 GeV/c were recorded during November 1999. The average multiplicity in the PesTOF tower was of 8.8 particles per event. The whole system operated without any failure for a data run of two weeks.

2.2.1.5 Summary of the Pestov spark counter

On the technological side, the counter design has been optimized so that a mass production scheme is within reach. The main problems, related to the choice of the proper materials and clean-room assembly procedures, have been solved. The successful introduction of high-resolution TDC ASICs allows the economical readout of large multichannel systems.

On the performance side, timing tails limit the particle separation to a certain extent. However, with the optimisation outlined above, a reduction of the timing tails to an acceptable level is achieved. The successful test of a medium size PesTOF array in NA49 has shown that the counters would work well in an experimental environment, typical of heavy-ion experiments, e.g. the GSI FOPI or CERN ALICE experiment.

2.2.2 The Parallel Plate Chamber

2.2.2.1 PPC as a Detector for MIPs

The parallel plate chamber (PPC) was also studied within the ALICE TOF R&D program. As described in Refs. [16–19], a Parallel Plate Chamber is a single-gap gaseous detector operated in avalanche mode. It consists normally of two planar electrodes made of metal, or metallized ceramic or plastic, kept apart at a fixed distance of 0.5–2 mm using precise spacers, with 5–10 μm accuracy. The inner surfaces of the electrodes are carefully polished so that the electric field produced will have excellent uniformity. The standard flatness precision is kept within 10 μm (depending on the gap width). The electrode sizes range from 10×10 mm^2 to 100×100 mm^2 or even larger; the total detector thickness is usually a few millimeters, depending on the design and the materials.

The high electric field of 2–6 kV/mm between the electrodes allows the immediate Townsend avalanche amplification of the primary ionization, at any point within the sensitive volume. As described in Ref. [20], the motion of the electrons in the avalanche induces a very fast signal (rise time less than 1 ns) on the electrodes. This fast signal is followed by a slow signal that lasts for several microseconds, which corresponds to the motion of positive ions. Depending on the gas filling, a gain of 10^3–10^4 can be reached with a very low spark probability (see Ref. [21]).

The advantages of the PPC technique, as summarised in Ref. [21], include a very fast response and a high rate capability of 10^7 Hz/cm^2. Thanks to these features, PPCs were widely studied for LHC applications at CERN during the early 1990s, particularly for the very forward muon calorimetry and the forward muon trigger in RD5 and RD37 frameworks. The use of PPCs as efficient detectors for MIPs (with the added possibility of high resolution timing) was not under investigation for two main reasons:

1. A naïve opinion dominated that the PPC timing resolution must be of the order of 1–2 ns for a 1 mm gas gap, caused by the intrinsic jitter of the avalanche. This opinion was supported by the experience which had been gained since 1966 of Pestov spark counters. As discussed previously, the good time resolution of the Pestov counters is only obtained under special conditions. These

are: (a) a very large value of the electric field (60 kV/mm), an order of magnitude higher than that used for a PPC; (b) a very narrow gas gap (100 μm); and (c) a high gas pressure (12 bars).

2. The PPC signals are small, about 1–10 fC. The amplitude spectrum in case of pure avalanche amplification has a 1/A-shape with maximum of events being close to zero. This made detection of MIPs rather inefficient; typically, with a gas mixture containing CO_2, i-C_4H_{10} and CH_4, the maximum efficiency was 50–80%, without any observable plateau. Front-end electronics, needed for accurate timing measurements, are much noisier and thus would further reduce the efficiency.

An R&D on PPCs for precise and efficient TOF applications was launched at ITEP (Moscow, Russia) with the participation of INFN (Florence) [21], and then continued as an ALICE R&D with the participation of CERN, ITEP, MePhI Moscow, YerPhi Yerevan, JINR Dubna, and PNPI Gatchina.

2.2.2.2 First Test Results at ITEP

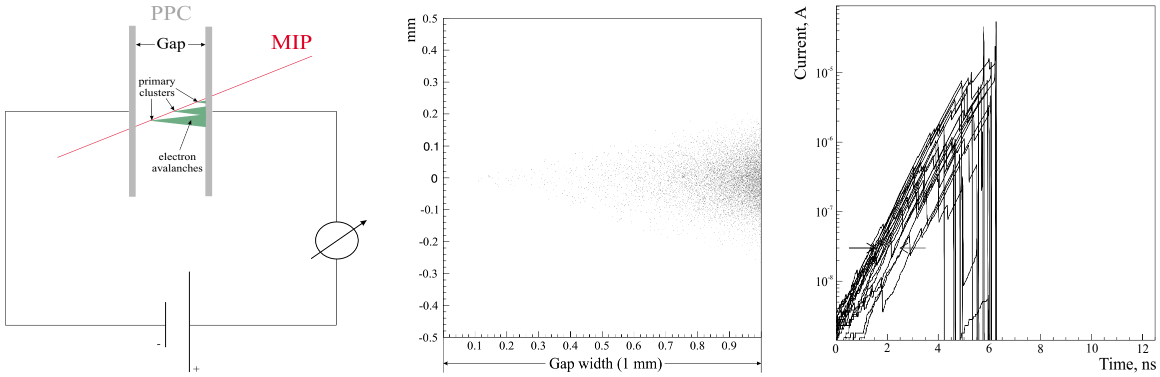

a *b* *c*

Figure 2.14: Simulations of the PPC operation, with 1 mm gap width, filled with pure iso-C_4H_{10}:
a — ionising particle crossing the chamber (schematic drawing);
b — charge produced in a simulated avalanche;
c — examples of electric currents induced in the outer circuit.

To test the possibility of using PPC as a base detector for ALICE TOF and to predict its timing properties, computer simulations of the processes taking place in the chamber were performed. The assumption was that the PPC operates in a Townsend mode of gas amplification [22]. Consider a single-gap PPC crossed by MIP as shown in Fig. 2.14*a*. Due to a high electric field applied between the PPC electrodes, electrons produced in the primary ionization give birth to avalanches developing towards the anode. Fig. 2.14*b* shows the positive charge distribution created by the avalanche. The separation of positive and negative charges induces an electric current in the outer circuit. The statistical nature of the primary ionization and fluctuations in the number of ionising collisions, during the first stages of the avalanche development, substantially influence the resulting signal. Fig. 2.14*c* shows the induced current for several events. The interval pointed with the arrows is roughly what may be called the PPC TOF resolution.

The R&D at ITEP first focused on 1.5 mm-gap ceramic PPCs previously used in RD37 project [21], and later on specially designed ceramic and metal PPCs, including a detector in which the gas gap could be externally adjusted between 0.5 and 2 mm. The ceramic electrodes were covered with Cr, Au and Cu. The cell sizes varied between 20×20 and 50×50 mm^2. One-, two- and three-component gas mixtures containing CO_2, i-C_4H_{10} and Ar were tested; these operated at different high voltage regions and had different absorptions of the self-produced ultraviolet.

The beam tests with MIPs were performed at ITEP PS for several years, using 3–10 GeV/*c* pions and protons. Initially the measured TOF resolution was of ~ 1 ns. The correlation between time and charge was used off-line to improve the PPC time resolution; this opened the way for using the PPC as a TOF detector.

One of the first results is shown in Fig. 2.15*a*. This figure shows the time (measured with a leading-edge discriminator) versus the charge. Off-line T(A) corrections and a quadratic subtraction of the start system jitter led to a 300–400 ps TOF resolution (see Fig. 2.15*b*). This value included the 200–250 ps intrinsic resolution of front-end electronics. The time resolution depended on the size of the signal (see Fig. 2.15*c*). With all studied gas mixtures, moving away from the pedestal to higher amplitudes improves the TOF resolution; however this also reduces the detector efficiency to 10–20%.

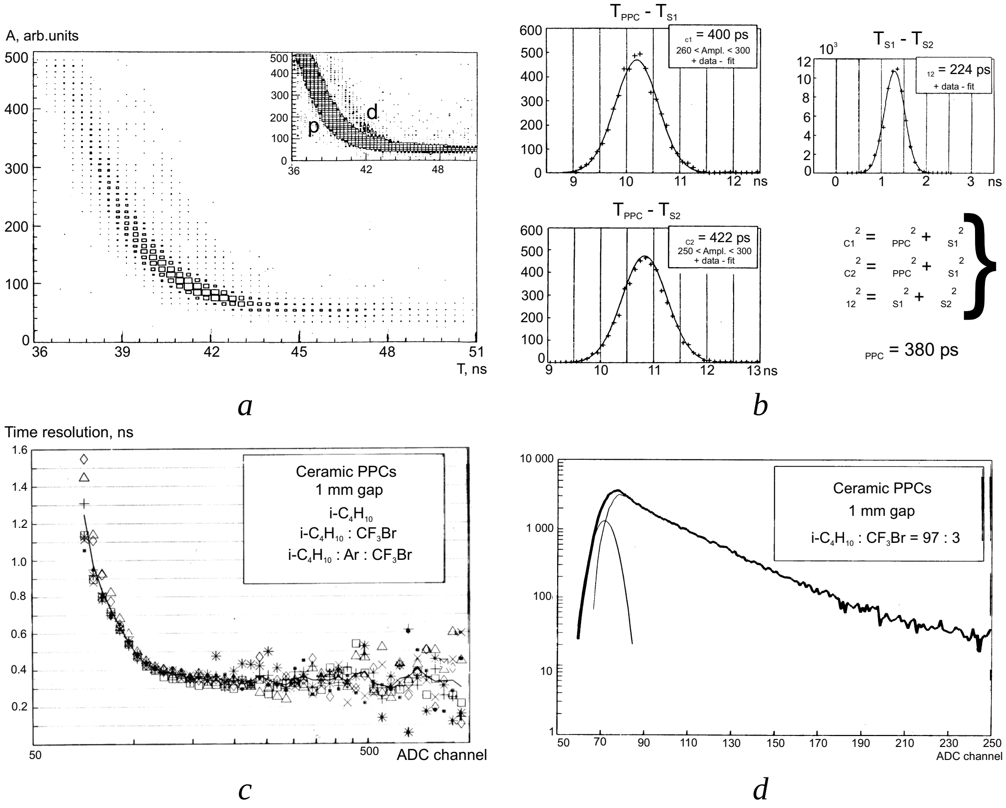

Figure 2.15: First ITEP beam test results on the PPC timing characteristics:
a — T(A)-dependence, the plot in the right top corner shows that an admixture of deuterons in the proton beam could be distinguished;
b — the TOF measurements idea, involving two identical start scintillator counters;
c — TOF resolution at different amplitudes measured on several gas mixtures;
d — amplitude spectra measured with a small admixture of CF_3Br.

A 5–10% admixture of a highly electronegative gas, CF_3Br, changed the situation dramatically. Under the same conditions, the average collected charge increased to 30–50 fC and the amplitude distribution became much broader (see Fig. 2.15*d*). This resulted in a PPC time resolution of 200 ps after subtracting the electronics jitter, with a 50–70% efficiency for MIPs. These results may be found in Ref. [21].

2.2.2.3 R&D on PPC Single Cells in 1995–97

In order to use the PPC as a TOF detector, the front-end electronics had to be substantially improved. The signal undergoes a double amplification, as shown in Fig. 2.16*a*. The preamplifier was placed as close to the PPC cell as possible (one of the reasons for this was to avoid possible cross-talk in future multicell modules). The diodes on the preamplifier input prevented the transistor being damaged by

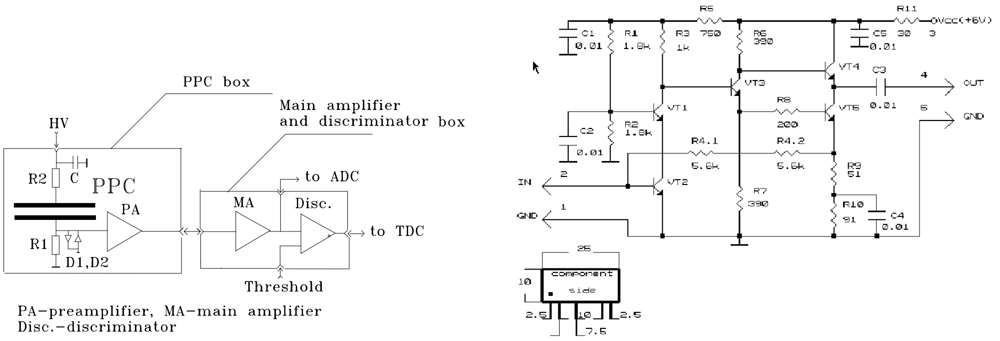

a *b*

Figure 2.16: Electronic channel for PPC:
a — main idea of the FEE connection;
b — example of the preamplifier design.

sparks. More than 10 different types of hybrid preamplifiers were constructed with the participation of ITEP, CPTA, PNPI, IHEP and CERN [23]. One of the intermediate versions of the preamplifier is shown in Fig. 2.16*b*. The ITEP preamplifier design used a cascade scheme with negative feedback to decrease the input impedance. The main amplifier, MAR6, commercially produced by Hewlett Packard and based on the INA-02184 chip, was usually placed at a distance from the detector.

Two types of discriminators were studied: a constant fraction discriminator (CFD) and a leading edge discriminator. Using CFD and omitting further T(A) corrections yielded worse time resolution than using a leading-edge discriminator followed by T(A) corrections. With CFD, an amplitude dependence on time was observed, but the shape of the correlation was different to that observed with a leading-edge discriminator. This indicates that the rise time of the signal from PPC depends on the amplitude. Using different T(A) corrections for each discriminator type, similar time resolutions were obtained. Since the leading-edge discriminator is a simple, cheap and stable device, the CFD was not used for further tests. A fast and low-noise front-end electronics, with well-measured characteristics, was developed. From then on, it could be considered to be a part of the detector, and its intrinsic time resolution was no longer to be subtracted from the total detector TOF resolution.

In addition, large improvements were made to the PPC itself. In 1995, the ITEP group proposed to use a double-gap design for each individual cell, schematically drawn in Fig. 2.17*a*. Simulations had shown that, compared to a single gap, the amplitude spectrum of the double-gap detector should have a non-zero maximum. This would considerably ease the setting of the threshold since it allows the use of higher thresholds without large losses in efficiency. Fig. 2.17*b* shows the amplitude spectrum measured with one of the ‘standard’ gas mixtures (Ar + i-C_4H_{10} + freon). It is clearly seen that the pulse-height spectrum had a non-exponential shape.

Different gas mixtures were studied under similar conditions. Figs. 2.17*b*–*d* show amplitude spectra for gas mixtures, based on different proportions of Ar, i-C_4H_{10} and DME but always with a 5% admixture of freon CF_3Br. Using DME instead of i-C_4H_{10} gives a significant increase of the signal-to-noise ratio and allowed a high detection efficiency for MIPs. A gap width of 1 mm, together with a reasonable discriminator threshold, produced an efficiency close to 100% with a high voltage plateau more than 200 V wide.

CF_3Br is banned by the Montreal convention, thus a replacement for freon that is not harmful to the ozone layer, had to be found. Gas mixtures based on $C_2H_2F_4$ were suggested. After tests, the choice of 0.6 mm gaps was fixed with a gas mixture containing 75% freon. DME also had to be replaced because of its negative effect on the chamber material. Based on the RPC R&D experience, an inflammable mixture of $C_2H_2F_4$, i-C_4H_{10} and SF_6 was finally chosen. The charge of the signal became more than one order of magnitude higher than in RD5/RD37 conditions, reaching 100 fC in the average. These gas mixture,s

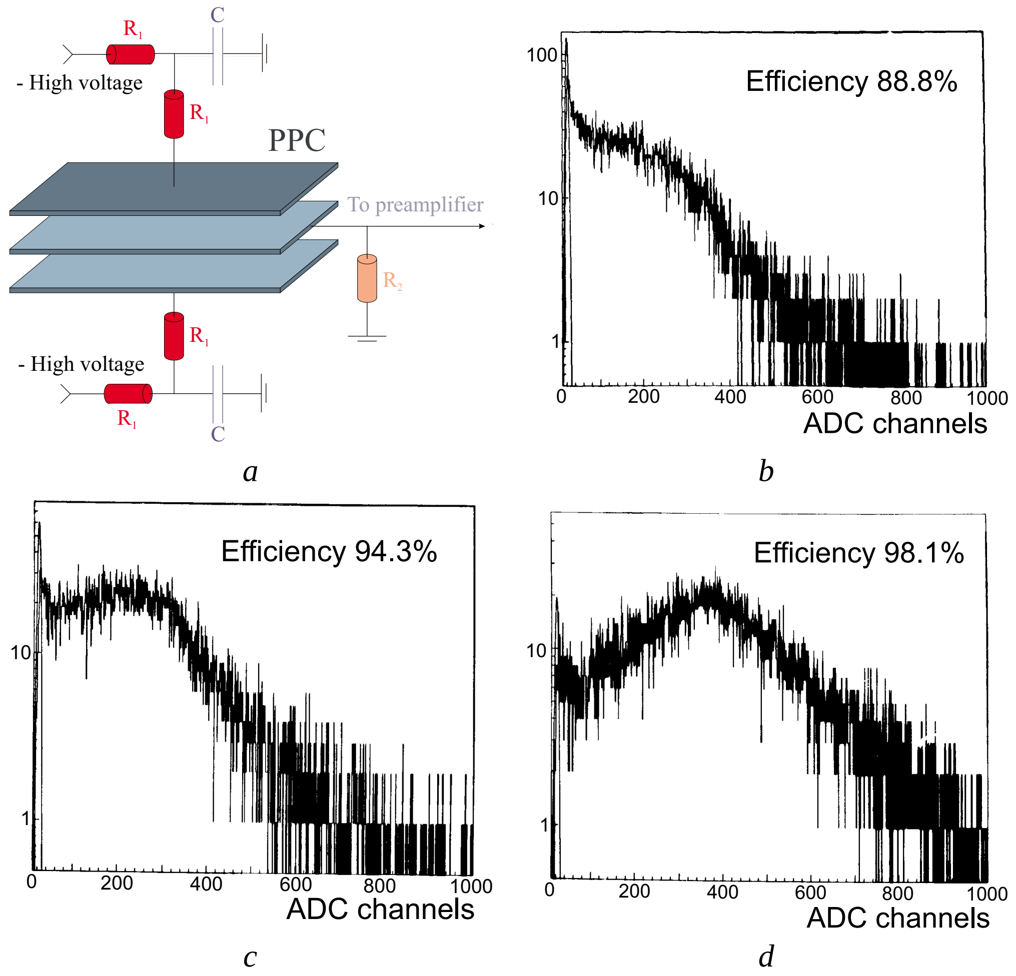

Figure 2.17: Double-gap PPC:
a — construction (schematic drawing);
b — amplitude spectrum measured with Ar + i-C_4H_{10} + freon;
c — amplitude spectrum measured with Ar + DME + freon;
d — amplitude spectrum measured with DME + freon.

together with new improved front-end electronics, led to an improvement of 2 orders of magnitude in the signal-to-noise ratio.

Concerning the PPC material, the R&D examined four options: ceramic, glass, plastic and metal. All electrodes, except the plastic, were spaced with quartz fibres of different diameters. All chambers consisted of two gaps. **Ceramic** electrodes had been used earlier for CMS and ALICE applications at CERN and ITEP. A special design of the ceramic electrodes was made for the TOF purposes. Alumina substrate Al_2O_3, used as the electrode material, was rigid enough to be processed by a polishing machine with a required accuracy of better than 5 μm. Grooves with rounded profiles, metallized for up to half of their width, were made, near the edges of the electrodes, to prevent breakdowns due to the increase of electric field in this region. Cheap optical **glass** used with the same scheme was smooth and flat enough to skip the polishing procedure. A few tests with **metal** electrodes were made using aluminium and stainless steel plates. An electro-chemical etching of large plates was necessary to prevent internal stresses during the aluminium electrodes production. To avoid their polishing, **plastic** electrodes were stamped from polysulfone and polycarbonate at a very high pressure (more that 100 bar) to achieve the required surface quality; the spacers were made as parts of the electrodes. A special low-temperature metal evaporation technique had to be employed to prevent the plastic from deformation. The plastic version of the detector is cheap and simple to produce and assemble.

All the detectors showed similar characteristics regardless of the material used. A typical time resolution and efficiency dependence on the 1×1 mm^2 beam position are presented in Fig. 2.18. The measurements were performed on ceramic electrodes and the scan was made from the centre of the cell to its edge. It may be seen that the change in the efficiency happened in a 1–2 mm wide zone at the edge, a size comparable to the size of the beam. The time resolution starts to degrade at a distance of 2–3 mm from the edge; this is about 10% of the electrode linear size, or 20% of its surface.

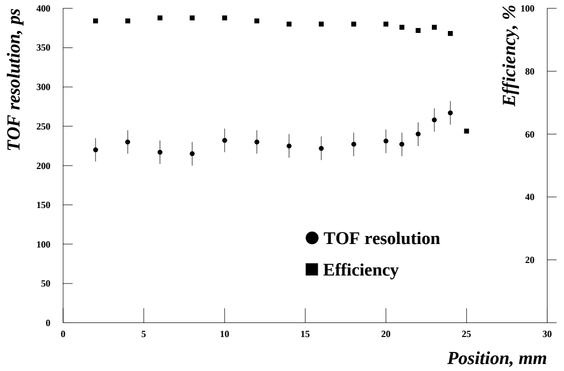

Figure 2.18: Scan of the TOF resolution and efficiency along the detector surface.

From the tests performed during 1997, the best detector options and parameters were found to be for:

detector	ceramic or metal, 50×50 cm^2
spacers	quartz fibres
gap width	0.6 mm
detector design	double-gap
preamplifier version	ITEP design
main amplifier version	ITEP design
discriminator type	leading-edge discriminator
gas mixture	DME + 3–15% CF$_3$Br, or $C_2H_2F_4$ + 25% DME
gas pressure	atmospheric
high voltage	3.4 kV/gap (for DME + 3.8% freon)
efficiency plateau width	>100 V
TOF resolution (PPC + FEE)	200 ps

Fig. 2.19 shows some typical plots. A two-dimensional distribution of time versus amplitude is plotted in Fig. 2.19*a*. This data was subjected to T(A) correction. The TOF resolution was calculated separately for narrow amplitude slices, using a Gaussian fit (shown in Fig. 2.19*b*). The resolution is better than 200 ps for most of the spectra, except the lower region. After polynomial T(A) correction and a small cut in the amplitudes, the total TOF resolution was calculated. As shown in Fig. 2.19*c*, the detector resolution, contributed from PPC and the electronics, was found to be 187 ps at a 93% level of efficiency. The jitter of the front-end electronics was $\sim$ 150 ps, and because of small input signals, this value could not be significantly improved. It follows that the intrinsic jitter of the PPC was 100–150 ps.

The PPC TOF resolution had always been calculated by Gaussian methods. For ALICE PID by means of TOF, it was very important to know the real shape of the timing spectra, especially of the late tail. The first investigations of the tails were made by the GSI group working with the Pestov spark counters. This device had large tails (see preceeding section) due to delayed secondary processes. The PPC timing spectrum was studied in 1997 both at the PS and the SPS. The conclusion was that for PPC with a total TOF resolution of 200 ps, there were no special sources of tails, and all deviations from the gaussian shape were a result of the time correlation to the amplitude, as shown in Fig. 2.19*b*. The

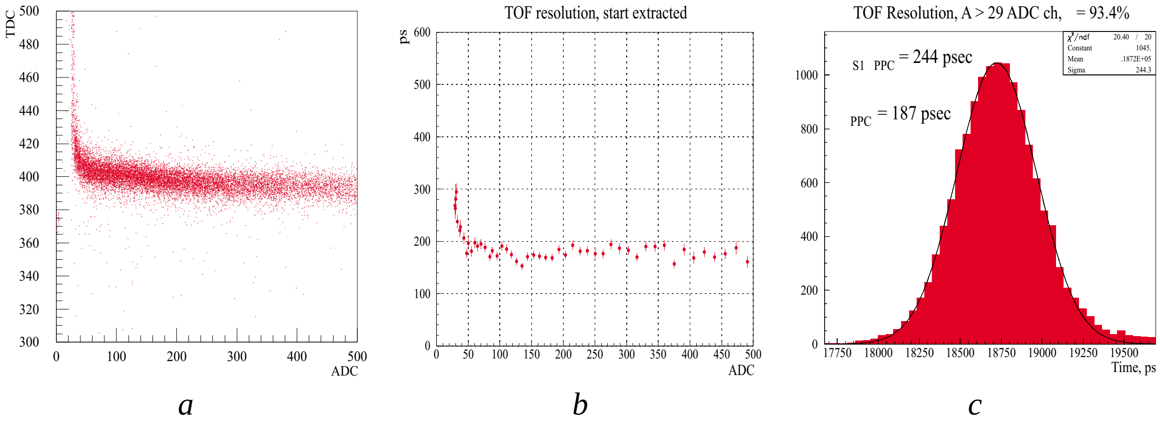

Figure 2.19: PPC TOF measurements results, 1997:
a — raw data in ADC and TDC units (ADC ch = 0.25 fC, TDC ch = 50 ps);
b — TOF resolution for different amplitudes;
c — resulting TOF resolution.

TOF distribution was an integral of Gaussian curves with slightly changing sigmas. An approximation of such a function with a sum of two Gaussians showed a 10–15% admixture of a wide distribution with a sigma of 300–350 ps. sigma. This resulted in an effective sigma of 220–230 ps and did not spoil the TOF performance significantly.

The conductive electrodes turned out to be one of the main PPC disadvantages, since they did not provide any self-quenching mechanism; thus retaining a probability for sparking. The probability of sparks was studied in the RD37 framework for the PPC usage in calorimetry, as reported in Ref. [24]; it was found there that, for a low gas gain of 10^2–10^3, the spark probability is very low. In highly efficient TOF detectors the gas gain is much higher and the effect had to be studied again. The results for a single-gap PPC with a 1 mm gap are shown in Fig. 2.20. A special trigger for very high amplitudes was employed to distinguish the spark signals. Fig. 2.20*a* (bottom) shows the measured probability of spark signals for different high voltages which can be compared to the efficiency (top). It should be noted that even at high efficiencies, the spark probability is still low, $\sim 10^{-4}$.

To learn more about the nature of the spark signals, separate studies were undertaken. Large amplitude signals were sent directly to an oscilloscope without any amplification. Fig. 2.20*b* shows several spark signals observed for different high voltage values within a 150 V range. All the spark signals had two peaks, with a total duration of about 200 ns and with $\sim$ 10 V amplitudes. No after-pulses were observed. The size of the spark signal was $\sim$ 100 nC; this corresponds to the total energy stored by the capacitance of the PPC.

Special front end electronics were designed to fit with these difficulties. The amplifier response to a spark event is shown in Fig. 2.20*c*. Immediately after a signal arrived, the amplifier became saturated, then returned to base line (with a small over-shoot). The output signal of the front end electronics was of the order of 1 V lasting for only a few microseconds. It was concluded that a single PPC could operate normally with a few rare sparks. A remaining unsolved problem was the existence of cross-talk between neighbouring cells inside a large detector module.

2.2.2.4 System Aspects and Modules

All attempts to build a multi-channel TOF system were based on an idea of a mosaic array of single cells, assembled to form a TOF module, as described in Ref. [25]. To obtain the time resolution and efficiency needed for the ALICE experiment, it was proposed to use several layers of such arrays, arranged on a chess-board matrix to avoid blind zones. Several PPC prototypes were built and tested with MIPs at

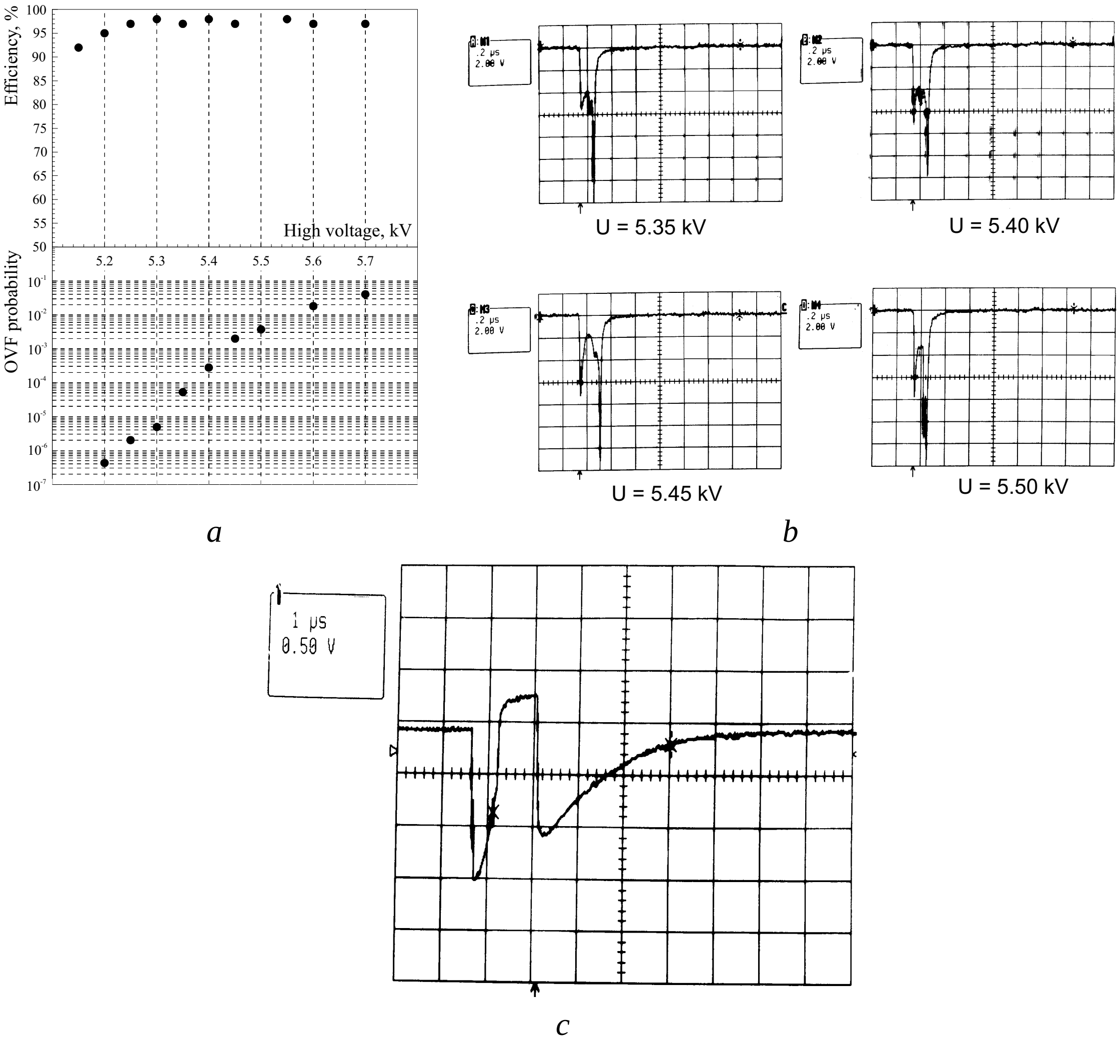

Figure 2.20: Spark signals study:
a — PPC efficiency and spark probability versus the high voltage for 68% Ar + 30% i-C_4H_{10} + 2% freon;
b — Spark signal shapes at several high voltages, scale units: 0.2 μs for the time, 2 V for the amplitude;
c — amplifier response for a spark signal, scale units: 1 μs for the time, 0.5 V for the amplitude.

CERN PS and SPS. Since the front end electronics was very fast and sensitive, the first problem was to suppress oscillations and achieve a stable module operation. The idea of putting together the chambers, each with its own preamplifier, turned out to be impractical.

A special multi-layer PCB was designed and built; this also served as a mechanical support. Sixteen PPC cells were placed in two rows on one side of the PCB and 16 preamplifiers were installed on the other side, as close to the individual detectors as possible, connected with wires through holes in the plate. Amplified signals were sent via a fast transmission line laid alongside the PCB and connected to its edge, where all the connections for further amplification, shaping, discrimination, HV and LV distribution were installed. The PCB layout consisted of 8 layers, included HV lines, and provided the fastest signal transmission possible. It was optimised to suppress cross-talk between the channels, both during cell operation and signal transmission. The HV supply had separate grounding and provided a common ground loop for all the 16 cells. Laboratory tests had shown that there was no degradation of the fast signal shape during its transmission along the PCB.

Two PCBs, each with 16 PPC cells, were placed together, with the detector planes facing each other and separated by 5 mm, to form the first 32-cell TOF module. They were put in a common gas volume.

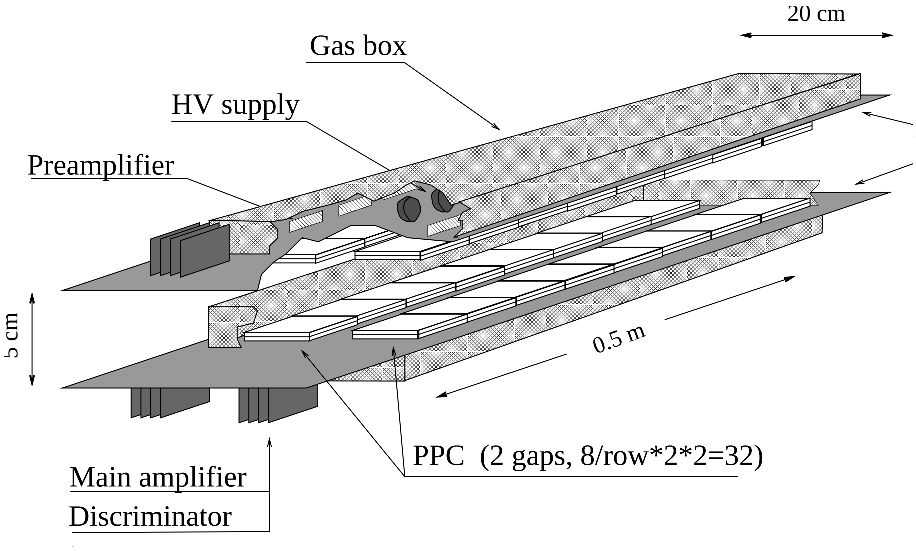

Figure 2.21: 32-channel TOF module.

A metallic box and the PCBs themselves provided the gas tightness. The outputs from the front-end electronics, HV and LV connectors and the test signal input were placed at the PCB edge outside the box, as shown in Fig. 2.21. A reason to take all the electronics, except the fast preamplifiers, out of the gas box and place them at the PCB edge, was to reduce the amount of material in the sensitive area.

Each PPC cell had two 0.63 mm gas gaps, the electrodes were made of chromed 50×50 mm^2 ceramic plates, with edge grooves. The distance between neighbouring chambers in a row was 2 mm. The main amplifiers-shapers and discriminators were placed together on a daughter card, two channels per card. The discriminator was a commercially available AD 96685BR comparator. Measurements had shown the front-end electronic noise to be at the level of 1 fC, and the time jitter was 150 ps. The readout was performed with LeCroy TDC 2228A (50 ps/bin) and ADC 2249A.

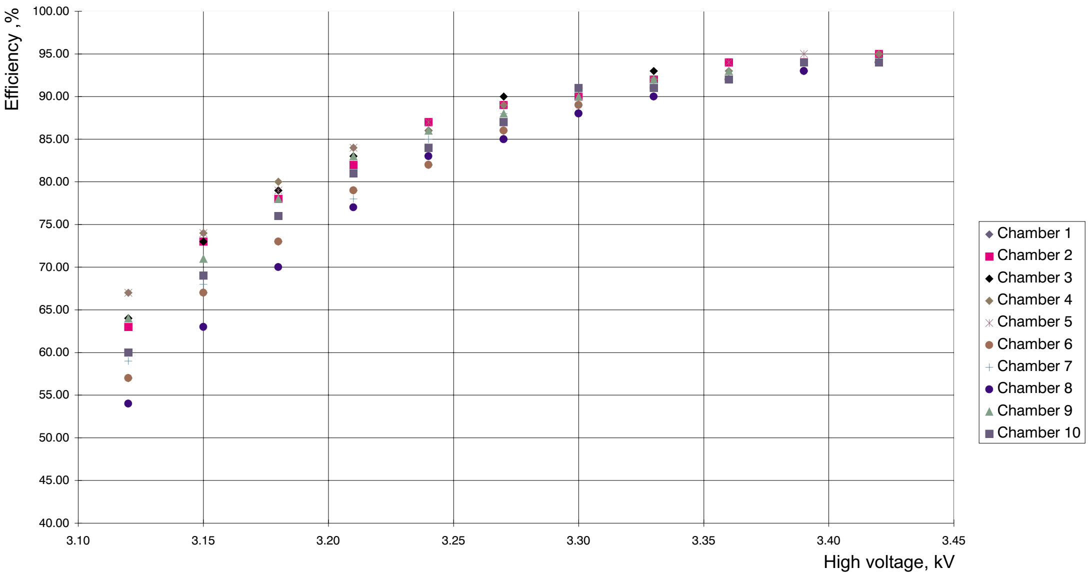

Figure 2.22: Cell efficiencies in the 32-channel TOF module.

The beam tests were carried out at CERN PS and SPS, using a MIP flux of 1 kHz/cm^2, with a beam spot at the module plane of 4 cm^2. The gas mixture was DME + 10% CF_3Br at the atmospheric pressure.

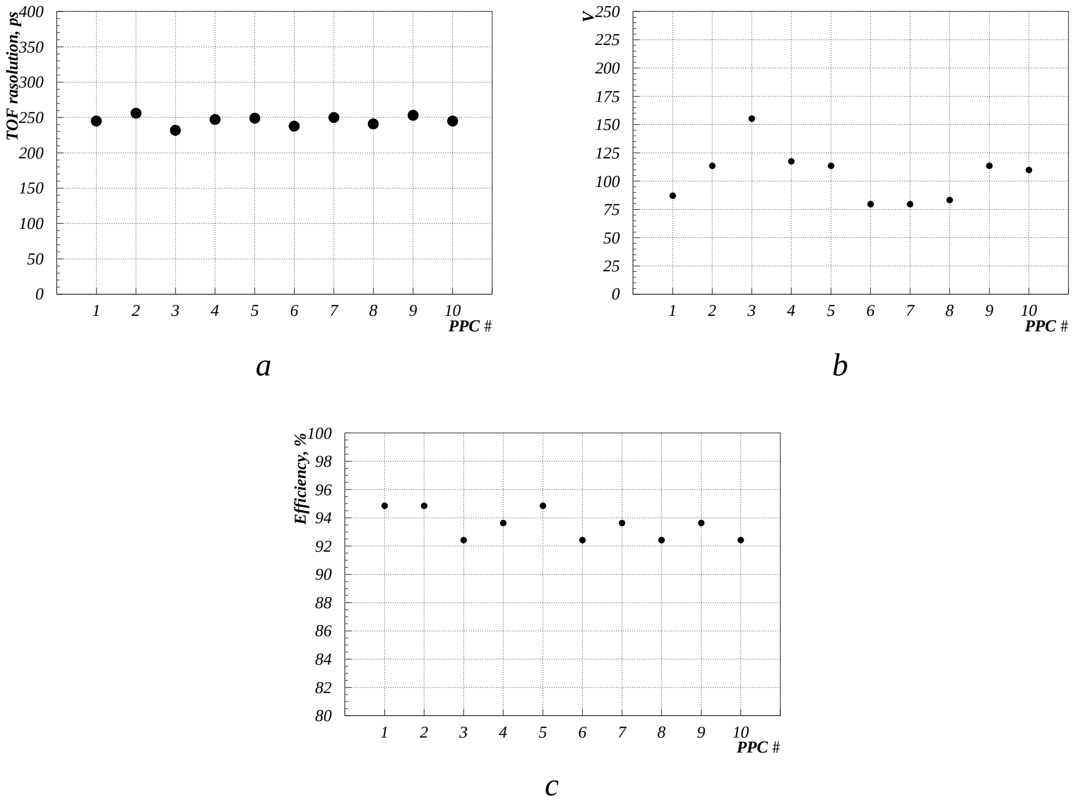

Figure 2.23: TOF module test results (10 PPCs shown):
a — TOF resolutions;
b — efficiency plateau widths;
c — efficiencies in the plateau centres.

After extracting the start counter resolution, which was measured continuously during the data taking, the intrinsic TOF module resolution was found to be 250 ps, including all sources of jitter. Fig 2.22 shows efficiencies of different cells inside the module. For many cells, a plateau $\sim$ 100 V wide, was observed at an efficiency of 90–95%. Significant distinctions between efficiencies were found at lower HV. Fig. 2.23 summarises the beam test results for different cells of the module.

The TOF array built of PPCs will be useful only if cross-talk between different cells is low. To measure the cross-talk, a wide beam crossing one of the cells was used. With a low probability, cells out of the beam produced signals with the amplitude spectrum similar to that of real particles. The cross-talk probability could be calculated by integrating that spectrum above the threshold value. As may be seen in Fig. 2.24*a*, the 20 mV discriminator threshold provided 1.5% of cross-talks probability in neighbouring cells, and about 0.5% in the others. The last value might be a result of common ground loops for detectors or the front-end electronics.

Cross-talk for spark events was measured by means of a special spark trigger. Since the spark probability for MIP is about 10^{-5}, an α-radioactive gas Rn was added to the gas mixture. The sparks were produced by low-energy α-particles, which made it possible to increase the spark count up to 100 Hz per cell. Fig. 2.24*b* shows that between cells connected to the same PCB there exists large cross-talk probability, slightly decreasing from 70% in the neighboring cells to 20–30% in the most distant ones.

In the same Fig. 2.24*b* it can be seen that the cross-talk probability in the neighboring PCB was at the 1 % level, like in non-spark events. This implied that if a spark occured in one layer, the TOF information could be taken from the other. Such a conclusion opened a way for building TOF modules with several TOF layers.

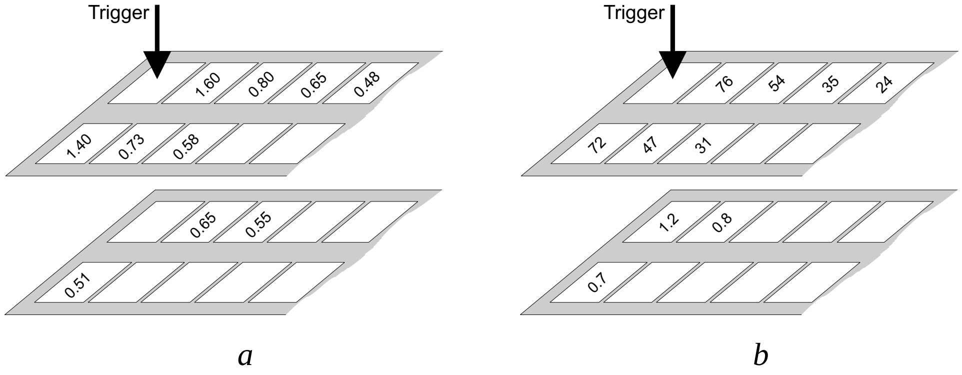

Figure 2.24: Percentage of cross-talk in the module:*a* — normal events;*b* — spark events.

2.2.2.5 Summary of the PPC R&D

A lot of progress has been made, during the years of R&D, on PPC as a gaseous detector for TOF operated in the avalanche mode. A very good performance was reached for single cell detectors and for the small-size multi-cell array; however the possibility of using this technology for large scale applications is still questionable.

The PPC's basic disadvantage is that sparks occur during its operation. This limits the gain and makes the PPC sensitive to a low energy background.

In spite of improvements, the PPC signals remain small (about 100 fC on average), which even in the double-gap design gives a low signal-to-noise ratio. To avoid this, the front-end electronics had to be made very low-noise and extremely sensitive, which is at odds with the fast rise time needed for timing purposes. The electronics limited the time resolution to 150–200 ps limit. Thus if the time resolution had to be better than this limit (as in the ALICE experiment), a multi-layer design had to be envisaged.

2.3 The development of the multigap RPC

2.3.1 History and the principle of the multigap RPC

The resistive plate chamber (RPC) is a parallel plate chamber with resistive electrodes (rather than the metallic plates used in PPCs). These resistive electrodes quench the streamers so that they do not initiate a spark breakdown. Thus RPCs can be operated at much higher gains in avalanche mode (this is the mode used with PPCs); streamer mode operation is also possible. Resistive plate chambers are well known for their use, for large area coverage, for muon detection. A common design for this application has a gas gap of 2 mm and resistive plates of Bakelite [26] or glass [27].

The LAA project at CERN has studied resistive plate chambers, over a few years, with the goal of improving their operation characteristics so they could be used in future hadron colliders. One of the earlier attempts to improve the 2 mm gap resistive plate chamber was to increase the size of the gas gap. This device (known as the "wide gap RPC") had a gas gap of 6 to 8 mm. It had many advantageous features when compared to the conventional 2 mm gap chamber. One obvious feature was that the gap tolerance was less critical for a wide gap compared with smaller gaps, which resulted in a corresponding easing of problems with the construction. Another advantage of the wide gap was that it allowed the use of a "light" gas (high fraction of Argon). This light gas mixture had a much lower electronegativity compared to the Freon-rich mixtures used in 2 mm gap chambers. The problem with electronegative gases is that there is a much-increased ionic current (i.e. there is a much higher charge produced in the gas gap); this compromises the rate capability. Indeed the wide gap chamber had a rate capability a factor 10 higher than the 2 mm gap RPC. These tests have been documented [28]. The only disadvantage of the

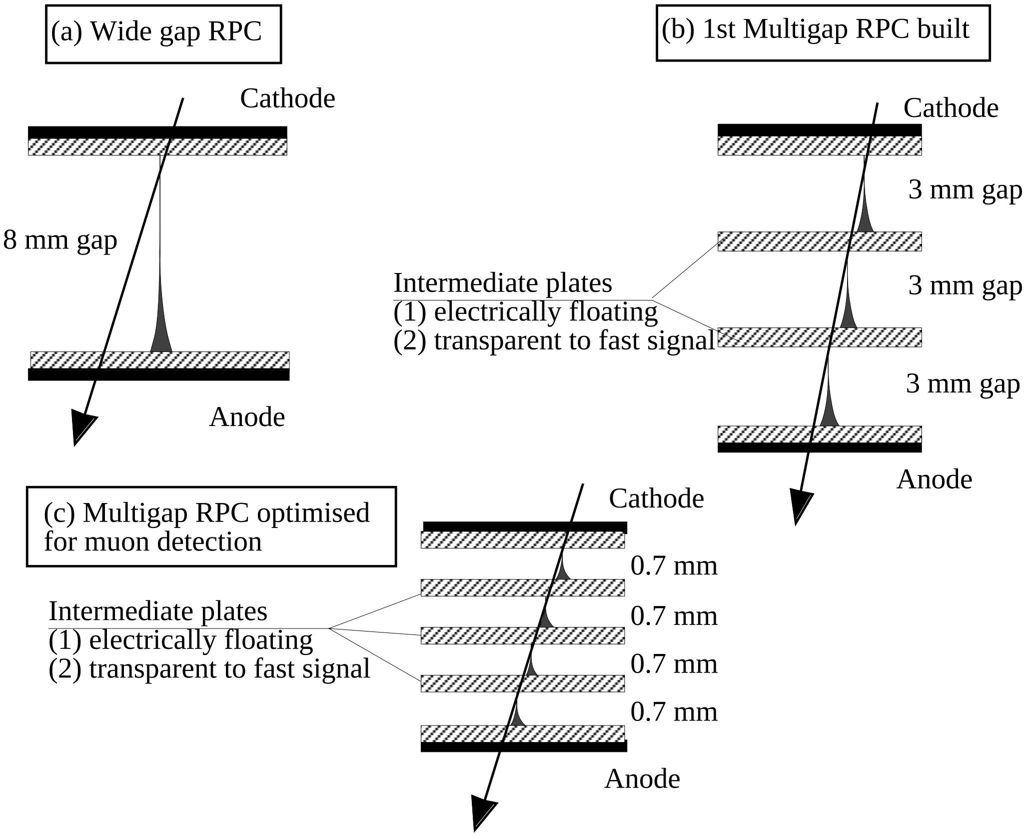

Figure 2.25: Schematic representation of (a) Wide gap RPC (b) 1st Multigap RPC built (c) Multigap RPC optimised for muon detection.

wide gap RPC was a significant worsening of the time resolution. It became clear that, ideally, one wants to keep the advantages of the wide gap (looser mechanical tolerance, improved rate capability) but, at the same time, dramatically improve the time resolution. The route to an improved time resolution is smaller gas gaps. The multigap RPC [29] is a solution that offers both small gas gaps and a large total gas gap. As stated above, the Pestov counter gives very good time resolutions of ~ 50 ps; however, there exists a tail of late signals. An obvious solution to this tail is to have more than one gas gap and use the earliest signal. The multigap RPC is just such a detector; a series of gas gaps, with one set of read-out strips reading out the analogue sum of all gas gaps.

In Fig. 2.25 we show schematically (a) a wide gap RPC and (b) a 3-gap multigap design. In both cases the total gas gap is similar ($\sim$ 9 mm), but the multigap is split into 3 sub-gaps of 3 mm each. The intermediate plates are electrically floating and achieve the correct voltage by electrostatic effect. They are kept at the correct voltage by the flow of electrons and positive ions, created by avalanches in the gas gaps. In fact, there is a strong feedback mechanism that forces the gas gain to be equal in all subgaps. We have now been building these types of detectors for over three years and find very reproducible behaviour. Thus this principle of the “floating electrode” is very stable (also shown by the construction and tests of the very large MRPC [30]). We obtained, with this 3×3 mm multigap, a time resolution similar to a single 2 mm gap. We however operated the multigap with an Argon-based gas mixture (which is not electronegative) and thus had a rate capability 10 times higher than a single 2 mm gap RPC, filled with a Freon gas mixture (strongly electronegative). There is a further advantage in subdividing the gas gap into many small gaps. A through-going particle produces individual and separate clusters of primary ionisation; each of these clusters will start an avalanche and the final signal will be the sum of all avalanches. However we discovered that these avalanches were not independent and the resultant signal was as if there was only one large “merged” avalanche - instead of the sum of many small discrete avalanches. The conclusion is that inherent fluctuations within the avalanche mechanism dominate for a single gap, while for the multigap the signal is truly the sum of independent avalanches (since the avalanches occur in independent subgaps). The resultant signal thus is the average of many avalanches and has, as a direct consequence, an influence on the shape of the charge spectrum: the single wide gap RPC has a charge spectrum of an exponential shape, while a multigap has a Γ function shaped charge spectrum, similar to a Landau distribution. An exponential-shaped charge spectrum makes life very difficult for detector builders, since one is forced to keep the threshold as low as possible, to avoid a large reduction in efficiency. The charge spectrum from the multigap has a peak well separated from zero, and thus the setting of the threshold is far less critical. This improvement of the shape of charge spectrum further improves the high rate capability of this device [31].

The original LAA-multigap design had 3 gaps of 3 mm. This had a time resolution of $\sigma \sim 2$ ns. Recently, the LAA group has been building multigap RPCs typically with 4 gaps of 0.7 mm, operating with a heavy Freon gas mixture at atmospheric pressure (shown in Fig. 2.25(c)). The result is a time resolution of less than 1 ns (without any corrections for pulse height). This is exactly the time resolution needed for the muon trigger and allows us to distinguish the direction of the particle passing through a typical LHC experiment. An additional point is that, for these very small gaps, we have to operate with a very high effective Townsend coefficient. This condition means that the attachment coefficient (a measure of the electronegativity) has to be small in comparison to the Townsend coefficient; thus, even though Freon (which is electronegative) is used, the working regime is where the electronegativity is not apparent; thus good rate capability is maintained.

In summary: the multigap RPC allows the simultaneous readout of many (sub) gaps; each gap is separated from its neighbour by a sheet of resistive material. These sheets, since they are highly resistive, are transparent to the fast signals generated by the avalanches. There are no electrical connections made to these sheets; they are electrically floating - however there is a strong feedback mechanism where the stable state is equal gain in all sub-gaps.

2.3.2 Tests during autumn 1998

In the previous section we discussed the development of the multigap resistive plate chamber, the goal of which was to profit from the good time resolution of the small gap, while keeping the advantages of having a large total gas gap. We then achieved a further improvement of time resolution by reducing the gas gaps to 700 μm. We pointed out that the small gap forces us to operate at a high effective Townsend coefficient, and this reduces the “electronegativity” of the Freon gas. It is not a big step to decrease this gap further (to 340 μm for example), to test whether this device can achieve a time resolution suitable for Time of Flight purposes.

In the initial tests during autumn of 1998, two designs of multigap RPCs were tested within the ALICE TOF R&D program. These are shown schematically in Fig. 2.26. Fig. 2.26a shows a cross section of a five-gap MRPC, each of 340 μm, constructed with melamine resistive plates, in a similar way to the large area muon chambers previously developed by the LAA group. In Fig. 2.26b we show a double MRPC: each MRPC having 2 gaps of 300 μm. This was based on the PPC being studied within the ALICE R&D program. The resistive plate (a commercial black glass used for welding masks) was placed between the anode and cathode electrodes of the two gas gaps. These electrodes were metallised ceramic plates. This glass plate is electrically floating but achieves the correct voltage due to the multigap RPC principle discussed above. This double two-gap device was a single cell of 4×4 cm^2. The active area of the melamine five-gap chamber was a 24×24 cm^2 device, divided into eight 3 cm wide read-out strips. The time resolution of the melamine chamber was 200 ps while the double two-gap device had a time resolution of 100 ps. We suspected that the poorer time resolution of the melamine chamber was caused by the non-uniformity of the gas gaps, since the melamine plates are less rigid than the glass-metal plates used in the single cell design. Indeed, recent tests show that chambers constructed with

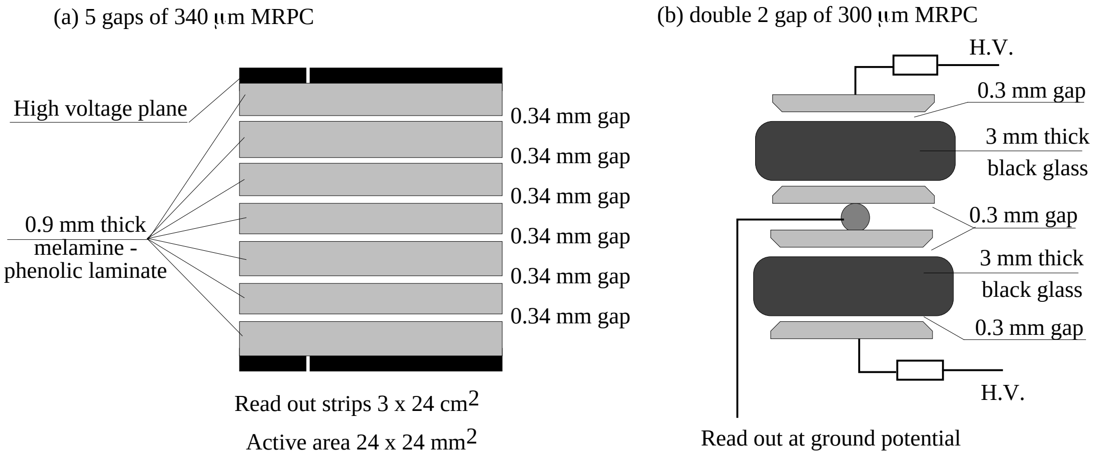

Figure 2.26: Schematic cross section of two MRPC devices tested during autumn 1998.

melamine plates give a time resolution of 100 ps when the chamber is mechanically strengthened, with two sheets of 12 mm honeycomb. A similar design of MRPC but using a stack of glass sheets (in place of melamine) gives a time resolution of $\sim$ 65 ps. These results will be described in detail in the next section.

2.4 R&D of the multigap RPC for the TOF

During 1999, we have been testing various devices in the T10 beam line at CERN. The principle goals were the following:

1. confirm the time resolution ($\sim$ 100 ps) obtained with a single cell design in 1998;
2. demonstrate that this resolution can be obtained with a TOF array (i.e. test an array of cells);
3. investigate tails - in particular the tail of late events;
4. check that the rate capability is sufficient for the ALICE experiment;
5. investigate edge effects and cross-talk;
6. investigate operational characteristics of the device, to find if there is some critical parameter (applied high voltage, gas mixture, resistive plate material, size of gaps, number of gaps).

2.4.1 Results from small glass MRPC

2.4.1.1 Description of the device

The cross section of the particular device described here is shown in Fig. 2.27. It was built with a variety of glasses; the two outer plates were 2 mm thick pieces of Schott 8540 (resistivity of 10^{10} Ωcm). Two of the four inner plates were Schott A2 (resistivity of 8×10^{12} Ωcm) and the other two were Schott A14 (resistivity of 1.5×10^{12} Ωcm). These internal plates were ground to a thickness of 0.5 mm and then polished. The glass plates were 5×5 cm^2; the size of the electrodes was 3×3 cm^2 and they were fabricated using self-adhesive copper foil. The gas gaps were 220 μm. Spacers, placed at the four corners, defined the gap size; these spacers were made from 50 μm Mylar, covered with 85 μm thick double-sided pressure- sensitive adhesive.

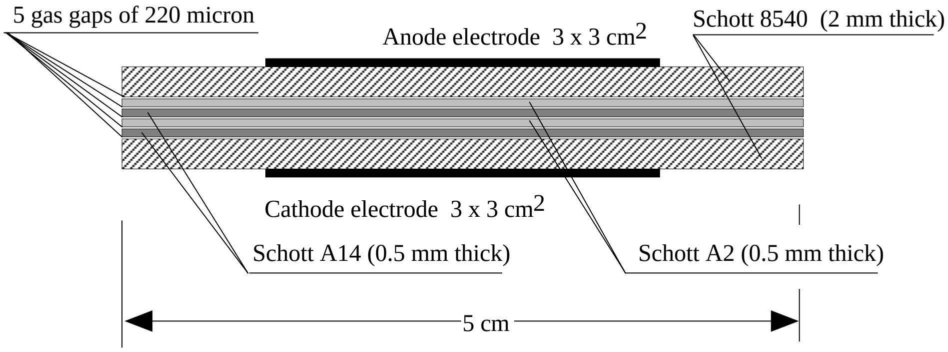

Figure 2.27: Cross section of a small glass multigap RPC.

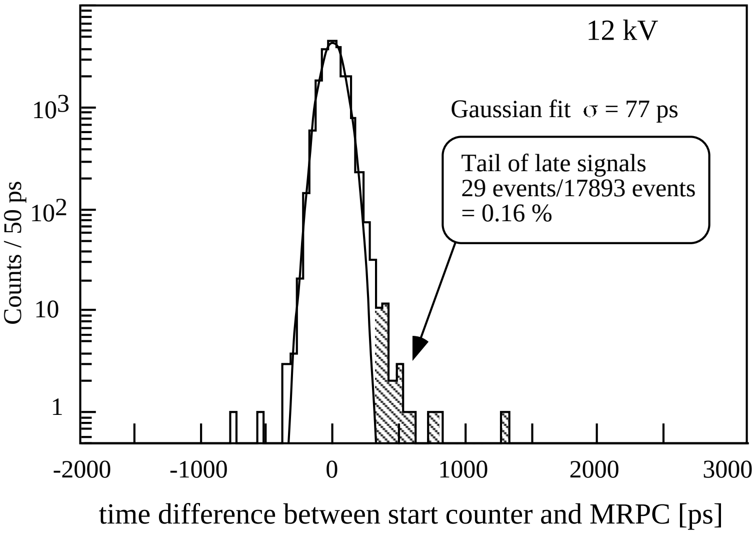

Figure 2.28: Typical time spectrum of a small glass multigap RPC.

A low-noise, high-speed amplifier (1 ns rise time) was connected to the anode electrode. The cathode was connected to the high voltage supply via a 1 MΩ resistor and coupled to ground with a 1 nF capacitor. The device was mounted in a gas-tight box, flushed with a gas mixture of 90% $C_2F_4H_2$, 5% SF_6 and 5% isobutane. The signal was further amplified and then fed to an ADC and a discriminator feeding a TDC. The time jitter of the amplifier and discriminator was measured to be 50 ps.

2.4.1.2 Results

As stated in [29], smaller gas gaps will produce better time resolution. Since we have 5 gas gaps of 220 μm, our expectations of excellent time resolution, high efficiency and no late tail in the time spectrum (since we are sensitive to the earliest avalanche signal from any of the five gas gaps) were fulfilled.

A typical time spectrum is shown in Fig. 2.28. The measured time resolution is 77 ps; we subtract the time jitter of the start counters, which was measured to be 33 ps, to obtain a time resolution of 70 ps. The jitter of the amplifier and discriminator was measured to be 50 ps when pulsed; thus the time resolution of the multigap RPC detector is $\sim$ 50 ps. To obtain this time resolution, a correction has to be made according to the pulse height of the signal. A scatter plot of time versus amplitude is shown in Fig. 2.29. This is divided into 32 bins; the time spectrum of each bin is fitted by a gaussian and then a 5th order polynomial fitted to the mean of the gaussian fits. The time of each event is then corrected according to the pulse height information, using this 5th-order polynomial. The time resolution and efficiency as a function of high voltage is shown in Fig. 2.30.

In Fig. 2.31, we show the change in absolute time versus high voltage (time-walk). The time plotted has been corrected for amplitude variation. For this study, we obtained a global correction by adding together the data corresponding to different high voltages and then performing the time-amplitude correlation. We use the same amplitude correction factors for each voltage value. As can be seen, the time-walk is very small (25 ps/kV) around the working voltage of 12 kV and gives us confidence that this device will produce stable timing.

The time resolution and efficiency were measured as a function of beam flux. This is shown in Fig. 2.32. The beam spill was 250 ms long and the beam spot defocused to cover the full active area of the device. The fast charge (due to the movement of the electrons) is 1 pC (see Fig. 2.35); thus the total charge in the gap is $\sim$ 10 pC for each through-going particle. Using this value, one could expect that it would be impossible to achieve such high rate capability, since the current flow through the resistive plates should create a voltage drop of many kV. Therefore we tested this chamber at the Gamma Irradiation Facility (GIF) at CERN.

At the GIF, one can test the performance of the detector with a muon beam in the presence of a large flux of gammas from a ^{137}Cs source. The intensity of the gamma flux can be varied by the insertion of various lead filters. We measured the gamma conversions in the chamber by measuring the single rate.

In Fig. 2.33 we show the efficiency and counting rate versus the gamma-induced rate from the source. The efficiency is slightly lower than measured in the T10 test beam; this was a geometric effect caused by having the trigger scintillators mounted far from the small test chamber. It is clear that this device works satisfactorily up to 500 Hz/cm^2. In Fig. 2.34 the upper three plots show the charge spectrum for 150 GeV/c muons with different gamma-induced count rates. The lowest plot is when we trigger on the chamber itself. The charge spectrum for the muons has a mean which is roughly twice the charge produced in the chamber by a gamma. This implies that the rate capability for a continuous flux of through-going muons is 250 Hz/cm^2.

In Fig. 2.35 we show the variation of the average fast charge versus high voltage, and the same versus the count rate of gamma conversions. We show, on the figure, that we obtain the same reduction of average charge when the voltage is decreased from 12 kV to 11 kV as when the gamma count rate is increased from 7 Hz/cm^2 to 500 Hz/cm^2. (N.B. this rate of 7 Hz/cm^2 was measured with the source off and is really the dark counting rate of this device). The total resistance of the stack of six glass plates is $10^{12}\Omega$/cm^2. Assuming that there is indeed a 1 kV reduction at 500 Hz/cm^2, we can calculate that the current is 1 nA/cm^2. Thus each gamma conversion generates 2 pC of charge in the MRPC. About 10 % of the total signal is observed as a fast signal. Consequently we would expect an average fast charge of 0.2 pC. This is in good agreement with the charge distribution shown in Fig. 2.34. This indicates that the rate capability of the detector can be calculated by simply knowing the resistivity of the plates and the amount of charge produced by the avalanche process.

The rate capability that we measure is above the maximum rate of 50 Hz/cm^2 expected at ALICE. We plan on constructing chambers with all resistive plates made from A14 glass (this will increase the rate capability by a factor 2) and we will study the possibility of using thinner glass if higher rate capability is needed. Of course, it is always possible to use glass of lower resistivity (such as the Schott 8540) and we plan on investigating this solution.

2.4.2 Results from an array of single cells

2.4.2.1 Introduction

As has been discussed earlier in this chapter, the time resolution of the PPC substantially worsened when an array, rather than a single cell, was tested. The reason for this was that, because the signal from the PPC is very small, it has to be operated at the lowest possible threshold to obtain the best possible

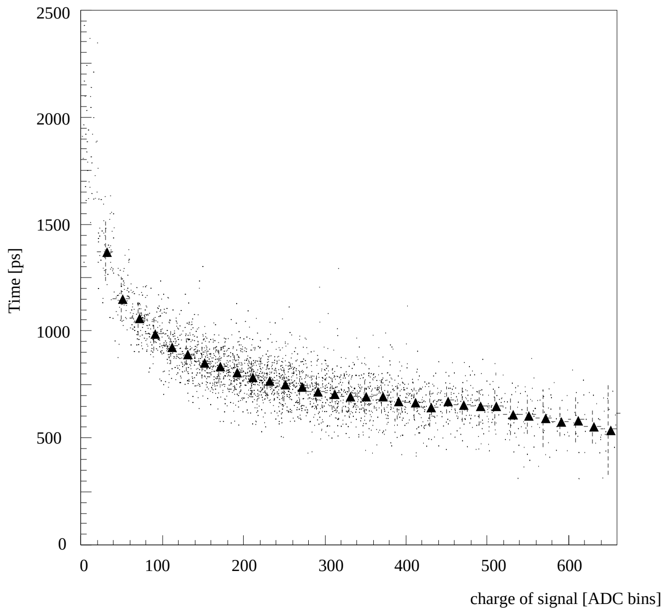

Figure 2.29: Scatter plot showing time versus fast charge. The black triangles show the average time value for an amplitude slice.

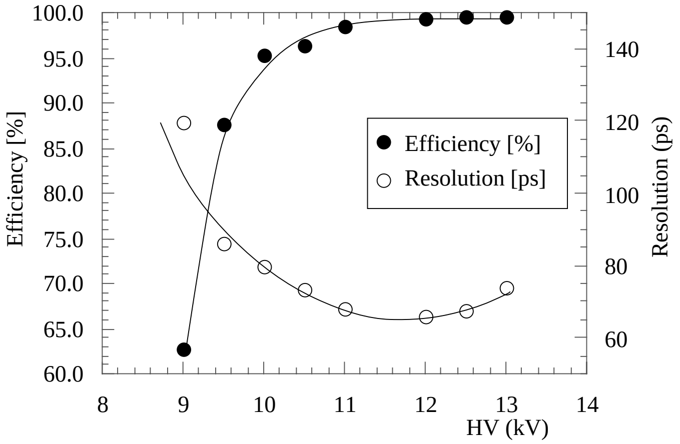

Figure 2.30: Efficiency and time resolution versus high voltage for the small glass MRPC.

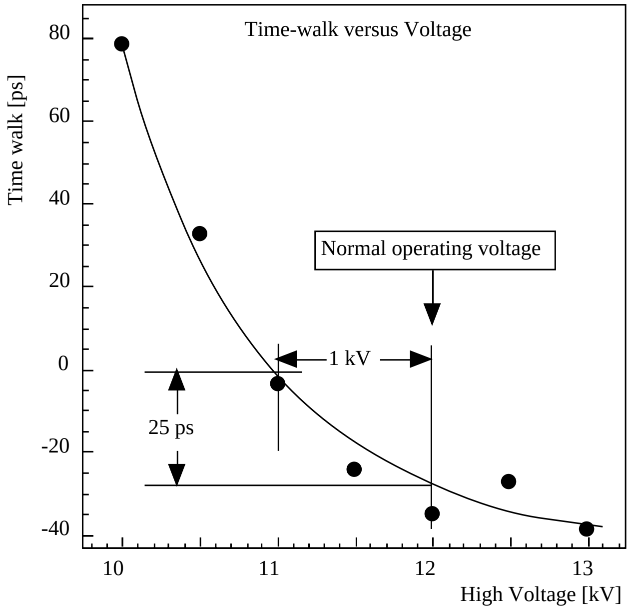

Figure 2.31: Change in absolute time versus high voltage for the small glass MRPC.

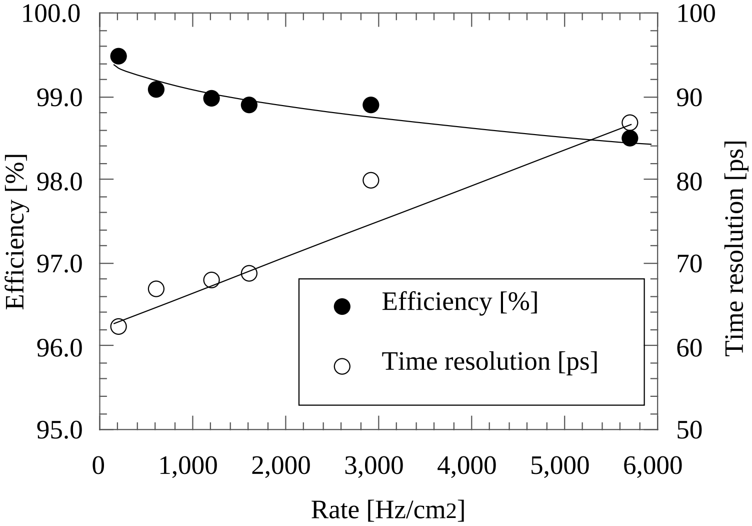

Figure 2.32: Efficiency and time resolution versus rate (measured at T10 with a 250 ms spill).

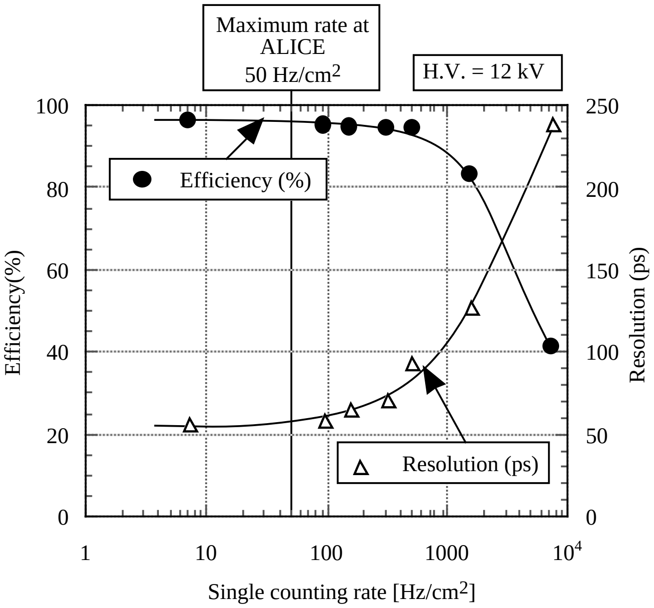

Figure 2.33: Efficiency and time resolution as a function of the counting rate due to the Cs source at the GIF (see text).

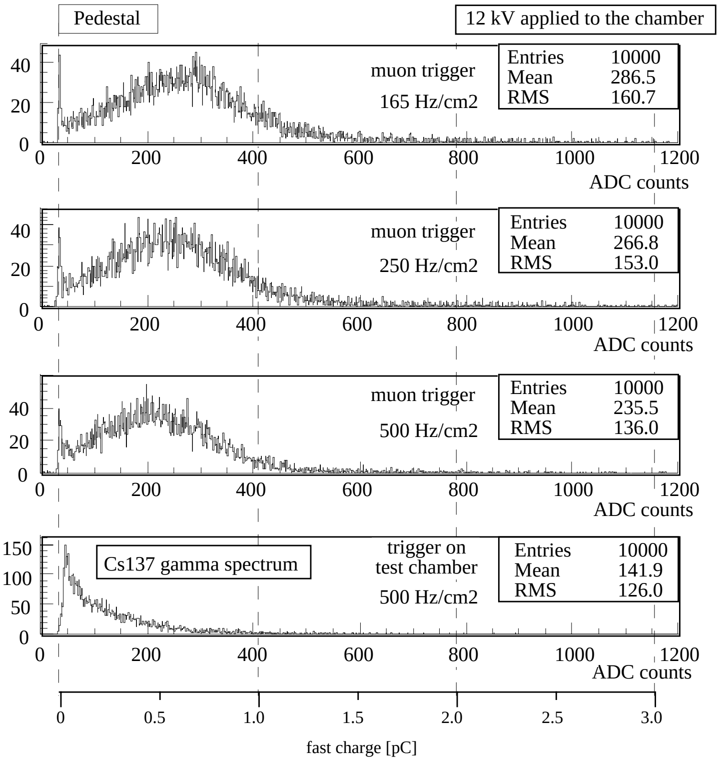

Figure 2.34: Fast charge distribution. The top three plots are for through-going 150 GeV/c muons for the indicated gamma-induced rates. The lowest plot shows the charge spectrum produced by gamma conversions in the chamber.

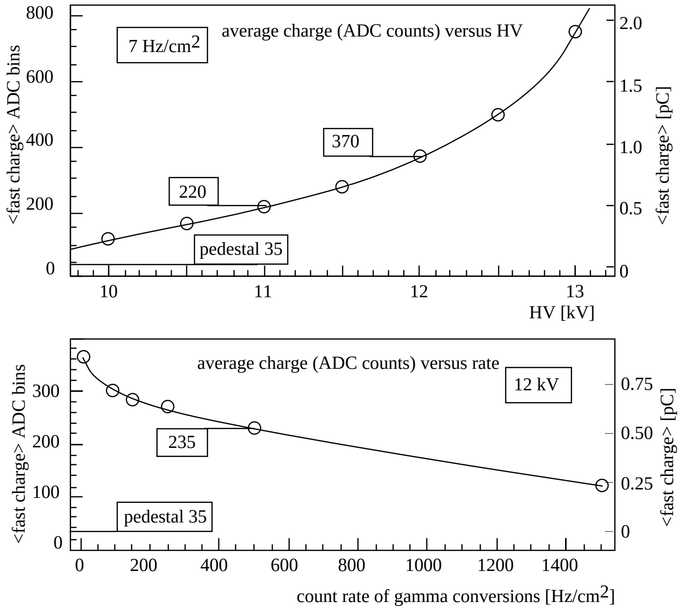

Figure 2.35: The variation of fast charge versus high voltage and rate.

timing. In addition the average signal is very close to this threshold value. Therefore any extra noise on the ground increases the time jitter of the front end electronics. The signals from the MRPC are substantially larger than the PPC so an array of MRPCs should therefore have a similar time resolution to a single cell. In order to test this and to discover any problems that may be introduced when working with an array, a 32 element single cell detector was built and tested. In addition the uniformity (time resolution and efficiency) was studied. The full results from these tests can be found in reference [32]; some of the main results will be discussed below.

2.4.2.2 Description of the single cell array

The detector cells are constructed from a pair of identical double-gap MRPCs. Each MRPC consists of two 2 mm thick aluminium plates (the anode and cathode) and a central resistive glass plate which is electrically floating, following the multigap RPC principle. The cathodes are connected to a negative high voltage; the two anodes (at 0 V) are connected together to feed a single amplifier. The 3 mm thick glass plate is made from Schott Nr. 10 welding glass with a resistivity of $\sim 2\times10^{12}$ Ωcm. The size of all plates is 32×32 mm^2. The edges of the aluminium plates are rounded and reduce the active area to 30×30 mm^2.

The elements are assembled in a plastic box that provides electrical insulation and mechanical rigidity. This box has holes for wires connected to the metallic electrodes, for gas circulation and for insertion of spacers that define the gaps. These spacers are short pieces of optical glass fiber ($\oslash$ 0.3 mm), that are inserted at the four corners of the chamber in each gap.

The detector cells are arranged in an array of four by eight squares, following a chessboard-like pattern in two layers (Fig. 2.36). The edges of the active areas in the two layers are aligned, providing a geometrical coverage of 97 % for normal incidence. Mechanical support for the cells is provided by plastic spacers glued onto the detector PCB, which carries the high voltage circuitry, the signal feedthroughs to the readout electronics and provides gas tightness on one surface.

The schematics of the high voltage distribution (Fig. 2.37) features multi-level high-voltage filtering to assure stable operation. The physical layout has been carefully optimized to suppress crosstalk between neighbouring channels across the electrical connections. In particular, the signal ground is sep-

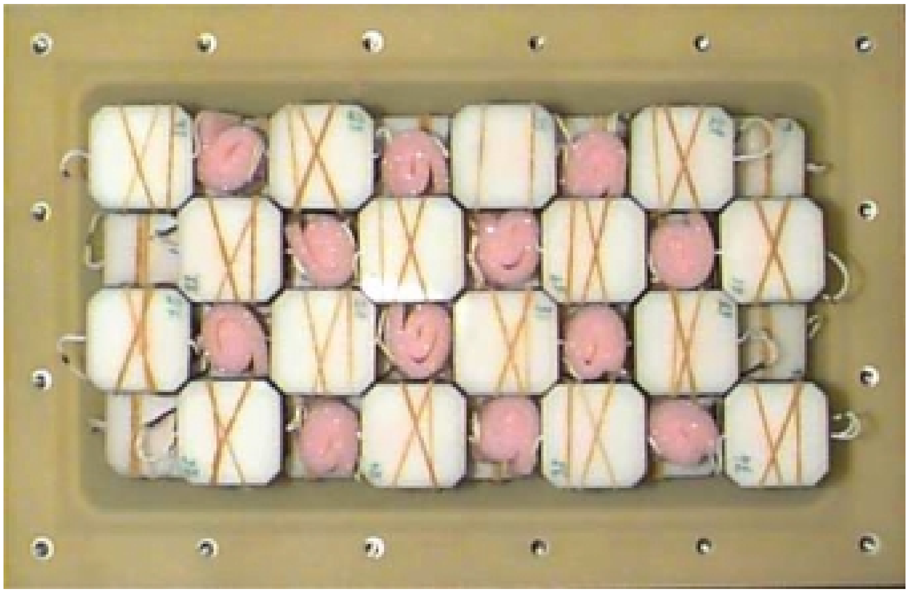

Figure 2.36: Arrangement of the 32 detector cells in two layers following a chessboard-like pattern.

arated from the HV ground to minimise pick-up noise and crosstalk, rendering adjacent cells almost electrically independent.

Fig. 2.38 shows the physical layout of one high voltage distribution PCB unit of 6×12 cm^2 serving eight detector cells. All metallic parts on both sides of the PCB, which are on HV potential, are concentrated in the centre of the unit and covered by protective glue[2] to avoid surface currents and discharges. The surrounding ground loop encloses a surface of ~ 50 cm^2 only, hence it is rather insensitive to external high frequency noise. The four 8-cell units of the PCB for the 32-cell module are interconnected by HV and ground jumpers to be supplied by one HV line.

For these tests, the detector PCB carrying the array of 32 cells was mounted in a metallic box that enclosed the gas volume, carried gas connections and allowed the module to be fixed to a moving table. All six faces of the box were covered by a thin PCB, with a copper layer connected to HV ground for electrical shielding, leaving only small holes for the connectors to the readout electronics.

2.4.2.3 Readout electronics

A signal pick-up card contained shaping amplifiers, discriminators and edge-detecting circuitry for eight channels (Fig. 2.39). Four cards were attached orthogonally to the detector PCB via connectors for chamber signals and, optionally, the high voltage ground. The connectors for low voltage, test signal input, and analog and digital outputs were placed at the opposite edge of the card.

Custom amplifiers were built from discrete components by ITEP-CPTA group; these have a rise time of less than 1.8 ns. The design of this amplifier called for the generation of a long tail so that time-over-threshold could be used to measure the input charge. There was also a built-in saturation to limit the dynamic range of very large input signals. The circuit, shown in Fig. 2.40, consists of a grounded-base input scheme that has an input impedance of 8 Ω. The time constant of the tail is controlled by C3 and R3 on the base of Q2. The differential cascade stage (Q4-Q5) is designed to saturate. Small PCB cards were designed to hold one of these amplifiers which were plugged into the prototype read-out card.

The fixed threshold discriminator scheme, with a hysteresis of 14 mV, is based on a commercial ECL comparator (AD96685BR). Circuitry, using components from the 10EL family, detects leading and

---

[2] CIBA Araldite, resin AW 106 and hardener HV 953 U.

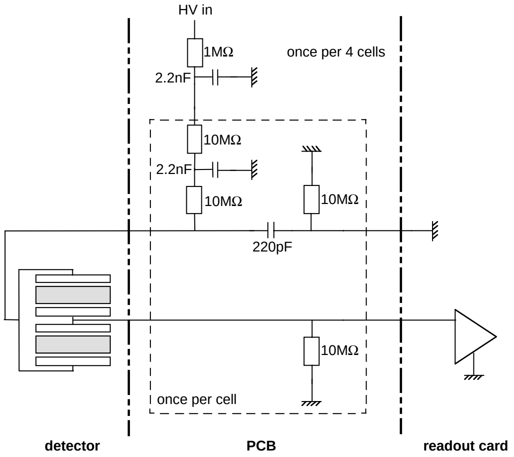

Figure 2.37: Schematics of the electrical connectivity of the array.

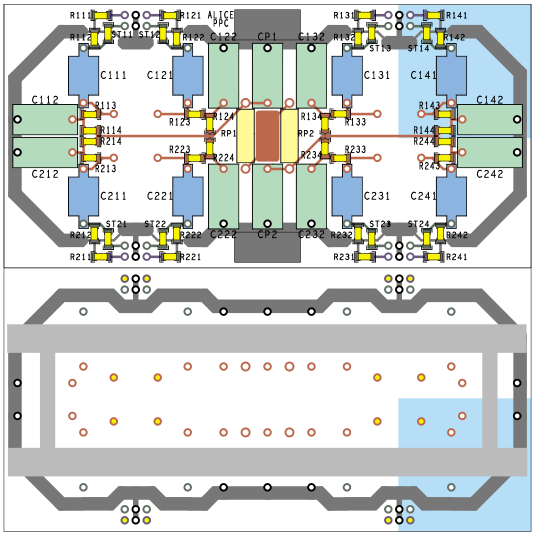

Figure 2.38: Detector PCB layout on the component side (top) and on the detector side (bottom) of one HV distribution unit serving eight detector cells. The light-grey bars in the bottom part indicate the plastic support bars for the detector cells.

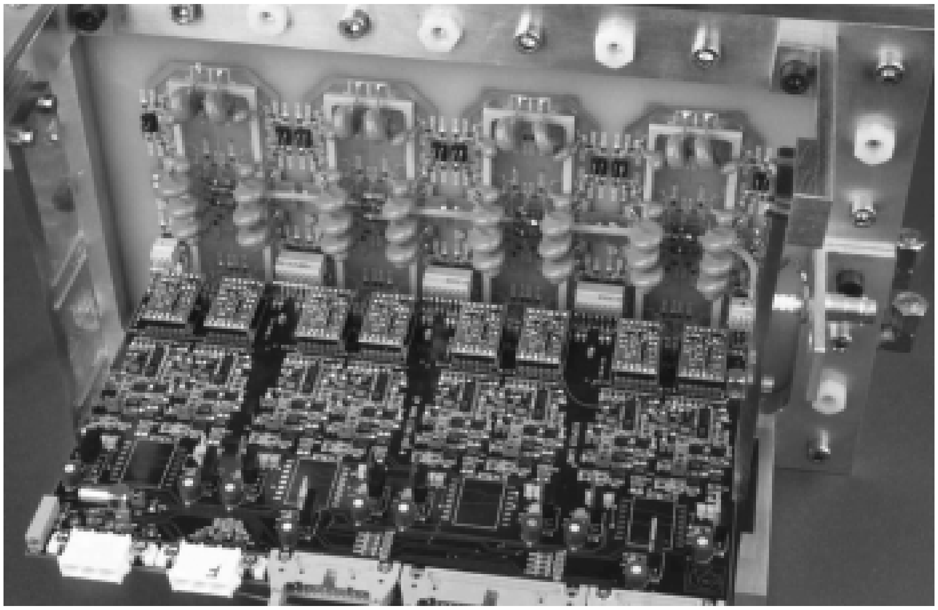

Figure 2.39: One eight-channel prototype read-out card mounted on the array of single cells. The card carries amplifiers made with discrete components, discrimination logics and voltage regulation. The same eight-channel read out card was used for the planar chamber discussed in the next section.

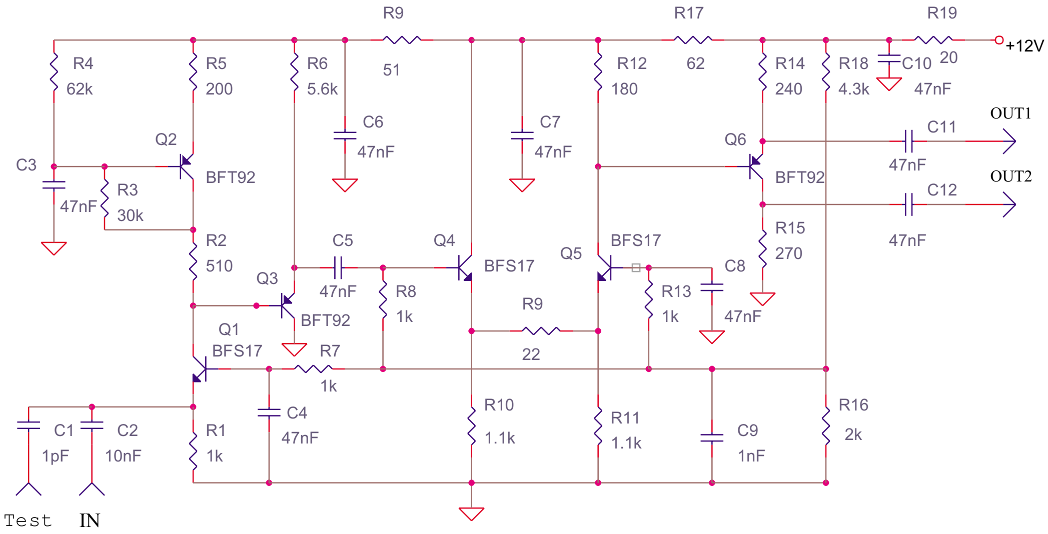

Figure 2.40: Circuit diagram of front-end amplifier used for the read-out of the array of single cells (and the planar MRPC discussed in the next section)

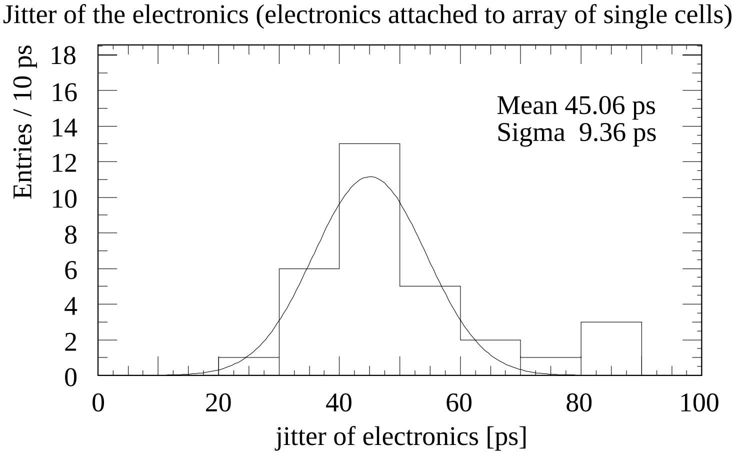

Figure 2.41: The distribution of time resolutions of all 32 electronics channels, measured by feeding all amplifiers with pulses of variable height triggered at random times. The parameters of a fitted Gaussian distribution are shown.

trailing edges corresponding respectively to time-of-flight and input signal amplitude.

With 20 m of 100 Ω twisted-pair flat cable (3M 2100) between the prototype cards and TDC electronics, an electronics time resolution of the leading edge signal of 45±9 ps (Fig. 2.41) and a total system noise level below 1 fC could be achieved.

2.4.2.4 Results

The results described below were obtained with optimal values of high voltage (5800 V) and discriminator threshold (20 fC). Pulse height spectra at different operating voltages are presented in Fig. 2.42. At the standard operating voltage of 5800 V, the fast signal has an average charge of ~ 1 pC, and discharges occur with small ($< 1\%$) probability in the form of streamer pulses of limited charge ($\sim$ 20 pC).

The dependence of the detector performance on the operating voltage can be seen in Fig. 2.43. The resolution curve shows a shallow minimum at 5800 V. At lower voltages, the resolution suffers from decreasing pulse height of the proportional signals. At higher values, the increasing probability for streamer pulses slightly degrades the detector performance. The spread of different measurements at the same conditions is $\sim$ 10 ps. The intrinsic detector efficiency stays better than 95 % above 5200 V.

The distribution of measured time resolutions and efficiencies for 31 detector channels (one readout channel was modified for special studies) is shown in Fig. 2.44. The mean cell efficiency is 98 %, with an excellent uniformity over the sample (1 % RMS error). The time resolution has a mean value of 89 ps, with an RMS error of 9 ps. The use of optimized readout electronics, with 20 ps resolution on one cell in the array, improved the time resolution from 87 ps to 75 ps, in agreement with single cell tests. Measurements of selected cells with inclined beam (20° and 40°) or lower beam energy (1 GeV/c) yielded similar timing and efficiency performance. From the first tests using the pulse width instead of the ADC value for the amplitude correction of one cell, we obtained 89 ps (time-width correction) instead of 81 ps (time-amplitude correction). More appropriate pulse shaping in future amplifiers (this is discussed in the next chapter) will assure equal performance of both amplitude measurements.

The analogue cross-talk between adjacent channels was found to be almost entirely due to capacitive coupling between the cells, inducing in these channels analogue signals of inverse polarity, and an amplitude of $\sim$ 1 % of that of the cell hit by the particle.

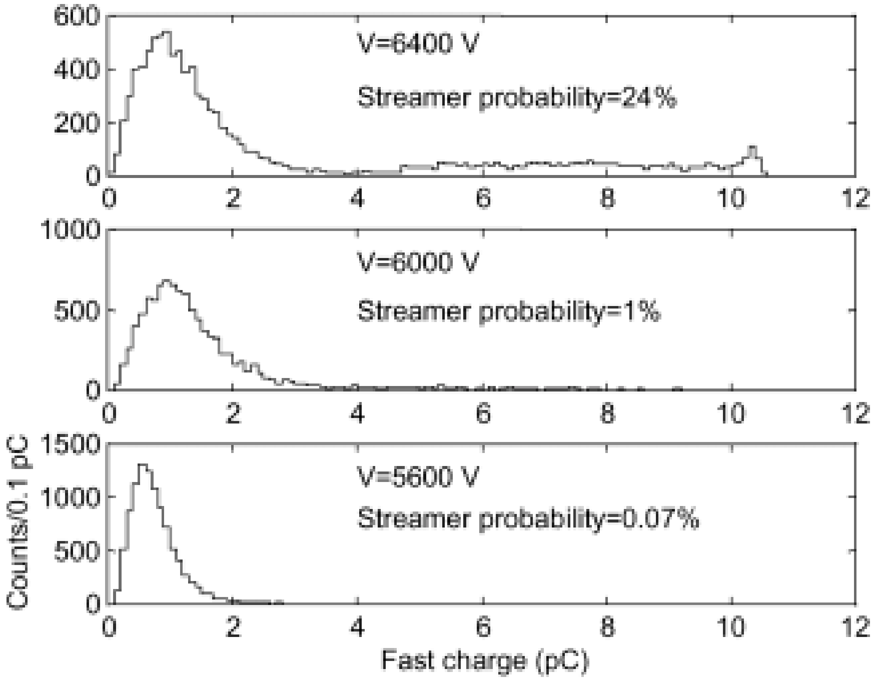

Figure 2.42: Pulse height spectra of 7 GeV/c pions at different operating voltages.

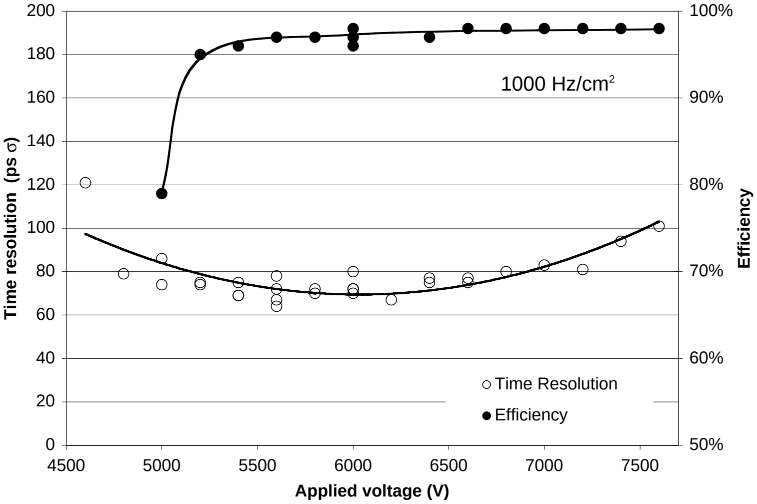

Figure 2.43: Detector time resolution and efficiency as a function of high voltage. The discriminator threshold was 20 fC.

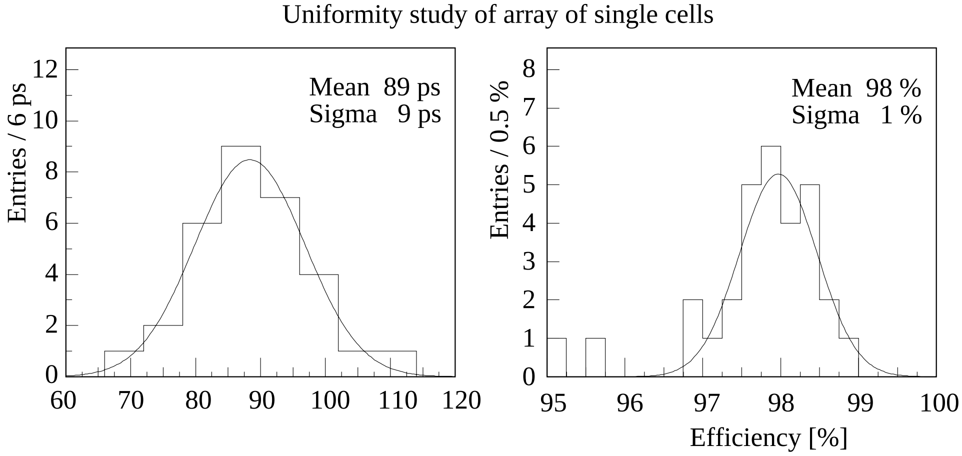

Figure 2.44: Distribution of measured time resolutions and efficiency for array of single cells. The statistical parameters of the distribution are given.

2.4.3 Results from planar chamber design

2.4.3.1 Introduction

The tests described previously were implemented with an array of single cells, with each cell having an active area of 3×3 cm^2. The matrix of 32 single cells, discussed above, has been successfully tested. We do not know however, how practical it would be to implement this enormous 160 000 channel array, built up from 160 000 single 3×3 cm^2 elements.

During 1999, we have implemented various planar designs, to verify that the multigap technique could be made to work with large areas of detector. As will be seen, the results indicate that it is possible to build planar chambers, with good uniformity and time resolution.

Initially, we built planar chambers segmented into 8×8 cells, using melamine orglass resistive plates. The cross sections of two planar designs we built and tested are shown in Fig. 2.45. One problem with this planar design is the connection between the electronics and the detector. In the previous section where the array of single cells was discussed, it was specified that the ‘signal ground’ was grounded at the input of the front-end amplifier; and thus each cell was electrically a separate detector. This scheme is not possible with the 8×8 cell planar design since the cathode signal has to be coupled to the ground plane and this ground plane is on the far side of the detector from the electronics; thus the signal return is achieved via the outer metallic box. This is shown schematically in Fig. 2.46. Since the signals for such

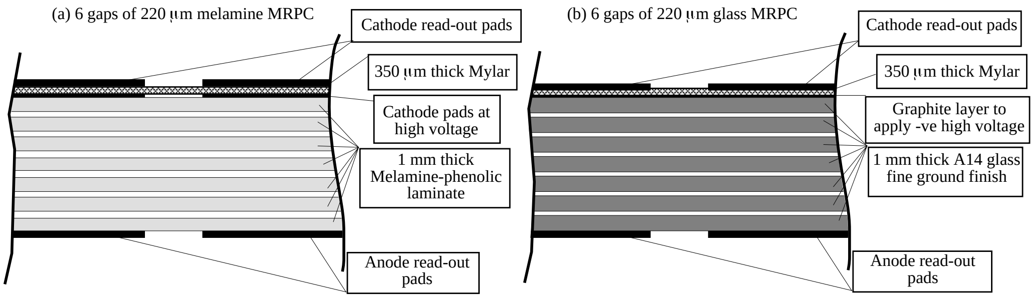

Figure 2.45: Two versions of planar MRPC tested during 1999 constructed with (a) melamine resistive plates and (b) glass resisitive plates.

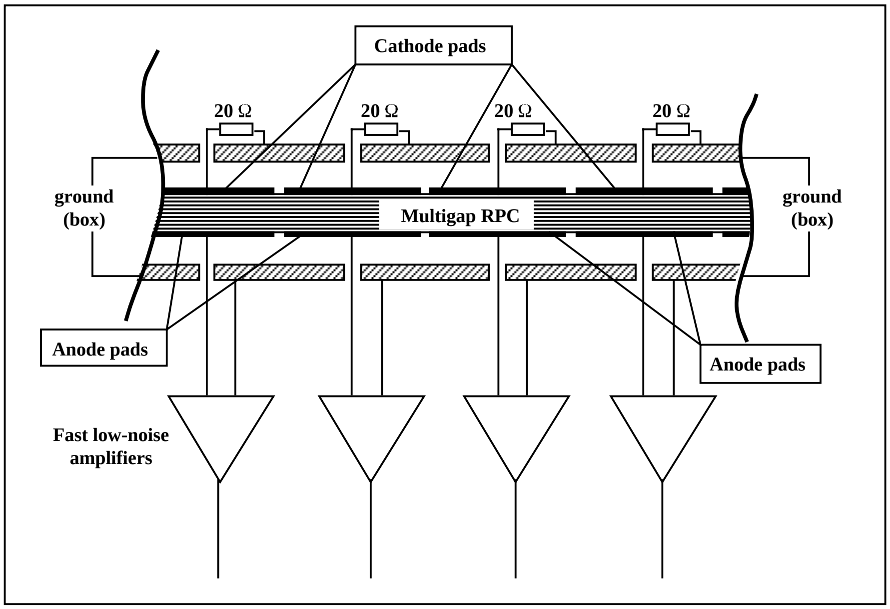

Figure 2.46: Schematic layout of readout of planar MRPC. The signal return has to travel around the outside of the chamber through the ground provided by the box.

a design are all measured with respect to a local ground, the electronics are very sensitive to noise on this ground plane. We also suffered from another source of noise generated by our use of the electronic cards designed for the single cell array, discussed in the previous section. The connection between the card and the pickup pad was made with a few centimetres of unshielded twisted pair, and the amplifier turned out to be very sensitive to the exact positioning of this twisted pair. Nonetheless, we were able to obtain good performance with this type of design. Time resolutions of $\sim$ 100 ps were measured with chambers built both with melamine and with glass plates.

2.4.3.2 Description of the strip MRPC

A detector that consists of a long strip of cells matches the ALICE requirements for geometric reasons. The actual design selected for ALICE will be discussed in the next section. If these strips are made 2 cells wide, it is easy to connect electronics to read out both the anode and cathode pads; we can thus obtain a differential signal from the detector. This is shown schematically in Fig. 2.47. We will discuss the importance of a differential readout in the next section, where we consider techniques to produce the sharpest 'edge' between one cell and its neighbour. In addition, we experienced at first hand the ease of connecting fast and sensitive amplifiers to a device that produces a differential signal. We will discuss the performance of this 8×2 cell module for the remainder of this section.

In Fig. 2.48 and Fig. 2.49 we show an artist's impression and the cross section of the 8×2 cell module that was tested in November 1999. In Fig. 2.50 we show a photograph of the strip detector just before it was inserted into the gas box. The signals on the pickup pads are connected to the electronics (mounted on the lower side of the box shown in Fig. 2.50) with the twisted pair cable.

The outer glass plates are 3.2 mm thick; this is thicker than we want to use for the ALICE TOF modules; however this glass is commercially available. If 1 mm thick plates are used, the induced signal on the pick-up pads will increase. The electronics were the same as those used for the single cell array described in the previous section.

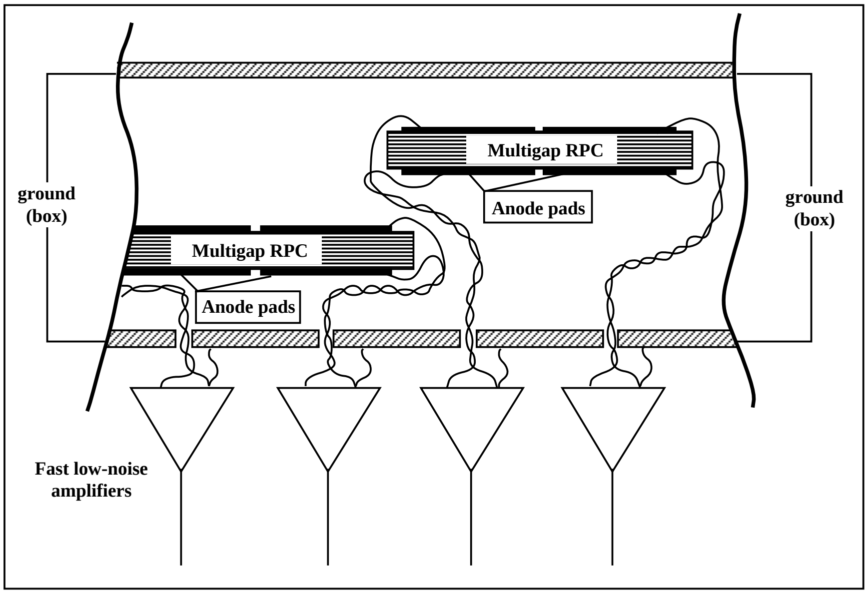

Figure 2.47: Schematic layout of readout of strip MRPC. The MRPC generates a differential signal; the signal return is not through the box.

2.4.3.3 Results

In Fig. 2.51 we show the efficiency, the time resolution and time-walk as a function of voltage for one of these cells. The time-walk is measured by combining all the data taken at various voltages, finding a global T(A) correction and then correcting each data set using the same global T(A) correction coefficients. The results are similar to those obtained with the single cell discussed previously (i.e. there is no degradation in performance by increasing the active area of the detector). In Fig. 2.52 we show the distribution of resolution and efficiency, measured at 12.5 kV, for all 16 cells. The mean time resolution is 62.5 ps with an efficiency of 96 %.

We have studied the boundary between two cells. For the tests described above, we used a trigger based on two pairs of crossed scintillators; the upstream cross defined a 2×2 cm^2 area while the downstream cross defined a 1×1 cm^2 area. Thus, even though we were using a defocused beam, the trigger selected a small area of the chamber under test. For examining the edges between two cells we removed the downstream 1×1 cm^2 scintillator from the trigger. We are much more reliant on the tracking chambers in this configuration. Some 5 % to 10 % of the through-going tracks were mis-reconstructed; this causes the efficiency of the cells to be lower than previously measured; we are however more interested in examining the boundaries. In Fig. 2.53 we show the layout of the cells and roughly the size of the scanned area. We are examining the boundary between cell 20 and cell 28 and the outer edge of pad 20 and 28. The front-end electronics are connected to the outer edge of the pad as shown in Fig. 2.53.

In Fig. 2.54 we show the efficiency versus distance. Outside the pads 20 and 28 the efficiency should be zero, however it has a value between 5 % and 10 % due to the tracking problem discussed above. There is a region, at the boundary between 20 and 28, where both pads have valid hits; this is the effect of the sharing of charge; this region will get smaller when the device is optimised. The efficiency remains high until the edge of the active area. In Fig. 2.55, we show the time resolution as a function of position. At the boundary, there is an observable degradation (up to 130 ps) of the time resolution. The time spectrum contains a mixture of events; some which are ‘true’ events and some which are ‘cross-talk’ events when the avalanche is really above the neighbouring pad. If we only select the events where the signal on a given pad is the bigger of the two pads, the time resolution is not much degraded the boundary

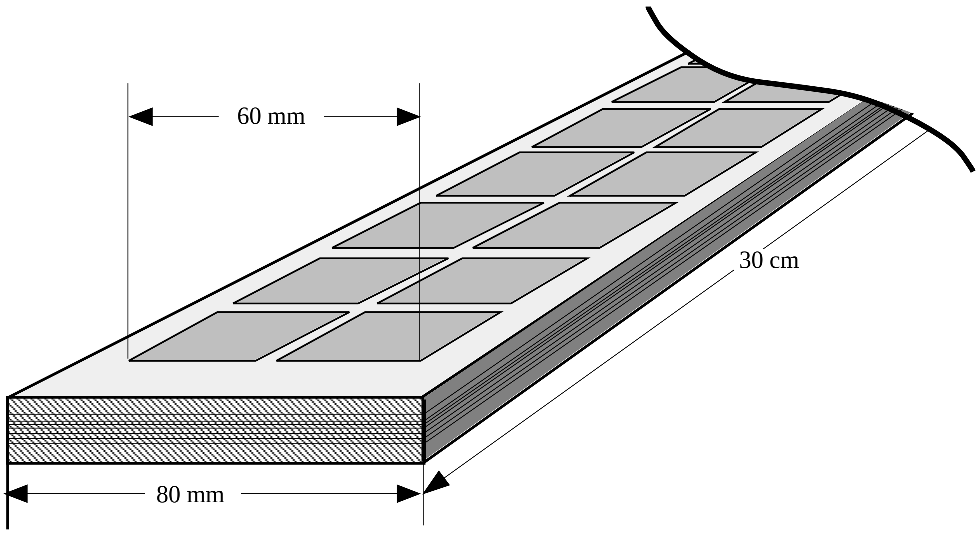

Strip design of MRPC tested in November 1999

Figure 2.48: Artist’s view of strip detector used in the November 1999 test beam.

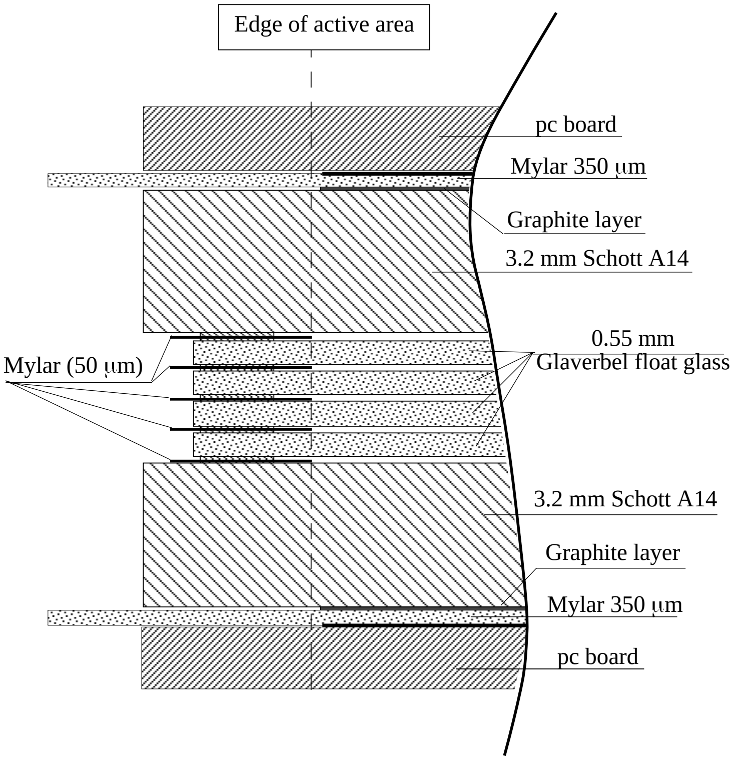

Figure 2.49: Cross section of the strip detector used in the November 1999 test beam.

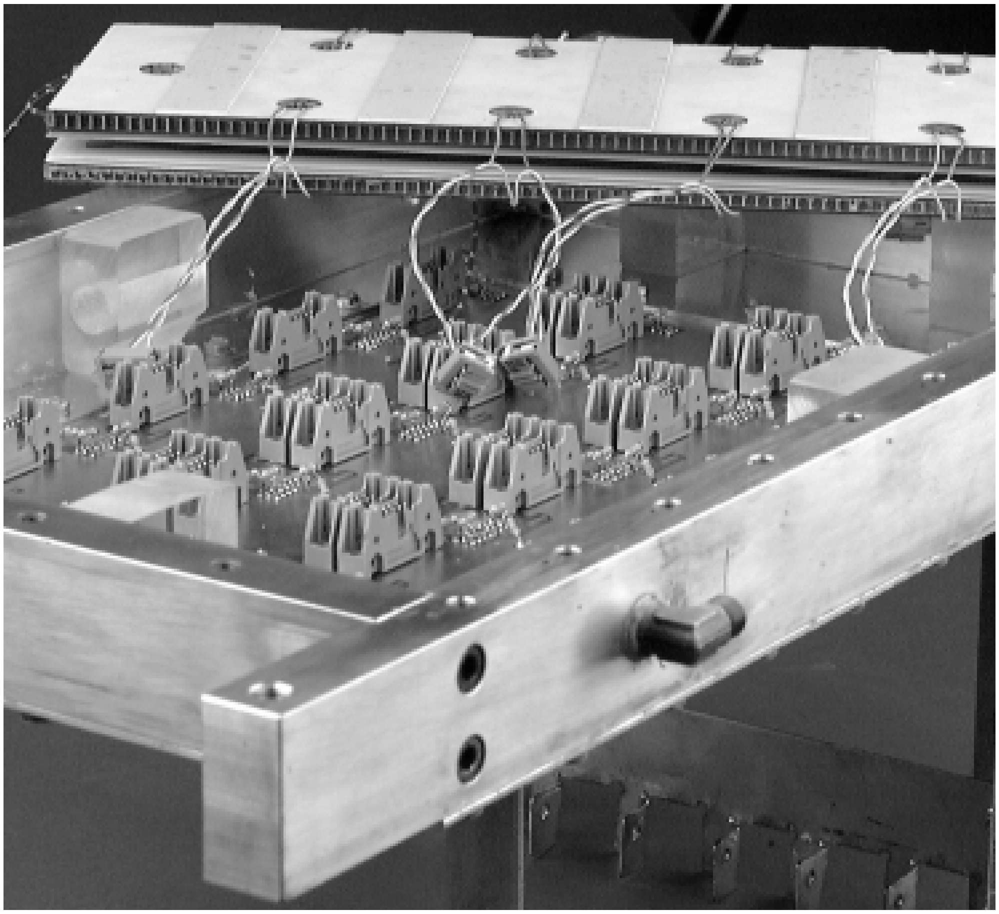

Figure 2.50: Photograph of the strip detector just before it was inserted in the gas box. The read out electronics was mounted on the lower side of the gas box. The signals from the read out pads were connected to the electronics with the twisted pair cable shown in the photograph.

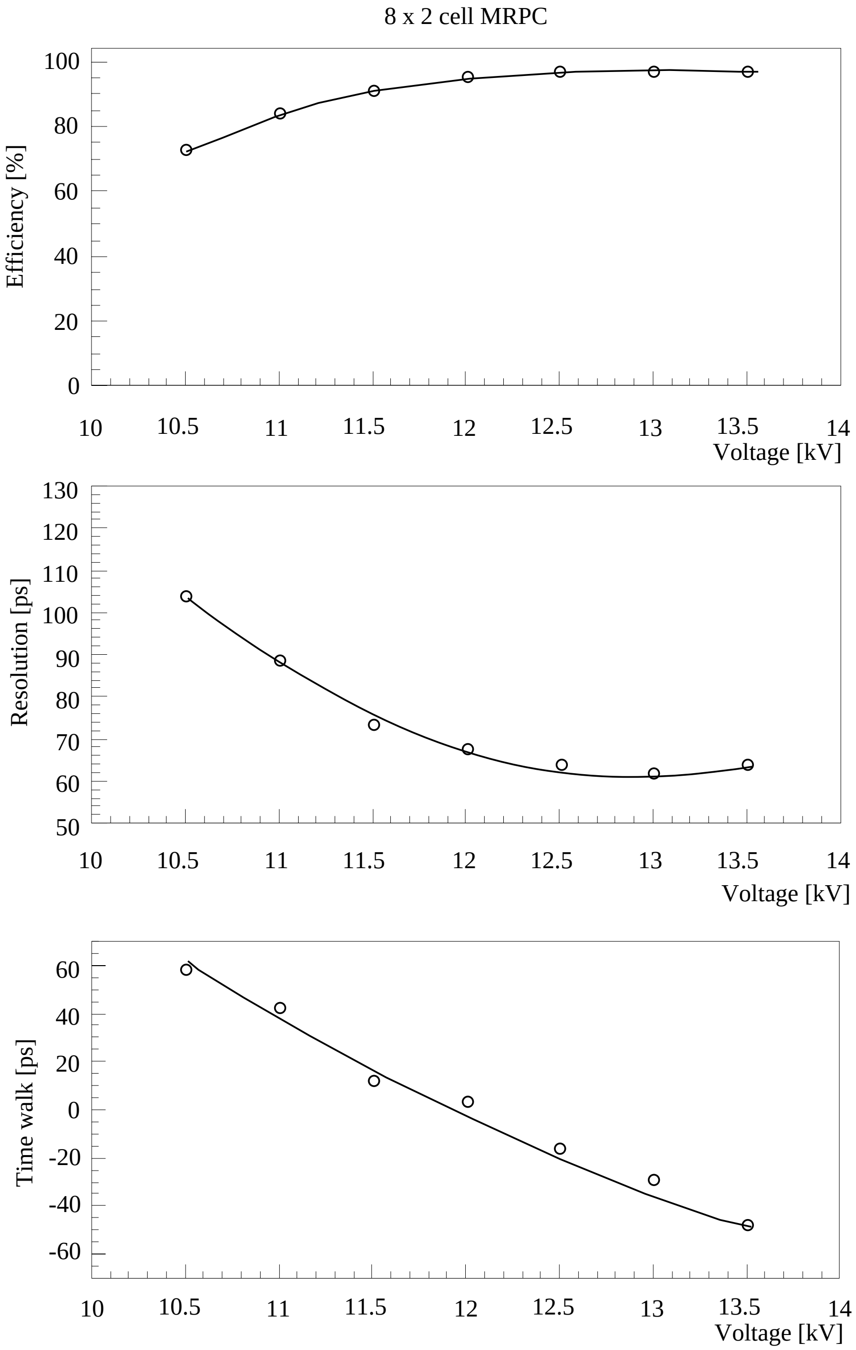

Figure 2.51: Efficiency, time resolution and time-walk as a function of applied voltage for one of the cells of the strip MRPC.

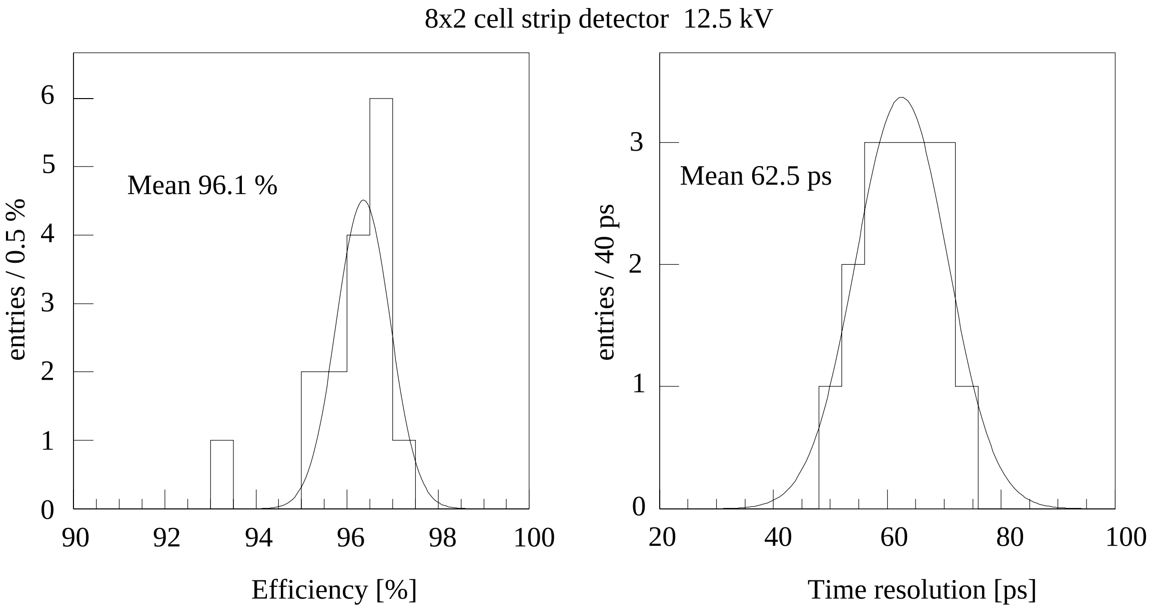

Figure 2.52: Efficiency and resolution of the 16 cells of the strip chamber.

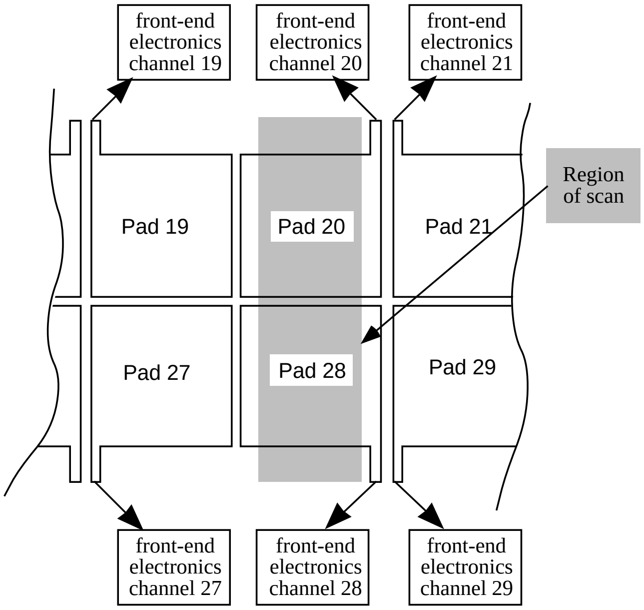

Figure 2.53: Layout of cells of scan of boundary between pad 20 and pad 28.

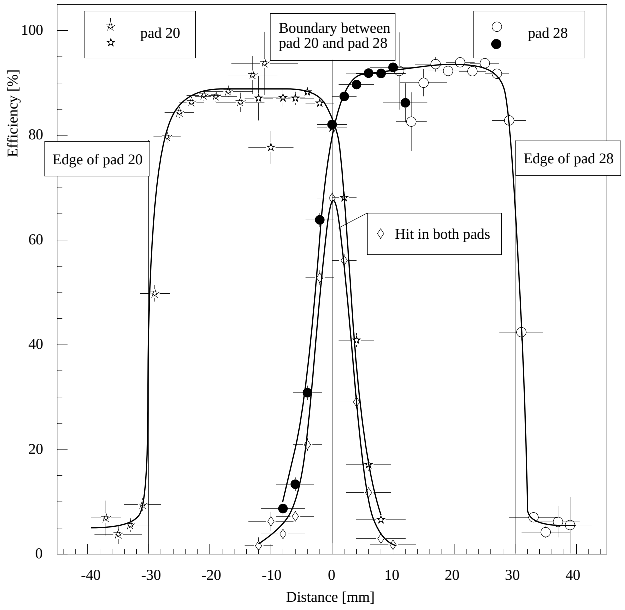

Figure 2.54: Efficiency as a function of position. The solid lines are to guide the eye.

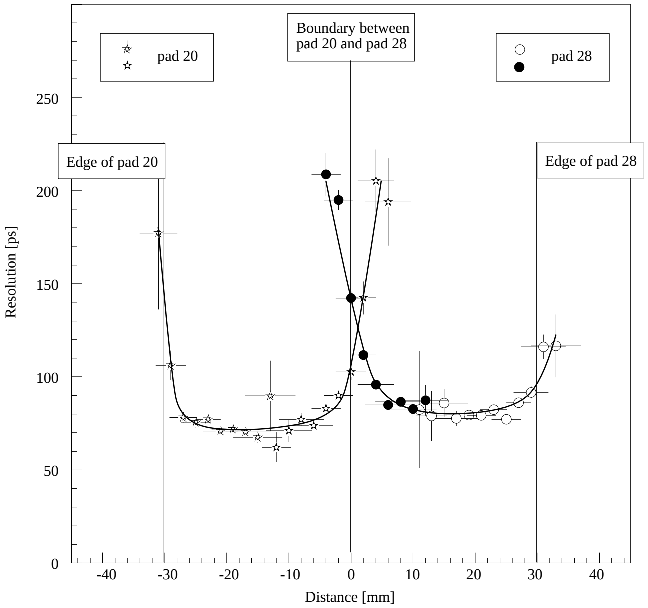

Figure 2.55: Time resolution as a function of position. The solid lines are to guide the eye.

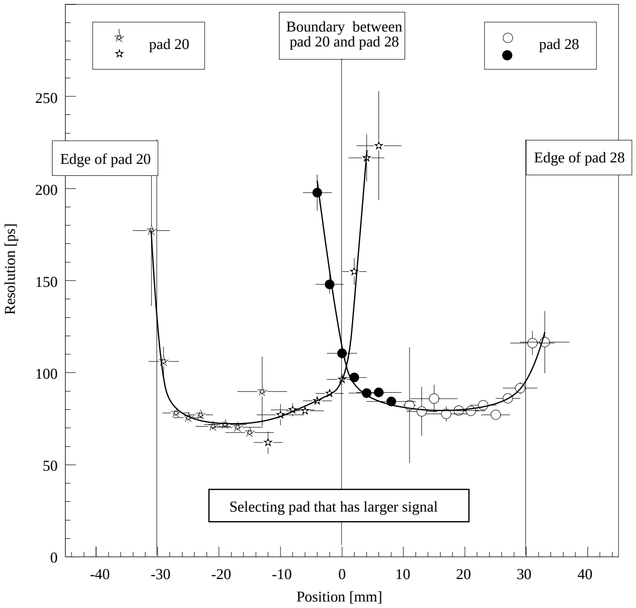

Figure 2.56: Time resolution as a function of position with the additional condition of choosing the pad with the larger pulse height. The solid lines are to guide the eye.

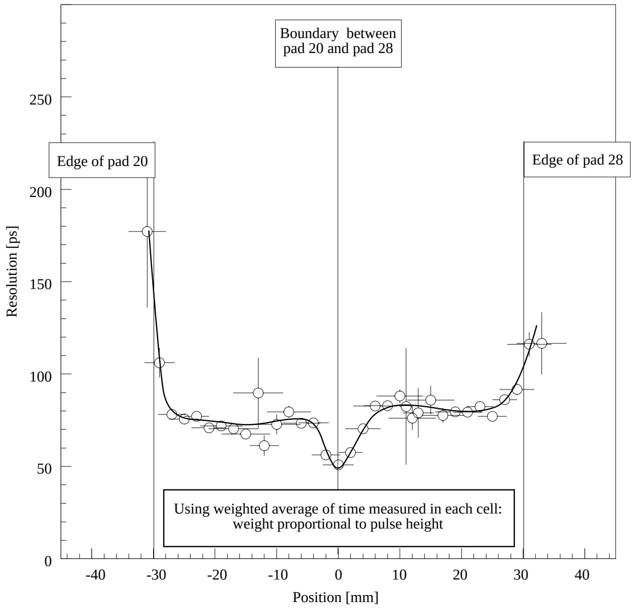

Figure 2.57: Time resolution as a function of position using the weighted average of the time measured by each pad. The weight is proportional to the measured pulse height from each pad. The solid lines are to guide the eye.

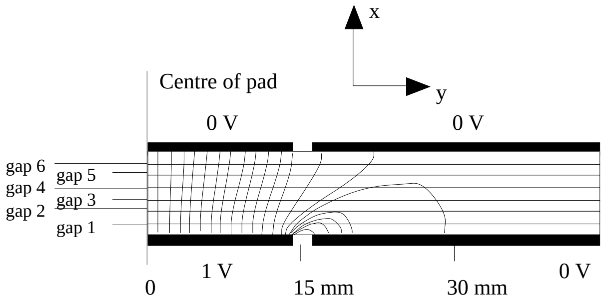

Figure 2.58: Field lines of the normalised weighting field used to calculate the coupling of the avalanche signal to the pick-up pads.

(worst value 110 ps). This is shown in Fig. 2.57. Finally, we show the time resolution using the weighted average of the time measured by each pad. The weighting is proportional to the measured pulse height. At the boundary between the pads there appears to be an improvement of the time resolution. One assumes that part of this improvement is due to having two independent electronic channels. Whether such techniques can be used to avoid the degradation of the time resolution at the boundaries between pads depends on the overall occupancy. However, we would only consider using such techniques if two neighbouring cells had very similar time measurements. Further Monte Carlo studies are needed.

2.4.4 Boundaries between cells

As discussed above, one concern for a multicell detector is the boundary between cells. If we have to treat each pad as a separate cell and cannot combine the data for hits close to the boundary, there will be a degradation of the time resolution. In addition, close to the boundary, there is a high probability that both pads will give a signal. Again, this is not a serious concern since it just leads to a modest increase of occupancy. We want to build the best possible TOF array and believe that, for high occupancy, the boundary between cells should be as sharp as possible. We will discuss, here below, how this edge can be made more precise by using a differential amplifier. We have already noted that we want the detector itself to produce a differential signal. Thus adding a differential amplifier should be a straightforward operation.

To study the edge effects of the cells, we used the ‘normalised weighting field’ technique as described by Radeka [33]. The induced current on a pickup strip is $j = - q.\vec{E}_W.\vec{v}$, where $\vec{E}_W$ is the normalised weighting field and $\vec{v}$ is the velocity with which the charge (in the avalanche) is moving. The normalised weighting field is calculated by applying 1 V to the electrode of interest and 0 V to all other electrodes. This ‘normalised weighting field’ is used only to calculate the coupling of moving charges to the pick-up electrodes; it has no connection with the actual electric field in the device itself. The field lines for $\vec{E}_W$ are shown in Fig. 2.58. We are only interested in the x-component of $\vec{E}_W$, since the electrons in the avalanche move only in this direction. A plot of E_x as a function of position for various gas gaps is shown in Fig. 2.59. It is clear that, for the gap 1 (closest to the pickup pads), the weighting field (and thus the magnitude of the induced current) is affected by the presence of the neighbouring pad. The signal increases as the avalanche position approaches the edge of the pad; when the avalanche is positioned above the neighbouring pad the signal is of opposite polarity. For avalanches in the gas gap 6 (furthest from the pickup pads), one can see that, as the avalanche position approaches the edge, the signal is reduced, since the induced signal is shared between two pads. These effects are large and detrimental to the performance of the detector. It should be noted that, for a given through-going particle, one does not know if detectable avalanches will be produced in all gaps, or in just one. Ideally, the coupling of the signal produced by the avalanche should be similar for all gaps. In the case of a differential readout, both anode and cathode pads are connected to a differential amplifier. Using the labelling from the previous

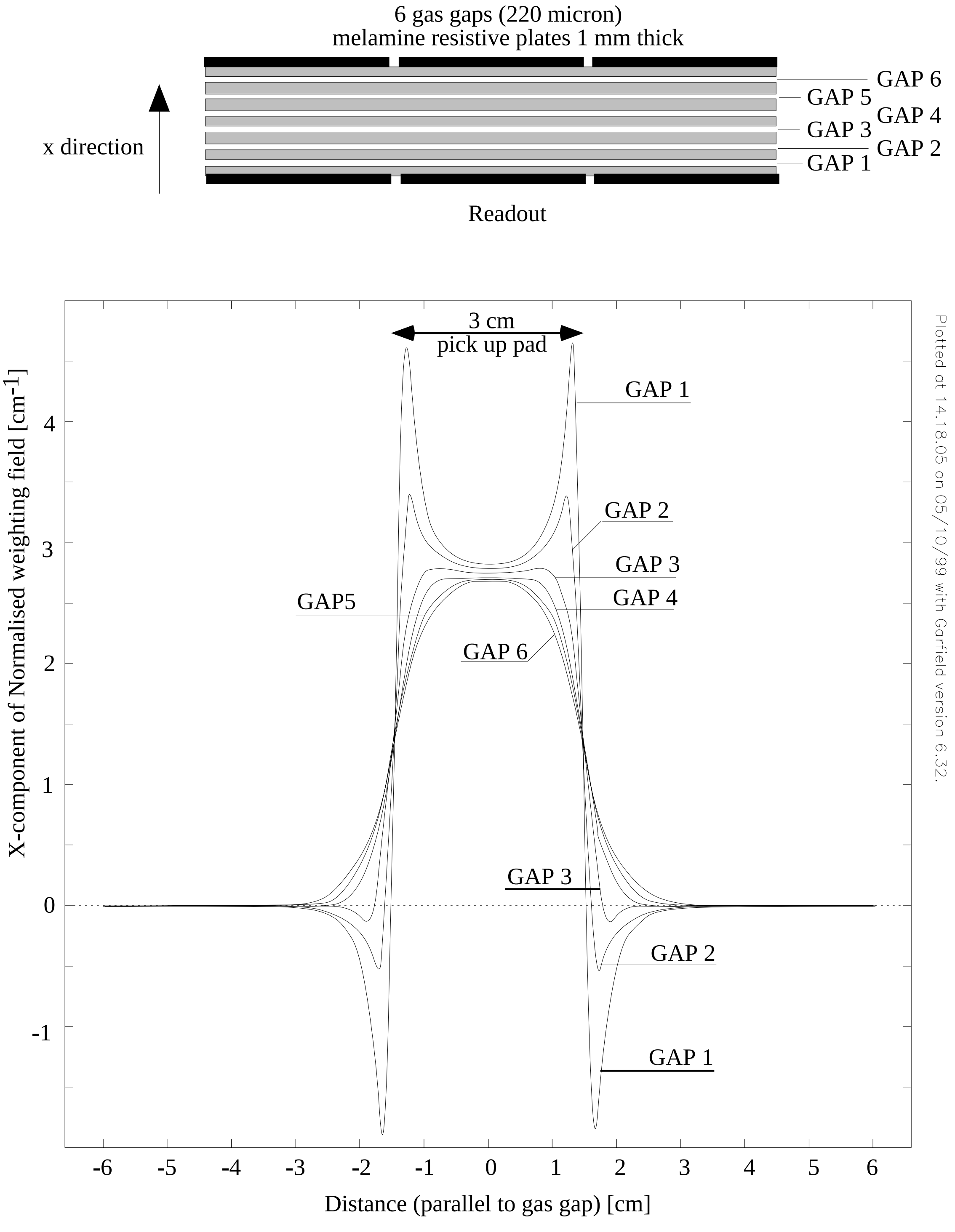

Figure 2.59: The x-component of the normalised weighting field as a function of distance for different gaps in a six gap MRPC (read-out pad 30 mm wide).

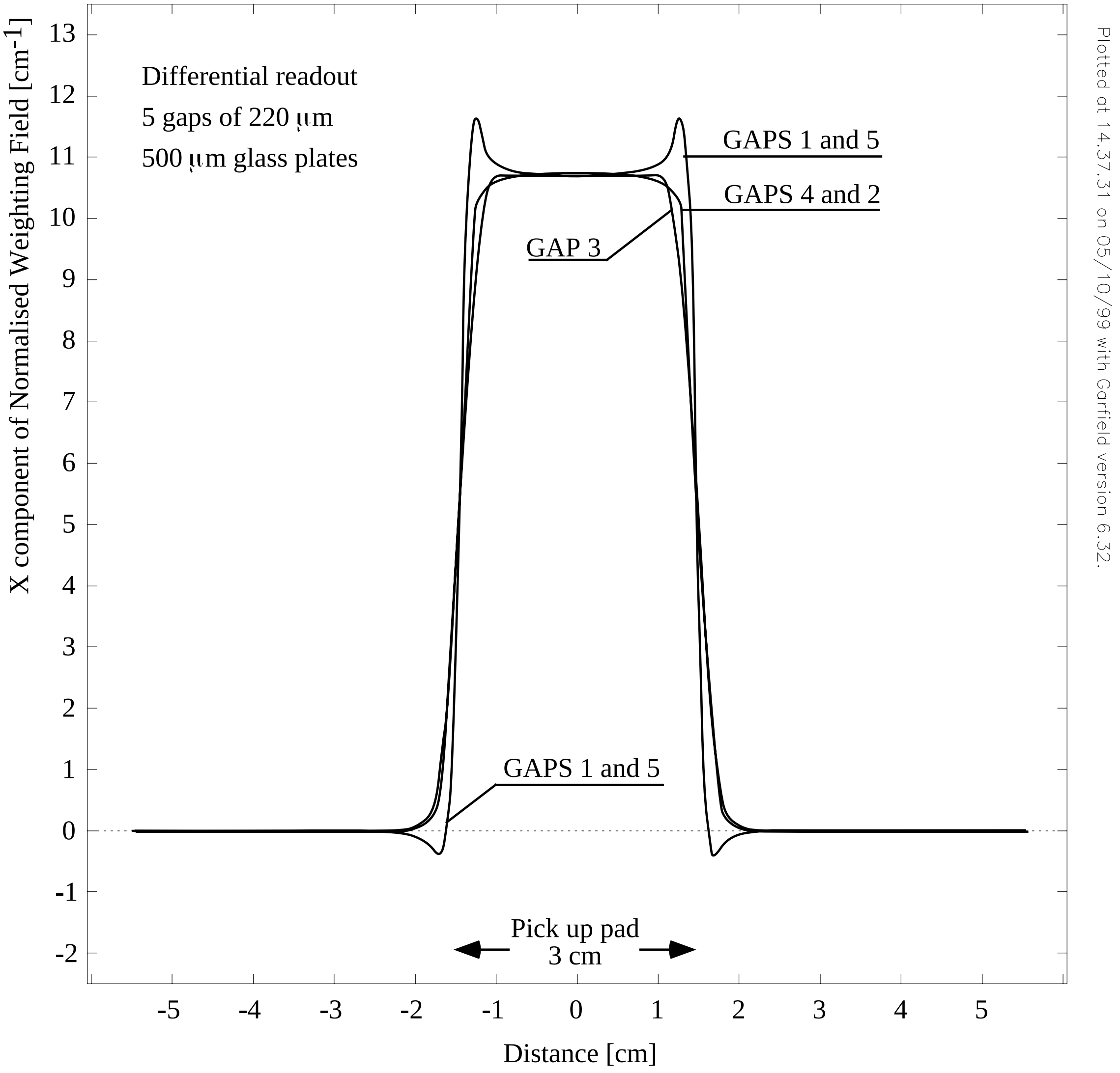

Figure 2.60: The x-component of the normalised weighting field as a function of distance for different gaps in a five gap MRPC using differential read out of the anode and cathode pads.

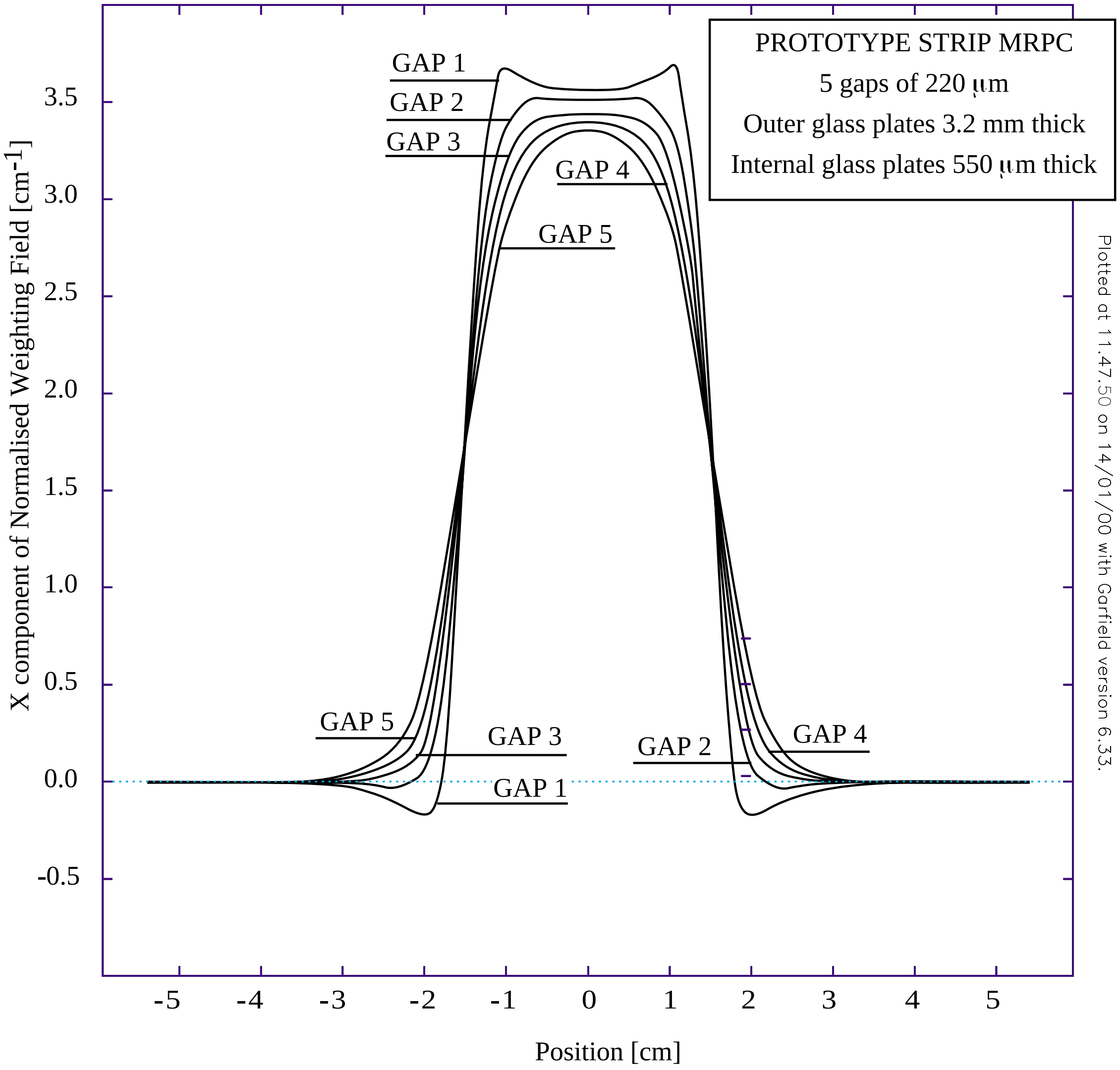

Figure 2.61: The x-component of the normalised weighting field as a function of distance for different gaps for the prototype strip MRPC.

figure (Fig. 2.59), gap 1 for an anode pad would be equivalent to gap 6 for the cathode pickup pad. Therefore, for differential read out, one has to add the response of gap 1 and gap 6. Consequently, as one approaches the edge of the pads, these big deviations in response cancel each other. In Fig 2.60, we show the expected response for a differential amplifier attached to a 5 gap MRPC. Although there is a small non-uniformity close to the boundary for gaps 1 and 5, the response is essentially similar for all gas gaps. In the previous section, we have shown results from a prototype ‘strip’ MRPC and stated that the boundary between cells would be sharper if the outer glass plates were thinner than the 3.2 mm used. The weighting field for this detector is shown in Fig. 2.61. It is clear that the ‘edges’ are sharper in the case where thinner glass sheets are used, as shown in Fig. 2.60

The results from the R&D show that there is not a serious problem at the boundaries of the cell; we will however investigate the possible improvement, using a differential amplifier. If some significant improvement is found, a differential amplifier will be used in the read out. The design of the front-end electronics assumes that a differential amplifier is necessary.

2.5 Materials for resistive plates

High pressure laminates (HPL) composed of melamine and bakelite have long been used as plate material for resistive plate chambers. Glass has also been used sucessfully by Pestov [2] and for large area muon detection for the Belle experiment [27]. We now discuss the choice of material for the resistive plates for the TOF MRPCs. We have been conducting long-term tests of various high-pressure laminates and various glass plates. For each material, we attach an electrode to either side of the plate and apply 100 V. Previously, we worried about surface conductivity and leakage around the edge of the plates so we tested this effect by constructing guard rings. We found that this was a negligible effect: all further tests were made without guard rings. Every day or so, we measured the current drawn by each plate under test and recorded the temperature and humidity in our laboratory where these tests were taking place. The resistivity plotted against temperature is shown, in figure 2.62, for the black welding glass (Schott A14). The line superimposed is an exponential fit to the data. In Table 2.1, we show the temperature and humidity dependence of all the plates tested. All the high-pressure laminate materials showed a variation with humidity; high humidity reduces the resistivity. There was no correlation between humidity and resistivity observed with the glass plates. During our testing of MRPCs, we added 1 % water vapour to the gas mixture when testing MRPCs built with high-pressure laminates, by bubbling the gas through a water reservoir at 8°C. RPCs built with glass plates for the BELLE experiment [27] operated well only if the gas mixture was completely dry. A small fraction of water vapour increased the dark current, and eventually the chambers became inefficient. For this reason, we always use dry gas when testing MRPCs built with glass plates.

The tolerance of the gas gap is one of the most critical dimensions of all parallel plate and resistive plate chambers. Obviously, it is easier to control this tolerance if a rigid plate material is used. For a given thickness, glass is more rigid and glass sheets are flat. High pressure laminates tend to have some curvature, especially when they are thin. However, as we have seen from the results of this R&D program, we can successfully use high-pressure laminates if we use a strong support structure and many spacer buttons. For optimal TOF MRPC performance we need the following: (a) smooth surface; (b) thin resistive plate and (c) low enough resistivity so as not to have rate problem. The maximum rates at ALICE are expected to be 50 Hz/cm^2. The strip detector discussed in the previous section has glass plates with a resistivity of 8×10^{12} Ωcm; extrapolating the rate measurement discussed earlier, we calculate a rate capability of 100 Hz/cm^2. Although this is adequate for ALICE, we would prefer to have a larger margin of safety (i.e. lower resistivity). It is clear that glass has a smoother surface than melamine-phenolic laminates; also thin plates (0.5 mm) of glass are more rigid than high-pressure laminates of a similar thickness. For these reasons, we choose the black A14 glass as the base line for the TOF MRPCs. We are currently investigating with Schott whether this glass can be made in a thickness of 0.5 mm. We will also practice building large modules with thin float glass ($\rho \sim 8\times10^{12}$ Ωcm) in order to estimate the

Table 2.1: Temperature dependence for various samples of Melamine-phenolic laminates and for various samples of glass. Recently we have been supplied with another sample of Pestov glass that has a resistivity of $3.10^{10}\Omega$cm.

Material	Temperature dependence (exp(-alpha*T))	Humidity dependence (exp(-beta*T))	Resistivity at 20°C and 50% Rel. Hum.
Bakelite (Italy)	0.2283	0.058	$4.9\ 10^{11}\Omega$cm
Melamine (Italy)	0.1262	0.023	$5.4\ 10^{11}\Omega$cm
Fenolico (Italy)	0.1280	0.025	$8.3\ 10^{10}\Omega$cm
Korean White	0.1779	0.040	$1.01\ 10^{12}\Omega$cm
Korean Top Tune	0.1772	0.015	$2.0\ 10^{12}\Omega$cm
Korean Brown	0.1530	0.012	$5.04\ 10^{12}\Omega$cm
Swiss Black	0.1326	0.026	$1.8\ 10^{11}\Omega$cm
Swiss White	0.0503	0.034	$1.5\ 10^{11}\Omega$cm
Schott A14 glass	0.1009	-	$1.6\ 10^{12}\Omega$cm
Pestov Glass	0.06424	-	$6.5\ 10^{11}\Omega$cm
Schott 8900	0.1107	-	$3.4\ 10^{12}\Omega$cm
Schott 8540	0.0614	-	$1.67\ 10^{10}\Omega$cm

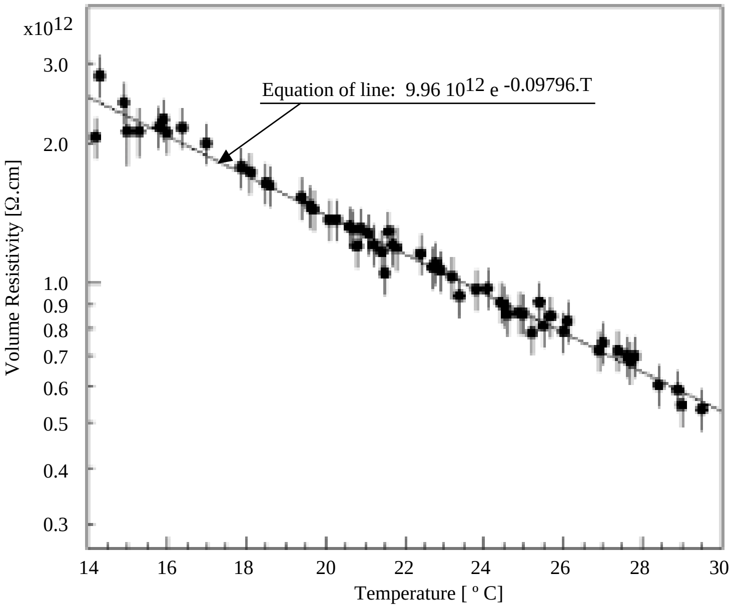

Figure 2.62: Resistivity versus Temperature for the black welding glass Schott A14.

most practical thickness for building the actual module.

2.6 Summary of R&D

In this chapter, we have described the R&D carried out for the ALICE TOF detector. Since a large area has to be covered, a gaseous detector is the only choice; this gaseous detector has to be based on the parallel plate chamber so that the time jitter, associated with the drift of electrons to a high field region, is avoided. We have discussed the Pestov counter that has a 100 μm gap, giving a time resolution better than 50 ps. Unfortunately, a long tail of late signals mars this excellent time resolution. The requirement of pressurising this detector to 12 atmospheres constrains the geometry and adds to the cost of this solution. This detector also requires a special semi-conductive glass that is non-commercial. For these reasons, a solution involving parallel plate chambers with two gaps of 600 μm was investigated. The problem with PPCs is that they have to be operated at low gains to keep the probability of producing a spark low. Thus there is a non-negligible contribution to the time resolution from jitter created in the electronics. It was difficult to operate a PPC with two gaps of 600 μm with a time resolution better than 250 ps, which worsened to 300 ps when the PPC cells were mounted in an array.

Many of the problems associated with the Pestov counter and the PPC have been overcome by the multigap RPC technology. It is operated at atmospheric pressure, constructed with commercially available glass, the signal is the analogue sum of signals from many gaps, so there is no late tail, the resistive plates quench the streamers so there are no sparks, thus high gain operation becomes possible. It has been shown that devices built with rather simple construction techniques give good time resolution. Both an array of single cells and a multicell strip design produce good uniformity. Various front-end electronics have been tested; all give good results so we do not expect any fundamental problems with the development of a front-end ASIC.

2.7 Further R&D

We have demonstrated that the multigap RPC can be used as an excellent Time-of-Flight device and is well suited to be the basis of a very large array. However, there is still a list of items that need to be studied to optimise the performance.

2.7.1 Material for the resistive plates

We have tested both glass and melamine and find that glass is mechanically more rigid, flatter and smoother than melamine, thus it is easier to construct a device, with a uniform gap size, using glass. Melamine has some advantages; it is less fragile and has lower resistivity; we will therefore keep it as a backup material at present. If we can build a device using thin sheets of black glass (Schott A14), which has a resistivity of 2×10^{12} Ωcm, we will have a rate capability of 500 Hz/cm^2 (c.f. ALICE maximum expected rate of 50 Hz/cm^2). This glass however is usually made in a thickness of 2.5 mm. We have an offer from Schott for 1 mm thickness; thinner sheets are probably possible but need some R&D. Another option is to use a commercial glass with a high content of Sodium such as Glaverbel Float. This has a resistivity of 8×10^{12} Ωcm and comes in various thicknesses (0.4 mm and 0.55 mm for example). Using this glass would produce a device with a rate capability of 120 Hz/cm^2, sufficient for ALICE but without a large safety margin.

Glass could possibly be attacked by by-products of the avalanche process with the gases used. For example, SF_6 can be transformed into sulphuric acid. It should be noted that the BELLE experiment has built and operated, in streamer mode, a large area of glass RPCs, using a gas mixture containing $C_2F_4H_2$. These chambers have undergone long-term testing and have no problem as long as the gas is kept very dry. Certainly, we will follow this lead and keep the gas dry; we must however perform our own ageing tests. If there is an ageing problem, it should be noted that, physically, the black glass has a far harder surface than the high sodium content glass and may thus have a surface which is more resistant to attack.

Points to investigate: (a) Production of thin sheets of black glass; (b) Long term tests for ageing.

2.7.2 Construction of modules

We have shown that we can construct a device containing 8×2 cells that has very good uniformity. For ALICE, we intend to build the modules from strips of detector which will be ∼1.3 m in length. It may be that glass sheets of 400 μm thickness are too fragile to handle in these dimensions, and constructing the modules with strips of 60 cm in length may be more practical. This we will test.

We also need a method to define the edge of the active area of the strip detector. Currently, we have a 50 μm thick Mylar sheet between the glass plates along the edges. It could facilitate the construction if we simply allowed the edge of glass plate itself to define the edge of the active area. Currently, the cutting procedure leaves a sharp edge; this can create a high field region and thus be a source of corona discharge. However there are machines that cut glass plates using a water jet or a laser beam; this cutting technique leaves a smooth edge on the glass.

For the prototype tested at the end of 1999, the read-out pads were connected to the PCB holding the electronics with a twisted pair. This was soldered onto the pickup pads. Although this technique worked well, we will want a more practical method for the mass production.

In the next chapter, we show drawings of strip detectors into a gas-tight box. There is no fundamental problem involved but we certainly expect to build several large prototypes before we arrive at the optimal construction technique.

Points to investigate: (a) Practical maximum size of thin glass plates; (b) Edge of active area: Mylar or rounded edge of glass; (c) Connection between read-out pads and electronics; (d) Assembly problems with large modules.

2.7.3 Front-end electronics

A simulation of the induced signals on the pick up pads of the chamber has shown that we can minimise the edge-effects between cells by using a differential amplifier. To build a very fast amplifier that is truly differential is non-trivial. Various amplifiers need to be tested in various configurations to validate this technique.

The amplifiers used until now in our tests have been constructed using discrete components. For such a large number of channels (160 000), this is not a practical or cost effective solution. We need to have all the front-end electronics in a single integrated circuit (probably 4 channels per ASIC).

Points to investigate: (a) Validate that a differential amplifier really reduces cross talk/edge effects between cells; (b) First prototype for a front-end integrated circuit.

2.7.4 Study of avalanches in various gas mixtures

An avalanche growth is characterised by $N=N_o\exp(\alpha_{eff}.x)$ where x is the distance the avalanche has travelled and α_{eff} is the effective Townsend coefficient ($\alpha_{eff} = \alpha - \eta$, where α is the Townsend coefficient and η is the attachment coefficient). Normally, RPCs are operated in avalanche mode with a gain that gives $\alpha_{eff}.D \sim 20$, where D is the size of the gas gap. The ratio of fast signal to the total charge in the gas gap is $1/\alpha D$. For the case of $\eta = 0$ this ratio is 5 %. However, when electronegative gases are used, η becomes large and the ratio of fast signal to total charge is reduced. The fast signal is used for the timing, but the rate capability will depend on the total charge produced in the gas gap by each avalanche. We have extensively measured the ratio of fast signal to total charge, for a 2 mm gas gap RPC [34]. We find that when using an electronegative gas mixture, this ratio increases from 0.5 % to 10 % at high gains. We have not measured this ratio with this multigap design, but the indications are that this ratio must also be around 10 %. We need to study this ratio and the effect of changing the gas mixture. Different Freons have different thresholds for streamer production, as well as different ratios of fast signal to total charge. We have had very satisfactory performance with the gas mixture we have been using, but it is not clear if this is the optimum.

Points to investigate: (a) Ratio of fast signal to total charge; (b) Different gas mixtures.

2.7.5 Will the neutron and gamma background produce streamers in our TOF device?

We have tested this device at the GIF. Naively, we expected to have many streamers produced in the MRPC. Conversions from the gamma into low energy (and highly ionising) electrons should produce clusters containing a large number of electron/positive ion pairs; these large initial clusters should produce extra-large avalanches and thus trigger streamers. However, the ionising particle needs to be moving to create the electron/positive ion pairs; for example, a 6 keV electron moves 200 μm creating 200 electron/positive ion pairs. In our MRPC, the ionising collision length is $\sim$ 10 μm. We can only consider a cluster, containing a large number of electrons, if it is contained in a size similar to the ionisation length (i.e. 10 μm). In addition, the size of the gap is 200 μm, so a heavily ionising particle is likely to cross the gap and deposit most of its energy in a resistive plate rather than in the gas. It therefore appears that the small gaps save us from producing streamers from heavily ionising particles. We have to make sure of this and therefore need to test our MRPC in a flux of neutrons.

Point to investigate: Test MRPC at neutron source to investigate streamer production from heavily ionising particles.

3 Detector description

3.1 Design considerations for the ALICE TOF detector

The R&D for the ALICE TOF has been discussed in the previous chapter. It is clear that the multigap resistive plate chamber provides the time resolution needed. In this chapter we will discuss the design of the detector that best suits the ALICE experiment.

3.1.1 Choice between double MRPC and single-stack MRPC

Two versions of MRPCs have been tested. One design follows the double-gap PPC. This design is a doublet of MRPCs. Each MRPC has a metallic anode and cathode. The gap between anode and cathode is divided into two, with a single resistive plate made of glass. This glass plate is at ‘floating’ electrical potential. We call this design as the ‘double’ MRPC. The other design has a single anode and cathode. In the space between anode and cathode there are a number of resistive plates, all electrically floating, which create a series of equal-sized gas gaps. We call this design a ‘single-stack’ MRPC.

The ‘double’ MRPC follows a similar construction technique to the PPC. The PPC has to be constructed with very high precision (5 μm) and it was expected that a MRPC cell built with similar precision would have exceptional time resolution. Indeed the time resolution of this array is better than 90 ps. However, the results from the R&D show that similar time resolution can be obtained with ‘single-stack’ MRPCs; a construction that uses relatively imprecise (tolerance $\sim$ 20 μm) spacers. Thus we do not need to construct devices with the precision used for the ‘double’ MRPC. Furthermore there are some disadvantages to this double MRPC design. The first disadvantage is that the sensitive region is rather thick, thus creating a parallax problem, even for tracks at moderate angles of incidence, and large edge effects for tracks coming at an angle. Although this cell could be modified so that the sensitive region is thinner, it is difficult to match the thin sensitive region of the stack MRPC shown in Fig. 3.1(b). Another disadvantage is that both halves of a double design have to be identical. Since detectable avalanches can be produced in one (or several) of the gas gaps, any differences in time response between the two halves of the doublet will degrade the time resolution. ‘Identical’ means that each half has to have the same dimensions, and that the signal leads and stray capacitance for each anode and cathode have to be the same. This is a very strong constraint that does not affect the ‘single-stack’ design, in which each cell has only one anode and cathode, making effects due to stray capacitance irrelevant. One advantage that the ‘double’ MRPC design has is that it needs a lower voltage (by a factor 2). Although it is simpler to operate with a lower voltage, we have not experienced any problems working at 12 kV and higher. Another apparent advantage of the double MRPC design is that the signal is larger than the single stack MRPC (by a factor of two). However, the capacitance of double design is also 2 times higher and thus one loses the advantage of the larger signal. Finally, the double MRPC was conceived as a ‘single-cell’ construction element, where it has been imagined that a large array would be built from a ‘chess-board’ type matrix as discussed in the preceeding R&D chapter. Such a design adds problems, especially at the ends of the barrel where the angle of incidence for the tracks is large. Consequently we have a strong preference for the ‘single-stack’ MRPC design over the ‘double’ MRPC design.

3.1.2 Choice between an array of single cells or a planar geometry

The ‘single-stack’ design can be used to construct single cells or multi-cell planar devices (shown in Fig. 3.1(b) and (c)). From the R&D, we have already experienced the advantages of having a device that produces a differential signal (i.e. the signal is obtained from both the anode and cathode). In addition,

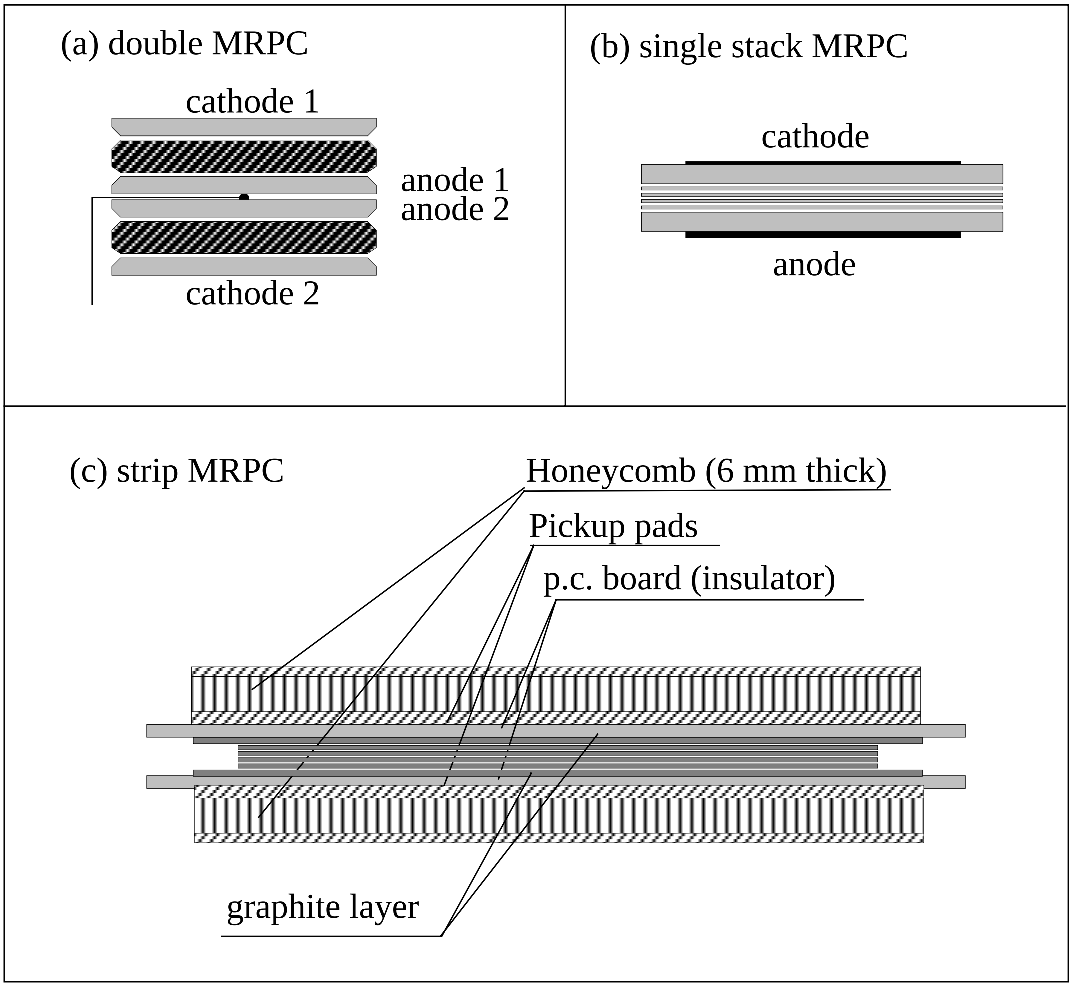

Figure 3.1: Schematic cross section of various MRPC designs: (a) double MRPC design, (b) single-stack MRPC design (c) strip detector using the stack MRPC design.

the sharpness of the edge can be improved by having differential readout, as discussed previously. The design is limited to a strip, the width of two cells, in order to allow easy connection to both anode and cathode.

At the ends of the TOF barrel, particles from the interaction point will enter the TOF detector at 45°. In order to minimise edge effects caused by oblique angles of incidence, the TOF detector should be tilted to face the interaction point. If one builds the TOF array from individual cells one has to arrange them in at least two layers since in a single layer arrangement, each cell is surrounded by some kind of support system that would introduce dead regions. It is possible to find an arrangement of staggered cells that creates a detector with close to 100 % geometric coverage. However this is very complicated, especially at the ends of the barrel. If we use a strip design instead, the geometric arrangement is far simpler.

Another reason in favour of the strip design is the decoupling of the signal from the high voltage source. In general we have been applying a negative high voltage to the cathode and zero volts to the anode. The generated signal is between the anode and cathode; the signal return from the anode is to the cathode. For the single cell array discussed previously the signal return to the cathode was via a high voltage capacitor (these are not cheap). For the strip detector discussed in the R&D chapter we applied the high voltage with a graphite layer insulated from the pick-up pads, thus no high voltage capacitors are needed. As a result, reading out the strip detector is straightforward. Identical cathode and anode read-out pads create a differential signal that is sent to the front-end amplifier. The PCB used for the single cell array that, among other things, held the high voltage capacitors, is not needed for the strip detector. Of course, a single cell could be constructed with a graphite layer together with a single pick-up pad (so avoiding the need for a high voltage capacitor). However, it is much easier to have many cells sharing a single graphite layer.

In conclusion, a strip detector design allows simpler mechanics for tilting the chambers to face the interaction point at the ends of the barrel. It is much easier and cheaper to build a detector of a strip design than individual cells. For these reasons we have chosen this design for the ALICE TOF detector. Our first prototype of 8×2 cells has been tested and the results presented in Chapter 2. We have started building and testing longer strip detectors.

3.2 Engineering system design

3.2.1 General system layout

The layout of the proposed TOF detector system, covering a cylindrical surface of polar acceptance $|\theta - 90^\circ| < 45^\circ$ and a full coverage in the ϕ angle using MRPC, is described hereafter. The system has a modular structure corresponding to 18 sectors in ϕ and five modules along the beam direction. The general design has been conceived taking into account the results of the simulations, the feasibility of the proposed solution, the performances of the detector and the need to keep the dead area inside the module to a minimum. In particular, it is important to minimise the transversal path of the incident particles through the strip chambers. This will reduce the number of very oblique transversal paths that can create a sharing effect of the signal among adjacent pads, thereby increasing the occupancy and the time jitter of the detected signals. To overcome this effect, a special positioning of the strips has been envisaged. Their angle with respect to the axis of the cylinder is progressively increased from 0° in the central part ($\theta = 90^\circ$) of the detector to 45° in the extreme part of the external module ($\theta = 45^\circ$). This arrangement makes the median zone of a strip perpendicular to a radius coming from the interaction point, giving a good approximation to paths of the incoming particles. To avoid dead areas, adjacent strips have been overlapped inside the modules so that the edge of the active area of one pad is aligned with the edge of the next one. This gives us the possibility of creating a full active area with no geometrical dead zones. The modules have been designed in such a way that as to avoid any loss of the sensitive area, along the z axis. The only dead area is due to the unavoidable presence of the supporting space frame structure.

3.2.2 Module description

The basic unit of the TOF system is a MRPC strip 1220 mm long and 100 mm wide. Due to the space constraints of fitting the strips inside the modules, it has been found that pads of size 35 x 25 mm (rather than the 30 x 30 mm initially considered) considerably ease constructional problems. An overall view of a strip is shown in Fig. 3.3. The cross section of the strip is shown in Fig. 3.4. The array of strips constitutes the sensitive part of a module. The strip length covers the width of a full sector. Five modules are needed to cover the full cylinder along the z direction. Three different types of modules are needed to cover the full length of the cylinder. They all have the same structure and transverse cross section (Fig. 3.5) but differ in length (Fig. 3.2). The actual dimensions are defined in such a way that the joining areas of the modules are aligned with the dead areas of the other detectors (TRD, HMPID, PHOS) projected from the interaction point, thus creating a configuration of minimal disturbance for the external detectors. The central module is 1.14 m long (Fig. 3.6), the intermediate ones are 1.47 m long (Fig. 3.7) and the external ones are 1.782 m long (Fig. 3.8). As explained before, since the MRPC strips are narrow, they are tilted and oriented inside a module so as to be perpendicular to a radius from the interaction point. Furthermore, the edges of each sensitive area are aligned with their neighbours so that no geometrical dead area is created. This arrangement implies a strip overlap. The MRPCs are contained in a gas-tight box. The frame of the gas box is constructed from 1 cm thick aluminium. This gives the overall necessary rigidity to the module to which the supporting and sliding system is connected. The gas box is separated from the electronics by a surface of PCB and aluminium. The signals from the strips are connected to the inner surface of the PCB. The front-end electronics is plugged onto the outer surface, in a similar fashion, to the prototype strip detector discussed in the previous chapter. The volume containing the electronics cards, input and output cables, water cooling pipes and radiators is closed by a cover attached to the space frame. This allows access to the electronics with no disturbance to the active part of a module. The front cover of the gas box (1 mm thick aluminium) should be able to withstand the pressure required for gas circulation inside the chamber (up to 5 mbar). The final design will present a solution which minimises the material in front of the detectors.

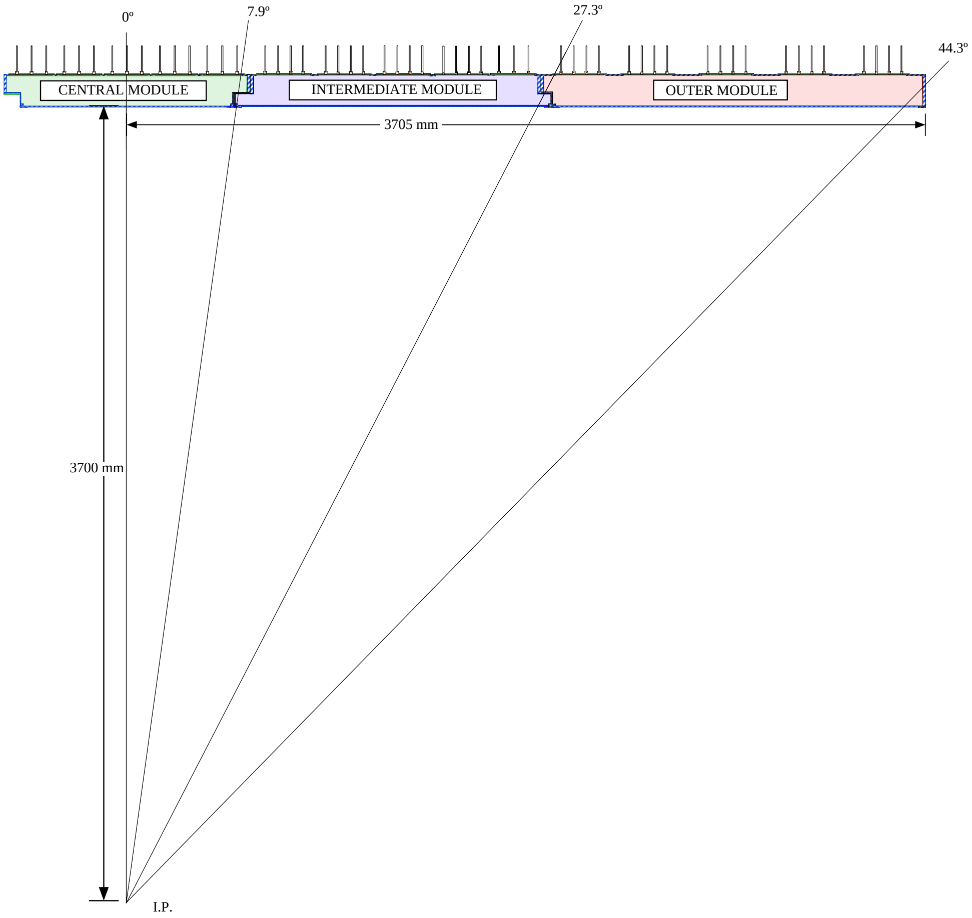

Figure 3.2: R-z view of the central, intermediate and outer modules.

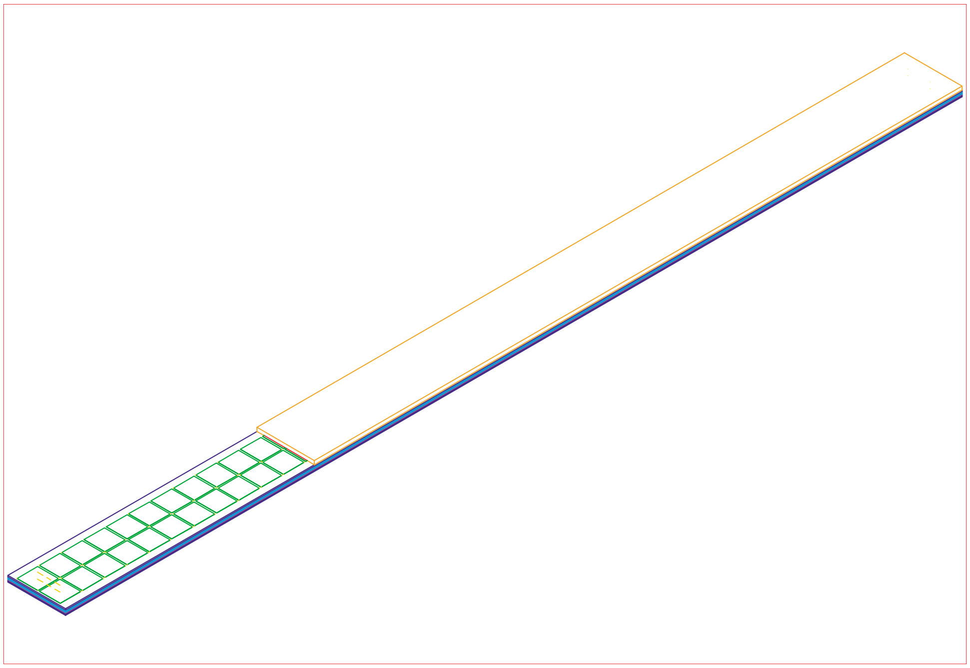

Figure 3.3: Overview of a TOF strip.

3.2.3 Supporting System

The complete TOF system consists of 90 modules with 3 different longitudinal sizes. This gives full coverage, without any empty area in front of the HMPID and/or PHOS. If, in the final design, some empty area should be left, the size of the modules will be adapted to match the projection of the other detectors. In this way, no extra dead area will be added, apart from that requested. The weight of each module has been estimated between 150 and 300 Kg depending on the size (see Table 3.1). The total weight of the system will be supported by a cylindrical tubular structure called the Space Frame. Five TOF modules in a row are located inside each of the 18 sectors defined by the structure, each being kept in position by two rails fixed to the Space Frame (Fig. 3.5). Four sliding bushes are fixed to the module body permitting the insertion of the modules into the supporting structure from either side (Fig. 3.5). The positioning precision requested is not high, so a simple mechanical reference is sufficient to define the position. Close to the rails, and parallel to them, will run the cooling and gas pipes and the HV cables, following a distribution that has been agreed with the CERN Service group (see Chapter 5).

3.2.4 Material budget

Table 3.2 gives the TOF material budget in terms of the radiation length, as seen by particles coming from the interaction region. The overlap of the strip chambers has been taken into account by a 50% increase of the material for items 2 to 5. The corresponding material budget due to the TPC amounts to 3.05 % radiation length.

3.2.5 Installation

The mounting of the TOF modules inside the supporting structure may be done from either end. A system of temporary rails bearing the module to be mounted must be placed in line with those positioned inside the Space Frame, then aligned to form a unique body. Once this is done, the module can slide inside till it reaches the requested position. As a consequence, the tools needed for the final installation are a few

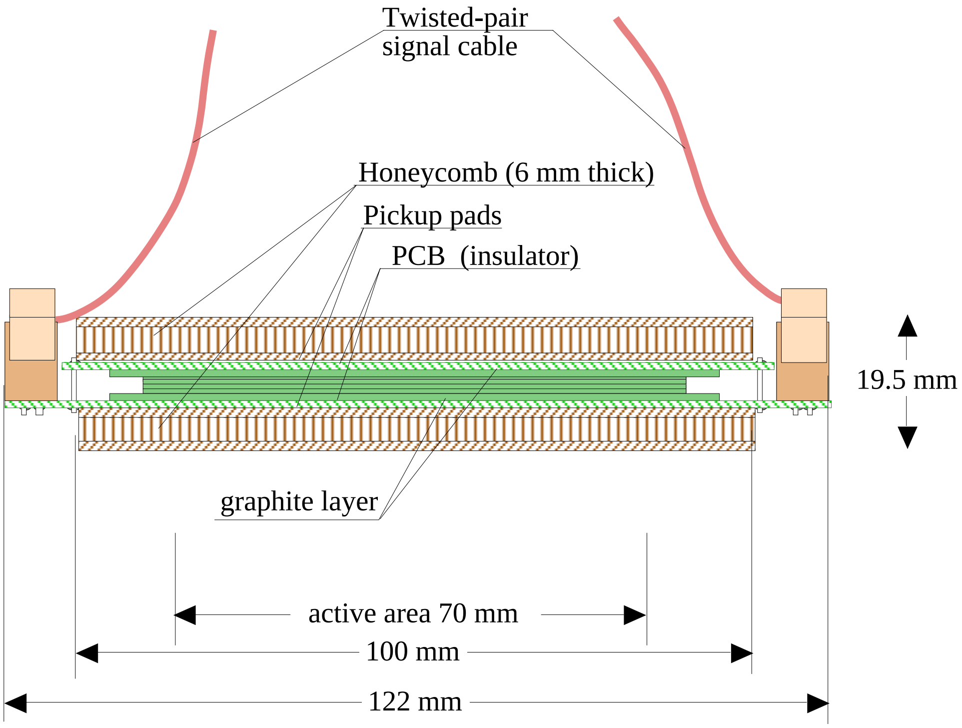

Figure 3.4: Construction details of a TOF strip detector.

transfer frames, with temporary rails fixed rigidly. These frames must, in turn, be connected to the Space Frame in such a way that they are strong enough to support the module weight and precise enough to be properly aligned with the rails mounted inside each sector. A system of this kind has already been used in other experiments and does not pose any special problem.

Table 3.1: Weight of a TOF module (Kg).

Module	Central	Intermediate	External
Strips	(2.0 × 15) 30.0	(2.0 × 19) 38.0	(2.0 × 20) 40.0
Cover	20.0	25.0	36.0
Support rails	35.0	40.0	45.0
Electronics	35.0	42.0	63.0
Electronics support	6.0	8.0	10.5
Cooling pipes	6.0	8.0	12.0
Cables and connectors	10.0	12.0	18.0
Total	142.0	173.0	224.5

Table 3.2: TOF material budget.

Material	Radiation Length X/X_0 (%)
Cover box (1 mm Al)	1.0
2 × Phenolic fiberglass honeycomb (6 mm, × 1.5)	1.40
2 × PC board (1 mm, × 1.5)	1.52
2 × Copper layer (25μm, × 1.5)	0.50
MRPC glass plates ($\sim$ 3 mm equivalent, × 1.5)	3.40
Gas box (2.5 mm Al/PCB)	2.80
Cooling pipes (Cu + water)	0.62
Electronics	5.0
Cover (2.0 mm Al)	2.20
Total	18.44

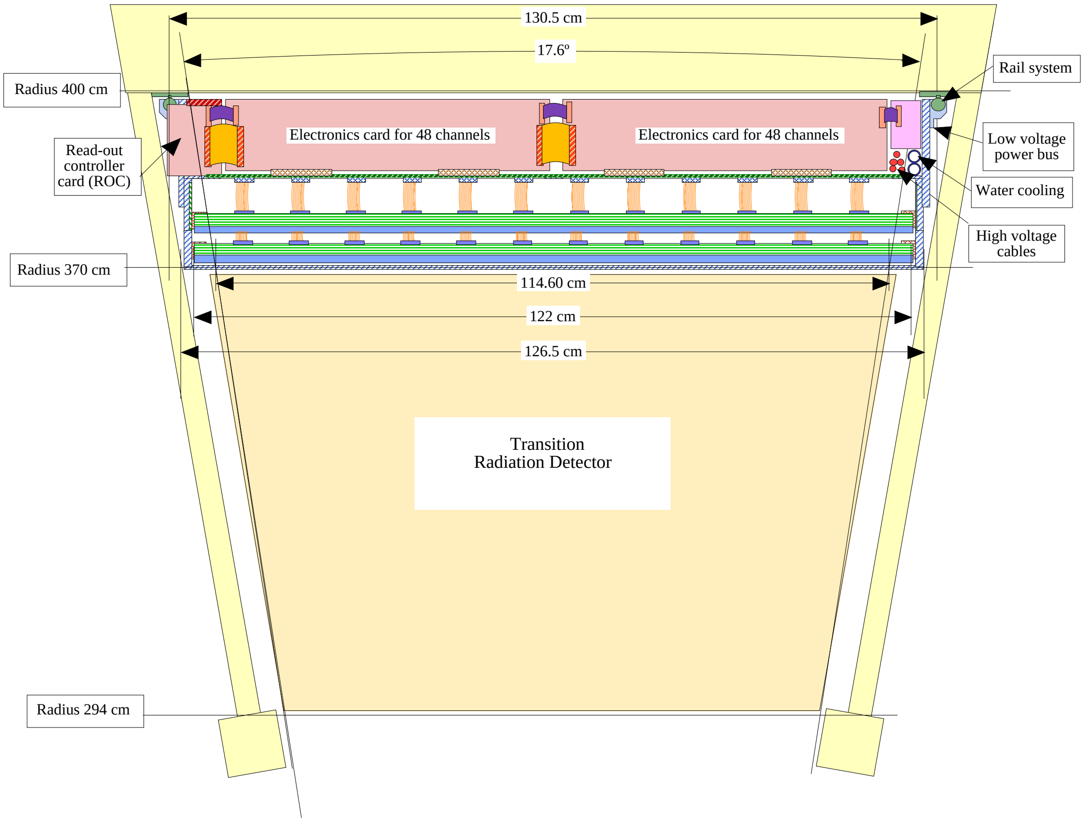

Figure 3.5: TOF module housing in the Space Frame.

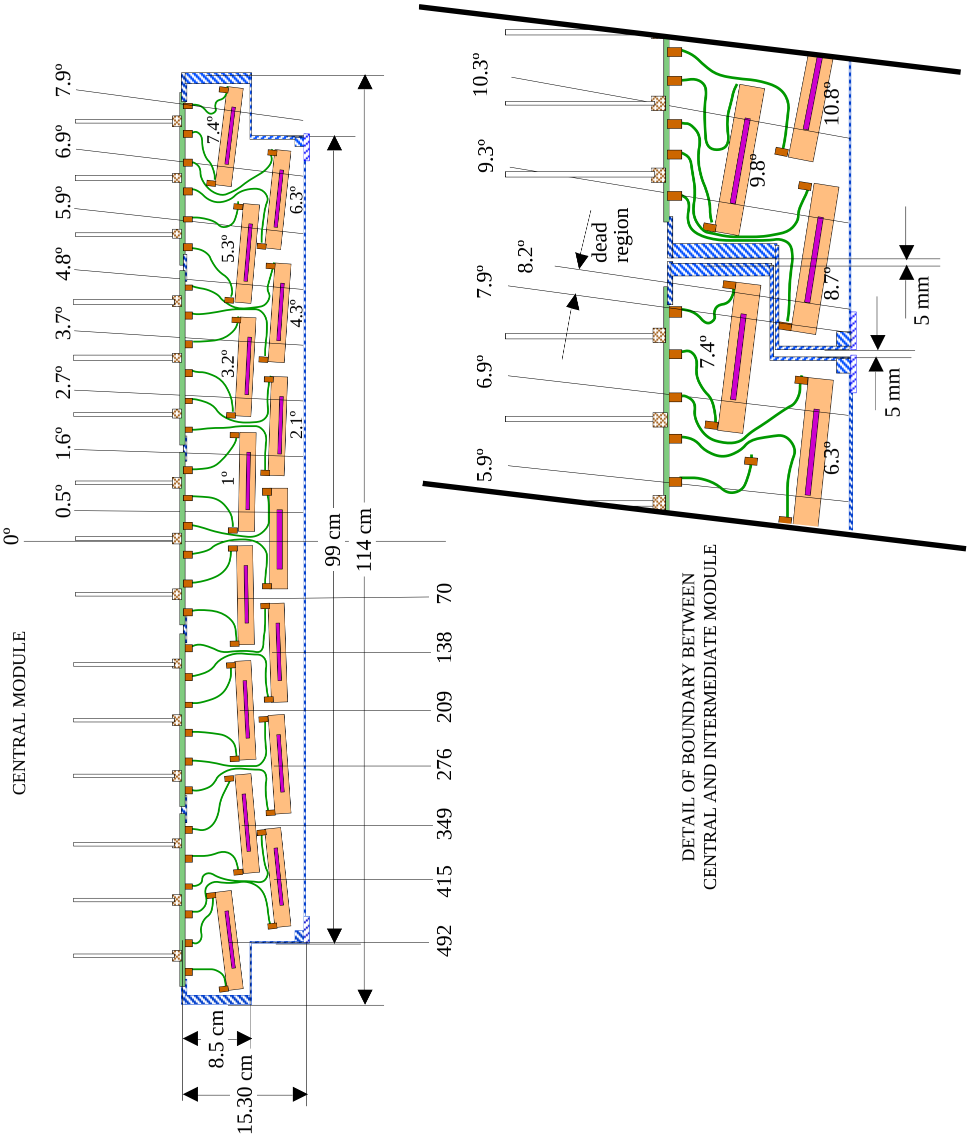

Figure 3.6: Longitudinal cross-section of the central module.

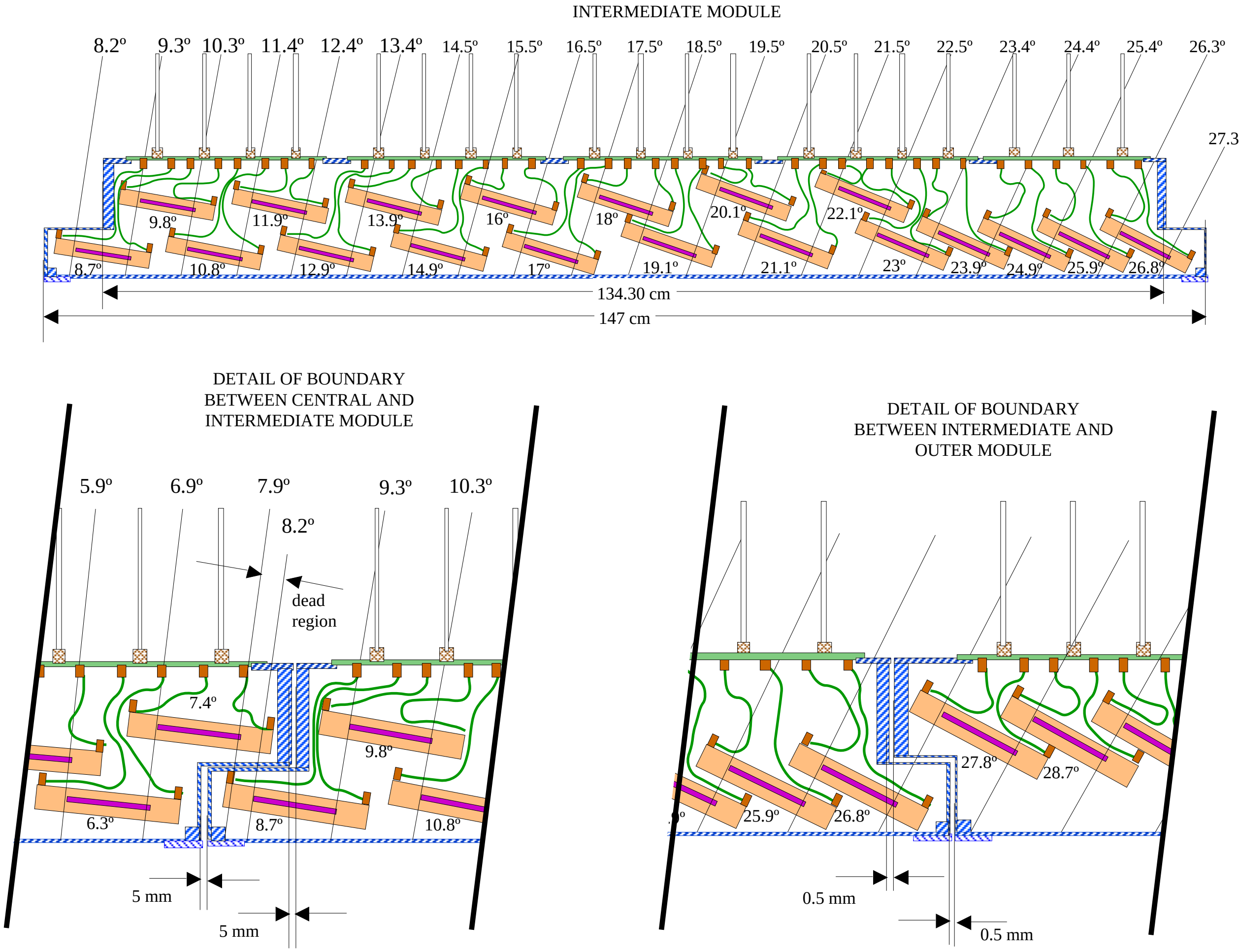

Figure 3.7: Longitudinal cross-section of the intermediate module.

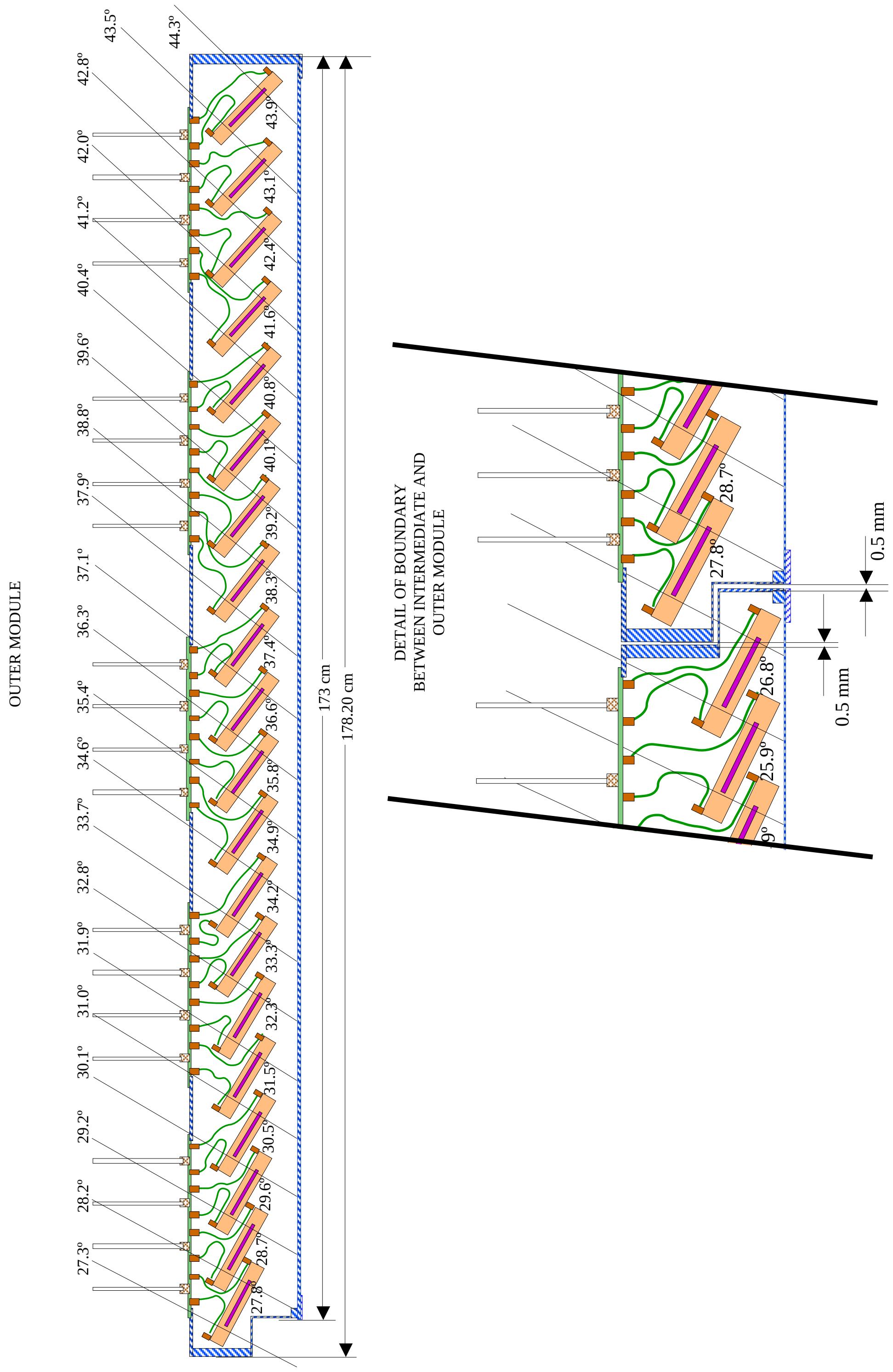

Figure 3.8: Longitudinal cross-section of the outer module.

3.3 TOF Gas System

3.3.1 Introduction

The modules of the Time of Flight detector (TOF) are located in the outer barrel section of the Space Frame, behind the TRD detector. There will be a maximum of 90 modules, comprising a total gas volume of approximately 16 m^3. Test results have shown that TOF detectors may be operated with a non-flammable freon-rich gas mixture containing $C_2H_2F_4$, i-C_4H_{10} and SF_6 (90%/5%/5%).

Table 3.3: Design parameters of the TOF gas system.

Total volume	16 m^3
No of modules (max)	90
Gas mixture	$C_2H_2F_4$, i-C_4H_{10}, SF_6 (90%/5%/5%)
Volume exchange/day	4
Total flow rate	2.7 m^3/h
Working pressure	<3 mbar
Fresh gas flow rate	0.14 m^3/h
Tolerable O_2 content	<1000 ppm
Tolerable H_2O content	<100 ppm

Although the gas volume of the detector is relatively small, the high cost of the gas mixture makes a closed loop circulation system necessary. The proposed system will consist of functional modules that are designed and built as standard units for all LHC gas systems. The design parameters of the system can be seen in Table 3.3. The mixing unit, purifier, and the optional gas recovery plant, will be located in the gas building on the surface (SGX2). The circulating rack will be located on the shielding plug in the pit (PX24). However, the component sizes and ranges will be adapted to meet the specific requirements of the TOF gas system. An overview of the gas distribution system can be seen in Fig. 3.9.

3.3.2 Mixer

The flows of component gases will be metered by mass flow controllers, which have an absolute precision of 0.3% under constant conditions. Flows will be monitored by a process control computer, which continuously calculates and adjusts the mixture percentages supplied to the system. The medium-term stability in constant flow conditions will be better than 0.1%: absolute stability will depend upon the absolute precision of the analysing instrument. The gas mixture is maintained non-flammable by permanent i-C_4H_{10} monitoring. Running flows will be typically about 30% of full-scale flow on the mass flow controllers. A schematic diagram of the mixer unit can be seen in Fig. 3.10. For reasons of safety, an independent system of measurement of the i-C_4H_{10} content of the mixture, using infra-red detection, will be installed.

3.3.3 Closed Loop Distribution System

The TOF detector comprises a maximum 90 modules which are supplied with gas from a manifold in groups of five. Internal module pressures due to hydrostatic height of the detector will be minimised by splitting the distribution system into two distinct height zones. Each height zone will have its own pressure control and protection system.This arrangement results in 18 gas segments.

The gas is circulated in a closed loop system with an expected regeneration rate of 95%. A gas exchange rate of one volume every 6 hours is foreseen for the detector. The expected circulation flow rate will be 2.7 m^3/h and, with a fresh gas injection of 5%, the entire gas volume will be renewed once every 4 to 5 days. A schematic layout of the gas distribution system can be seen in Fig. 3.11.

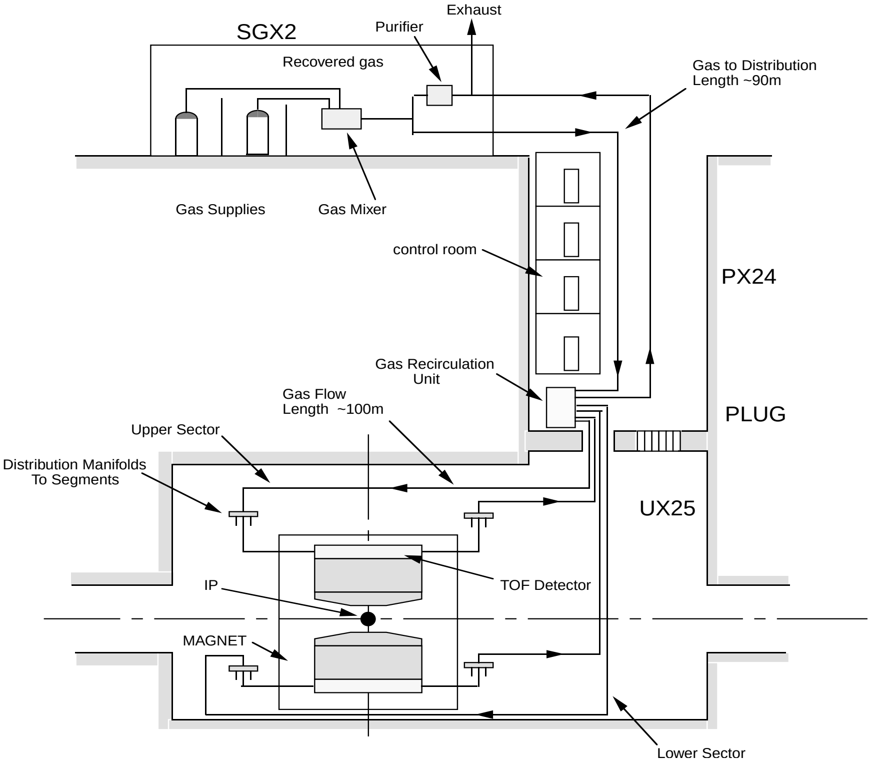

Figure 3.9: Overview of the TOF gas system.

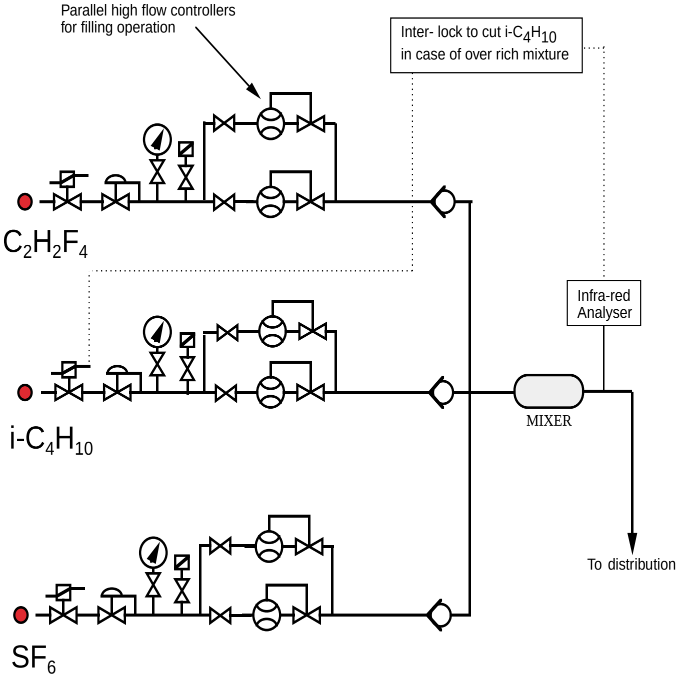

Figure 3.10: Schematic of the gas mixer unit.

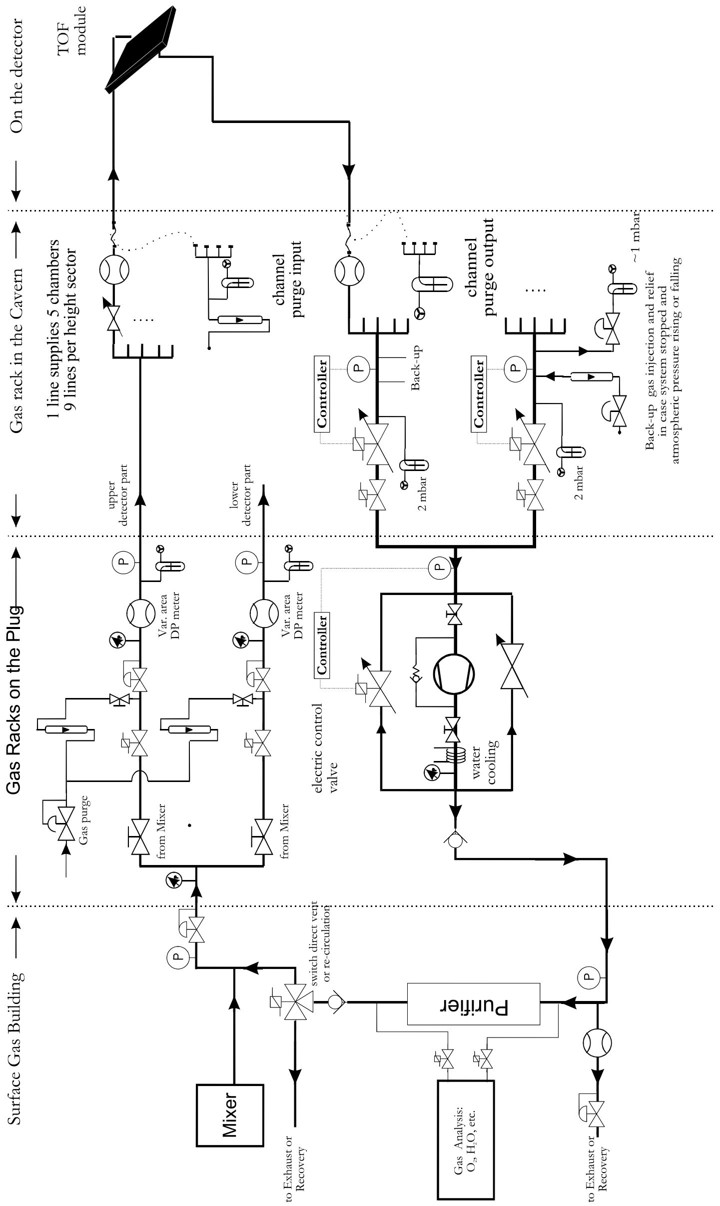

Figure 3.11: Schematic of the closed loop distribution system.

Gas flow from the surface building will be split into two sectors at the Plug level (PX24), as stated above. Each of the two sectors will have its own pressure regulation and protection system. The pressure in each sector will be adjusted to account for hydrostatic pressure differences of the two height zones. The mechanical stability of the modules must, however, be sufficient to support the full hydrostatic pressure of about 5 mbar for correct filling or purging.

A pump, located at the Plug level, compresses the return gas from the modules to approximately 200 mbar for return to the surface gas building, and recycling through the purifier. A regulator valve, in parallel with the pump, controls the compressor input pressure to between –5 and –10 mbar. This under pressure will allow the gas to be lifted the 20 metres to Plug level whilst maintaining the module gas pressure at 1 mbar. In case of power failure or during the long shutdown, a back-up cylinder will provide gas to compensate for fluctuations in atmospheric pressure.

Each of the two sectors is then split into 9 segments in the cavern (UX25). It is planned to equip each segment with a manual flow regulator and differential flow measurement. Each individual gas segment can be separately disconnected, if necessary, and connected to a local purge system using flexible pipes and self-sealing couplings. A projected layout of the gas pipes around the detector can be seen in Fig. 3.12.

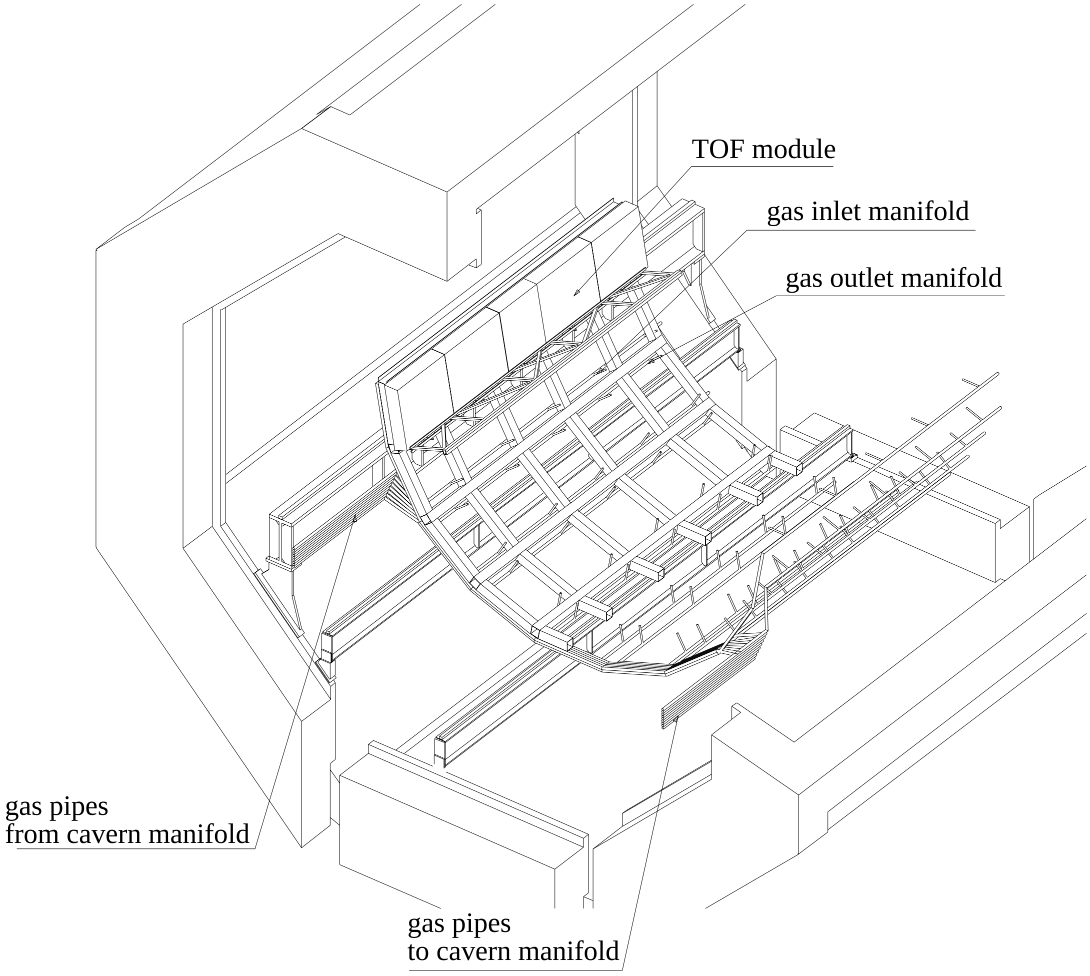

Figure 3.12: Layout of gas pipes around the detector.

Each segment supplies gas to 5 modules, which are connected in parallel along the length of the Space Frame. Pipe diameters vary to ensure that each module will have the same gas flow.

3.3.4 Purifier

Although gas purity requirements for ionization chambers of this design are not very high, the installation of a drying unit is envisaged to maintain a constant humidity in the gas flow. The amount of water vapour to be removed will be determined mainly by the out-gassing rate of the modules. The estimated quantities suggest that a purifier with automated in-line regeneration will be required. Moisture can be removed by cycling the gas through a cartridge filled with a drying agent, e.g. molecular sieve (3A). A twin column design as shown in Fig. 3.13 allows to operate one column whilst the other parallel cartridge is being regenerated at 180 ^{0}C with argon flow. If necessary, a second cleaning agent for oxygen removal could be added in the same column. A humidity meter must be available to monitor the moisture concentration in the system both upstream and downstream of the purifier.

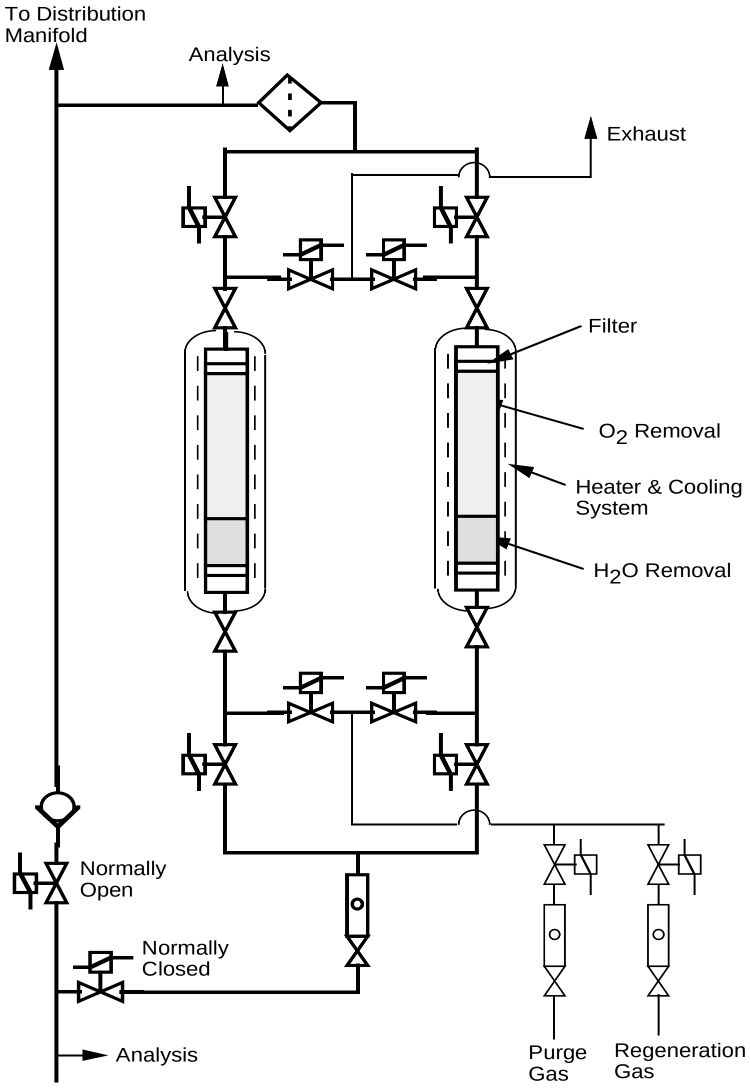

Figure 3.13: Schematic layout of the purifier unit.

3.3.5 Distribution Pipework

All tubes and fittings within the systems will be made of stainless steel or copper. Existing pipes at point 2 will be re-used as far as possible. Table 3.4 shows an overall view of the main piping parameters. The tubes (at the shielding plug end) will be modified to link up with the new position of the distribution rack. In the experimental cavern (UX25) they will be extended into the L3 solenoid magnet and up to the detector modules.

Table 3.4: Main piping parameters

	No of Pipes	Length [m]	Inner Pipe Dia. [mm]	Max. Flow[1] [m^3/h]	Pressure Drop [mbar]
SGX-Plug	1	90	33	8.00	9.30
Plug-Cavern	2	100	26	4.00	9.50
Cavern-Detector	18	20	14	0.44	0.80
Detector-Cavern	18	20	14	0.44	0.80
Cavern-Plug	2	100	26	4.00	9.50
Plug-SGX	1	90	33	8.00	9.30

3.3.6 Safety Aspects

Although the gas used in the detector will be a non-flammable mixture, one of the components (i-C_4H_{10}) is flammable. Therefore suitable precautions will be taken to close down the mixer unit if the mixture approaches the lower flammable limits.

---

[1] Includes a safety factor of 3

3.4 TOF Readout Electronics and Data Acquisition

The ALICE detector is designed to be sufficiently flexible to acquire data during the different run periods and the various types of physics and trigger investigated. The heavy ion runs (calcium, lead) will account for about 10% of the LHC running time. During pp running proton-proton interactions will also be collected. Table 3.4 summarizes the luminosities and trigger rates foreseen for the different collision modes [1].

Table 3.5: Trigger parameters at ALICE.

Collision mode	Pb-Pb beam	Ca-Ca beam	p-p beam
Bunch crossing (ns)	125	125	25
Luminosity ($\mathrm{cm}^{-2}\mathrm{s}^{-1}$)	10^{27}	$2.7 \cdot 10^{27}$–10^{29}	10^{30}
Interactions rates (Hz)	8000	8000–3 $\cdot 10^{5}$	10^{5}
L0-trigger latency (μs)	1.2		
Max L0-trigger rate (kHz)	1.3	1.3–3.0	1.2
L1-trigger latency (μs)	5.5		
Max L1-trigger rate (kHz)	1.1	1.1–0.7	1.1
L2-trigger latency (μs)	≤ 100		
Max L2-trigger rate (Hz)	40	40	≤ 500
TOF occupancy (%)	13	≤ 13	—
Max TOF Event size (Kb)	180	≤ 180	16
Max ALICE Event size (Mb)	64	6	0.5

The trigger and the readout systems will therefore be designed with a very large bandwidth in order to cope with the very high particle multiplicity produced in ion-ion interactions, as well as the low multiplicity events obtained at high rate during the p-p running mode.

3.4.1 ALICE trigger

The ALICE trigger system is based on four detectors: the Forward Multiplicity Detector (PMD), the Zero Degree Calorimeter (ZDC), the Dimuon spectrometer, and the planned Transition Radiation Detector (TRD). The first two select centrality, define a fiducial interaction region and reject beam gas events.
The trigger consists of three successive decision levels, the first two having fixed latency:

- The Level Zero Trigger (L0) is issued in order to strobe the detector front-end electronics. The trigger latency with respect to the time of the interaction is fixed at 1.2 μs. The detectors respond to the L0 with *Detector BUSY* signals. The front-end is held on L0 and the logic waits for either a first level trigger L1 or for timeout in case of missing L1. The trigger is distributed with a fast fan-out to all the front-end cards.

- The Level One Trigger (L1) is issued at a fixed latency of 5.5 μs with respect to the interaction time. A positive L1 trigger causes the event number to be distributed to the detectors and starts the transfer of the data from the front-end event registers to the multi-event buffers.

- The Level Two Trigger (L2) causes (after data reduction and packing) the data transfer to the ALICE data acquisition. The L2 reject signal ($L2_r$) can be issued at any time before the fixed latency corresponding to a level 2 accept ($L2_a$) trigger (100 μs).

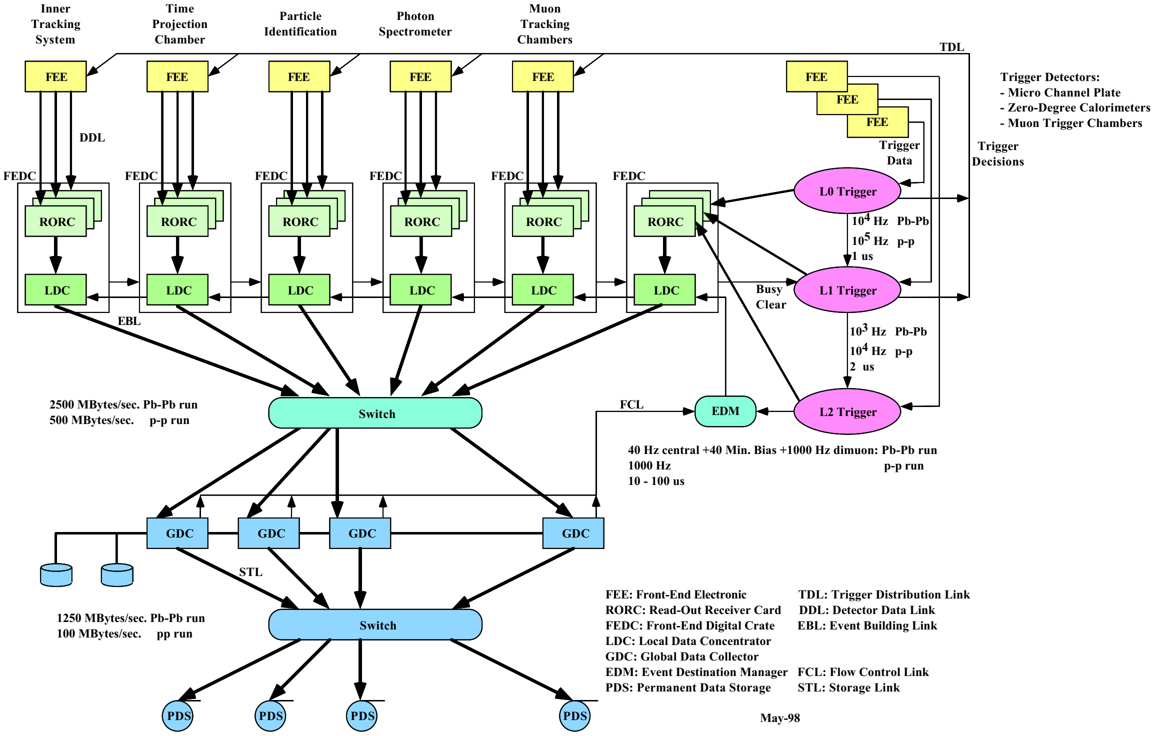

Figure 3.14: Alice Data Acquisition General Scheme.

3.4.2 ALICE Data Acquisition Architecture

The architecture of the ALICE Data Acquisition (DAQ) system is as follows: event fragments are collected from the front-end electronics (FEE) by readout and sub-event building systems (FEDC) operating in parallel. The connection between the sub-event building system and the front-end electronics is established by the ALICE Detector Data Link (DDL). Each sub-event building system is able to acquire data in stand-alone mode. A Local Data Concentrator (LDC) drives each sub-event building system.

The event building and distribution system assembles the sub-events into full events and records them onto permanent data storage (PDS). Each Global Data Concentrator (GDC) receives event-fragments from the LDCs via a switch, and sends full events to the PDS through a second switch.

The architecture of the DAQ and the actions corresponding to the three trigger levels are shown in Fig. 3.14.

At level 0 the data are held on the front-end registers and, in the case of positive L1 trigger without timeout, are transferred from the front-end electronics to local event memory waiting for the L2 trigger decision. On a positive L2, the data are then transferred to the Front End Digital Crate (FEDC) via Detector Data Link (high speed optical fiber). The protocol is common to all the sub-detectors.

The aggregate bandwidth is up to 2.5 GByte/s at the level of the GDCs. After processing and data compression, the maximal bandwidth is reduced to 1.25 GByte/s towards the PDS.

3.4.3 TOF ALICE ReadOut and Data Acquisition system (TARODA)

The readout and data acquisition architecture (Fig. 3.15) is designed to be compatible with the different running modes and to withstand the trigger rates, occupancy of the TOF and data transfer rates of the ALICE experiment. The system will also perform slow controls, data quality and performance monitoring during data-taking without conflicts with the main readout activity.

The readout scheme follows the modularity of the detector and the ALICE trigger requirements. In the present design, the detector is divided into 18 sectors, each sector consists of 5 modules. A module contains many strip chambers: 15 for the central, 19 for the intermediate and 20 for the external. Each strip chamber consists of 2×48 pads of $\sim 3.5\times2.5$ cm ^{2} surface.

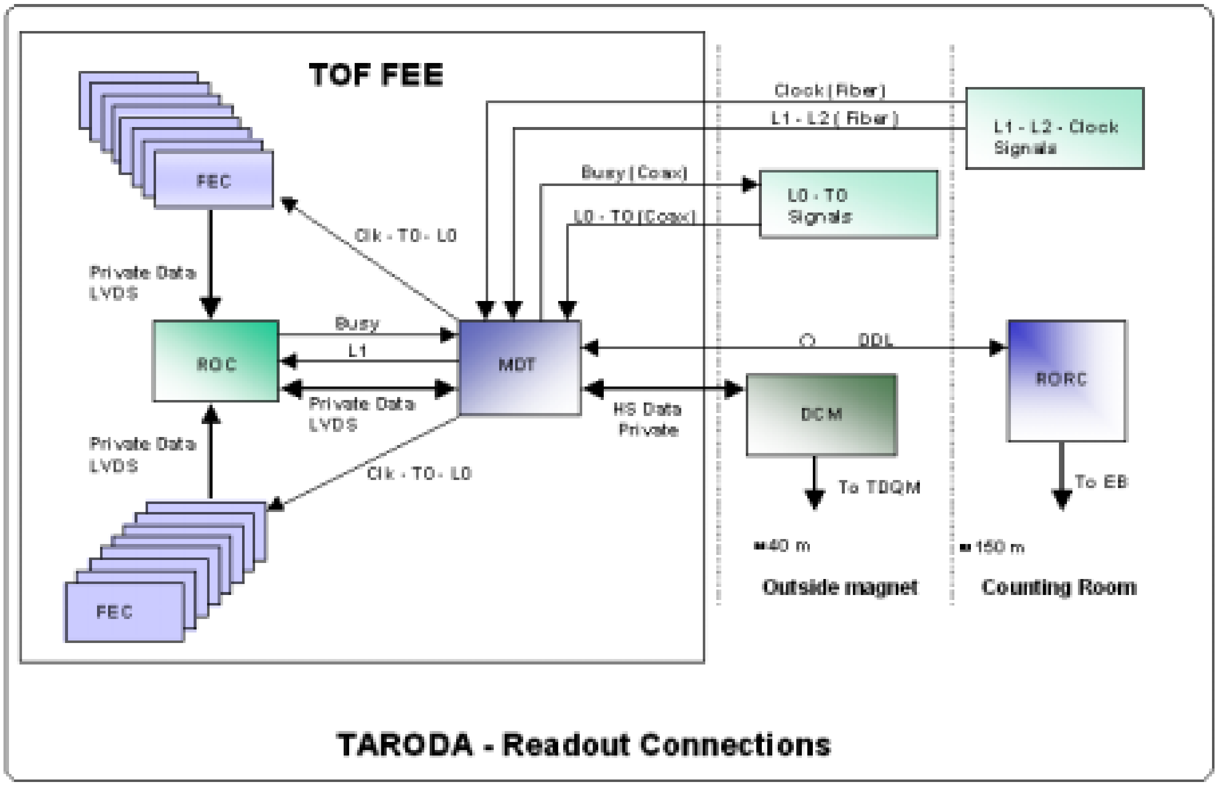

Figure 3.15: ALICE TOF Data Acquisition Scheme

The readout and the data acquisition chain of the TOF consists of the following elements:

- **F**ront-**E**nd controller **C**ard (**FEC)**
- **R**ead**O**ut **C**ontroller card (**ROC)**
- **M**ultiplexer and **D**ata **T**ransfer card (**MDT)**
- **D**ata **C**oncentrator **M**odule (**DCM)**
- **D**etector **D**ata **L**ink (**DDL)**
- **S**low **C**ontrol **M**anager card (**SCM)**
- **CL**ock **D**istribution (**CLD)**
- **T**0 **S**ignal **F**anout (**TSF)**
- Slow Control, Run Control and Data Quality Monitor hardware systems.

3.4.4 Front-End controller Card (FEC)

The front-end electronics for the TOF detector performs the following tasks:

- a fast discrimination of the signal coming from the chamber,
- a measurement of the signal amplitude (charge) for T(A) corrections.

Signals from each pad are sent to a fast amplifier followed by a low threshold discriminator. The output of the front-end circuitry consists of the leading as well as the trailing edges of the chamber signal which is digitized by a multihit TDC (Time-to-Digital Converter). The trailing edge of the signal is obtained from an ATC (Amplitude-to-Time Converter) circuit, that uses a time-over-threshold technique. This circuitry will be implemented in a custom Front-End ASIC (FEA — four channels per chip). The output of the FEA is delivered to a high resolution TDC (described in Sec. 3.6). This TDC has 8 channels per chip and requires a 40 MHz reference clock.

Two TDCs per side will be housed in the Front-End controller Card (FEC). Serial temperature sensors will be installed on both sides of the FEC and will be sampled with one extra TDC channel.

The card will be built with analog and digital parts electrically decoupled. The analog part contains the FEAs and a DAC (Digital to Analogue Converter) that will be used to set the discriminator thresholds.

3.4.5 Front-End analogue ASIC (FEA)

To achieve the time resolution of less than 100 ps with the proposed detector, it is clear that the front end amplifier and discriminator have to be high speed. The amplifier and discriminator circuits used for the tests have been described in Chapter 2. This amplifier was built with discrete components and had an integration stage built into it. The purpose of this integrator was to stretch the pulse so that time-over-threshold would give a measurement of the charge. This technique of measuring charge was shown to be sufficient to perform the T(A) correction. This concept is illustrated in Fig. 3.16. Even though this circuit was shown to work satisfactorily, there are some problems. These are:

- At the input of the discriminator, the signal has been integrated; thus there is a long tail that introduces base-line jitter. This introduces a time jitter that results in the tail of late pulses.
- The trailing-edge of the signal has a rate-dependent long decay time; this creates oscillations on the trailing edge.

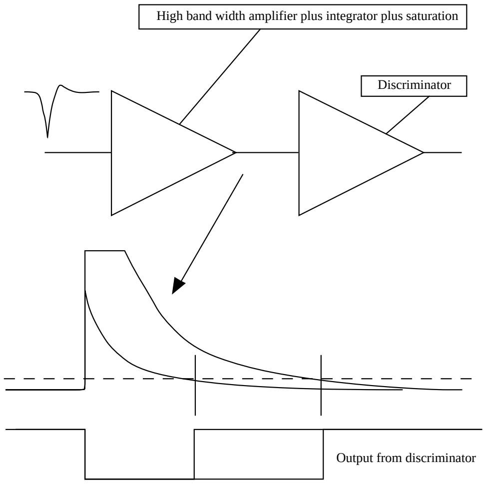

Figure 3.16: Conceptual diagram of the front-end electronics used in the R&D phase in 1999.

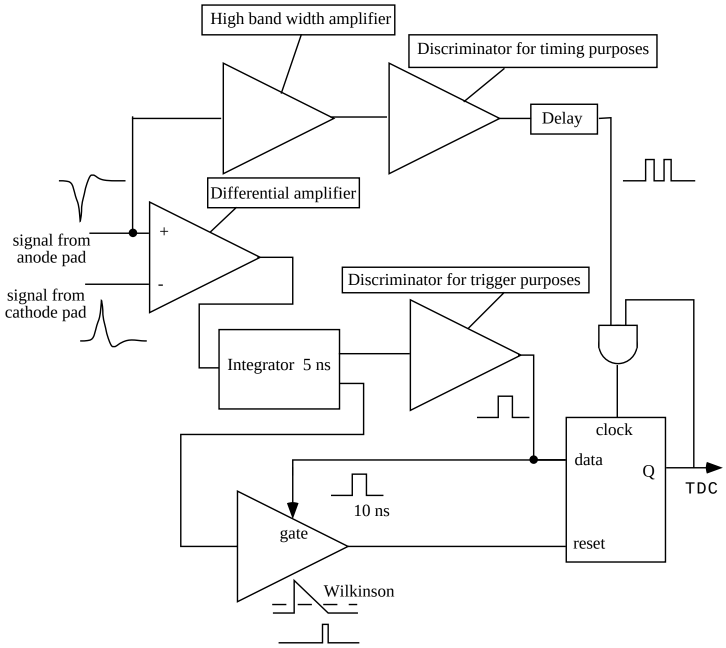

Figure 3.17: Schematics of proposed Front End Electronics.

To solve these problems we need to separate the integration stage from the high-speed discrimination stage used for the timing. In addition, as discussed in chapter 2, we expect to sharpen the boundary between two neighbouring pads by using a differential amplifier. It is not clear whether a differential amplifier can be used for the time measurement since inequalities between the two inputs would add extra jitter. We therefore want to use a differential amplifier to define a pad hit, and a fast single-ended amplifier for the time measurement. The time-over-threshold could be performed with a Wilkinson amplifier (this is the same technique as used in the LRS 2249 ADCs used in our tests). A schematic is shown in Fig. 3.17. For a 160000 channel system it is clear that the front-end electronics has to be integrated in an ASIC. This type of front-end as shown does not create a very complex ASIC design. Fig. 3.18 shows the circuit design of the current prototype of a differential amplifier.

The FEA will have the following connections :

- 4 input channels (differential).
- A test input:
  this input is used to inject a known signal to the input stage of the amplifier under control of a mask register.
- A mask register input:
  this is used to select a specific channel pattern during test/calibration runs.
- 4 threshold inputs for discrimination and channel disabling.
- 4 outputs to feed the multihit TDCs.
- 1 output for “electronic temperature stability” to be sent to a TDC channel. This temperature monitoring, controlled by a FPGA, is active during the data taking.

The FEAs are controlled by FPGAs located on the FECs.

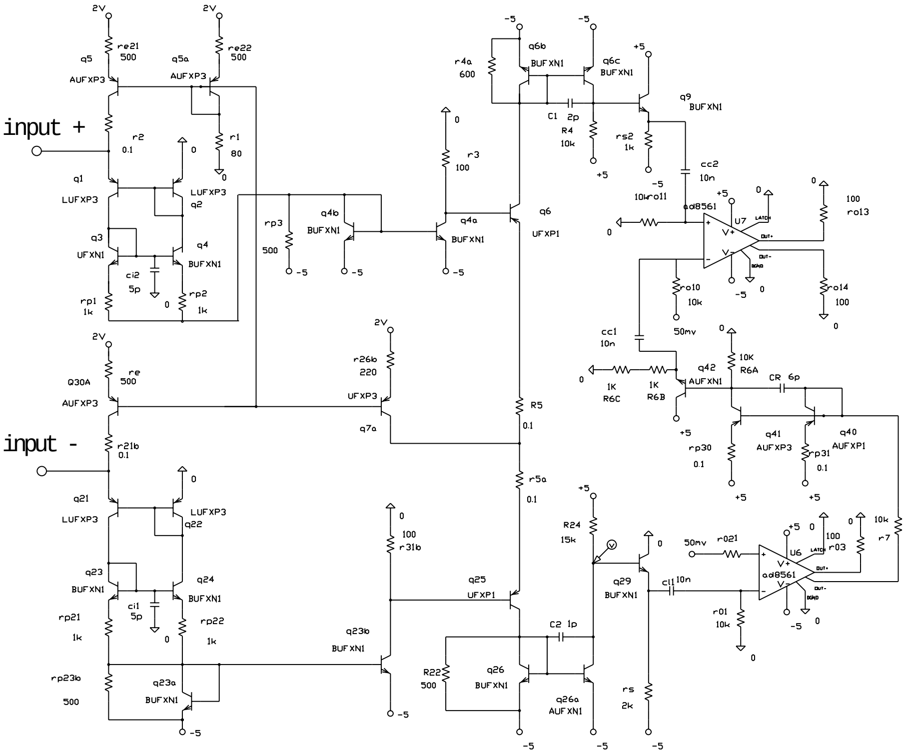

Figure 3.18: Circuit diagram of the differential amplifier that will be part of the ASIC.

FEC readout and control

The FECs will be connected in daisy-chain to the readout data bus (8 addresses and 4 clocks + 32 data differential bus) and to the JTAG and private control bus (8 differential, 3 wired-or). The T0 and trigger signals and reference clock are also distributed to the FECs. The sequence of the data readout and the functionality of the FEC is guaranteed by an ALTERA APEX 20K family FPGA. The FPGA program will be downloaded at boot time from the ROC via JTAG bus. The configuration on the readout FEC could be changed at run-time. The logic on the FPGA:

- Controls the trigger synchronisation; on L0 it holds the readout and issues a BUSY signal.
- On L1 positive, moves the TDC data from the event register to the internal TDC memory and waits for the request of the ROC to transfer data. A negative L1 produces a reset of the TDC hits registers, removes the BUSY and restarts the normal data taking.
- Starts, in sequence, the readout of the TDCs after a data transfer request from the ROC. In order to format the data, an ALU unit, a LUT table and a micro sequencer are implemented inside the FPGA.

The full description of data format is given in Sec. 3.4.12. The pad data consist of two words 32-bits wide:

- The first word contains the identification of the channel and the charge measurement. The FEC number is coded on the board with switches, the channel number of the TDC is stripped from the hit data and packed with the FEC card identification. More information can also be added to this word.

- The second word contains the time measurement and the error bits for the hit channel of the TDC. The error bits are: the buffer full, hits error and event mismatch flags.

The FPGA packs the data and calculates their CRC. The CRC algorithm is implemented using a LUT table to accelerate the processing time. The packed data are stored in an “internal” FIFO, and sequentially transferred via the LVDS output bus to the ROC. The last data of the packet contain the CRC value and the FEC error flags. The FPGA could use this internal FIFO to store patterns necessary for the simulation/test of the readout chain. Up to 1024 patterns are stored and are sent to the FEA mask register after a simulated trigger. The FPGA also controls the timing and logic for the calibration procedure of the FEC. The transfer of the data is made via the LVDS bus, on a multiplexed twisted pair connection, and is active only when the card is selected by the ROC. A first version of the complete logic configuration and simulation will be developed with the ALTERA QUARTUS software.

3.4.6 ReadOut Controller card (ROC)

The ROC collects the data after a positive L1 trigger, controls the FEC cards, removes errors and generates the first packing and compression of the data. At this stage, two solutions to determine the best mechanical configuration are envisaged: the use of a backplane or a multipoint Twisted Pair (TP) connection between the FEC and the ROC. In this document the solution with cables is presented.

The data are transmitted to the ROC, after a positive L1, and stored in a DPM RAM and will stay there waiting for the L2 decision, before transfer to the ALICE data acquistion. The timing and the input/output operations are controlled by a FPGA. The configurations of the FPGA, as well as those of all other parts of the readout chain, are downloaded at boot time from the TOF Slow Control System. The ROC card is based on a DSP controller equipped with internal FLASH ROM where code and configurations are stored/downloaded at boot time. The configuration data contain the logic of the FPGA corresponding to the FECs and ROC, calibration data, TDCs settings, and the thresholds of the FEAs. The ROC includes a master for the JTAG bus, is controlled remotely via a CAN bus and is the supervisor of the calibration procedure.

Readout and Slow Control on the ROC

The basic functions of the ROC may be subdivided into the following tasks:

- Detector Busy signal generation and processing.
- Data readout from the FECs and header formatting.
- Data reduction (if necessary). The algorithms will be downloaded at boot time.
- Event distribution to the MDT cards.
- Mask and strip-out bad channels with packing errors on special packet to be sent with the data to the TOF Data Quality monitor.
- Calibration procedure for the FEAs and the TDCs.
- Monitoring and control of the data flow.

3.4.7 Multiplexer and Data Transfer card (MDT)

The MDT is the last concentrator located on the detector and controls the transfer to the Front End Digital Crate (FEDC) via Detector Data Link (DDL) and to the TARODA Data Concentrator Module (DCM). This card, equipped as the ROC with a DSP and CAN bus, prepares the data in packets compatible with the ALICE Data Format and strips out information for Slow Controls and Monitoring. A special packet with event data, alarms, errors, temperature and calibration data produced by the ROC is also sent to the DCM and will be used by the TOF Data Quality Monitor (TDQM).

3.4.8 Data Concentrator Module (DCM)

The DCMs communicate directly with the TDQM. These modules are located in VME crates outside the magnet. They accumulate and compress the readout and slow control data, and send them to the TOF TDQM. The data buffer uses a dual port data memory (DPM). In the VME crate a real-time processor communicates via a private network with the TOF equipment computer where the TDQM runs. A description of the TDQM is given later in this chapter.

3.4.9 Detector Data Link (DDL)

The transfer of data from the front-end electronics to the DAQ is performed by the ALICE DDL. This link has been proposed as a standard interface between the detector electronics and the DAQ system. A set of documents [3,4] describes the DDL interface. The logical interface of the DDL can be seen in Fig. 3.19. The DDL is a bidirectional link with flow-control.

The DDL is composed of three hardware items: the Source Interface Unit (SIU), the fibre pair and the Destination Interface Unit (DIU). The SIU has been designed to be plugged into or even integrated in the front-end electronics of most ALICE detectors. The integration with the TOF electronics should not cause any particular problems in terms of real estate or radiation tolerance. The fibre pair will be the only media used by the data acquisition between the ALICE detectors in the experimental area and the computing room located in the access pit. It is foreseen to have one DDL for each sector of the TOF. The DIU will be inserted on a mother card (the ReadOut Receiver Card) inside a crate or a computer located in this computing room

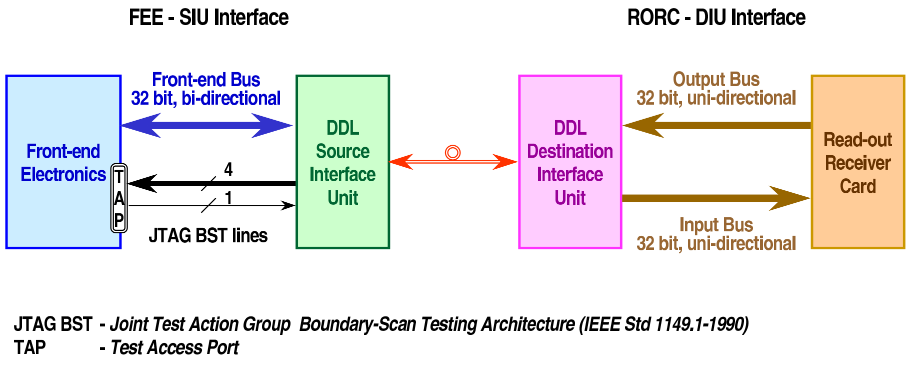

Figure 3.19: DDL logical interface.

A prototype of the DDL DIU and of the RORC have been developed. A prototype of the DDL SIU is currently under test. Its main characteristics correspond to the needs of the TOF. The specifications of the DDL will be frozen after a successful integration test has been done with the TOF and the other major ALICE detectors. Production will be started one year before the assembly of the TOF.

Two modules have been produced to allow an easy stand-alone test of the front-end electronics. These two modules simulate a complete DDL and DAQ system by simple and cheap electronic boards [5, 6].

ReadOut Receive Card (RORC)

The physics data transferred by the DDL are buffered in the ALICE RORC [7]. The RORC has several functions:

- be the mother card for 4 DDL Destination Interface Units (DIU);
- act as the transmitting memory for the commands and the data transferred by the DDL to the readout system;
- act as a remote master for the front-end control and test;
- act as the receiving memory for the physics data transferred by the DDL to the DAQ;
- detect the end of the data blocks and manage the data blocks received through the DDL;
- raise the DDL “link full signal” to request a pause in the data transfer when the buffer is full.

Once the data have been transferred in the RORCs, they are under the control of the DAQ system. The RORC includes enough buffering to store several events from the TOF. Once in the RORC, the data are processed completely asynchronously from the trigger signals.

Front-End Digital Crate or Computer (FEDC)

The FEDC is the smallest autonomous entity of the ALICE DAQ system. It consists of the following items:

- one or more RORC receiving data from the DDLs;
- one LDC doing the sub-event building and participating to the event building;
- an interface to the trigger system.

The architecture of the FEDC is shown in Fig 3.20.

An FEDC is able to acquire data independently from the other FEDCs but an entire FEDC cannot, at a given moment, participate in more than one trigger. This independence is needed to allow for different kinds of triggers. It is also extremely useful for the debugging and installation period of the experiment.

Local Data Concentrator (LDC)

The LDC is the processing element of the FEDC. The current prototypes of the data transfer system use VME crates, and the LDC is implemented as a single board computer running the UNIX operating system. The implementation will most probably evolve with the technology but the main functionalities will remain.

The main functions of the data acquisition system, when it takes part in a global run with the other ALICE detectors, are [8]:

- to validate or discard the event fragments depending on the trigger level 2 decision;
- to readout the data fragments from several RORCs and assemble them into one sub-event;

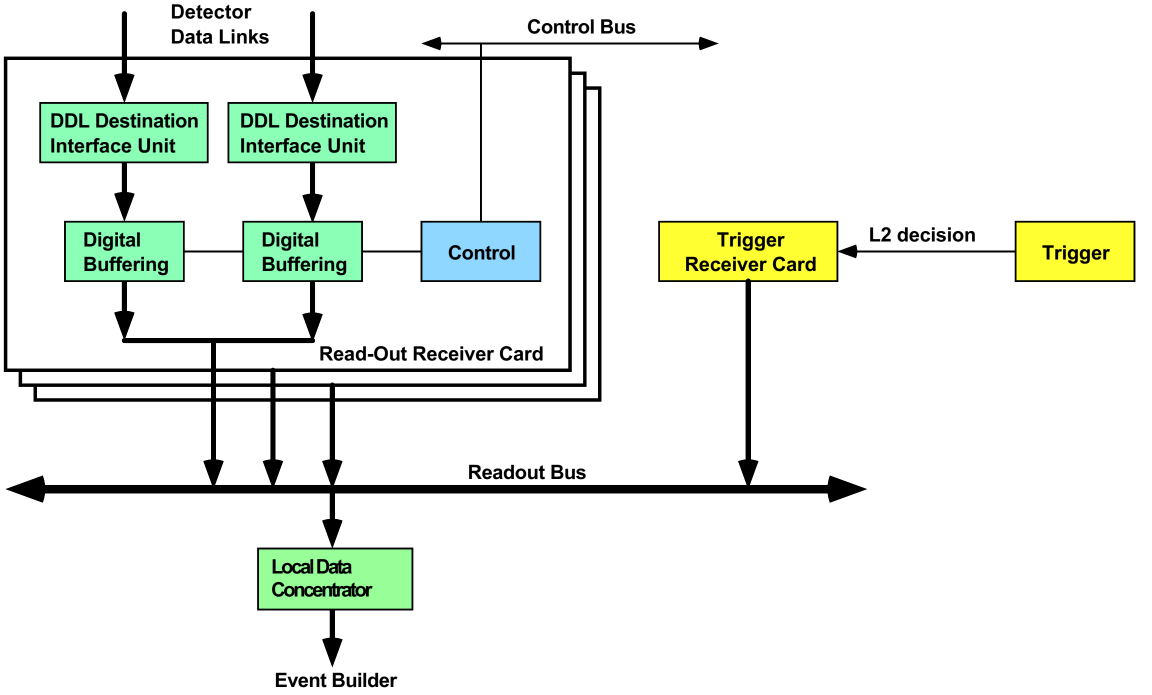

Figure 3.20: FEDC architecture.

- to send the sub-event to the computer designated by the event building and distribution system as event-builder, to build the complete ALICE event.

The data acquisition system allows the collection of data in stand-alone mode as well. In this case, the LDC records the data locally instead of sending them to the event-builder computer. This facility can be used for the tests during the preparation and the installation phases of ALICE. During the production phase, it will also allow calibration runs independently from the other detectors and acquire the pedestal needed for the readout electronics. In this case the DAQ will acquire data from all the channels and will prepare pedestal tables which will be loaded at the beginning of the runs.

A prototype of the DAQ system has been set up for the TOF. It includes a first version of the DAQ software [9].

3.4.10 Slow Control Manager card (SCM)

The SCMs are the control boards used by the TOF Slow Control System to communicate with the detector electronic chain. The main jobs of the SCM are:

- to prepare the data for the ALICE Detector Control (DCS), the TOF Data Quality Monitor (TDQM) and the TOF Run Control (TRCO) sub-systems
- to take care of the alarms (hardware)
- to handle communication and protocols for the electronic chain
- daisy-chain booting of cards on the FEE
- to interrupt the slow control processor on critical condition, and send action signal (e.g. kill HV channel on gas leak)
- to be master of the CAN field bus used to communicate with the FEE hardware.

3.4.11 t_0 and Reference Clock

To take full advantage of the intrinsic resolution of the proposed MRPC, the time measurement operated by the TDC must have an intrinsic resolution better than 50 ps. The digitization precision within the TDC depends on the quality of the clock used. A stable 40 MHz clock as well as a jitter free t_0 are necessary to accomplish the measurement. The TTC (Trigger Timing and Control) system [10] can, in principle, distribute the LHC reference clock with a resolution of 30 to 50 ps depending on the optical power available. The interaction time t_0 has an interval variation of 180 ps depending on the finite LHC interaction region size. A specific detector will have the task of generating this t_0, possibly with a precision better than 50 ps. At present we think we will adopt the procedure to distribute to each FEC (Fig. 3.21) and digitize on separate channels both the 40 MHz clock and the t_0.

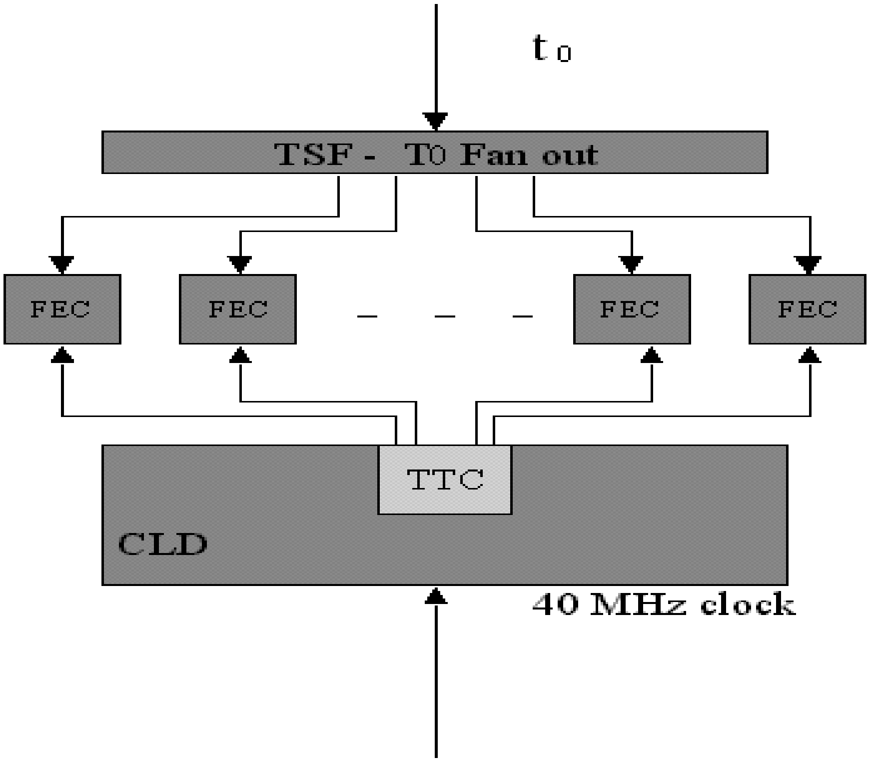

Figure 3.21: RF and t_0 distribution.

A proper system of synchronization will be implemented on each of the fan-outs to reduce the time jitter introduced at each level. In Table 3.6 an estimate of the global resolution obtainable with such a system is given.

3.4.12 TOF Data Format

The following characteristics of the TOF detector are relevant to the organisation of the data:

- 18 sectors each containing 5 modules
- one module has up to 2000 pads
- the information from every 4 pads is acquired by a FEA
- the outputs of 2 FEAs are digitised by a TDC
- 4 or 2 TDCs (depending on the modularity of the electronic cards) are housed in a FEC

Table 3.6: Time resolution.

Jitter source	typical (*ps*)	max. (*ps*).
t_0	50	70
Detector	70	90
TDC	25	40
Clock distribution	30	50
t_0 fan-out	20	30
RF distribution	20	20
system time jitter	99	135

- 32 FECs are collected in a ROC
- 14 ROCs constitute a sector
- the pad output information consists of two quantities: the time coming from the TDC and the deposited charge information derived from a TDC time-over-threshold measurement.

The raw data per sector will be organized as follows (word means 32 bits, see Table 3.7):

1. A first header of one word containing the sector identification number and the overall sector data size.
2. A second header (14 words) containing the ROC identification number and the size of the memory occupied by that ROC data.
3. Two control words.
4. The ROC data (up to a size of $2 \cdot 10^4$ words). For each ROC, the allocated memory will be twice that indicated in the second header. For each pad, the data consists of 2 words: the first containing the TDC identification number and the charge-related value, and the second containing the time value.
5. One word for control and total checksum.

3.5 Slow Controls and Data Quality Monitor

The variation of many characteristic parameters with temperature will affect the time and charge measurements of our detector. It is therefore vital to set up a slow control expert system to monitor the data quality. The system needs individual channel calibration for both the TDC time and charge measurements. This correspond to 2×160000 slowly varying “constants” needed for off-line processing of the data. Control of bad channels, temperature measurements, gas mixture and, in particular, variation of the occupancy, needs constant online monitoring. Important parameters that summarise the status of the detector will be sent to the ALICE Slow Control System. A custom histograms/event presenter is under design.

3.5.1 TOF Slow Control System (TSCS)

The TSCS (TOF Slow Control System) software package will integrate most of the functions required to monitor and control the component sub-systems such as gas, high voltage, and readout electronics.

Table 3.7: TOF data format. (Each row represents a 32-bit word).

Sector ID	total data size
ROC ID 1	size1 ROC ID 1
ROC ID 2	size2 ROC ID 2
ROC ID 3	size3 ROC ID 3
....	....
Error Flags	Header control words
....	....
Channel 1 ID ROC 1	Charge
Error Flags MSB Time	LSB Time
....	....
	twice size1 - 1
SC Info for ROC 1	Checksum
Channel 1 ID ROC 2	Charge
Error Flags MSB Time	LSB Time
....	....
....	....
	twice size2 - 1
....	....
Sector controls info	Global Checksum

A unique package for all components of the TOF has the advantage of giving the users an easy-to-learn homogeneous environment. Another advantage is that, in general, the components of the TSCS use the same hardware. Finally, the package solution makes it easy to design quite sophisticated monitor and general control functions.

TSCS system overview

The TSCS hardware is based on the VMEbus standard: both the TOF and the ALICE slow control systems can access the TSCS hardware and its data (Fig. 3.22). Real time processors[2] (one per VME crate) control and monitor:

- LV and HV via Ethernet.
- Data from SCM.
- Gas system (flow, pressure, temperature).
- Communications with the central ALICE Detector Slow Control System (DCS).
- Communications with TDQM.

TSCS Description

The main features of the TSCS, produced using the SASD (Structured Analysis Structured Design) tool, are summarized in the DFD (Data Flow Diagram) in Fig. 3.23.

The most important elements of the TSCS are:

---

[2] MVME2604 Motorola or CES Raid running UNIX or LynxOS OS

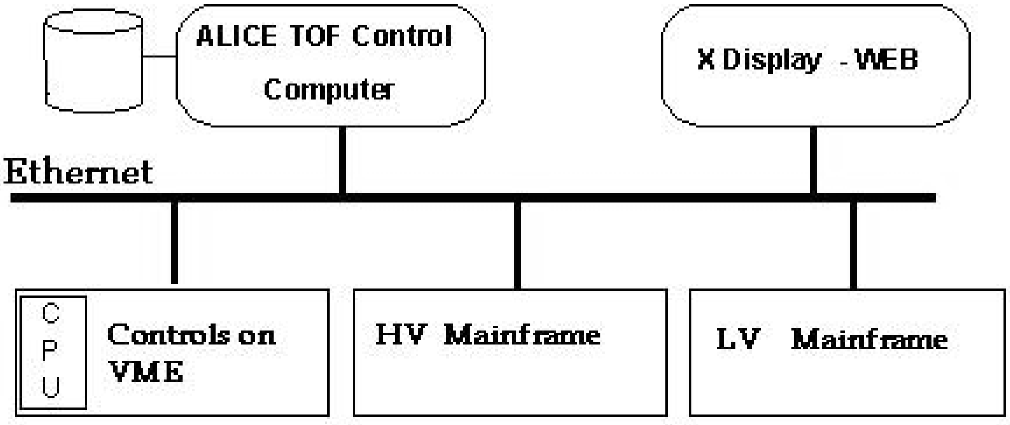

Figure 3.22: TSCS Hardware Layout.

- A *Control Data-Base Management*; a set of management applications used in building and keeping the Slow-Control database up to date. The use of Objectivity relational database management system is envisaged. An example of a TSCS normalised database describing the data dictionary corresponding to a VME module is given in Fig. 3.23.
- An *Acquisition*; set of processes running on the VMEbus controller which, starting from the slow-control database description, acquire and configure the appropriate Input/Output modules.
- A *Monitor and Control utility* which allows the users to monitor and set parameters from/to the Input/Output hardware.
- *Archive* utilities which acquire parameters in the online slow-control databases and store them in remote files.
- *Alarms*; processes which look at specific situations in the TOF detector.
- Communication with the DCS of the ALICE experiment.
- A GUI user interface based on Motif, XForms or ROOT.

All the above tasks will run on the real time VME controllers and on the TOF equipment detector computers. The diagram of the physical layout and connections is given in Fig. 3.25.

3.5.2 TOF Data Quality Monitor (TDQM)

The TOF Data Quality Monitor (TDQM) surveys the performance of the TOF detector and gives a preliminary overview of the data. The TDQM spy program runs on a local realtime processor in the VME crate, collects the data from the DCMs and transfers them to the equipment computer. The flow of the data and the hardware layout is shown in Fig. 3.26. The main tasks of the TDQM are:

- Readout of the data from the TPMs located in the DCM cards.
- Readout of the Slow Control data from the TPMs located on the SCM cards.
- Merging of the Slow Control information and of the detector data.

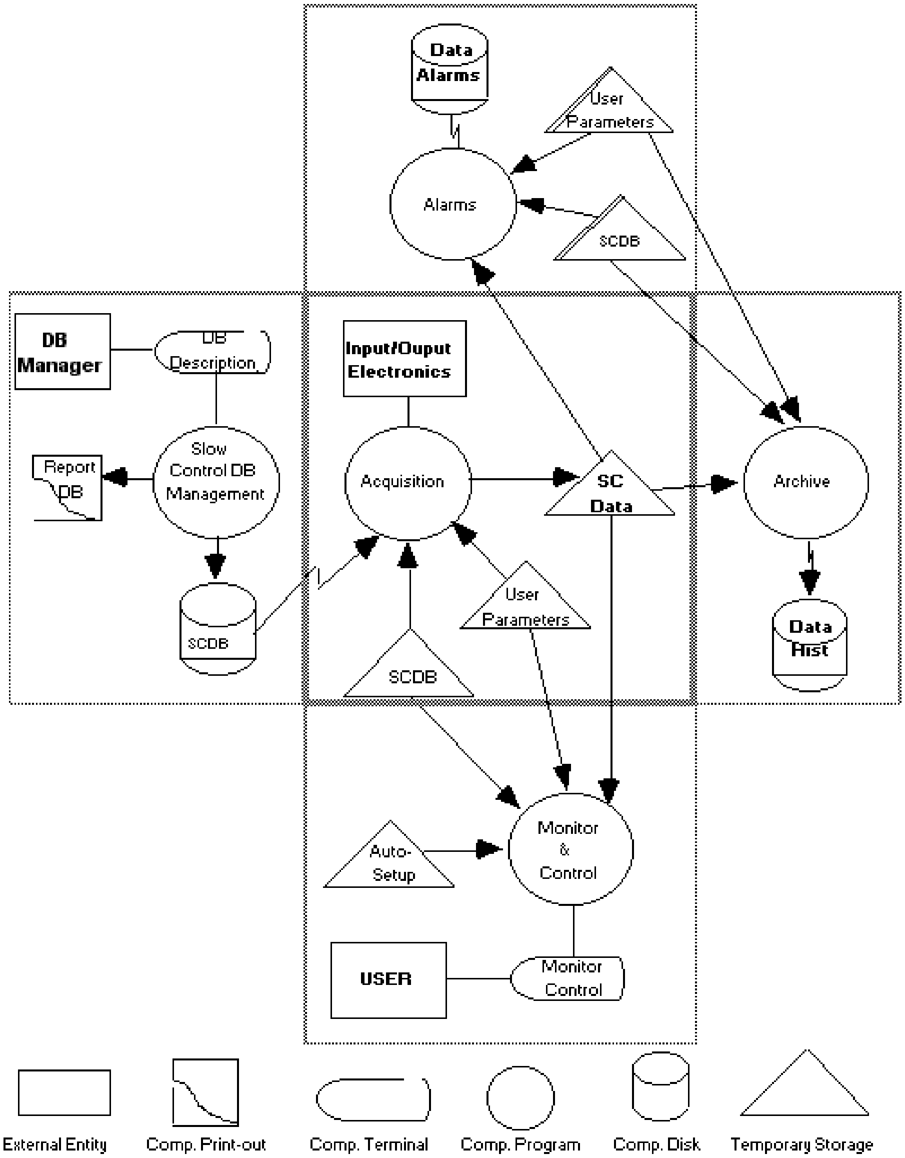

Figure 3.23: Data Flow Diagram of TOF Slow Control System.

- Compression of the data and transfer to the TOF main computer.
- Analysis (spy) online of the data collected.

The TDQM system can also be used to acquire data in stand-alone mode for detector testing.

3.5.3 TOF Run and DAQ COntrol system (TRCO)

The TRCO consists of several processes that run on the TOF on-line computer and on the VME systems, and is organized into three different layers:

- the TRCO-*program* layer,
- the TRCO-*control* layer,
- the TRCO-*physical* layer.

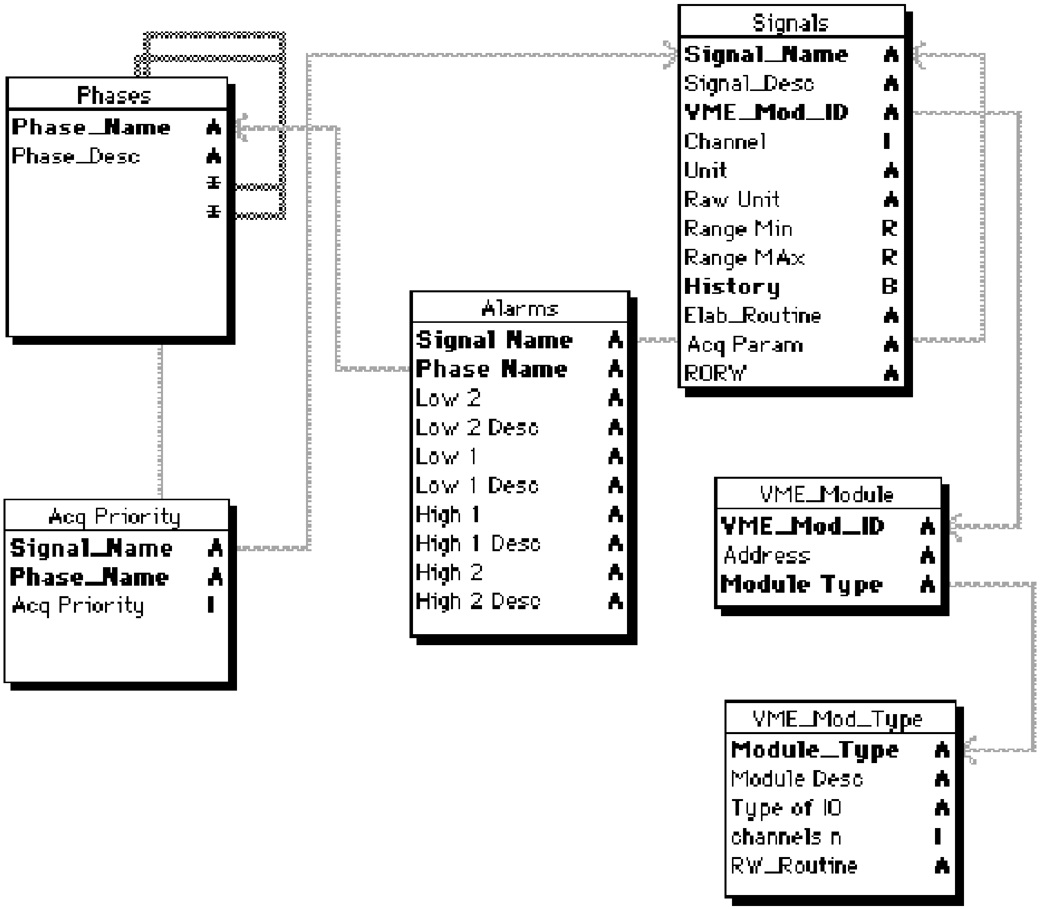

Figure 3.24: Example of a TSCS Database Description.

The *program* layer and the *control* layer comprise all the services and programs; the *physical* layer consists of the physical connection (hardware/software) common to all systems.

The principal functions of the TRCO-*program* layer are:

- handling of the startup of the TOF system with booting of the readout chain, initialisation of the TSCS and TDQM systems and setting up of the communication with the ALICE Detector Control System (DCS),
- data logging, histogram presenter and GUI controls for the TOF detector,
- database handling of the online TOF DB via SQL using ORACLE,
- coordination of the activities of the TSCS, TDQM and DCS systems,
- supervision of the calibrations,
- initialisation and control of the TOF detector running in stand-alone mode to test the performances of the full readout.

The TRCO-*control* layer is responsible for:

- The collection and dispatching of all the communications within the TOF system.
- Synchronization with ALICE DCS and Run Control systems.

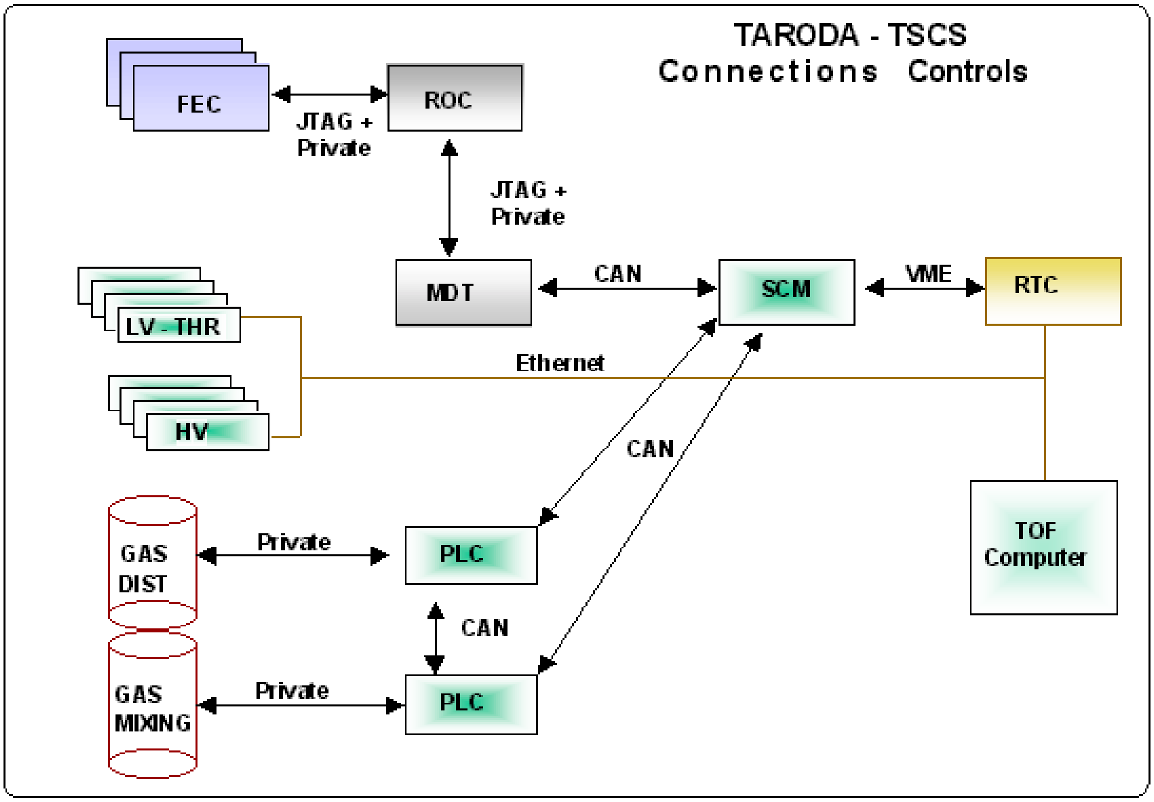

Figure 3.25: TSCS physical layout and connections.

- Calibration runs of the TOF detector, using generated sequences of operations via field bus (CAN). The collected information is transferred to the *program* layer to be dispatched to the TDQM and TSCS systems.

- Handling of alarms, errors and interlock logic of the detector.

- Programs and monitoring tasks on the different TOF sub-systems, handling crash and critical hangs.

- The PLCs (Programmable Logic Controller) which perform several tasks (e.g. gas controls).

The TRCO-*physical* layer is based on the TCP/IP communication protocol between the different systems (DCS, TSCS and TDQM). It uses the following field and controller buses and devices:

- JTAG and CAN protocols to communicate and access the readout chain.

- VME bus to read field Input/Output channels.

- Ethernet hardware interfaces for TPC/IP protocols and HV/LV communication.

As with the other TOF sub-systems, the TRCO will be based on Expert systems, and will be complemented with a powerful human interface. The layout of the TRCO is shown in the Fig. 3.27

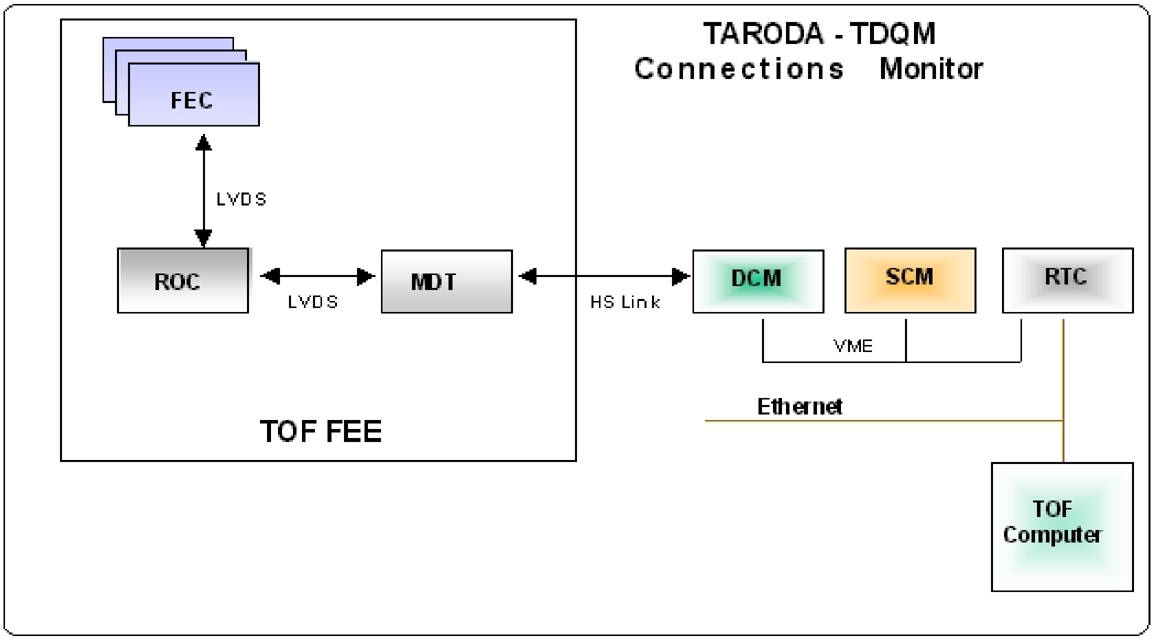

Figure 3.26: TDQM Hardware Layout.

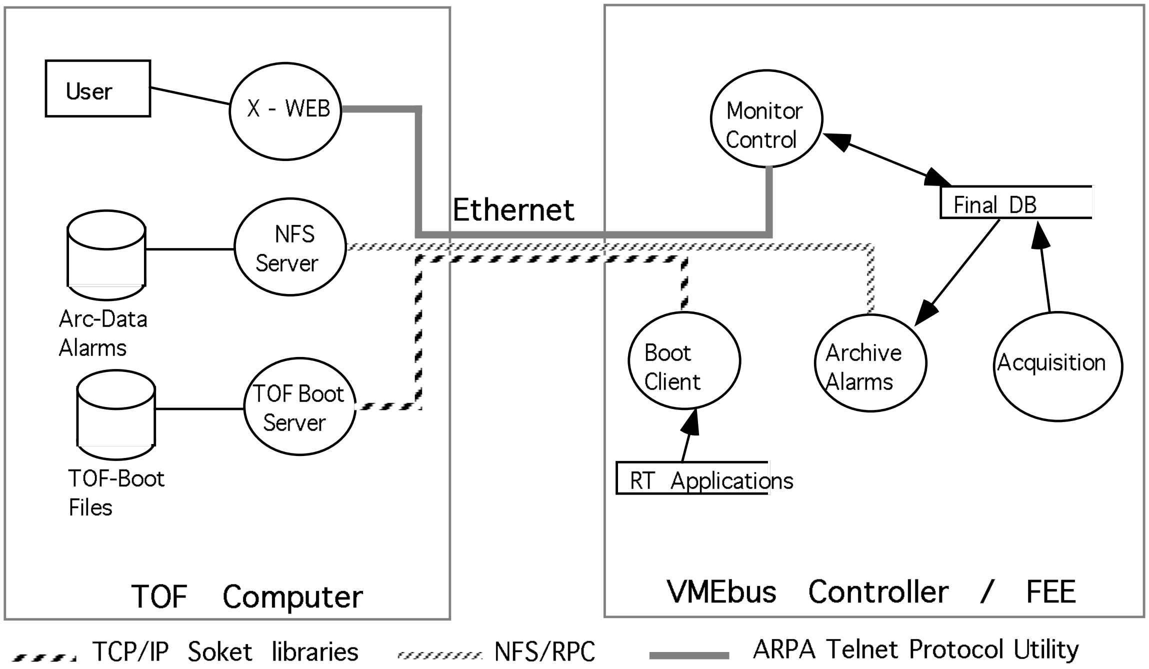

Figure 3.27: TRCO Layout.

3.6 High-Resolution TDC proposal

To take full advantage of the ALICE's Time of Flight (TOF) detector timing characteristics, the TDC unit performing the time capture and conversion into a digital format, must have high resolution. The monolithic circuit described here includes 8 channels, each having a bin size of 48.8 ps and an expected RMS resolution better than 25 ps across an extended dynamic range of 102 μs. Extensive buffering and optional trigger-matching are also integrated, to facilitate the design of the system in which it will be included. This IC will be implemented in a modern 0.25 μm CMOS technology, which guarantees its availability during the time-frame of the construction of the ALICE detector.

3.6.1 Architecture

This high performance TDC is based on a series of TDC's developed in the microelectronics group at CERN. Previous versions of general purpose TDC's have shown that the concept of a programmable TDC such as the one being proposed is highly appreciated in the high energy physics community [11]. The general architecture (use of time tags) developed for the previous versions of TDC's is reused in the new TDC implementation. This architecture has proven to be extremely flexible and works well in many different kinds of experiments. The use of modern technology will enable a significant increase in the performance of the TDC, introducing minor changes to this well-proven architecture. A bin size of 200 ps can be obtained directly by using a Delay Locked Loop (DLL) with 32 delay elements, driven from a 160 MHz reference clock. This results in an RMS resolution of 60–70 ps. The microelectronics group has shown that the time resolution obtained from a DLL based TDC can be improved by using either an array of phase shifted DLL's [12] or an RC delay chain to control the sampling of the signals from a single DLL [13]. The latter scheme requires the DLL signals to be sampled several times (four, in the present case) and controlled from a precisely calibrated on-chip RC delay line, thereby obtaining an RMS resolution of 25 ps (and a 50 ps bin size). Alternatively, the four sets of registers required for the multiple sampling of the DLL can be used as independent lower resolution (60–70 ps) channels. Due to its flexibility, low power and simple calibration procedure, this TDC architecture has been chosen for the TOF system. The dynamic range of this TDC covers the full LHC machine cycle, thus enabling the direct identification of the bunch crossing which generated the hits. A coarse time counter, synchronous with the same reference clock, allows for this extension of the dynamic range. A 40 MHz reference clock is the preferred choice for the time reference, because of its immediate availability in the front-end and the possibility of synchronization of the acquisition of detector signals with the bunch crossings of the LHC machine. A clock-multiplying PLL is therefore integrated in the TDC in order to generate the necessary 160 MHz clock. PLL's have the ability to remove jitter on the incoming clock signal, thereby easing the problem of distributing a stable (low jitter) 40 MHz clock. In the high resolution domain in which the TDC is intended to operate, the time-critical inputs must accept differential signalling levels in order to avoid common mode noise coupled into these signals at board level. For this reason, all inputs related to the time measurements (hit inputs and clock) and the interface to the trigger system can be programmed to use either differential LVDS signalling levels or single-ended 3.3 V TTL levels. The correct operation of the high-resolution TDC requires only an initial calibration of the RC delay line. This calibration is performed at the system level, by collection of a number of random hits from which the calibration parameters can be obtained, using a short iterative procedure. The data collected in the 8 high-resolution channels are merged into four data paths. After trigger-matching data reduction (optional), these four data paths are merged into a common read-out buffer.

Several read-out interfaces are implemented: A 32 bit parallel read-out interface is available for high bandwidth read-out. A serial read-out at 80 MHz and below, using LVDS signalling levels, is available for low bandwidth read-out. Read-out data is formatted in 32 bit packages (words) with a 4 bit type identifier. Finally, a byte-wise read-out is also available, enabling the TDC to drive commercial serializing IC's (Hot link, LVDS links, etc.). A token passing mechanism enables up to 16 TDC chips to share a

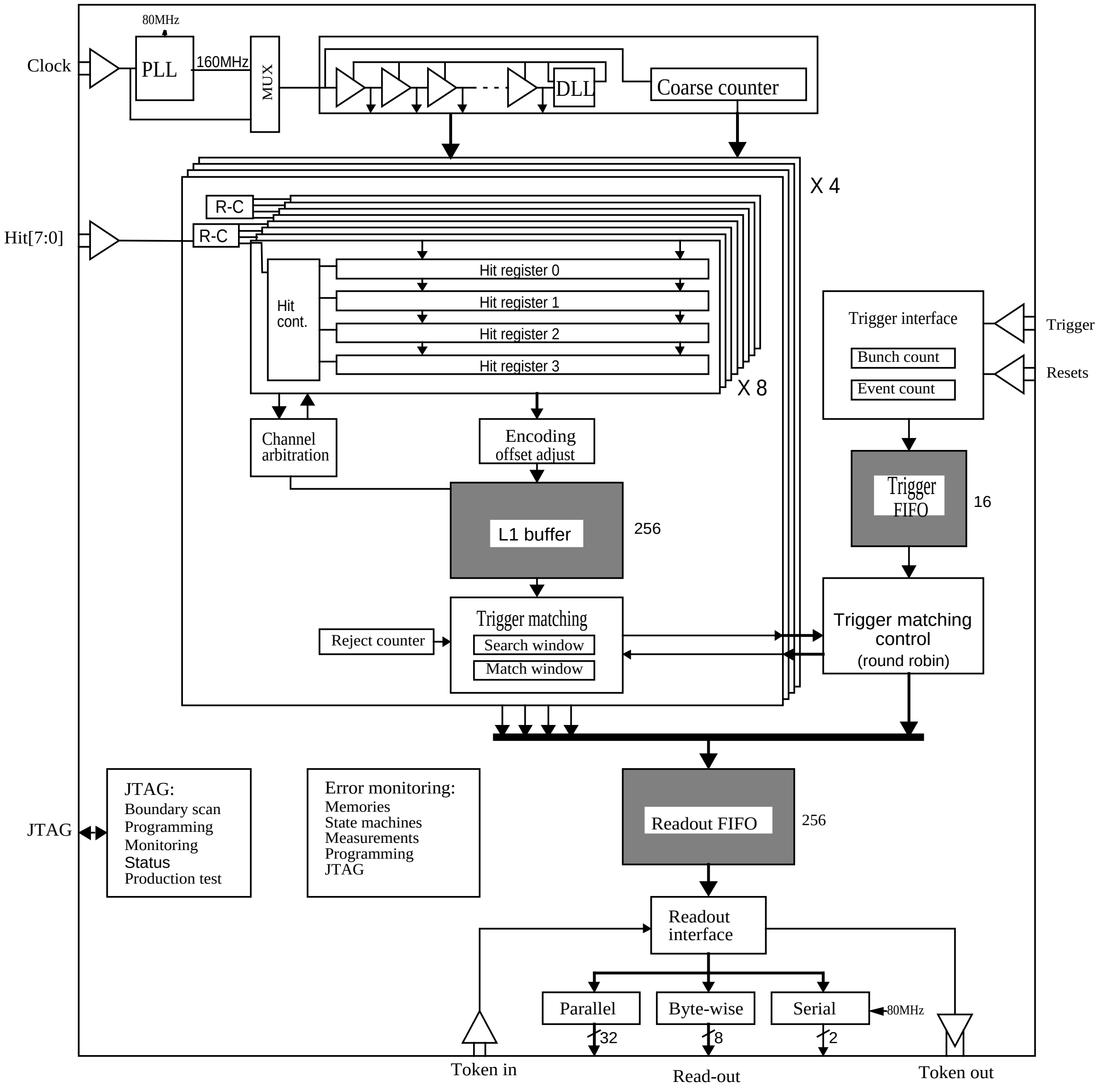

Figure 3.28: TDC's block diagram.

common read-out bus or serial link. A JTAG port is also implemented. It is used for programming and performing tests on the IC. The sub-micron technology in which the TDC will be probably implemented allows the circuit to work correctly up to levels of 30 Krad total dose, with a slight increase in power dissipation. A self-checking mechanism will be implemented in all internal memories and state machines so that any malfunction (for example, due to a Single Event Upset - SEU) can be properly identified. A hit measurement is performed by storing the state of the DLL and the coarse counter when a hit (leading or trailing edge) is detected. Each channel can buffer 4 measurements (each made of four samples) until they can be written into a 256 words deep level 1 buffer shared by two channels. The individual channel buffers work as small derandomizer buffers for the samples. The time interpolation is created from the four samples of the DLL state and then written into the L1 buffer. Measurements stored in the L1 buffer can be passed directly to a common 256 words deep read-out FIFO, or a trigger-matching function can select events related to a trigger. The trigger information, consisting of a trigger time tag and an event id., can be stored temporarily in a 16 words deep trigger FIFO. A time window of programmable size is available for the trigger-matching, to accommodate the time spread of hits related to the same event. The trigger time tag can optionally be subtracted from the measurements so that only time measurements relative to the trigger need to be read out. Accepted data can be read out in a direct parallel format or be serialized at a programmable frequency.

3.6.2 Phase Locked Loop

The PLL performs clock multiplication, from a 40 MHz input clock to the 160 MHz needed for the high resolution time measurements. A PLL is a sensitive second-order control loop consisting of the components shown in the figure below. The Voltage-Controlled Oscillator (VCO) generates a symmetrical clock signal whose frequency and phase is compared with the reference signal. If a frequency or phase discrepancy is detected by the Phase-Frequency Detector (PFD) the control voltage to the VCO is adjusted via a charge pump and filter circuit. By dividing the signal generated by the VCO before comparing it with the input reference, the VCO frequency becomes multiplied with the intended factor. The PLL must be initialised after a stable reference clock has been supplied to the TDC chip. The correct frequency and phase lock will be obtained after 10 ms.

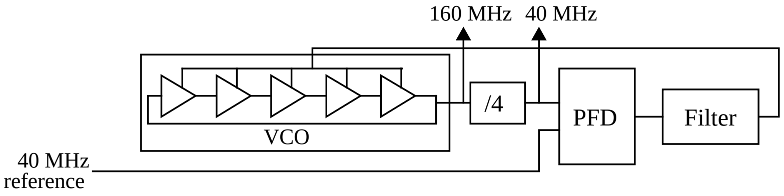

Figure 3.29: Block diagram of the PLL.

An identical PLL has already been implemented in a prototype using the same technology, and the measurements [14] have shown an RMS jitter of only 15 ps (peak-peak of 87 ps).

3.6.3 Delay Locked Loop

The DLL, which generates the basic timing signals for the required time resolution, consists of three major components: a chain of 32 delay elements whose delay can be adjusted by a control voltage, a phase detector which permanently measures the phase error between the clock and the delayed clock in the opposite extremes of the delay chain, and a charge-pump and loop filter which generate the control voltage to the delay elements based on the measured phase error from the phase detector. Time measurements are performed by capturing the state of the DLL and storing it in the hit register. This word is a time tag that is a measure of the time interval between the beginning of the reference clock period to the instant the hit occurred. The use of a clock synchronous counter, which state is also captured, enables an extension of the dynamic range of the measurements. During normal operation the DLL is continuously monitored. If locking is lost (which may happen if the clock has been removed for some time or a large clock frequency change has occurred) and a time measurement is performed, a vernier error status is set. If this happens the DLL must be reinitialized to guarantee correct function. A DLL is sensitive to jitter on its input clock. Any jitter on the clock will directly degrade the precision of the time measurements. If the jitter is larger than one time bin in the DLL, it will result in the vernier error status bit being set.

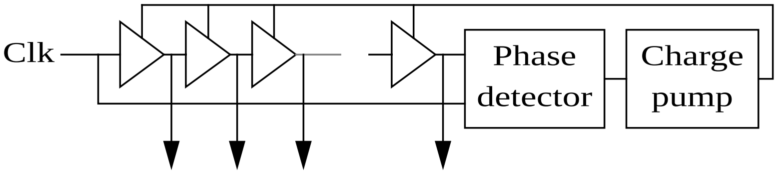

Figure 3.30: Block diagram of the DLL.

3.6.4 High resolution time measurements

By capturing multiple samples of the DLL state at instants controlled with a precisely calibrated RC delay line, the time resolution of the single DLL can be improved significantly. An interpolation within a DLL cell is obtained by sampling the DLL signals four times, equally spaced over the interval of a delay cell. The sampling signals must be generated with very small delays (50 ps) and high precision and stability. This is done using an RC delay line, which has very low dependency on temperature and supply voltage. However, such an RC delay line has high dependency on processing parameters, therefore each chip needs an initial calibration. Afterwards, the calibration parameters can be considered to be constant within reasonable variations of temperature and voltage (30 °C, 10% VDD).

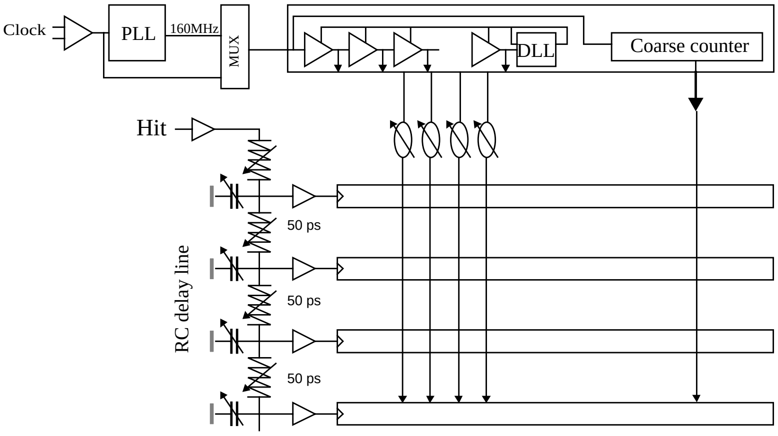

Figure 3.31: RC delay line time interpolation.

Each of the four DLL samples can be considered an individual time measurement from which a high resolution interpolation is performed. Each of these measurements can be read out individually (for debugging), or an on-chip interpolation can be performed to compress them into one single high resolution time measurement. Because of the process variations of the RC delay line, a start-up calibration of its parameters is required. Such a calibration can be performed using statistical code density tests based on a source of random hits. Such a calibration can, in principle, be completely integrated on the chip but will increase the complexity of the design. It has been proven, with prototype chips [13], that when the correct calibration parameters have been determined they do not need to be changed under normal working conditions. It is therefore acceptable that the calibration procedure is software driven from the outside and is only performed infrequently (e.g. once per year, once per month). This scheme has been tested in a prototype circuit, which was built using old 0.7 μm CMOS technology. In this circuit, the delay chain of the DLL was made of 16 delay elements, running with an 80 MHz clock. A bin size of 48.8 ps was obtained by sampling the state of the DLL 8 times. Tests carried out with this prototype have shown an RMS resolution of 25 ps (with a maximum error of 1.5 LSB). The temperature sensitivity was measured and found to be smaller than 1% per 10 °C [13]. Therefore, calibration need only be performed infrequently. It was also seen that additional adjustments to the delays in the DLL can improve the time resolution even further.

3.6.4.1 RC delay line calibration

In order to calibrate the RC delay line, it has to be adjustable. A digital adjustment scheme is the most appropriate because of its simplicity and its immunity to potential noise sources. The scheme used in this TDC consists of partitioning the delay line into small fixed segments, with a sensing buffer at the output of each segment (see Fig. 3.33). The adjustment of the delay taps is performed simply by selecting the best segment buffer to drive each individual tap. A complication of this otherwise simple scheme is that

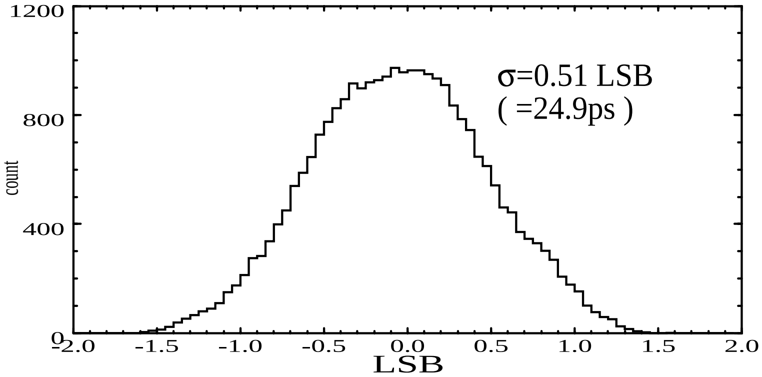

Figure 3.32: Measurement error (from prototype).

the total variation with process is so large (30%) that some segment buffers must be capable of being connected to one of several taps. This requires a carefully planned layout of the delay line.

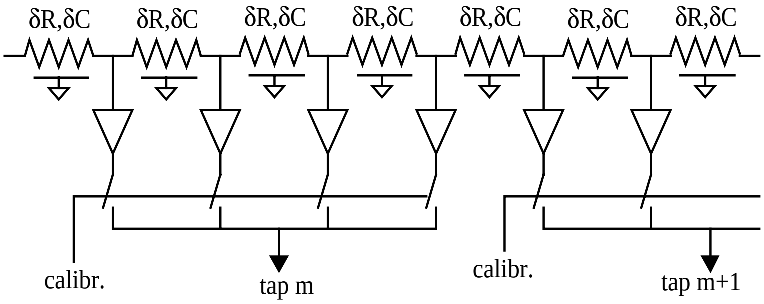

Figure 3.33: Adjustable RC delay line using tap selection.

In order to obtain improved time resolution in comparison to alternative implementations, the automatic self-calibration of the time interpolation circuit is critical. The DLL then automatically locks itself to the reference clock and does not need any further calibration. The total delay of the RC delay line must be matched to the delay cells in the DLL. The individual tap positions must be evenly distributed over the total delay of the RC line. The calibration procedure is based on statistical code density tests. These tests have the advantage of enabling each RC tap to be calibrated individually, using as a reference the average delay of the DLL cells. In a code density test for a time interpolator, a large number of random hits must be generated, and the number of hits registered in each time bin histogrammed. The relative difference between the bin contents in the histogram is a direct measure of the relative size of each time bin. In this simple way, the characteristics of the RC delay line can be measured and be used to perform a calibration. The statistical nature of this calibration procedure ignores all sources of random noise (clock jitter, DLL jitter, thermal noise, etc.); which is an advantage. The statistical code density test only requires a random-hit generator and a simple software routine to derive the optimal calibration parameters from the histogram data. The random hit generator can be a simple uncorrelated oscillator. The calibration algorithm is quite simple, since each tap can be calibrated individually. It is sufficient to select, for each tap, the correct line segment output that leads to the minimum non-linearity. It can be run in an iterative fashion, whereby the accuracy of the calibration can be improved.

3.6.5 Coarse time count

The dynamic range of the fine time measurement, extracted from the state of the DLL, is expanded by storing the state of a 14 bit clock synchronous counter. However, the hit signal may arrive asynchronously to the clocking and the coarse counter may be in the middle of changing its value when the hit arrives. To circumvent this problem, two count values, half a clock cycle out of phase, are stored when the hit arrives. Based on the fine time measurement from the DLL, one of the two count values will be selected and a correct coarse-time value is thus always obtained. The 12 most significant bits of the coarse count are used as the bunch identification (coarse time at the level of 40 MHz) and the 2 least significant bits are appended to the fine time from the DLL (in this case 2 + 5 = 7 bits fine time). At reset, the coarse-time counter is loaded with a programmable coarse-time offset. The bunch structure of LHC is not compatible with the natural binary roll-over of a counter. The coarse counter can therefore be reset separately by the bunch count reset signal and the counter can be programmed to roll-over to zero at a programmed value. The programmed value of this roll-over is also used in the trigger-matching to match triggers and hits across LHC machine cycles.

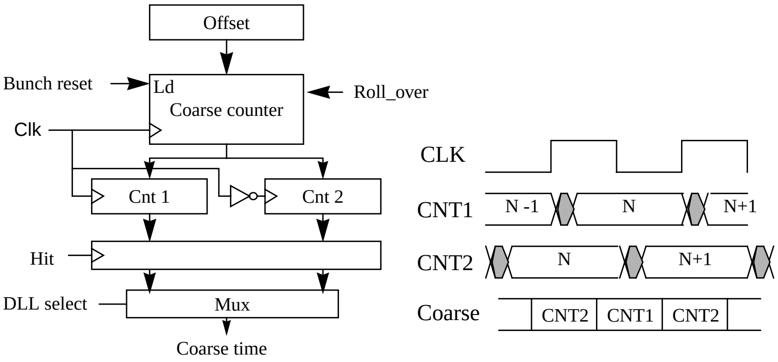

Figure 3.34: Phase shifted coarse time counters loaded at hit.

3.6.6 Channel buffer

Each channel can store 4 TDC measurements before being written into the L1 buffer, shared between two channels. The channel buffer is implemented as a FIFO controlled by an asynchronous channel controller. The channel controller can be programmed to digitize individual leading and/or trailing edges of the hit signal. If the channel buffer is full, when a new hit arrives it will be ignored. The minimum time between two consecutive time measurements is 5 ns. For the hits stored in the channel buffers to be written into the clock-synchronous L1 buffer, a synchronisation of the status signals from the channel buffers is performed. Double synchronisers are used to prevent any metastable state from propagating to the rest of the chip, running synchronously at 40 MHz. It is at this stage that the four samples from a hit measurement are merged into a single high resolution measurement (they can, optionally, be stored as independent, lower resolution measurements).

3.6.7 Level 1 buffer

The four L1 buffers are 256 hits deep and are written into like circular buffers. Reading from a buffer is random access such that the trigger matching can search for data belonging to the received triggers. If a L1 buffer runs full, the latest written hit will be marked with a special full flag. When the buffer recovers from being full, the first arriving hit will be marked with a full recover flag. These flags are used by the trigger-matching described here after, to identify events which may have lost hits because the buffer was full.

3.6.8 Trigger-matching

Trigger-matching is performed as a time-match between a trigger time tag and the time measurements themselves. The trigger time tag is taken from the trigger FIFO and the time measurements are taken from the L1 buffer. Hits matching the trigger are passed to the common read-out FIFO, shared by the four channel groups. Optionally, the trigger time tag can be subtracted from the measurements such that all time measurements read out are referenced to the time (bunch crossing) when the event of interest occurred. A match between the trigger and a hit is detected within a programmable time window. The trigger is defined as the bunch ID (coarse count) when the event of interest occurred. All hits occurring from this trigger time until the trigger time plus the trigger-matching window will be considered as matching the trigger. The trigger-matching being based on the bunch ID means that the “resolution” of the trigger matching is one clock cycle (25 ns) and that the trigger-matching window is also specified in steps of clock cycles. The maximum trigger latency which can be accommodated by this scheme equals half the maximum coarse time count $2^{12}/2$ = 2048 clock cycles = 51 μs. The trigger-matching function is capable of working across roll-over in all its internal time counters. The search for hits matching a trigger is performed within an extended search window, to guarantee that all matching hits are found, even when the hits have not been written into the L1 buffer in strict temporal order. To prevent buffer overflows and to speed up the search time, an automatic reject function can reject hits older than a specified limit when no triggers are waiting in the trigger FIFO.

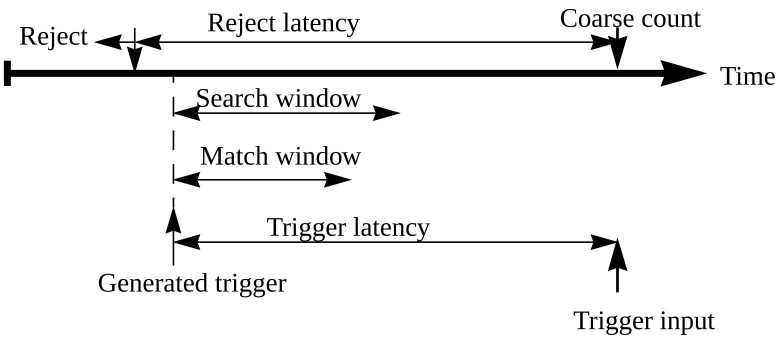

Figure 3.35: Trigger, trigger latency and trigger window related to hits on channels.

In case an error condition (L1 buffer overflow, Trigger FIFO overflow, memory parity error, etc.) has been detected during the trigger-matching, a special word with error flags is generated for each event that may have been affected. All data belonging to an event are written into the common read-out FIFO with a header and a trailer. The header contains an event ID and a bunch ID. The event trailer contains the same event ID plus a word count. The trigger-matching function may also be completely disabled, causing all data from the L1 buffer to be passed directly to the read-out FIFO. In this mode the TDC has an effective FIFO buffering capability of $4 \times 256 + 256 = 1280$ measurements, and a special error word will be generated whenever an error condition has been detected in the TDC (see read-out). When hits extracted from the four channel groups are written into the common read-out FIFO, the priority between the individual groups is given in a round-robin fashion which guarantees fair bandwidth sharing.

3.6.9 Trigger interface

The trigger interface takes care of receiving the trigger signal and generates the required trigger time tag to be loaded into the trigger FIFO. In addition, it takes care of generating and distributing all signals required to keep the TDC running correctly during data taking. The TDC needs to receive a global reset signal that initialises and clears all buffers in the chip before data taking. A bunch count reset and event count reset is required to correctly identify the event ID and the bunch ID of accepted events. These signals can either be generated separately or be coded on a single serial line at 40 MHz. The TDC is capable of running continuously even when bunch count resets and event count resets are issued. Matching of triggers and hits across bunch count resets (different machine cycles) are handled automatically if the correct roll-over value has been programmed. Alternatively, it is possible to insert special separators in the trigger FIFO and the L1 buffers when a bunch count reset or an event count reset have been issued. These would ensure that hits and triggers from different event count or bunch count periods (machine cycles) are kept separate. In this mode, it is not possible to match hits across bunch count periods.

3.6.10 Read-out FIFO

The read-out FIFO is 256 words deep and its main function is to enable one event to be read out while others are being processed in the trigger-matching. If the read-out FIFO runs full we are faced with two options:

- Back propagate: The trigger-matching process will be blocked until new space is available in the read-out FIFO. When this occurs, the L1 buffers and the trigger FIFO will be forced to buffer more data. If this situation is maintained for extended periods the L1 buffers or the trigger FIFO will finally overflow.

- Reject: As soon as the read-out FIFO is full, event data (not event headers and trailers) will be rejected. Any loss of data will be signalled with an error flag.

3.6.11 Read-out interface

All data accepted from the TDC can be read out via a parallel or serial read-out interface in words of 32 bits. Up to 16 chips can be joined together, using a token passing scheme, to perform local event building. The read-out of an event is started by the master chip sending a group event header (if enabled). The master then sends the token to the first slave chip in the chain, which then starts sending its data. The event data from each chip typically consists of a single chip event header (if enabled), accepted time measurements, error flags (if any error detected for event being read out) and, finally, a single chip event trailer (if enabled). The token is then passed on to the following TDCs in the chain until it arrives at the master. The master chip asserts its own event data and finally ends the whole event with a group event trailer (if enabled). A slightly different read-out protocol is available, when trigger matching is not enabled, as data are not grouped in events. In this case, each TDC having data can be programmed to wait for the token, then send one measurement and immediately give the token to the next chip, even if it has more data to send. This ensures that all TDCs get equal opportunity to send data and prevents a TDC with a noisy channel from blocking all the other TDCs in the read-out chain. The cost of this is that the token is circulated continuously which implies some overhead. The TDC can also be programmed to keep the token until all its data have been read out. The use of a token ring to perform local event building is simple and effective but is sensitive to any failure in a single component in the chain. A set of additional inputs for the token and serial data are available to enable a slave TDC to be bypassed in case of failure.

3.6.12 Error monitoring

All functional blocks in the TDC are continuously monitored for error conditions. Memories are continuously checked with parity on all data. All internal state machines have been implemented with a “one hot” encoding scheme and are checked continuously for any illegal state. DLL signals captured when a hit is detected are checked to verify that the DLL is in a correct locking state. The JTAG programming data and the JTAG instruction register also have a parity check to detect if any of the bits have been corrupted during loading or by a Single Event Upset (SEU). The error status of the individual parts can be accessed via the JTAG status scan path. Any detected error condition in the TDC sets its corresponding error status bit, which remains set until a global reset of the TDC is performed. All the available error flags are or-ed together with individual programmable mask bits, to generate a global error signal. When the global error signal becomes active, the TDC can respond in a number of different ways:

- Ignore: No special action will be performed.
- Mark events: All events being generated after the error has been detected will be marked with a special error flag.
- Bypass: From the following event the TDC will suppress all its own data and directly pass the token and serial data.

3.6.13 JTAG test and programming port

A JTAG (Joint Test Action Group, IEEE 1149.1 standard) port is used to set up the programmable features in the TDC, and get access to test facilities built into the TDC. Full boundary scan is supported with the capability of performing extensive testing of TDC modules while located in the system. Testing the functionality of the chip itself is also supported by the JTAG INTEST capability. In addition, special JTAG registers have been included in the data path of the chip which are capable of performing effective testing of registers and embedded memory structures.

3.6.13.1 Programmable features

This TDC has a large number of programmable features which have not been mentioned in this report. They allow for a very flexible operation under different conditions. A listing of the most important features is presented in the next lines:

- selection of time-critical input signalling levels (LVDS/LVTTL)
- enabling trigger-matching
- trigger-matching control (size of search/match windows, latencies, etc.)
- selection of action in case of full read-out buffer (reject hits or back propagate into L1 buffer)
- enabling measurement of rising and/or falling edge of hit signal
- enabling four-sample merging on chip (high resolution measurement)
- selection of measurement mode (high resolution/lower resolution)
- independent offset per channel
- independent enabling of channels
- coarse counter offset
- DLL control
- calibration of RC delay line
- adjustment of DLL tap delay
- PLL control
- selection of reference clock origin (PLL/external)
- enabling test and debugging modes
- selection of action in case internal errors are detected
- selection of read-out interface

3.6.14 Technical specifications

Number of channels:	8
Clock frequency:	40 MHz / 160 MHz
Time bin size:	48.8 ps
Time resolution:	25 ps RMS
Dynamic range:	12 + 7 + 2 = 21 bit
Double pulse resolution:	5 ns (if two hit registers free).
Max. recommended Hit rate:	8 MHz per channel
Event buffer size:	4 × 256
Read-out buffer size.:	256
Trigger buffer size.:	16
Power supply:	2.25–2.75 V Typical 100 mA, max 200 mA
Temperature range:	-40–80°C
Hit inputs:	LVDS or LV TTL (3.3 V)
Remaining I/O:	LVTTL (3.3 V)

A full description of this TDC may be found in [15].

3.6.15 Glossary

ADAQ	ALICE data acquisition system
ADC	Analog to Digital Converter
ASIC	Application-Specific Integrated Circuit
ATC	Amplitude to Time Converter
CAN	Controller Area Network
CLD	Clock Distribution
DAC	Digital to Analog Converter
DCM	Data Concentrator Module (TARODA)
DCS	Detector Control System (ALICE)
DD	Data Dictionary (SASD)
DDL	Detector Data Link (ALICE)
DFD	Data Flow Diagram (SASD)
DLL	Delay Locked Loop
DSP	Digital Signal Processing
FEA	Front End ASIC (TARODA)
FEC	Front-end Electronic Card (TARODA)
FEDC	Front End Digital Crate (ALICE)
FEE	Front End Electronics (ALICE)
FIFO	First In First Out
FPGA	Field Programmable Gate Arrays
HPTDC	High Performance TDC
JTAG	Joint Test Action Group - IEEE standard 1149.1-1990
LDC	Local Data Concentrator (ALICE)
LVDS	Low Voltage Digital Signal
MDT	Multiplexer and Data Transfer card
PLC	Programmable Logic Controller
PLL	Phase Locked Loop
ROC	Read Out Controller (TARODA)
RORC	Read Out Receiver Card (ALICE)
RTC	Real Time Controller
SASD	Structured Analysis Structured Design
SCM	Slow Control Manager card (TARODA)
TARODA	TOF ALICE Read Out and Data Acquisition system
TDC	Time to Digital Converter
TDQM	TOF Data Quality Monitor software package
TOF	Time Of Flight
TRCO	TOF Run and DAQ COntrol system
TSCS	TOF Slow Control System software package
TSF	T0 Signal Fanout
TTC	Trigger Timing and Control
TTL	Transistor to Transistor Logic

4 TOF Detector Performance

4.1 Introduction

The performance of a very large TOF system covering the central rapidity region ($|y| \lesssim 1$) for particle identification (PID) in the intermediate momentum range (from 0.2 to 2.5 GeV/c), which includes the majority of all charged particles produced in this region, is of crucial importance in the ALICE experiment [1]. This intermediate range will provide relevant observables, to investigate the nature and the dynamical evolution of the hadronic system produced in ultra-relativistic heavy ion collisions, at LHC energies.

The basic physics motivation for the ALICE TOF detector has already been pointed out in Chapter 1. This detector, coupled with the ITS [2] and TPC [3] detectors for track/vertex reconstruction and for dE/dx measurements in the low momentum range (up to about 0.5 GeV/c), will provide a unique feature in the experiment: the event-by-event (E-by-E) identification of large samples of pions, kaons and protons. The TOF identified particles will be essential for many relevant physics studies on a single event basis. In addition, at the inclusive level, identified kaons will allow various invariant mass studies, in particular to detect open charm states. In this respect, above 2.5 GeV/c, the TOF will be complemented by the smaller HMPID [4] detector.

A large-coverage, powerful TOF detector, operating efficiently in extreme multiplicity conditions, should have an excellent intrinsic response and an overall occupancy not exceeding the $10-15\%$ level at the highest expected charged particle density ($dN_{ch}/dy = 8000$). This implies a design with more than 10^5 independent TOF channels.

In this chapter we explore, by means of detailed Monte Carlo simulations, the performance and limitations of the TOF system we envisage building, in order to test our assumptions and verify its foreseen PID power in a ”real” heavy ion collision environment. We discuss the PID procedure in terms of acceptances, efficiencies and contaminations for different particle species, focusing on π/K/p separation and on the E-by-E physics analysis.

4.2 Detector description

The TOF detector design has been described in detail in Chapter 3. In our Monte Carlo simulations, different detector layout options have been studied, as illustrated in the following paragraphs. These correspond to close approximations of the ultimate detector design presented at this stage of the project.

4.2.1 Software tools for detector description and particle tracking

The present Monte Carlo simulation studies have been performed using AliRoot 3.02 [5], the latest release of the ALICE off-line code implemented in the ROOT [6] framework for event simulation, reconstruction and analysis. Let us briefly recall that AliRoot includes the well-known GEANT 3.21 [7] detector description and tracking package in a user-friendly environment handled by C++. AliRoot has been installed on workstations running HP-Unix 10.20 and on PCs running Linux Red Hat 6.0. The AliRoot framework is interfaced with several event generators (JETSET [8], PYTHIA [9], HIJING [10], SHAKER [11], etc.) thus providing a complete set of instruments to simulate ion-ion collisions.

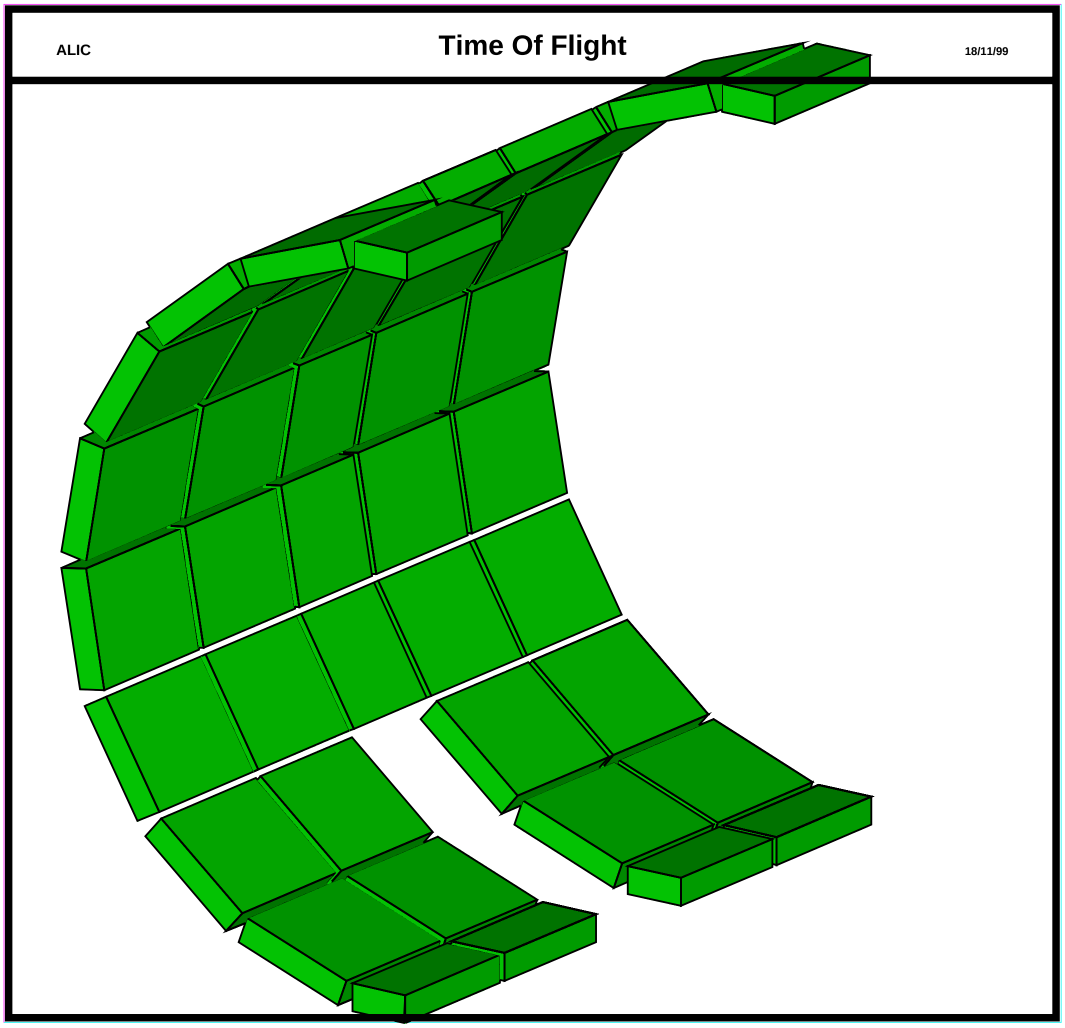

Figure 4.1: Time-Of-Flight (TOF) detector layout in AliRoot, with holes for the HMPID and PHOS detectors.

4.2.2 Detector layout for Monte Carlo simulation studies

Let us briefly recall the basic features of the detector presented in Chapter 3. The detector covers a cylindrical surface of polar acceptance $|\theta - 90°| < 45°$. It has a modular structure corresponding to 18 sectors in ϕ (the azimuthal angle) and to 5 segments in z (the longitudinal coordinate along the beam axis), as shown in Fig. 4.1.

Each module has an internal structure organized in sensitive pads (as we will see later on) and an overall thickness of 29 *cm*. The whole device is inscribed in a cylindrical shell with an internal radius of 370 *cm* and an external one of 399 *cm*. In terms of material, the whole device thickness corresponds to $\sim 19\%$ of a radiation length.

Along z, we have a central module (module A), two intermediate modules (modules B) placed on both sides of the central one and two outer modules (modules C). Modules A, B and C have the same width (130 *cm*) and increasing lengths, adding up to an overall TOF barrel length of 750 *cm*. This 5-module design has been adopted in order to match the geometry of the TRD detector inserted between the inner TPC and the TOF itself. Two holes could be foreseen in the TOF barrel, corresponding to the positions of the external HMPID [4] and PHOS [12] detectors, in the upper and lower regions at 90°. In this case, we would have 3 sectors with only C modules in the upper part of the TOF barrel (for HMPID) and 5 sectors without A modules in the lower part (for PHOS). This layout, shown in Fig. 4.1, corresponds to the requirement of minimal disturbance to particles reaching the HMPID and PHOS detectors.

In the Monte Carlo detector description, an insensitive frame (3.5 *cm* wide) is foreseen inside each module, to account for dead regions in between modules, along z and ϕ. The TOF barrel area is $\sim 176\,m^2$. The holes for HMPID and PHOS correspond, respectively, to $\sim$ 10% and $\sim$ 5% of this area and the dead space in between TOF modules to $\sim$ 10%. Hence the actual area of the detector is $\sim$ 75% of the total. In the detector design presented in Chapter 3, the dead regions along z have been eliminated by overlapping the module edges, thanks to an appropriate moulding of the module walls. Hence the overall dead space in between TOF modules is only $\sim$ 5% of the total barrel area.

Another version of the detector has been also considered in our simulations, with 18 identical sectors, each made of 5 modules (A, B and C). We will refer to it as the full coverage version. In addition, we have envisaged two possible TOF detector layouts, with different configurations and positionings of the signal readout pads inside the modules.

Tilted-strip design

Each module has an internal structure organized in planar sensitive strips. A sensitive strip is made of two rows of $\sim 3 \times 3\,cm^2$ sensitive copper pads. The pad rows, in all the modules, are always transverse with respect to the z axis (see Chapter 3). The distance between two consecutive pads (centre-to-centre) is 3 *cm*, with an interpad gap (edge-to-edge) of 2 *mm*. Each row contains 40 pads, and an array is made up of 80 sensitive pads per strip. Each strip has an insensitive frame 1 *cm* wide all along its border. The interpad area of the strip is sensitive and a particle passing between pads will induce a signal on the closest pad (or sometimes on both). Therefore the total active surface of the detector is $120\,m^2$, corresponding to $\sim$ 133500 pads ($141\,m^2$ and $\sim$ 157000 pads in the full coverage version of the detector).

In the tilted-strip design of the detector, the strips are tilted inside the modules to minimize the traversal path through the strips for particles coming in from the interaction vertex (for details, see Chapter 3). In the Monte Carlo, this is achieved by introducing a strip tilting angle, progressively increasing with the z-position of the strip, in such a way that, in the median side view of each of the 18 sectors, the strip face is perpendicular to the straight line connecting its centre to the vertex. In order to minimize the dead area, the strip arrangement inside the modules is such that the frame of each strip (transverse to the beam axis) is overlapped with the sensitive pad rows of the neighbouring strips. This tilted-strip version of the detector, shown in Fig. 4.2, meets the requirement for incident tracks to be as perpendicular as possible to the TOF pads in the longitudinal view, so as to reduce the number of very oblique traversals, in particular in the C modules at both ends of the TOF barrel. These avoids signal sharing among adjacent pads, with increased time jitter. The average radius of the detector sensitive surface is 3.76 *m*.

It should be noticed that in the real tilted-strip detector design presented in Chapter 3, where the dead regions in between the modules have been further minimized with respect to the present Monte Carlo detector description, the total number of pads is $\sim$ 160000 (full coverage), i.e. 2% higher.

Planar design

Here each module contains a unique plate configured as an array of $\sim 3 \times 3\,cm^2$ sensitive pads. The interpad space is again 2 *mm*. The only dead area of the plate corresponds to the already mentioned inner border frame of the module (3.5 *cm* wide). Each plate lies on a cylindrical surface of 3.72 *m* radius. In this case, the total active area is $137\,m^2$, corresponding to $\sim$ 147500 pads, with a pad area slightly (3%) larger than for the previous design ($159\,m^2$ and $\sim$ 171500 pads in the full coverage version). This planar design corresponds to an untilted-strip version of the detector. It represents, however, a less realistic detector due to the total absence of internal frames or edges within each module.

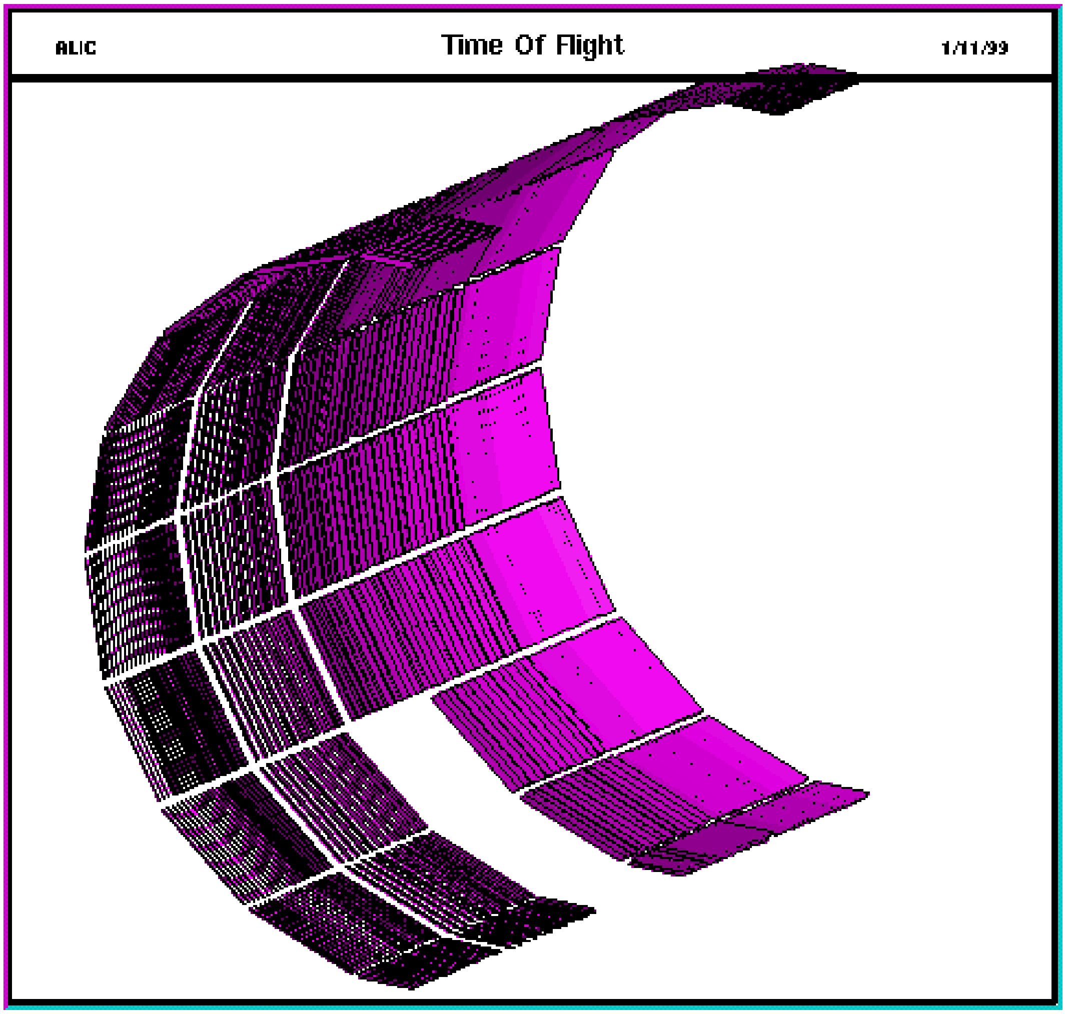

Figure 4.2: View of the tilted-strip TOF detector (with holes for the HMPID and PHOS).

4.3 Monte Carlo event generators

Different event generators are available to simulate central Pb-Pb collisions at beam energy of 2.76 TeV/nucleon [1]. We have, essentially, used two of them, SHAKER and HIJING, to simulate the global features of the events relevant for detector design (in particular for the detector granularity, which determines the number of readout channels and the data volume and hence the DAQ architecture) and E-by-E analysis. These event generators have been used as an input for the GEANT3 tracking package of AliRoot, as follows:

- HIJING [10] alone, over the full solid angle.
- SHAKER [11] for the central rapidity region, i.e. $|\theta - 90^\circ| < 45^\circ$, coupled to HIJINGPARAM [13] for the forward and backward regions, in order to estimate the background contribution from the $|\theta - 90^\circ| > 45^\circ$ outer region.

4.3.1 HIJING event generator

The HIJING event generator has been developed using as input the results of current heavy ion experiments [10]. It combines the Dual Parton Model [14], which provides a unique picture for particle production in hadron-hadron, hadron-nucleus and nucleus-nucleus interactions at high energies, with the Lund FRITIOF [15] and the successful implementation of perturbative QCD processes in PYTHIA [9].

HIJINGPARAM [13] is an inner AliRoot generator which uses parametrised pseudorapidity and transverse momentum distributions of pions and kaons (charged and neutral). The pseudorapidity distribution has been obtained from a HIJING simulation of central Pb-Pb collisions [11]. The transverse momentum distribution was obtained from a parametrisation of the pion transverse momentum distribution, measured at CDF. The corresponding kaon p_t distribution was obtained from the pion distribution by m_t-scaling. These distributions can be found in [13].

A sample of $N = 5$ HIJING events has been generated over the full solid angle, with an average charged particle density in the central region $dN_{ch}/dy = 6700$ for $-1.5 \leq y \leq 1.5$ ($dN_{ch}/dy = 7200$ for $-1 \leq y \leq 1$). The total multiplicity of primary particles per event is $\sim$ 78000 while the total charged multiplicity is $\sim$ 44000. The particles are produced following the HIJING hadronization algorithms. Figure 4.3 gives the average particle yields per event. In particular, we have the following particle ratios: $\mathrm{K}/\pi = 0.13$ and $\mathrm{p}/\pi = 0.079$. For the central barrel region with $|\theta - 90^\circ| < 45^\circ$, in each event we have $\sim$ 9300 $\pi^\pm$, $\sim$ 900 $\mathrm{K}^\pm$ and $\sim$ 500 $\mathrm{p}(\overline{\mathrm{p}})$.

4.3.2 SHAKER event generator

The SHAKER event generator has been developed to describe the central rapidity region of heavy ion events at LHC [11]. It is derived from the Lund model, within the framework of JETSET 7.3 [8]. The main ingredient of this simple phase space generator is the density of particles at central rapidity, according to which the various particles (π^0, η, π^+, p, K^+, K^0) and antiparticles are produced. A rapidity plateau can be obtained between fixed limits. The p_t spectra of the generated particles reproduce those measured at the Tevatron [16]. For the η particle, the p_t distribution is derived from the experimental π^0 distribution using m_t-scaling [17]. Particle ratios are derived from Tevatron measurements [16] and isospin invariance. In SHAKER particle ratios, multiplicities and p_t distributions are easily adjustable.

A sample of $N = 25$ SHAKER events has been generated in a rapidity window $-1.5 \leq y \leq 1.5$, with a flat charged particle density $dN_{ch}/dy = 8000$ and the following particle ratios: $\mathrm{K}/\pi = 0.2$, $\eta/\pi = 0.17$ and $\mathrm{p}/\pi = 0.074$. Some amount of $\mathrm{e}^\pm$ comes from primary π^0 and η decays. For the central barrel region with $|\theta - 90^\circ| < 45^\circ$, in each event we have ~ 10100 $\pi^\pm$, ~ 1500 $\mathrm{K}^\pm$, ~ 500 $\mathrm{p}(\overline{\mathrm{p}})$ and ~ 150 $\mathrm{e}^\pm$. Notice that the very high value of the charged particle density chosen for SHAKER events will be useful to test the TOF detector performances in a critical environment.

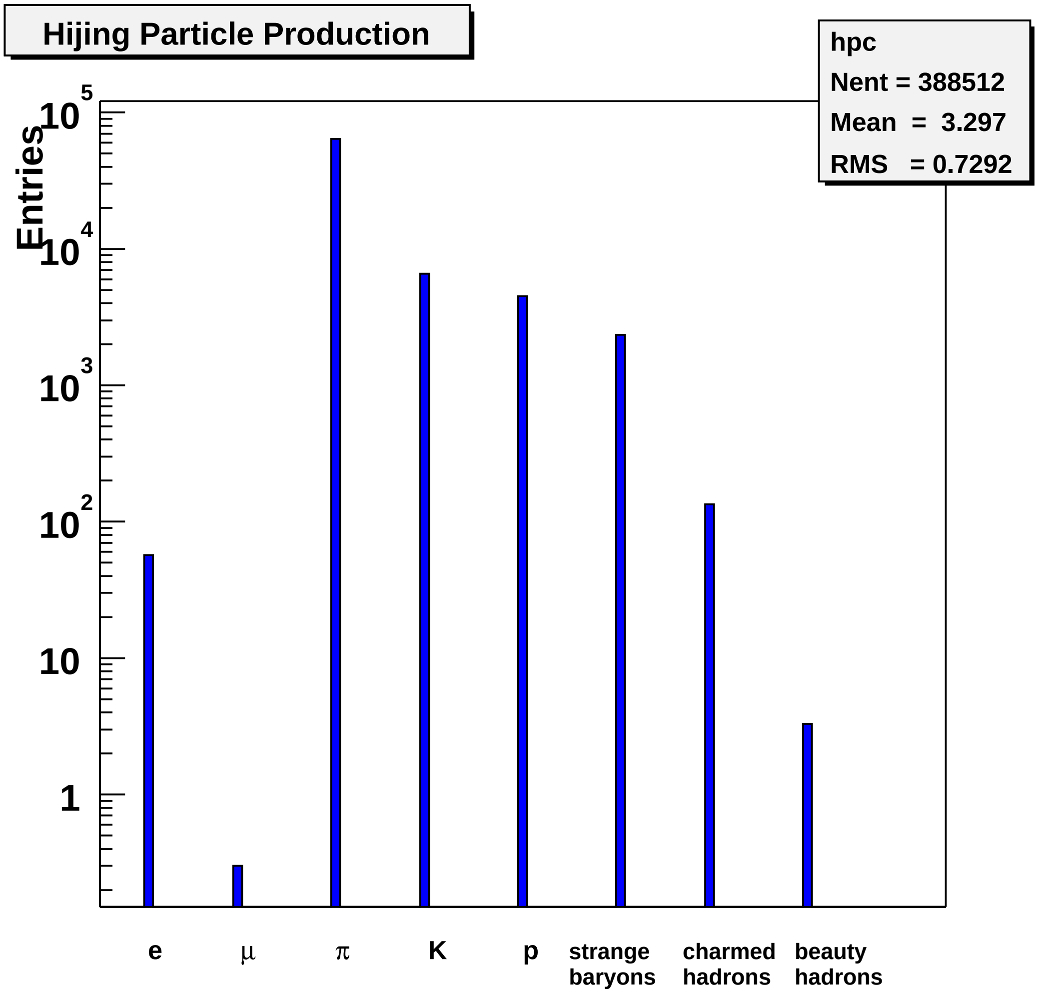

Figure 4.3: The average charged plus neutral particle yields per event in HIJING full phase-space simulations.

4.4 Detector acceptance studies

We use as a baseline input the following parameters and simplifications.

Concerning the TPC:

- It is assumed that a charged particle will have a TPC track if:
    - the radius of its production vertex (R_{vtx}) is $< 50\ cm$[1];
    - it has a hit in the last pad row of the TPC;
    - its total number of hits in all pad rows of the TPC is ≥ 30.
- The momentum and space errors in the TPC are not taken into account.
- A 100% track finding and reconstruction efficiency in the TPC is assumed.

Concerning the TOF:

- The overall time resolution of the TOF pad is taken to be 150 *ps*.
- The intrinsic efficiency of the TOF pad (ε_{eff}) is taken to be 95%.
- No provision is made for noise hits generated by the TOF detector itself (crosstalk, edge effects).

The present studies are, of course, performed taking into account the presence of the 0.2 T solenoidal magnetic field along the beam axis, since the TOF barrel is internal to the ALICE magnet [1].

4.4.1 Momentum spectra

Figure 4.4 shows the distributions of various kinematical and geometrical variables for all charged primary particles generated with HIJING in the region $|\theta - 90°| < 45°$. The HIJING momentum and transverse momentum spectra, separately for primary $\pi^{\pm}$, $K^{\pm}$ and $p(\overline{p})$ in this angular region, are shown in Fig. 4.5. The momentum spectra of charged primaries, as obtained with SHAKER, are shown in Fig. 4.6. Let us recall that the HIJING and SHAKER particle spectra and yields are similar but not identical (see Section 4.3). The differences between the two event generators used herein will show up in terms of detector (TPC and TOF) acceptances and, later on, in the E-by-E analysis (see Section 4.7).

Superimposed in Fig. 4.4 we show the HIJING kinematics and geometry distributions for all charged primaries produced in the $|\theta - 90°| < 45°$ region and tracked in the TPC (according to the above definition). These represent 72% of the original sample. In Fig. 4.5 the HIJING p and p_t spectra for different hadrons with TPC tracks are also shown. The spectra, of course, become harder when the TPC geometrical constraint is imposed. The individual TPC acceptances for π, K and p are reported in Table 4.1. These percentages are obviously different, depending on the hadron species, due to decays and to the presence of the magnetic field.

4.4.2 Acceptance

The occupation of the (p_t, y) plane by primary hadrons reaching the TOF barrel is shown in Fig. 4.7 for HIJING events and the tilted-strip detector version with holes for the HMPID and PHOS. Different empty regions for pions, kaons and protons are due to magnetic field and $|\theta - 90°| < 45°$ polar acceptance. Particle decays are also taken into account. Hence the K/π and p/π ratios at the TOF detector level turn out to be lower than the initial ones. The dead regions between the 5 modules of each sector are clearly visible in Fig. 4.7.

---

[1] Such a value would ensure a good tracking efficiency in the TPC.

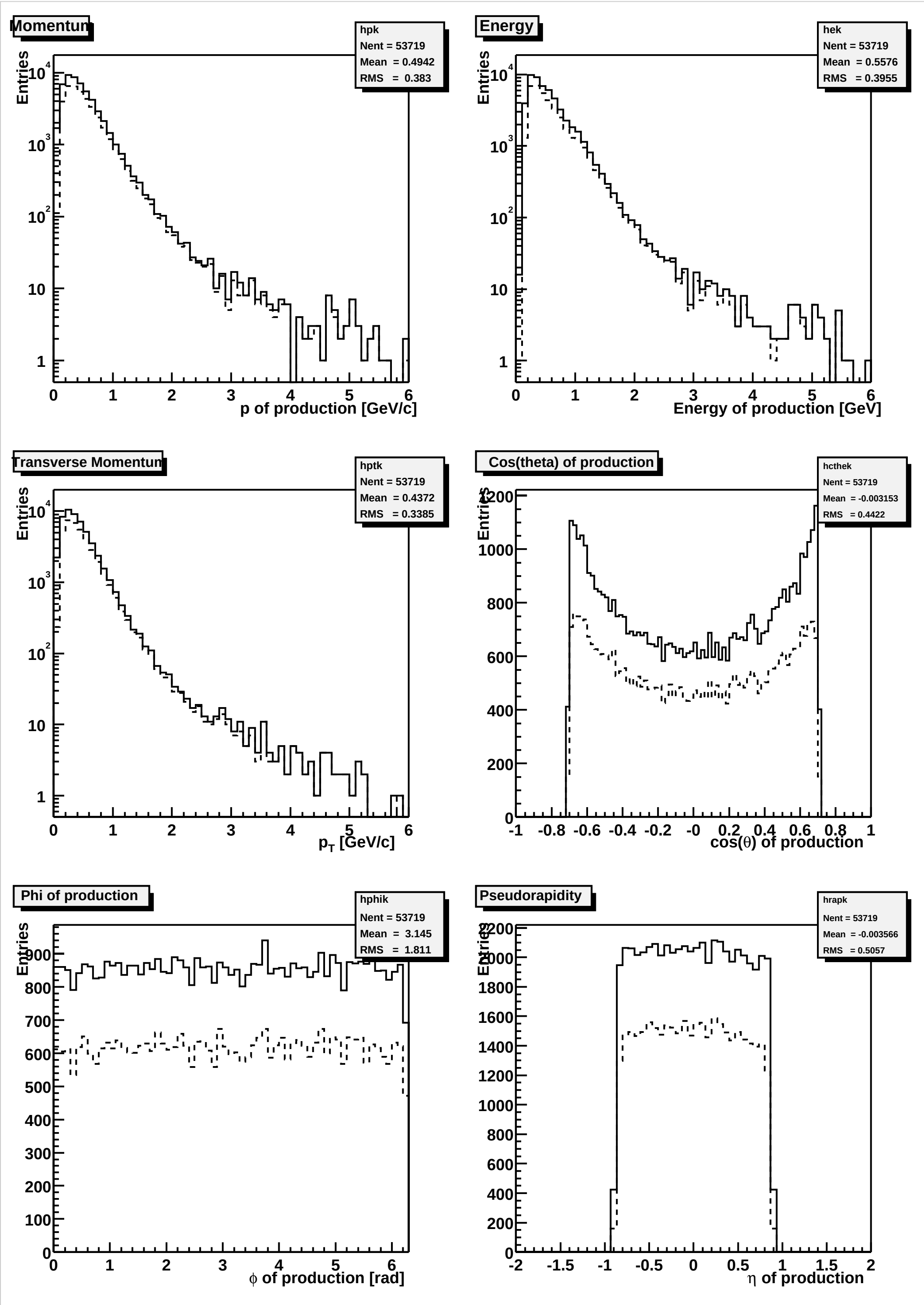

Figure 4.4: Kinematical and geometrical variables of all charged primary particles generated with HIJING (5 events) in the $|\theta - 90°| < 45°$ central region (solid-line histograms). Superimposed the same distributions for particles tracked in the TPC (dashed-line histograms).

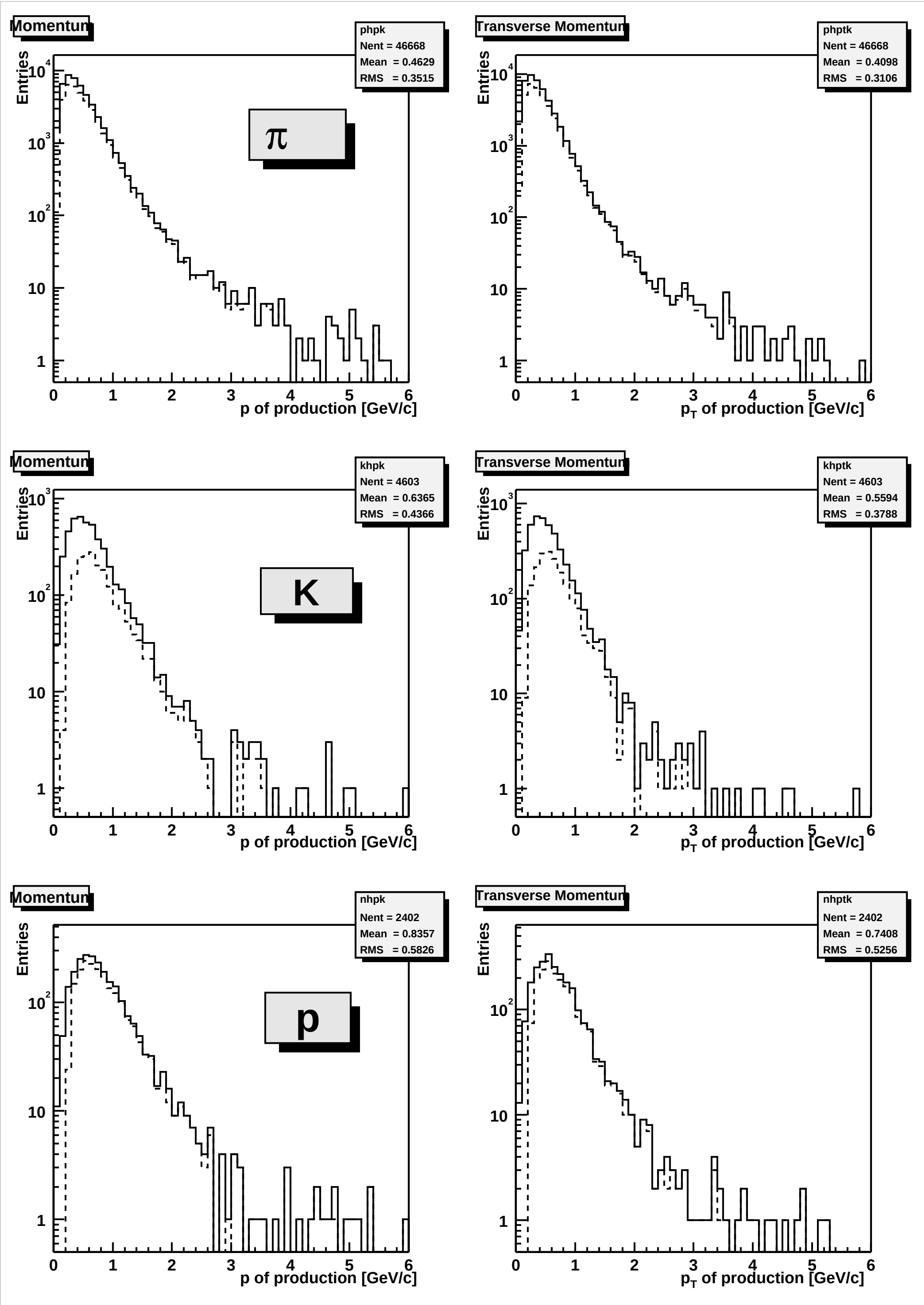

Figure 4.5: Momentum and transverse momentum spectra of charged primary hadrons generated with HIJING (5 events) in the $|\theta - 90°| < 45°$ central region (solid-line histograms). Superimposed the same distributions for hadrons tracked in the TPC (dashed-line histograms).

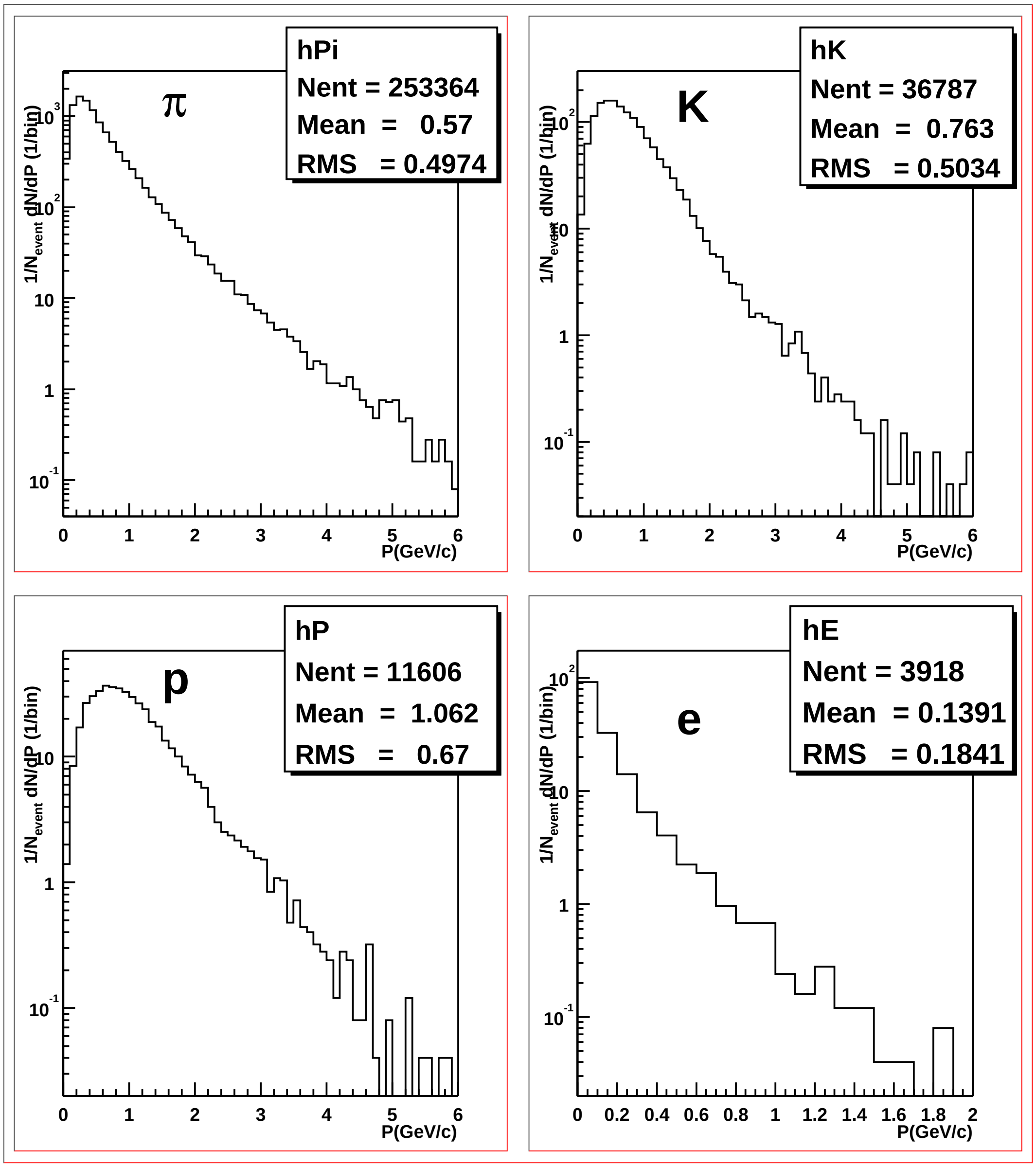

Figure 4.6: Momentum spectra of charged primary particles generated with SHAKER (25 events) in the central region ($|\theta - 90°| < 45°$).

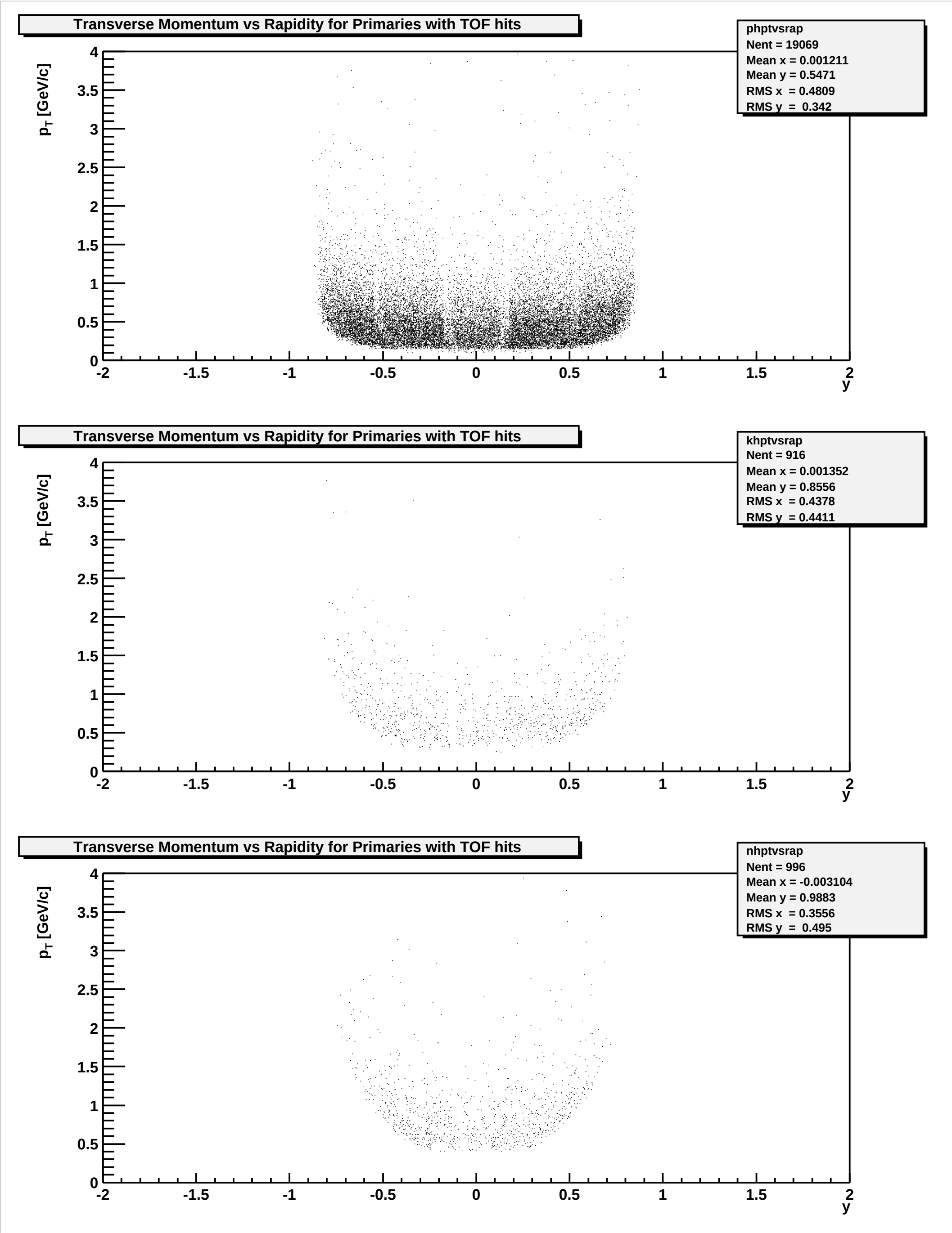

Figure 4.7: TOF acceptance regions for primary hadrons produced with $|\theta - 90°| < 45°$, relative to the tilted-strip version of the detector (5 HIJING events): from top to bottom, for pions, kaons and protons.

Table 4.1: TPC and TOF acceptances (%) for primary particles produced in the $|\theta - 90°| < 45°$ region (5 HIJING events).

Detector	$\pi^{\pm}$	$K^{\pm}$	$p(\bar{p})$	All
TPC	75	42	81	72
Tilted-strip TOF (with holes)	41	20	41	39
Planar TOF (with holes)	44	22	44	42
Planar TOF (full coverage)	52	26	53	49

Table 4.1 gives the overall TOF acceptances for charged primaries produced in the $|\theta - 90°| < 45°$ region and, in particular, for different hadron species. Both detector versions (tilted-strip and planar) with holes for the HMPID and PHOS are considered. Most of the particles (94%, irrespective of the detector version) reaching the TOF barrel have TPC tracks. Conversely, if we consider the primary hadrons tracked in the TPC, only 54% hit the tilted-strip TOF-sensitive surface (58% for the planar geometry version). Their momentum and transverse momentum distributions are shown in Fig. 4.8, with and without the TOF requirement.

The corresponding ϕ and $cos(\theta)$ distributions for all primary particles are shown in Fig. 4.9 where the holes (for the HMPID and PHOS) and the longitudinal dead spaces in the TOF barrel are clearly evident. Let us recall that these dead spaces along z are absent in the real TOF detector design (see Chapter 3 and Section 4.2.2).

With a full coverage, planar geometry detector, i.e. without holes, the overall TOF acceptance for primaries tracked in the TPC increases by 18%. The TOF acceptance values corresponding to this version of the detector are again given in Table 4.1. The two versions of the planar TOF detector, with and without holes, are compared in Fig. 4.10 in terms of ϕ and $cos(\theta)$ distributions, for all primaries with TPC tracks.

It is also worth mentioning that a TOF barrel 40 *cm* shorter could be envisaged to ease the assembly and installation of the detector through the LHC pit in the ALICE experimental hall. Such a shortening could also meet the geometrical restrictions introduced by the TPC trigger and DAQ design [3], where tracks close to 45° polar angle would only be partially recorded. This would imply an acceptance loss of 5% for the tilted-strip detector with holes.

Finally, in Fig. 4.11, a comparison is made of the tilted-strip geometry with respect to the planar geometry (both with holes for HMPID and PHOS) using again the ϕ and $cos(\theta)$ distributions of primaries tracked in the TPC. The detector acceptance increases by 7% when using the planar geometry version. The reason is that, as already pointed out, the planar geometry detector does not include a realistic strip layout inside the modules but very large plates whose dead areas are obviously underestimated (in particular at the module borders, see Fig. 4.11). However, we will use this version for many other purposes, as we will see later on.

4.4.3 Incident angle studies

Due to the magnetic field, multiple scattering and energy loss, a charged primary track reaching the TOF surface at a given impact point, with ϕ_{TOF} and θ_{TOF} angles, deviates from a straight line connecting the vertex to the same impact point by the quantities: $\Delta\phi = \phi_{geom} - \phi_{TOF}$ and $\Delta\theta = \theta_{geom} - \theta_{TOF}$, where ϕ_{geom} and θ_{geom} are the angles relative to the straight line. The $\Delta\theta$ and $\Delta\phi$ distributions in Fig. 4.12 for primary particles show, as expected, the effect of the magnetic field in the plane transverse to the beam axis, namely on the $\Delta\phi$ distribution (while $\Delta\theta \approx 0$). Notice that only the first crossing point of a track

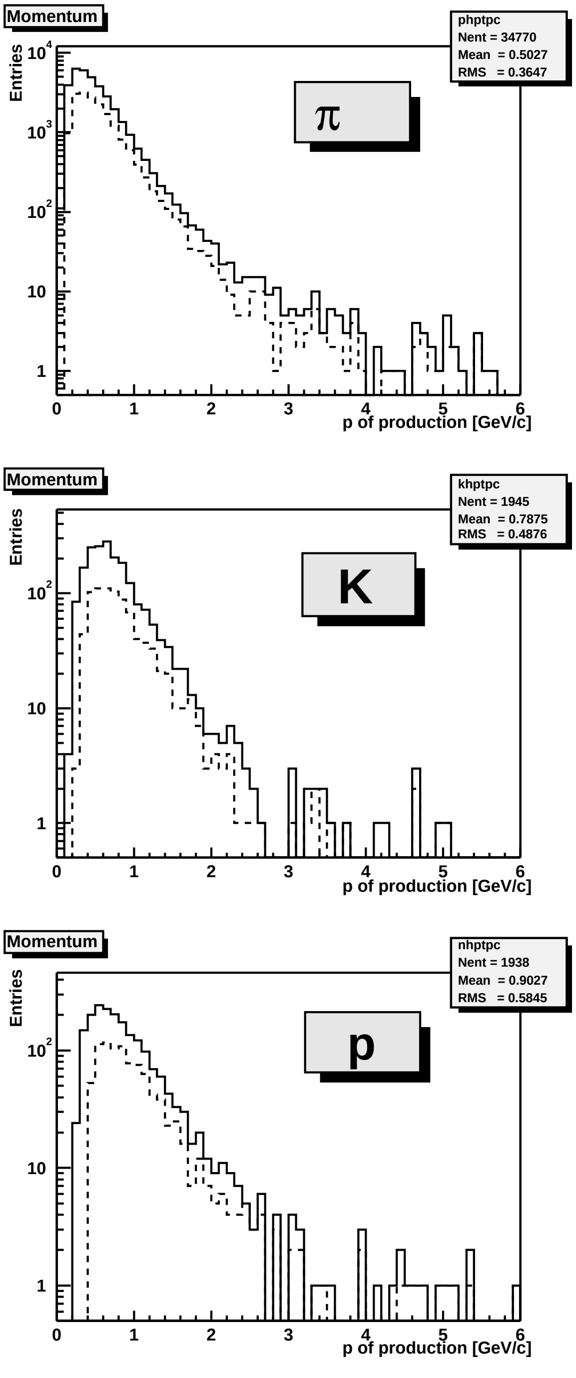

Figure 4.8: Momentum and transverse momentum spectra (HIJING) for charged primary hadrons tracked in the TPC (solid-line histograms); sumperimposed the same distributions for hadrons with TPC tracks and TOF hits (dashed-line histograms) in the tilted-strip detector version.

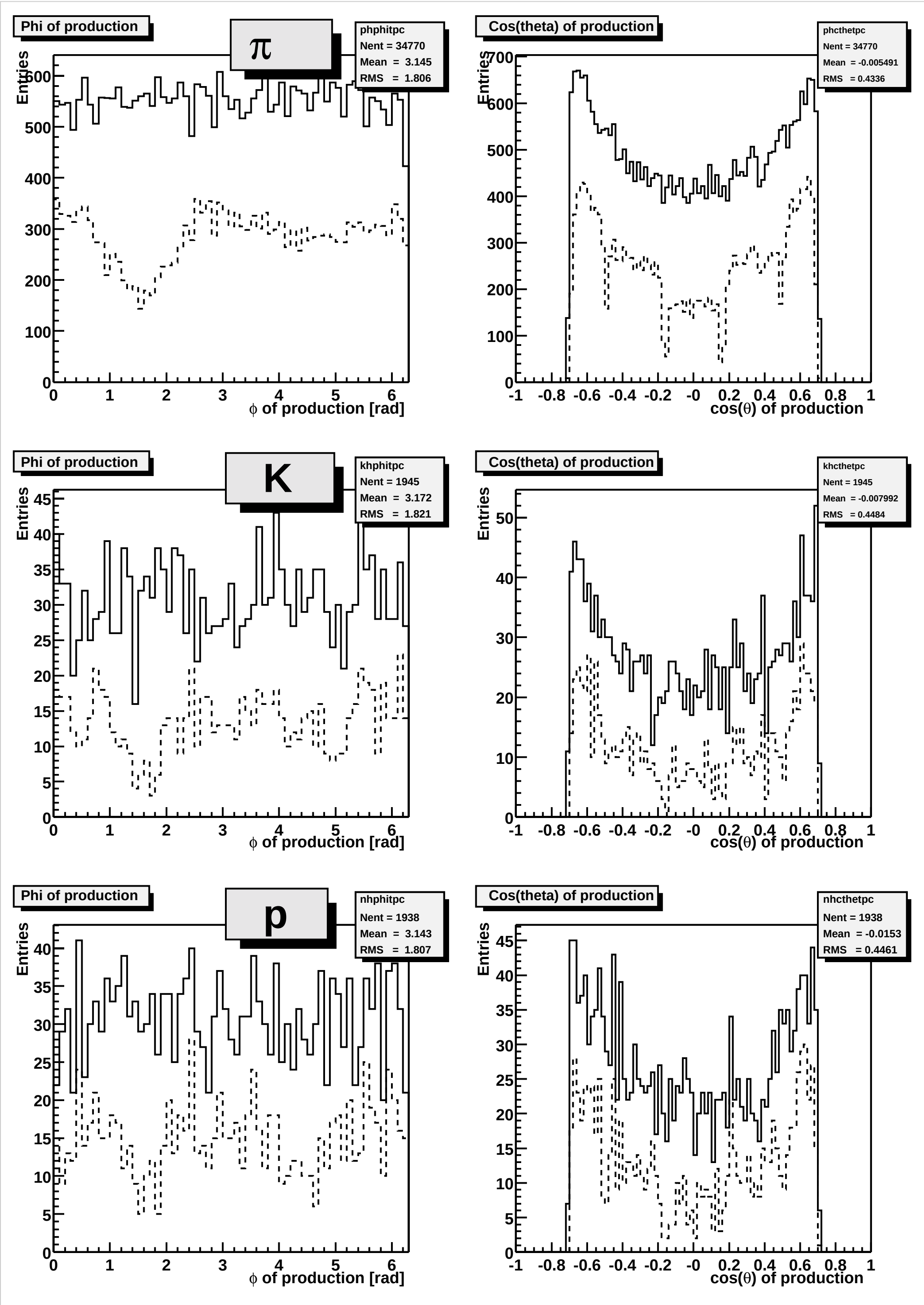

Figure 4.9: Azimuthal angle and polar angle cosine distributions (HIJING) for charged primary hadrons tracked in the TPC (solid-line histograms); sumperimposed the same distributions for hadrons with TPC tracks and TOF hits (dashed-line histograms) in the tilted-strip detector version.

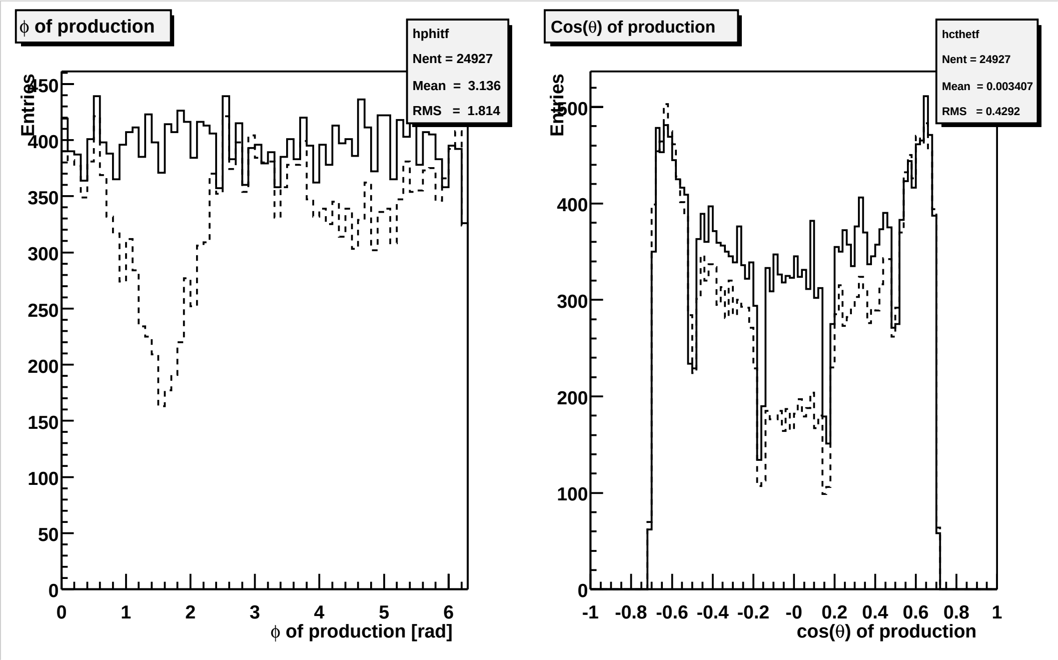

Figure 4.10: Azimuthal angle and polar angle cosine distributions (HIJING) for all charged primaries with TPC tracks and TOF hits in the planar detector version with different coverages (solid-line histograms: full coverage; dashed-line histograms: with holes for HMPID and PHOS).

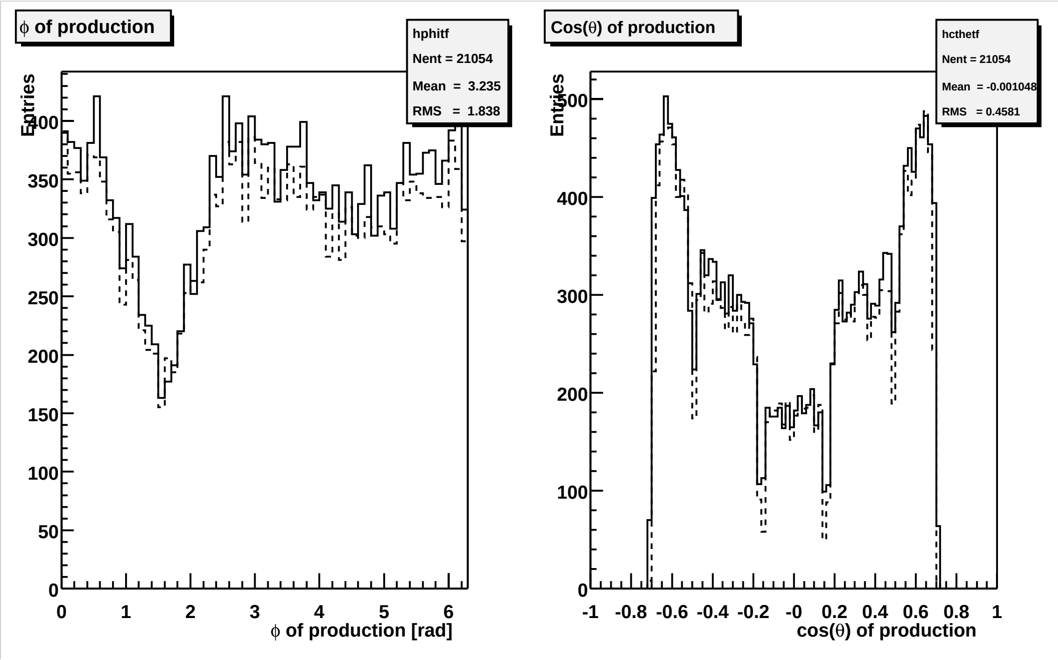

Figure 4.11: Azimuthal angle and polar angle cosine distributions (HIJING) for all charged primaries with TPC tracks and TOF hits in different detector versions (solid-line histograms: planar geometry; dashed-line histograms: tilted-strip geometry).

on the TOF surface is considered here as the track impact point (see Section 4.4.4).

Figure 4.12 was obtained using the TOF detector version with planar geometry. However, in any transverse plane, all the TOF pads are practically perpendicular to the straight lines defined above (i.e. radii), which is not the case in any longitudinal view.

Let us now consider the angular deviation $\Delta\alpha$ of an incident track direction, at a given impact point, with respect to the normal to the TOF pad at the same point. Figure 4.13 shows, for both planar and tilted-strip versions, the distributions of this angular deviation for primary particles, i.e. of their traversal angle through the TOF detector.

In the planar geometry, it clearly appears that most of the incident particle directions on the TOF pads deviate by a large $\Delta\alpha$ with respect to the perpendicular directions. The deviation increases with the z coordinate of the pad, to reach a value of 60° at the ends of the barrel. By tilting the strips as described in Section 4.2.2, the same $\Delta\alpha$ distributions in Fig. 4.13 show a substantial reduction of this undesired effect, with a peak at 10° for all z values.

4.4.4 Occupancy

In a single SHAKER event there are on the average $\sim$ 12000 primary charged particles in the $|\theta - 90^\circ| < 45^\circ$ central region. About 9000 (75%) of them have tracks in the TPC. There are in addition $\sim$ 2000 secondary charged particles (with $R_{vtx} < 50\ cm$) which also have TPC tracks.

Considering the planar geometry TOF detector, with holes for HMPID and PHOS, there are $\sim$ 20000 fired TOF pads (with 95% efficiency) and we have a TOF occupancy of 20000/150000 $\approx$ 13%.

Only 25% of them are fired by particles having TPC tracks in the first crossing of the TOF-sensitive surface. A further 40% are fired by particles without TPC tracks (in one or more crossings) as well as by particles with TPC tracks in their second, third, etc. crossings. We define the latter percentage of hits as noise from the central region (collectively produced by charged and neutral primaries). The contributions to the noise hits according to particle species are as follows: 71% are $e^\pm$, 16% are $\mu^\pm$, 10% are $\pi^\pm$, 3% are $p(\overline{p})$. Most of the $e^\pm$ noise originates from the TPC and TOF walls and from the TRD. These are also important sources of hadron noise. For hadrons the main production mechanism is due to hadronic interactions. For muons, to particle decays. For $e^\pm$ to photon conversions, δ-ray emissions and Compton scattering.

The rest of the fired pads, 35%, is hit by particles originating from the $|\theta - 90^\circ| > 45^\circ$ outer region. To estimate the number of TOF hits due to this outer region, a sample of charged and neutral primary particles has been generated in each of the forward and backward regions, using the HIJINGPARAM generator of AliRoot. There are additional TOF pads hit by the charged products (from decays, interactions, backscattering, etc.) of these primaries. The contributions to the noise hits from different particle species are as follows: 69% are $e^\pm$, 13% are $\pi^\pm$, 11% are $p(\overline{p})$, 7% are $\mu^\pm$. A large fraction of the $e^\pm$ background still originates from the TOF itself. These additional TOF hits, summing up to a total of $\sim$ 7000 per event, have been also taken into account.

The space and time distributions of the background hits from the outer region are shown in Fig. 4.14, still obtained with HIJINGPARAM and the planar geometry detector with holes (the statistics correspond here to 3 events). Due to the presence of the absorber of the ALICE Dimuon Forward Spectrometer [18], the z distribution of the hits on the TOF surface is asymmetric, with an excess in the backward region. The time spectrum of these hits has an exponential shape. Notice that this time corresponds to the particle time-of-flight as obtained by GEANT3 tracking. No detector time resolution is included at this level. The same space and time distributions, now obtained for the full coverage version of the planar geometry TOF detector, are shown in Fig. 4.15. We shall include the background hits from the outer region in our Monte Carlo simulations, using an approximately uniform z distribution on the TOF surface and an approximately exponential time distribution, i.e. $\sim \exp[-t(ns)/20]$.

Similar results can be obtained using HIJING full phase-space simulations. In Fig. 4.16, we show the distributions of the track multiplicity per fired pad for the tilted-strip TOF geometry, with holes for

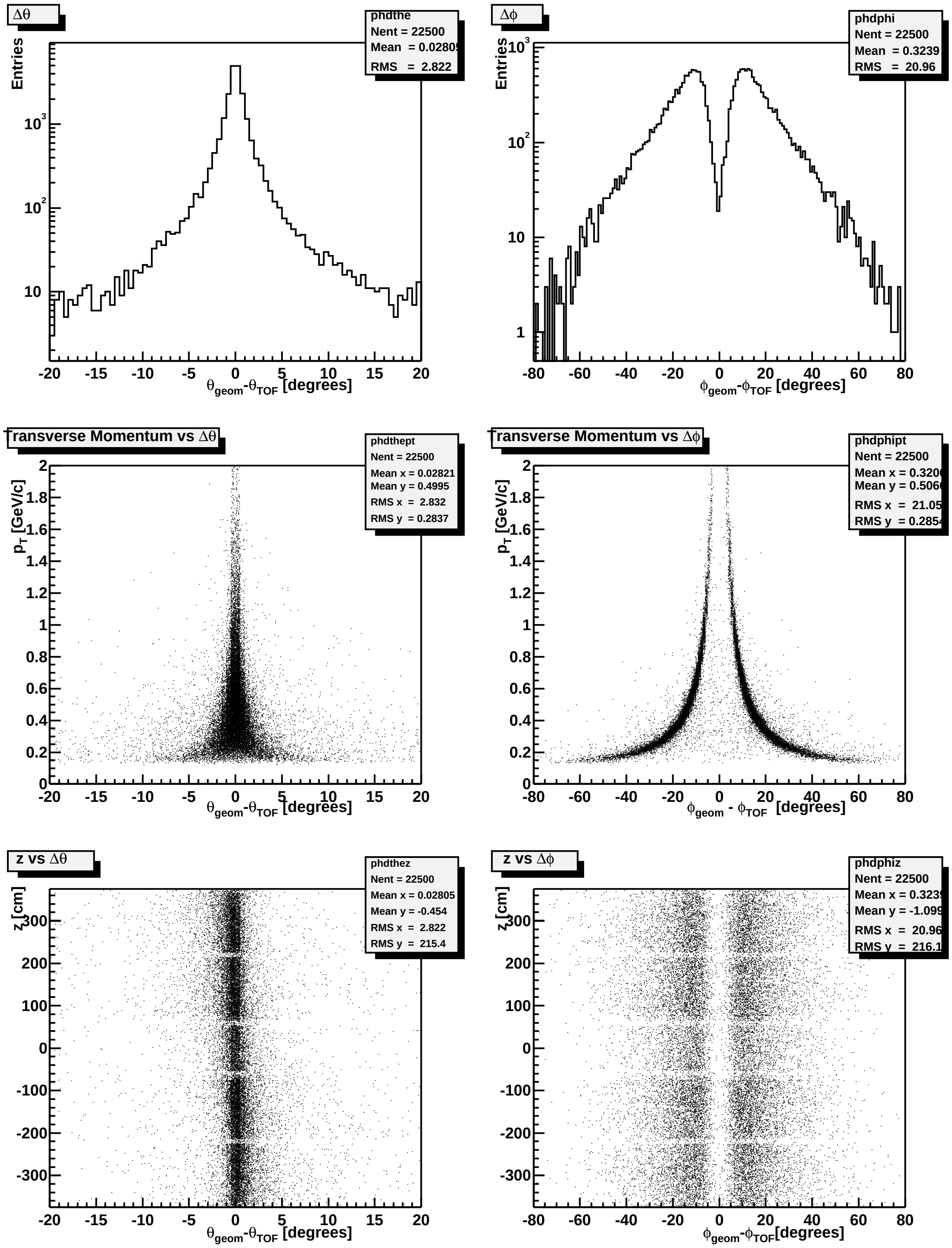

Figure 4.12: Distributions of Δθ (left column) and Δϕ (right column) angular deviations for primary particles from the $|\theta - 90°| < 45°$ region reaching the planar geometry TOF; the corresponding scatter plots as functions of p_t and z position on the TOF are also shown (5 HIJING events).

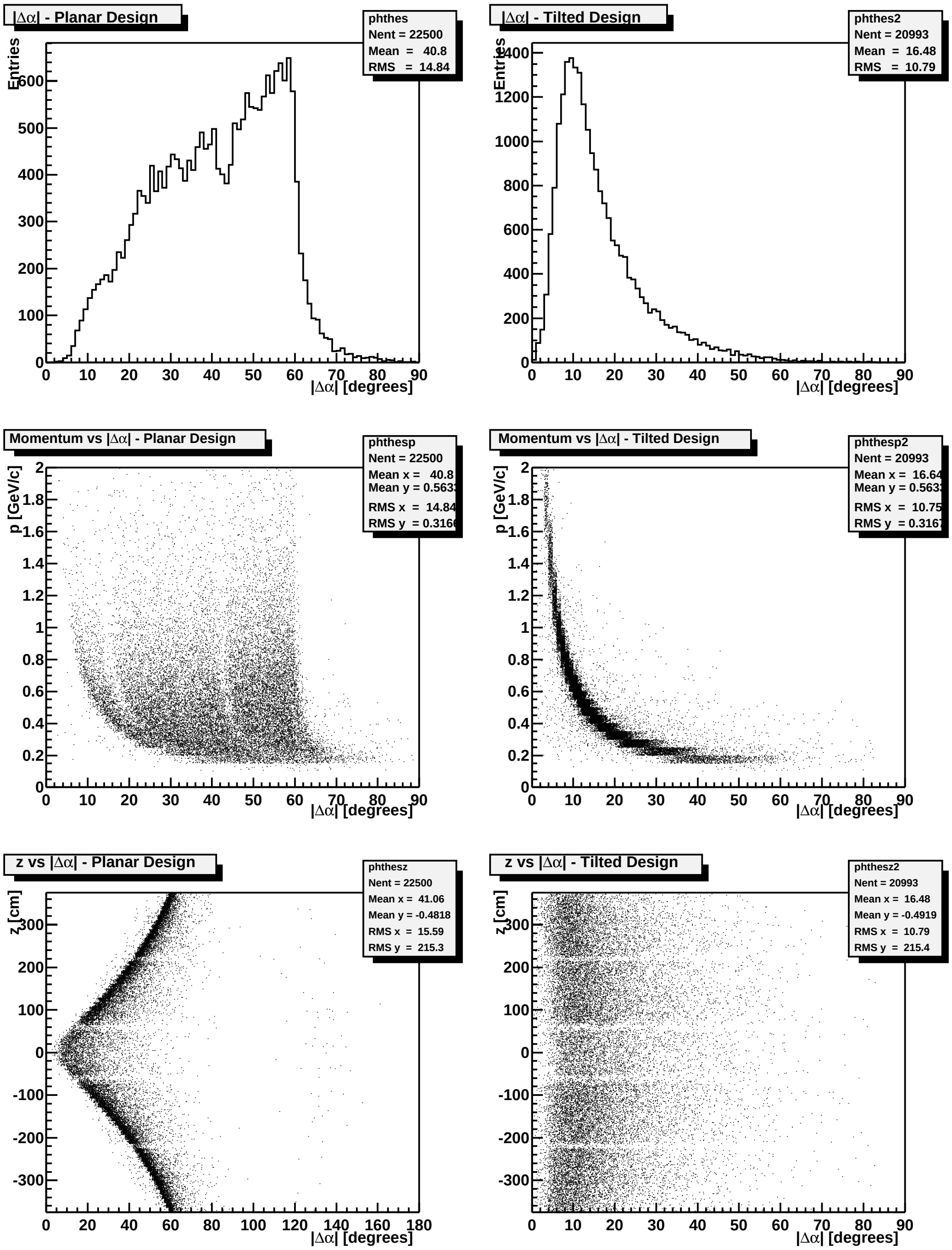

Figure 4.13: Distributions of $\Delta\alpha$ angular deviation (absolute value) for primary particles from the $|\theta - 90°| < 45°$ region reaching the TOF with planar (left column) and tilted-strip (right column) geometry; the corresponding scatter plots as functions of momentum and *z* position on the TOF are also shown (5 HIJING events).

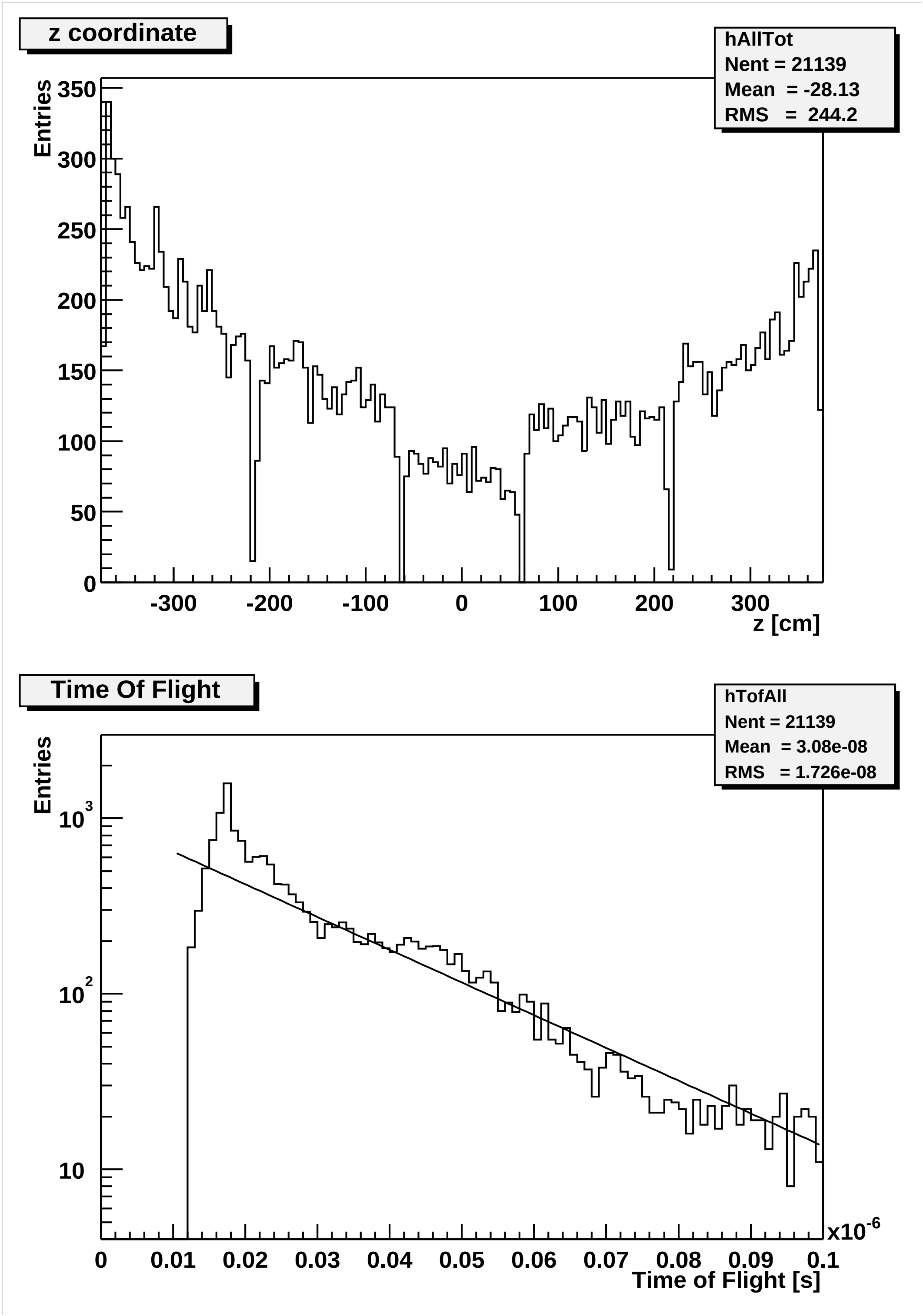

Figure 4.14: Longitudinal coordinate and time-of-flight distributions for hits produced in the planar geometry TOF, with holes for HMPID and PHOS, by particles generated in the forward and backward outer regions (HIJINGPARAM). The exp[-t(*ns*)/20] approximation of the time-of-flight spectrum is also shown.

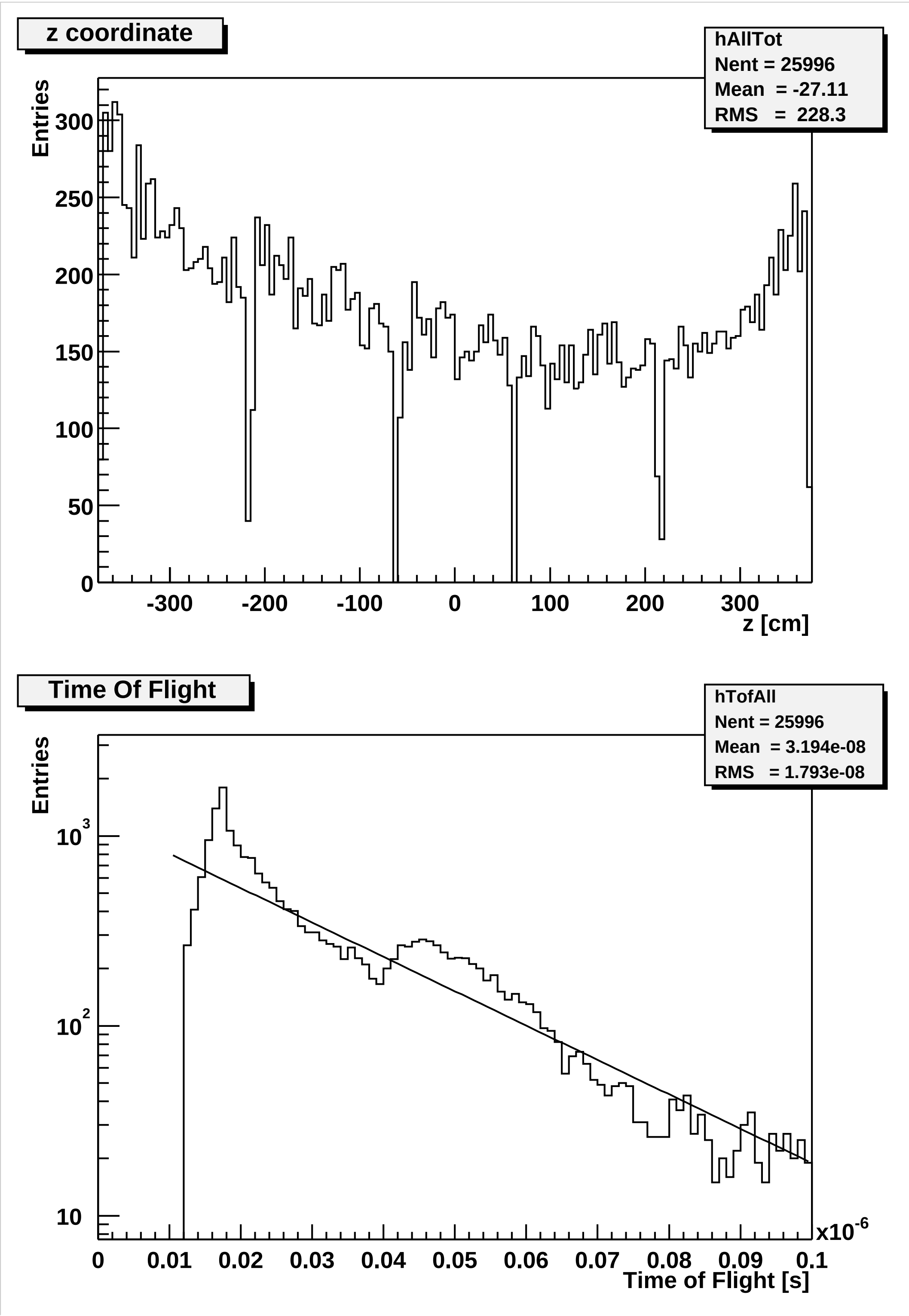

Figure 4.15: Same as Fig. 4.14 for the planar geometry TOF detector with full coverage.

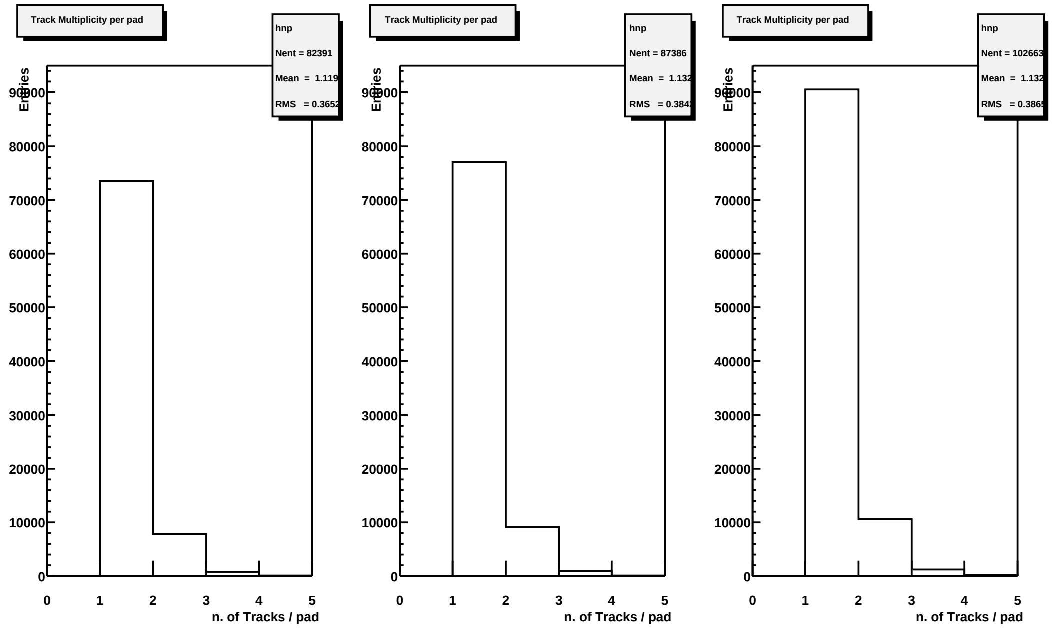

Figure 4.16: Track multiplicity per fired pad distributions: from left to right, for the tilted-strip TOF with HMPID and PHOS holes, for the planar TOF with holes and for the planar TOF without holes. All charged particles from the whole event are included (5 HIJING events).

HMPID and PHOS and, for the planar geometry, with and without holes. These distributions contain all the hits produced on the TOF surface by primary and non primary (i.e. background) charged particles present in the whole event. One can notice in Fig. 4.16 that the mean track multiplicity per pad is slightly lower for the tilted-strip (1.12) than for the planar (1.13) TOF detector with holes. It remains unvaried in case of full coverage. These mean values are consistent with the above quoted detector occupancy.

In Fig. 4.17 the distribution of the number of crossing points per track is shown, also as a function of momentum, separately for all primary and non primary particles in the tilted-strip TOF detector. Low momentum particles, which are more abundant in the non primary sample, give rise, as expected, to multiple crossings of the TOF surface. The corresponding maps of TOF crossing points for primary and non primary particles are shown in Fig. 4.18.

4.4.5 Time-of-flight spectra

The time spectra of the TOF hits from all the particles generated with HIJING in the $|\theta - 90^\circ| < 45^\circ$ central region are shown in Fig. 4.19, separately for primary and non primary particles. The planar geometry TOF with holes for HMPID and PHOS is again used here. The primaries must have TPC tracks and the time-of-flight distribution shown is relative to their first crossing of the TOF surface. This is the time-of-flight spectrum that will be used in the PID procedure, as it will be described later on. For the non primaries, we consider here successive crossings of primary particles with or without TPC tracks and the hits produced by all secondaries from decays or interactions.

4.5 Track matching

In what follows, unless mentioned otherwise, the TOF detector layout with planar geometry and holes at 90° for the HMPID and PHOS detectors has been considered (see Section 4.2.2), the SHAKER event generator has been used with standard input parameters (see Section 4.3.2) and the background from

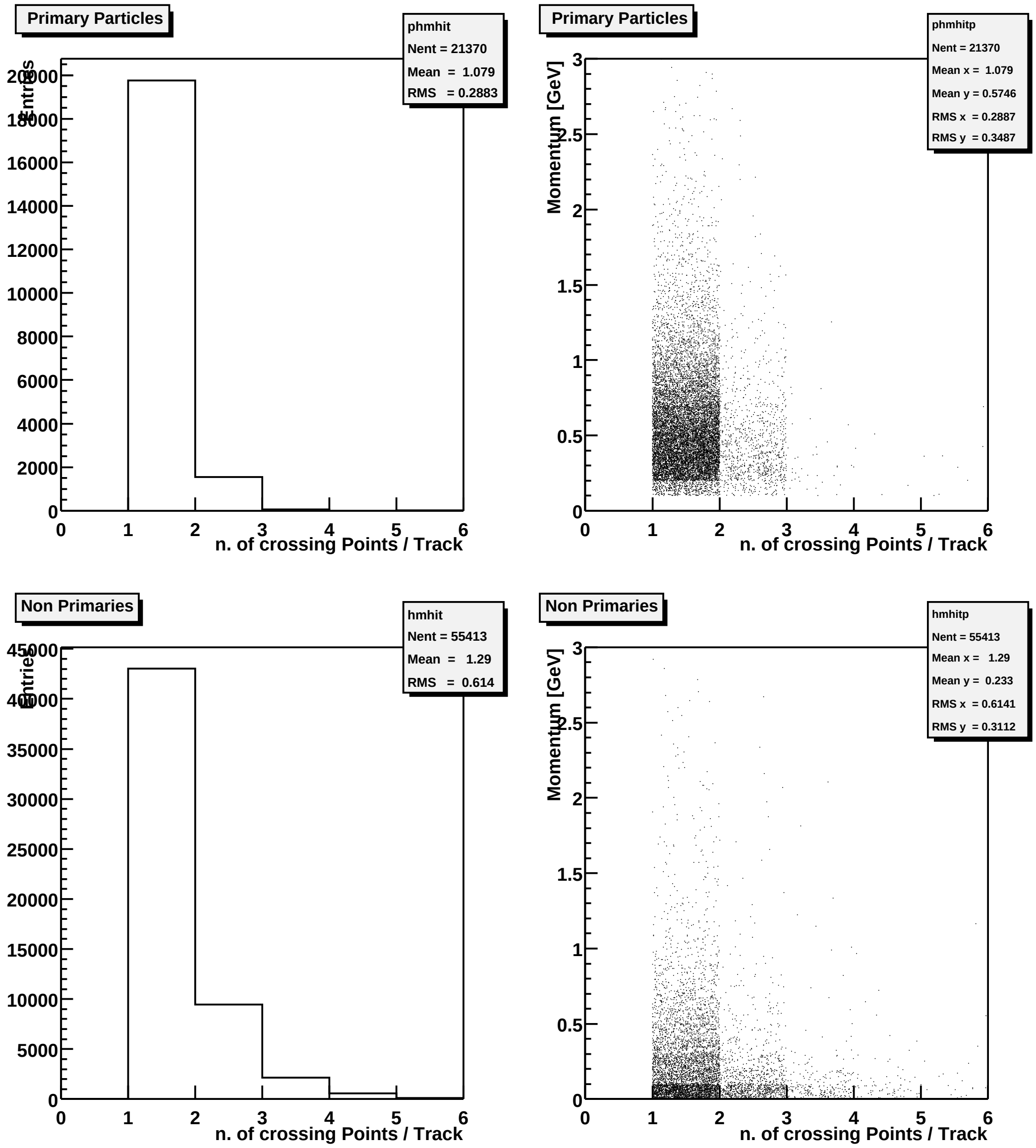

Figure 4.17: Distributions of the crossing point multiplicity per track, also shown as functions of momentum, in the tilted-strip TOF detector with HMPID and PHOS holes for all primary (upper row) and non primary (lower row) particles produced in the whole phase-space (5 HIJING events).

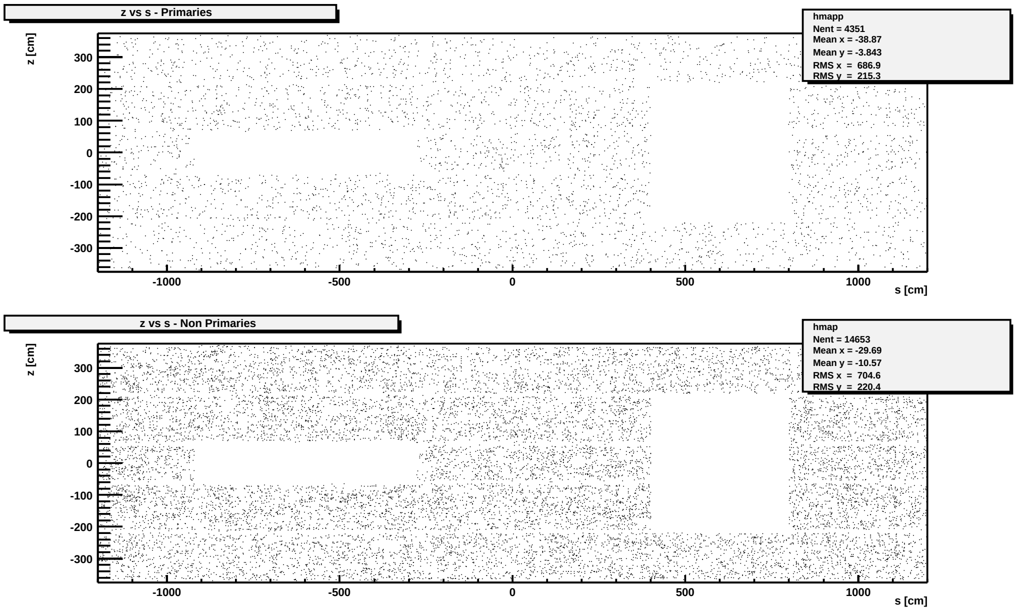

Figure 4.18: Crossing point maps relative to the tilted-strip TOF detector with HMPID and PHOS holes, for all primary (upper plot) and non primary (lower plot) particles produced in a single, full phase-space HIJING event. The maps are shown as z (longitudinal coordinate) versus s (transverse curvilinear coordinate) plots.

both the central and outer regions have been included (see Section 4.4.4). No interpad dead space or edge effects have been considered.

4.5.1 Matching with TPC tracks

It is interesting to consider, in a qualitative way, the factors influencing the matching of tracks extrapolated from the TPC to the TOF with the corresponding fired TOF pad. This is a long distance extrapolation, from the TPC outer layer at 2.5 m radius up to the TOF surface at 3.7 m. Let us assume that the hit point (first crossing) of a track on the TOF-sensitive surface could be exactly determined, i.e. without multiple scattering or any other source of extrapolation uncertainty from the TPC to the TOF. Let us call this point an ”ideal” hit point. On the other hand, if we consider the realistic tracking of a particle from the TPC to the TOF, as performed by GEANT3, we obtain a ”real” hit point (more than one in case of multiple crossing). The success of the track matching depends then on the ratio $<\Delta R>/<R_{min}>$, where ΔR is the deviation of the real hit point (first crossing) of a track from the corresponding ideal hit and R_{min} the minimum distance of this real hit with respect to all the other real ones (first or successive crossings) present on the TOF surface. ΔR is mainly determined by the multiple scattering on the outer wall of the TPC while R_{min} depends on the particle and noise density on the TOF barrel, i.e. on the occupancy. The lower the ratio, the better will be the matching efficiency.

Figure 4.20 shows the R_{min} and ΔR distributions in one SHAKER event. The narrow peak at $R_{min} \approx 0$ corresponds to δ-ray background. The fraction of tracks with $\Delta R > R_{min}$ is equal to 26%. Without the TRD in between the TPC and the TOF, this fraction decreases to 21%.

Let us describe the matching algorithm used in our simulation. All TPC tracks are ordered according to their transverse momentum. Starting from the highest p_t track, for each track, a statistically significant sample of probe tracks is generated and tracked in the magnetic field from the TPC (i.e. from the hit in the last TPC pad row) to the TOF. These probe tracks deviate from our track in the last TPC hit point according to a Gaussian distribution with standard deviation given by θ^{rms}_{plane}, the mean deflection angle

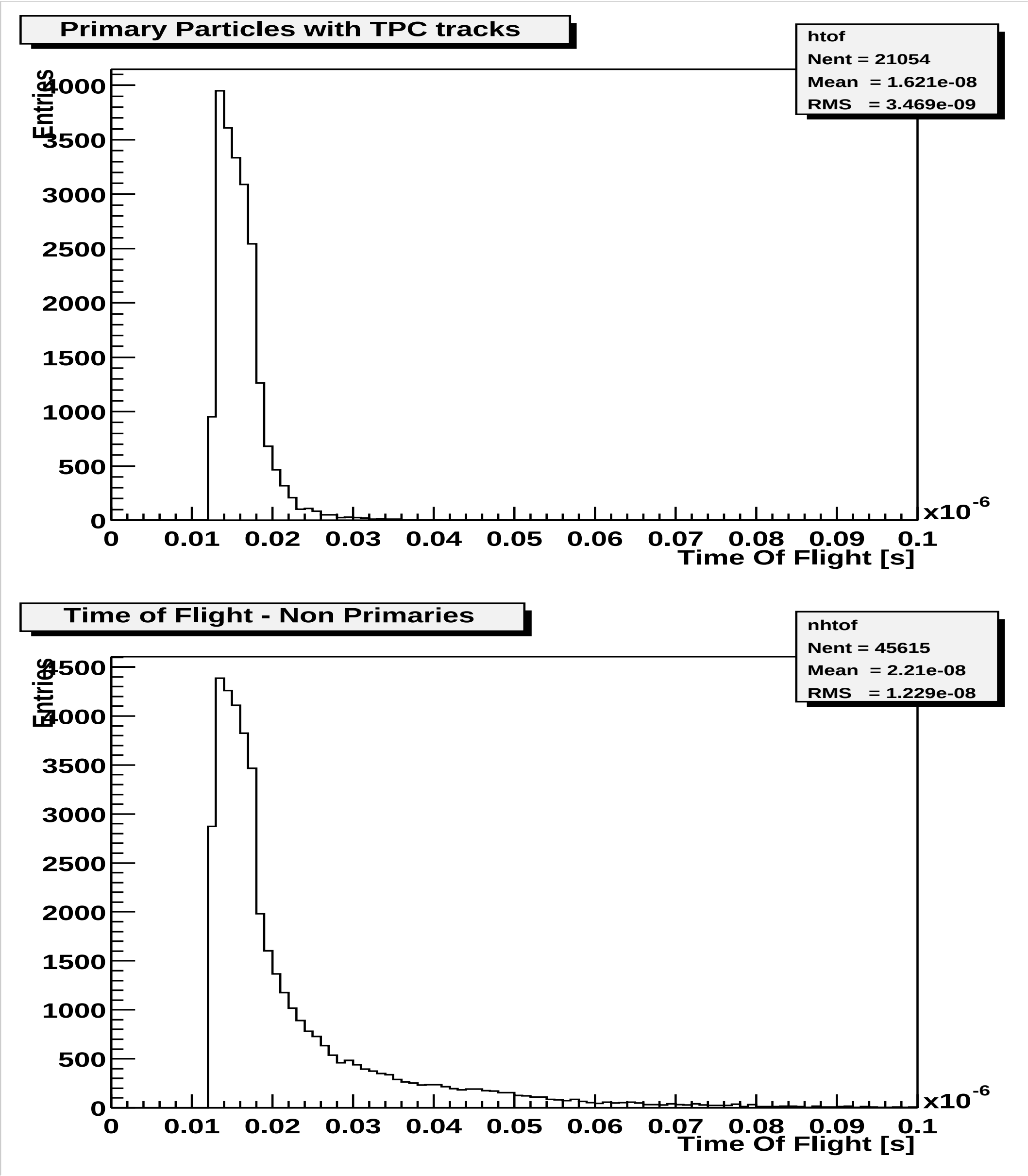

Figure 4.19: Time-of-flight distributions for primary particles with TPC tracks and for non primary particles, all produced in the $|\theta - 90^\circ| < 45^\circ$ region and reaching the planar geometry TOF with holes for HMPID and PHOS (5 HIJING events).

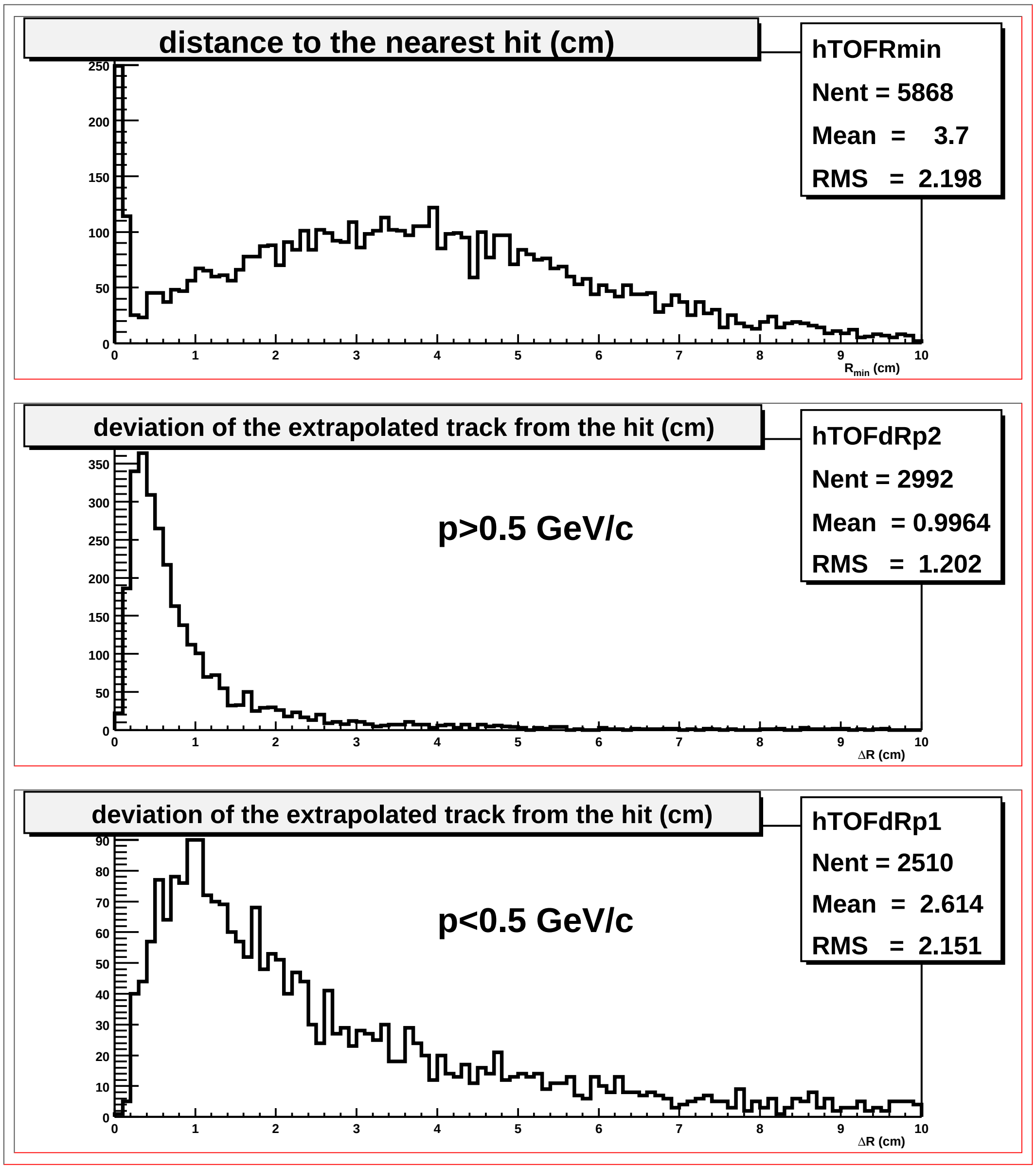

Figure 4.20: R_{min} and ΔR distributions for one SHAKER event.

due to multiple scattering in the outer wall of the TPC[2]. Every probe track can cross a TOF pad or a TOF dead region and be assigned a weighting contribution: ε_{eff} if the sensitive pad hit is fired (i.e. if the pad has given a time signal), $1-\varepsilon_{eff}$ if the sensitive pad hit is not fired, 1 if an insensitive region is hit. Thus, for a given TPC track, we have a set of TOF pads and TOF dead regions crossed by the probe tracks. For each TOF element (sensitive pad or dead region) a weight is defined as the sum of the weighting contributions from all the probe tracks that cross it. The element with the largest weight is chosen to be the match for the track. Notice that this match is a first crossing match on the TOF surface, for each track.

Although the TRD is foreseen as a detector with some tracking capability, this has not been taken into account in the present matching algorithm.

4.5.2 Matching efficiency and contamination

Let us introduce some definitions used in the matching analysis [19], [20]. Given N tracks matched with the TOF system, these are subdivided into two sets: mismatched tracks, N_{mis}, and well matched ones, N_{match}, with

$$N = N_{mis} + N_{match}.$$

A mismatched track is a track to which we cannot unambiguously attribute a time-of-flight value. This set of tracks can be presented as follows:

$$N_{mis} = N_0 + N_2,$$

where N_0 includes the cases when the TOF pad corresponding to the track is not fired or when the track is matched with a TOF dead region; N_2 is the number of tracks for which the fired pad was matched to more than one track. Physical reasons for the presence of set N_0 are related to the intrinsic inefficiency of the pad (5%), the extension of the TOF dead region (10%) and the possibility of particle decays between the TPC and the TOF. For the well matched tracks, one can distinguish between those matched with true time, N_t, and those matched with wrong time, N_w, with

$$N_{match} = N_t + N_w.$$

The wrong time assignment corresponds to the matching of the extrapolated track with a pad fired by another particle, mostly due to noise from the central or outer regions (see Section 4.4.4). The true time assignment corresponds to the correct matching of the extrapolated track with the pad it has actually fired. The percentage abundance of the various sets for primary particles matched with the TOF, with or without the TRD, is reported in Table 4.2.

Table 4.2: Subsets (%) of primary particles matched with the TOF, as specified in the text (25 SHAKER events).

TOF detector	N_0	N_2	N_t	N_w
with TRD	24	4	45	27
without TRD	22	4	55	19

The matching procedure can be evaluated in terms of efficiency and contamination. These are defined as follows:

$$efficiency = \frac{N_t}{N}$$

$$contamination = \frac{N_w}{N_{match}}.$$

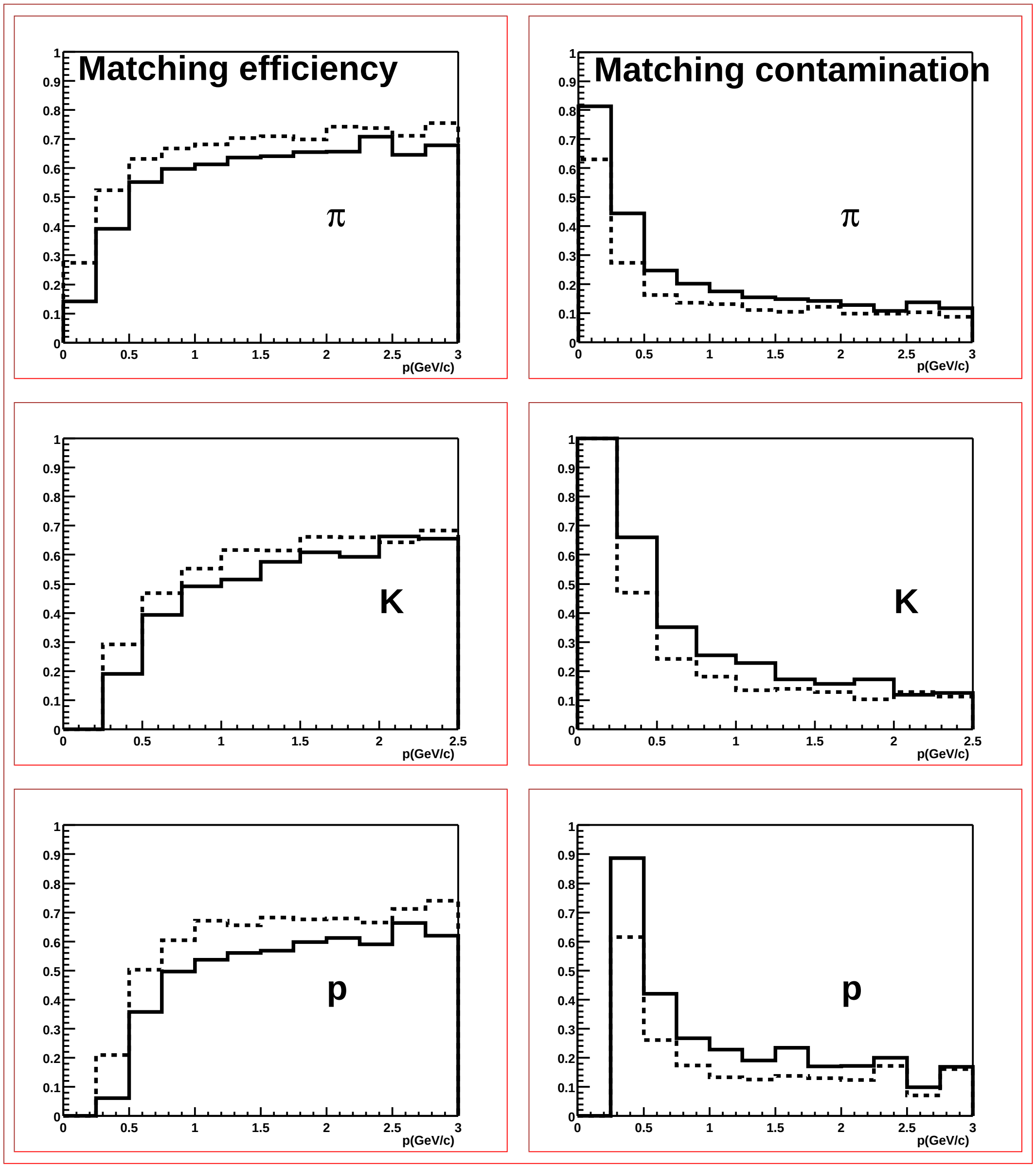

Figure 4.21: The momentum dependence of the efficiency (left column) and contamination (right column) of the TOF matching procedure (solid-line histograms: with TRD; dashed-line histograms: without TRD) for primary particles of different species originally generated in the $|\theta - 90°| < 45°$ region (25 SHAKER events).

The momentum dependence of our matching results is presented in Fig. 4.21, with and without the TRD.

In Figs. 4.22 (with TRD) and 4.23 (without TRD) the acceptances relative to the various steps of the matching procedure, for primary particles of different species originally generated in the $|\theta - 90°| < 45°$ central region, are reported as a function of momentum, together with the original particle momentum spectra. The acceptances concern: first, the particle tracking in the TPC, then their extrapolation to the TOF surface and, finally, their correct matching to TOF pads (with true time). The corresponding percentual losses are also indicated in these figures: the loss ”without TPC tracks”, referring to particles not fulfilling the TPC track requirements, entering the TPC dead space or decaying before or inside the TPC. The loss ”out of geometry”, refers to extrapolated TPC tracks missing the TOF surface[3]. The loss ”without/wrong time”, refers to the above defined sets $N_0 + N_2$ (”without”) and N_w (”wrong”) and finally, the percentage ”with true time”, refers to the residual set N_t.

The same acceptances, when considering a full coverage TOF detector version with planar geometry, are shown in Fig. 4.24 where it appears that the percentage of tracks ”with true time” increases by $\sim 20\%$ with respect to the TOF detector version with holes for HMPID and PHOS (see Fig. 4.22).

The results are summarized in Table 4.3, showing that the TOF acceptance for TPC extrapolated and well matched primary tracks is obviously affected by the presence of the TRD. However the acceptance loss caused by particle absorption/interaction and multiple scattering in the TRD would be totally compensated in case of full coverage.

Table 4.3: TOF acceptances (%) of primary hadrons ”with true time” after TPC-TOF matching (25 SHAKER events).

TOF detector	$\pi^{\pm}$	$K^{\pm}$	$p(\bar{p})$
with HMPID and PHOS holes (with TRD)	28	17	31
with HMPID and PHOS holes (without TRD)	34	20	39
full coverage (with TRD)	33	21	37

4.5.3 Factors affecting the matching efficiency

Pad shape

In previous studies [19], [20] it was proven that, in a planar pad configuration where the longer dimension of the pad is transverse to the beam axis,the TOF matching results are better for square pads than for rectangular ones. This is also true in our present simulations, as shown in Fig. 4.25, where the results for different pad shapes of equal area, i.e. $3 \times 3\ cm^2$ and $1 \times 9\ cm^2$, are presented. However the spatial and angular errors for track reconstruction in the TPC were not considered. As we will see later on, these are expected to be larger in the longitudinal direction. Therefore further studies are needed to better understand if, in a tilted-strip geometry, rectangular pads oriented differently (i.e. with their longer dimension parallel to the beam axis) could improve the results once the TPC uncertainties are taken into account. In this respect, the influence of tracking implementation in the TRD should also be studied.

---

[2] Here the pion mass is assumed for all tracks.

[3] Here, only the TOF coverage (with holes for HMPID and PHOS) is taken into account. TOF dead regions and particle decays or interactions between the TPC and TOF are ignored at this stage. The TOF matching procedure concerns the remaining percentage of extrapolated TPC tracks hitting the TOF surface (corresponding to the above defined set N).

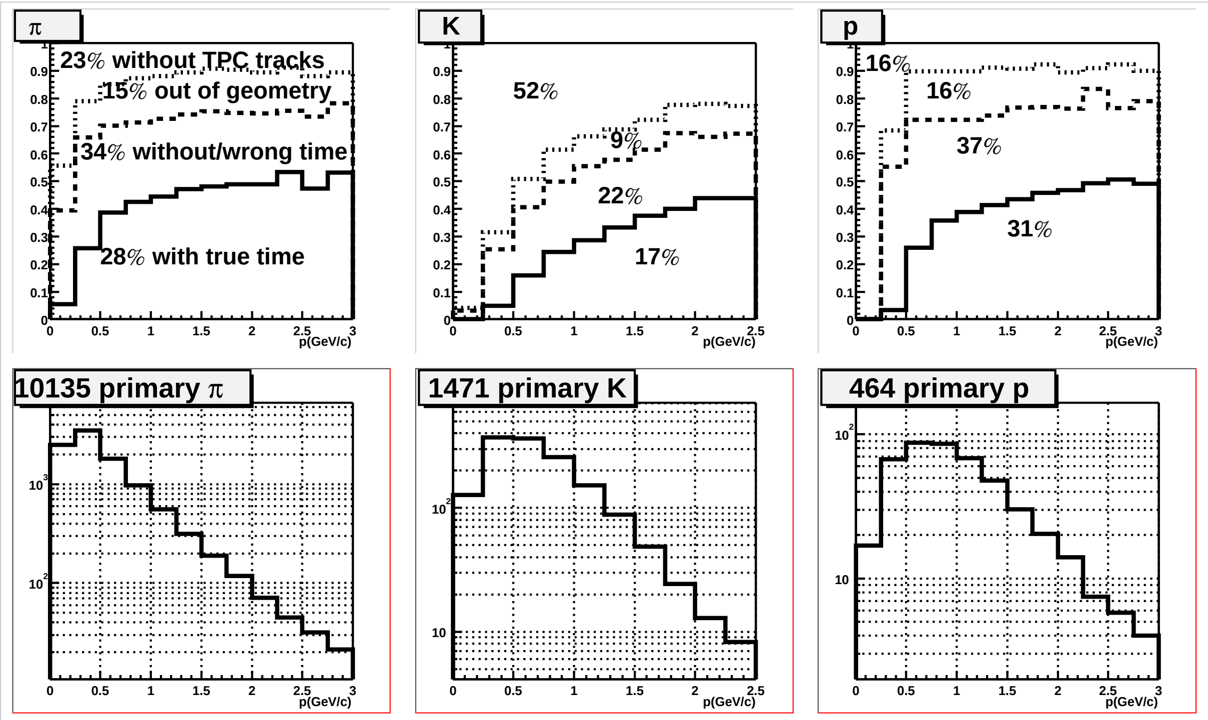

Figure 4.22: Acceptances of primary particles of different species, as functions of momentum, for: tracking in the TPC (dotted-line histograms), extrapolation to the TOF surface (dashed-line histograms), correct matching with TOF pads (solid-line histograms). The momentum spectra (lower histograms) refer to the primary particles originally generated in the $|\theta - 90°| < 45°$ region (25 SHAKER events).

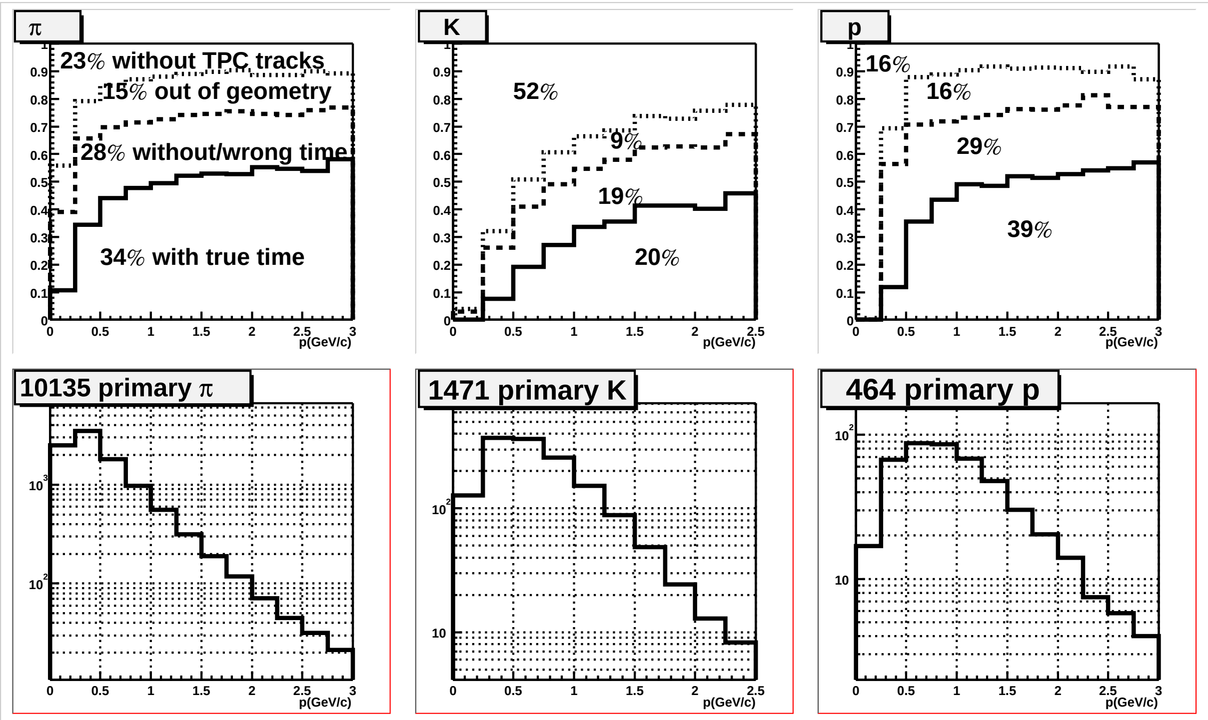

Figure 4.23: Same as Fig. 4.22 but without the TRD.

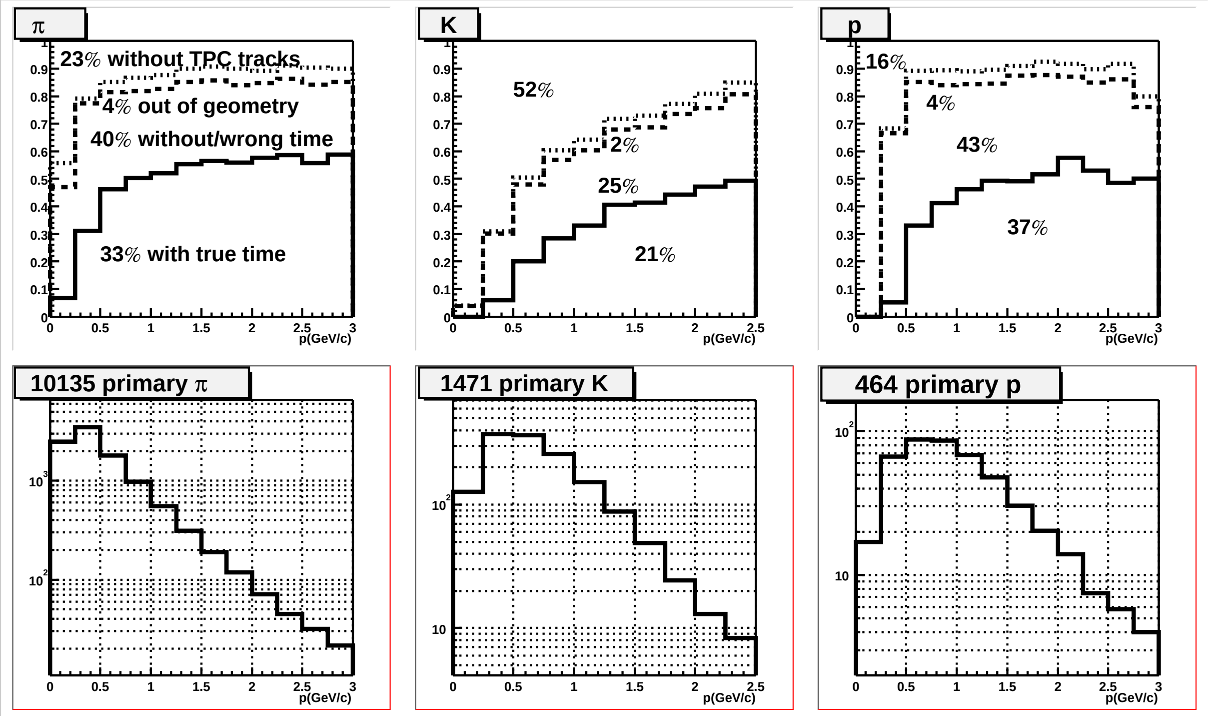

Figure 4.24: Same as Fig. 4.22 for a full coverage TOF detector.

Occupancy

To study the sensitivity of the matching results with respect to the occupancy of the TOF detector, simulations have been made with square pads of different dimensions. The larger the pad size is, the larger the occupancy will obviously be. The matching results have been compared for three increasing pad sizes: $3\times3\ cm^2$, $4\times4\ cm^2$ and $5\times5\ cm^2$, corresponding to the occupancy values: 13%, 23% and 33%, respectively, for $dN_{ch}/dy = 8000$. As the pad size increases, the matching efficiency and contamination undergo a slow deterioration (slower for the efficiency than for the contamination). This is not surprising since our TPC-TOF matching is dominated by spatial dispersion, due to multiple scattering (see Fig. 4.20), when the TPC tracks are extrapolated over a long distance up to the TOF. Hence the occupancy becomes a relatively less critical parameter.

Using another approach, 25 SHAKER events have been generated at a lower charged particle density, i.e. $dN_{ch}/dy = 4000$. Also the background from the outer region has been reduced by a factor of two. Due to the lower density of hits on the TOF surface, the fraction of tracks with $\Delta R > R_{min}$ is lower, 20% instead of 26%. This results as a whole in a 3% higher efficiency and a 9% lower contamination. A detailed study of the influence of the occupancy on the track matching can be also found in [19].

Further studies will be performed to evaluate how edge effects between adjacent pads would increase the occupancy. As already pointed out, no interpad dead space was considered in our simulations since a particle between two pads will induce a signal on one pad, or sometimes on both. This could also happen for particles hitting pads very close to their edges. Hence a detailed quantitative estimate of these additional contributions to the overall detector occupancy will be shortly provided. As far as the electronics crosstalk between pads is concerned, this is expected to give a negligible contribution.

Finally, here as well, the role of TRD tracking should be investigated.

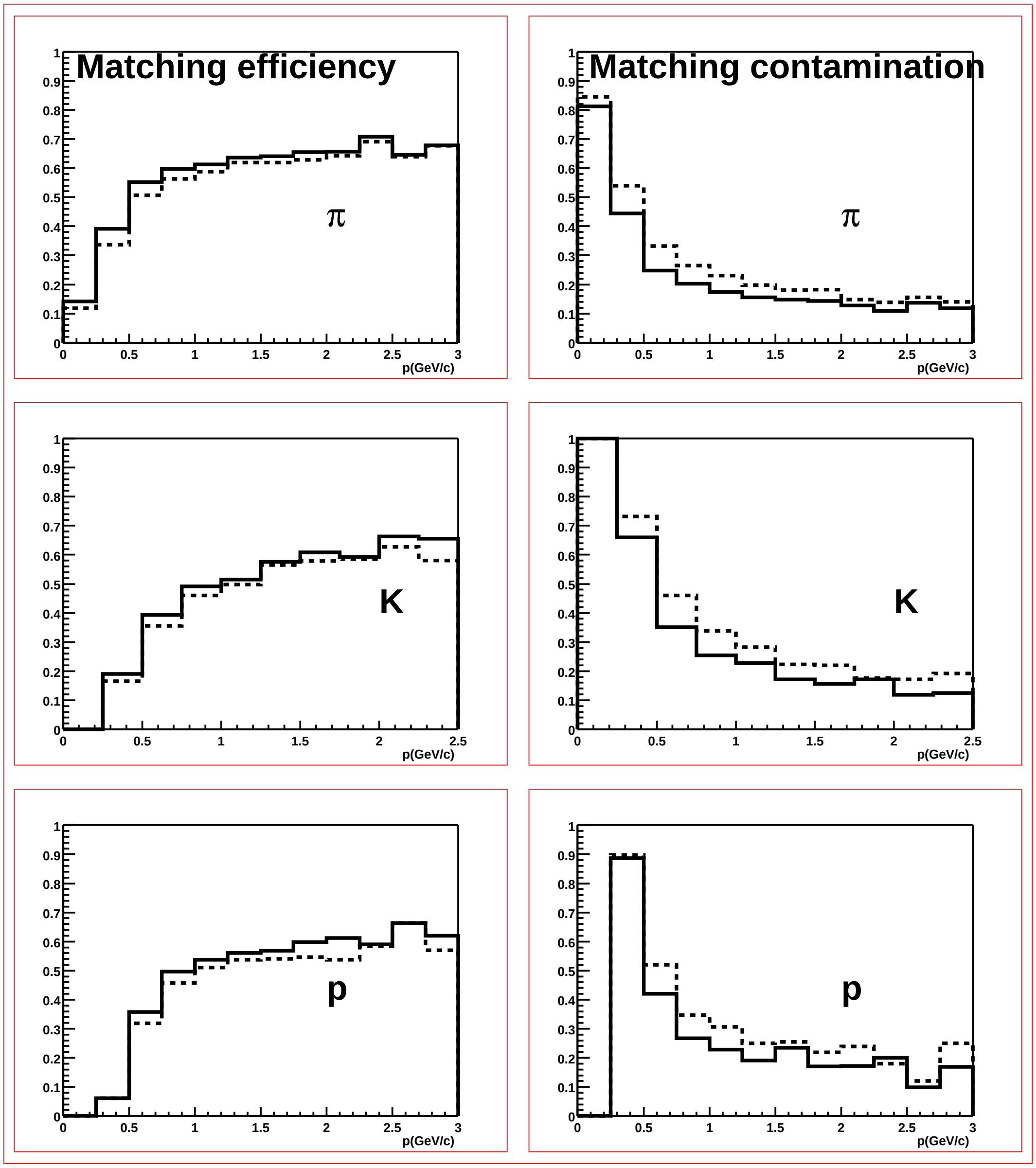

Figure 4.25: The momentum dependence of the efficiency (left column) and contamination (right column) of the TOF matching procedure (solid-line histograms: with 3×3 cm^2 pad size; dashed-line histograms: with 1×9 cm^2 pad size) for primary particles of different species originally generated in the $|\theta - 90°| < 45°$ region (25 SHAKER events).

Tracking error

A detailed study of the TPC tracking performance and track reconstruction capability in a very high multiplicity environment can be found in [3]. We shall use the following inputs for the momentum and space errors at the outer wall of the TPC [21]:

- $\sigma_\phi = 5$ *mrad*
- $\sigma_\theta = 3.5$ *mrad*
- $\sigma_p/p = 1.9\%$
- $\sigma_z = 0.44$ *mm*
- $\sigma_{r_\phi} = 0.23$ *mm*.

These uncertainties give rise to additional deviations of the extrapolated tracks from the ideal hits on the TOF surface (see Section 4.5.1) and the fraction of tracks with $\Delta R > R_{min}$ becomes obviously larger, 29% instead of 26%. This implies a lower efficiency and a higher contamination. The momentum dependence of the matching results in these conditions is presented in Fig. 4.26.

4.6 Particle identification (PID)

As already discussed in Chapter 1, the performance of a TOF system for particle identification does not only depend on the intrinsic timing resolution of the detector, but on the whole system resolution. The particle mass resolution, at relatively high momenta, is predominantly affected by the errors in the time-of-flight and track length measurements, rather than by the error on the momentum determination. Other evident parameters influencing the mass resolution are related to the electronics (errors due to the TDC time digitisation, to the event start time, to the amplification/discrimination circuits, to the time signal distribution, etc.) and to the online/offline calibrations and corrections (pad-to-pad relative timing, time versus amplitude corrections, etc.). In our design, we estimated the different contributions to the system TOF resolution to be:

- track length error (30 *ps*);
- momentum error (20 *ps*);
- overall TDC digitisation error (40 *ps*);
- T0 start signal error (50 *ps*);
- additional electronics error (50 *ps*);
- calibration/correction error (50 *ps*).

Taking into account the intrinsic TOF detector resolution ($\lesssim 100$ *ps*) we obtain an overall system resolution of approximately 150 *ps*, as anticipated in Section 4.4. Thus we smear the time of each pad according to this number.

4.6.1 PID procedure

All TPC reconstructed and TOF matched primary particles are entered in a momentum versus mass plot as shown in Fig. 4.27. Negative mass values correspond to negative square root arguments in the mass determination formula $m = p(t^2/l^2 - 1)^{1/2}$, p, t and l being the particle momentum, time-of-flight and

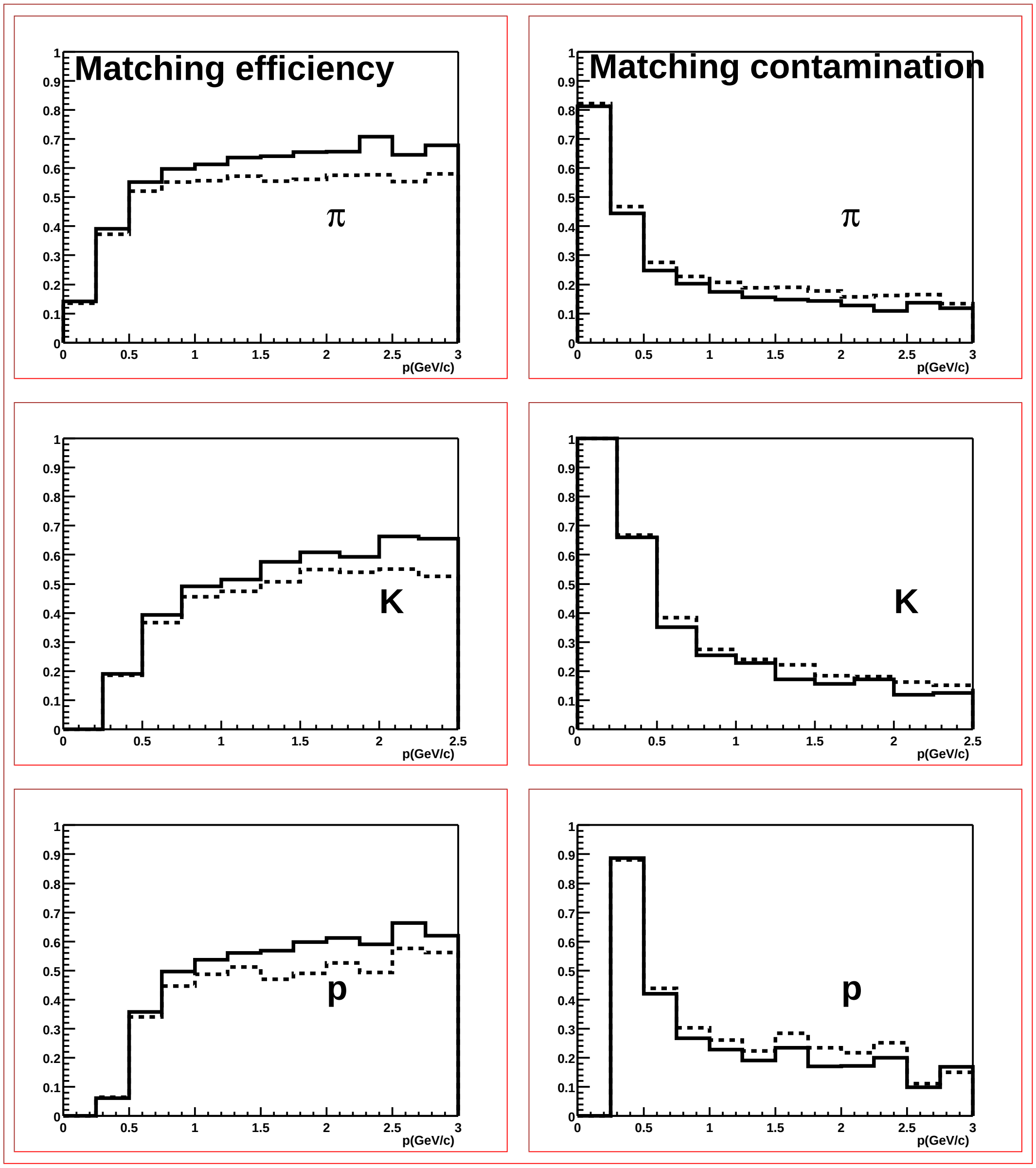

Figure 4.26: The momentum dependence of the efficiency (left column) and contamination (right column) of the TOF matching procedure (solid/dashed-line histograms: without/with TPC tracking errors) for primary particles of different species originally generated in the $|\theta - 90°| < 45°$ region (25 SHAKER events).

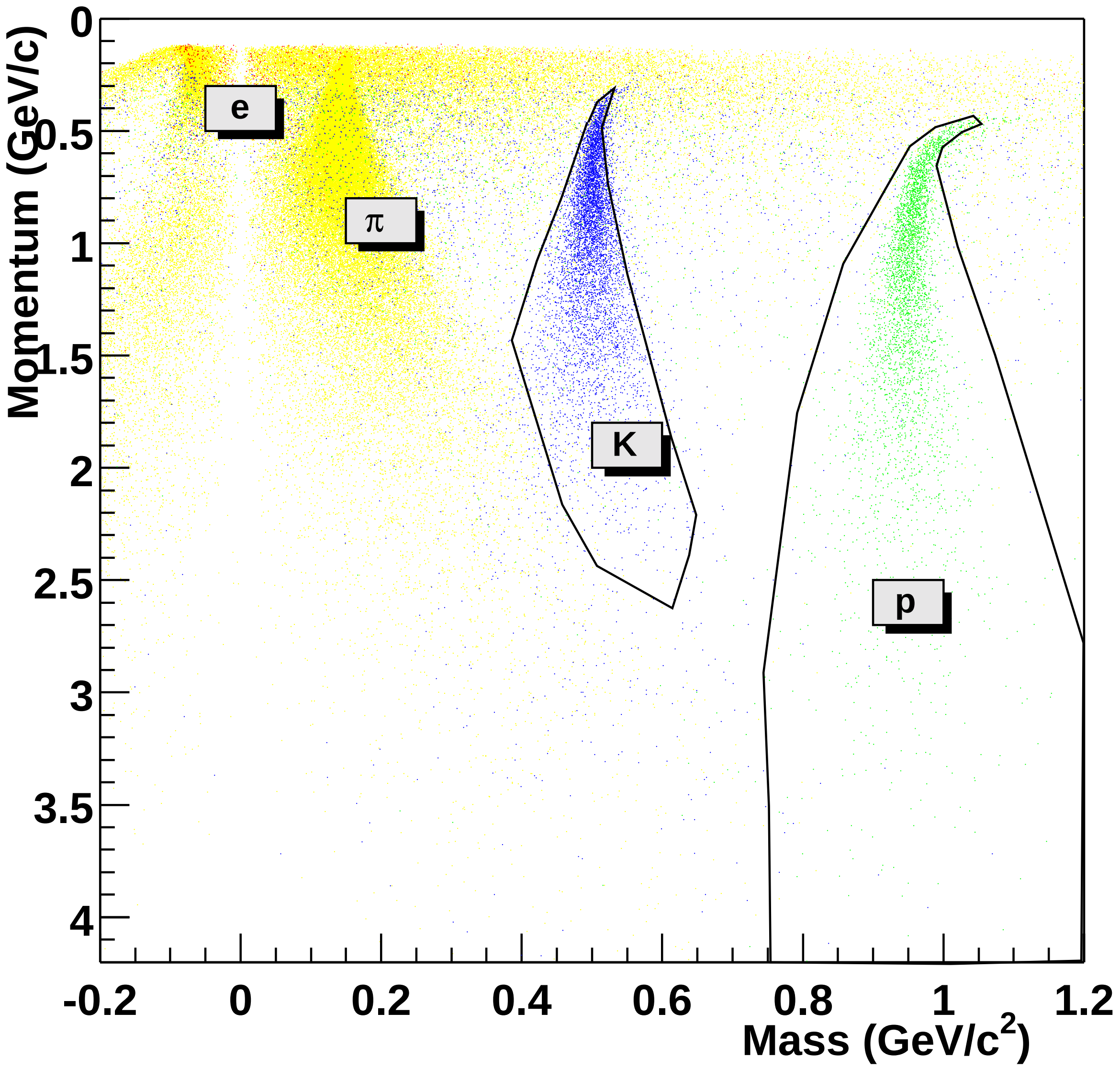

Figure 4.27: Mass separation with the TOF detector (time resolution: 150 *ps*) as a function of momentum (25 SHAKER events).

track length. Let us recall that these primary particles have so far been analyzed in the presence of background from the central and outer regions producing spurious firing of pads in the detector.

Notice that in this plot we have all the particles belonging to set $N_{match}+N_2$, as defined in Section 4.5.2, i.e. all the particles associated with fired TOF pads. Set N_2 (tracks matched with multihit pads) has been included here in order to check the full particle identification power of the detector, as we will see later on. We observe distinct clusters corresponding to pions, kaons and protons as well as a horizontal broad band which corresponds to mismatched tracks, with pads giving wrong times (see Section 4.5.2). This leads to contamination, even in momentum regions where the time resolution is good. For the identification procedure we introduce specific contour cuts, shown in Fig. 4.27, for kaons and protons. The shape of the contours is dictated by the need to extend the range of pure identification to the largest momenta, even at the expense of efficiency.

Besides these graphical cuts, in the PID procedure, different matching cuts were applied to different particle species. The strongest matching cuts were applied to kaons (because of the large pion contamination): only unambiguous correspondences between tracks and TOF pads were selected, i.e. only pads matched with single tracks (set N_{match}, as defined in Section 4.5.2). For protons also, pads matched with more than one track were considered (set $N_{match}+N_2$ in Section 4.5.2) since we expect one half of these tracks to have true time and the other half to be outside the PID contour cuts. Unless differently identified (as kaons or protons), all the other TPC reconstructed primaries, matched or mismatched with the TOF (set $N_{match}+N_{mis}$ in Section 4.5.2, with $N_{mis}=N_0+N_2$), were regarded as pions. This does not lead to a very large contamination due to the overwhelming percentage of pions in the events. In the present analysis, we neglect the possibility of some electron identification at low momenta. Further studies will be necessary to better understand, in this case, the background contamination level.

4.6.2 PID results

Let us call $N_{id}(i)$, with $i=\pi$, K, p, the number of identified particles of different species according to the criteria specified in our previous Section 4.6.1. This number is obviously given by

$$N_{id}(i)=N^t_{id}(i)+N^w_{id}(i)$$

where $N^t_{id}(i)$ is the number of well identified particles of type i and $N^w_{id}(i)$ the number of non-type i particles misidentified as particles of type i. The efficiency and contamination of the PID procedure, for each type of particle, are then:

$$efficiency=\frac{N^t_{id}(i)}{N(i)}$$

$$contamination=\frac{N^w_{id}(i)}{N_{id}(i)}$$

where $N(i)$ is the total sample of particles of type i matched with TOF system and, due to the different matching selections adopted, $N(\pi)=N_{match}(\pi)+N_{mis}(\pi)$, $N(\mathrm{K})=N_{match}(\mathrm{K})$ and $N(\mathrm{p})=N_{match}(\mathrm{p})+N_2(\mathrm{p})$. The momentum dependence of the results relative to the last step of our PID procedure (i.e. once the TPC-TOF track matching is achieved) is presented in Fig. 4.28 for various options: for different particle densities (dN_{ch}/dy), i.e. different occupancies, with and without the TRD. One can easily see that, at this stage, the occupancy up to the level so far considered (with $dN_{ch}/dy=8000$, $r_{TOF}=3.72\,m$ and $3\times 3\ cm^2$ pads) only weakly affects the PID capability of the detector. The same holds true as far as the presence of the TRD is concerned. More detailed studies on the occupancy dependency can be found in [19].

In Fig. 4.29 we show the overall PID efficiency, i.e. the PID power of the TOF detector, as a function of momentum, for π, K and p primary particles produced in the $|\theta-90^\circ|<45^\circ$ central region. This overall PID efficiency, for each momentum bin, is equal to the fraction of primaries produced within the TOF geometrical acceptance which are actually identified. The acceptances concerning the particle tracking

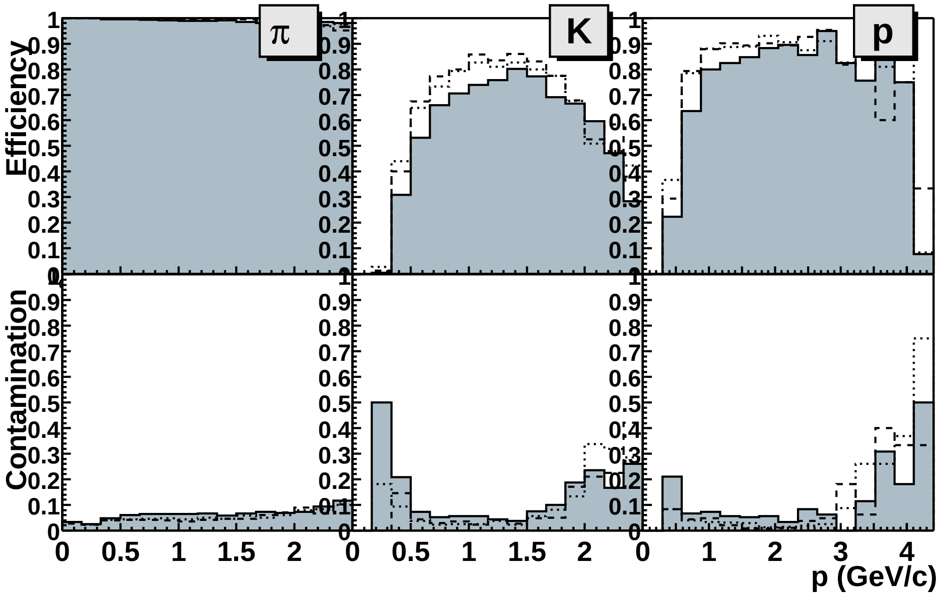

Figure 4.28: The momentum dependence of the efficiency and contamination of the last step of the PID procedure for primary charged particles of different species in the $|\theta - 90°| < 45°$ region (25 SHAKER events) and various options (full histograms: with $dN_{ch}/dy = 8000$; dashed-line histograms: with $dN_{ch}/dy = 4000$; dotted-line histograms: with $dN_{ch}/dy = 8000$ but without the TRD).

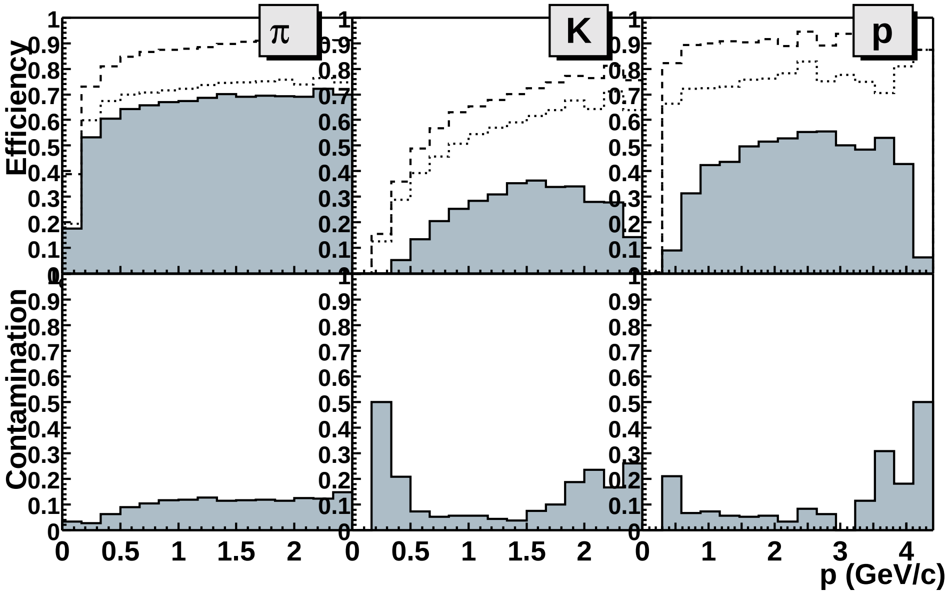

Figure 4.29: The momentum dependence of the overall PID efficiency and contamination (full histograms) obtained with the TOF detector for primary charged particles of different species in the $|\theta - 90°| < 45°$ region (25 SHAKER events). The primary particle acceptances for tracking in the TPC (dashed-line histograms) and extrapolation to the TOF surface (dotted-line histograms) are also shown.

in the TPC and their extrapolation to the TOF surface (already shown in Fig. 4.22) are superimposed for comparison.

4.6.3 Influence of time resolution

Following the method described above, the overall particle identification efficiency and contamination have been determined for several (100, 150, 200 and 300 *ps*) time-of-flight resolution values, as shown in Fig. 4.30. The momentum versus mass plots, corresponding to the lower and higher values, are shown in Fig. 4.31. The TOF performance as a function of time resolution in the range 100-300 *ps* has also been investigated, in similar but less realistic conditions, with respect to several physics parameters: inverse slopes of π, K, p momentum spectra and K/π ratios extracted from single events, inclusive detection of ϕ mesons and open charm D mesons. For details, see [22].

4.7 Event-by-event physics simulations

In this section, we will only focus on the event-by-event (E-by-E) analysis of Monte Carlo simulated events where PID is achieved with the TOF detector. One of the most important goals of ALICE is the measurement of global event characteristics [23] such as event shapes, momentum spectra of identified particles and particle ratios on an event-by-event basis (see Chapter 1). Having developed a detailed simulation of the particle identification efficiency and contamination, we can apply our results (Section 4.6.2) to the analysis of single events. In what follows we will use the TOF detector version with planar geometry and holes at 90° for the HMPID and PHOS.

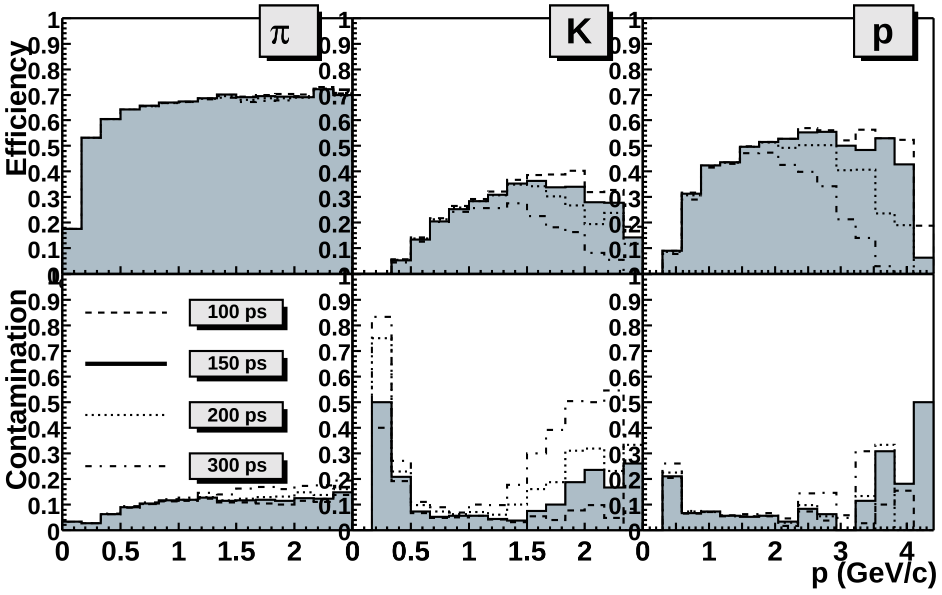

Figure 4.30: Same as Fig. 4.29 but for different time resolutions, as indicated.

Further studies are under way concerning other crucial physical observables, in particular the detection of open charm states [1], in order to fully test the performances of this detector.

4.7.1 Slopes of inclusive spectra

The raw p_t spectra of identified π, K and p in a single SHAKER event are shown in Fig. 4.32. Notice that we have $\sim$ 6000 identified pions, $\sim$ 250 kaons and $\sim$ 150 protons per event. The $\frac{dN}{p_t dp_t}$ spectra of π, K and p originally generated in the central rapidity region ($|y| < 0.9$) and in the TOF geometrical acceptance region ($|\theta - 90^\circ| < 45^\circ$) are shown in Fig. 4.33, for one event. From these spectra a correction for TOF geometrical acceptance could be derived. The single event $\frac{dN}{p_t dp_t}$ spectra of identified hadrons, once corrected for this acceptance and for the overall PID efficiency and contamination, are also shown in Fig. 4.33. Let us call these spectra the reconstructed spectra.

All the original and reconstructed event spectra were fitted with one or two exponentials. This has only a limited value since the spectra do not, in general, have an exponential slope [11]. However, we follow this approach because we are only interested in the fluctuations of the spectrum slopes when compared to the original inputs, namely in the distortions introduced by the PID procedure. Concerning the original spectra, the fitting procedure was applied to those relative to the $|\theta - 90^\circ| < 45^\circ$ region, after correction for TOF geometrical acceptance, with a lower momentum cutoff (300 MeV/c for kaons and protons, 200 MeV/c for pions). In the pion case, a double exponential was used to reproduce the spectrum shape better.

In Fig. 4.34, we show the distributions of the inverse slopes (“temperatures”) obtained by fitting both the original and TOF reconstructed invariant p_t spectra of 25 SHAKER events. The results in Fig. 4.34 appear to be in good agreement with the SHAKER generator parameters used in our simulations, the SHAKER input “temperatures” being 160 MeV/c for pions, 271 MeV/c for kaons and 357 MeV/c for protons[4]. For pions in particular, we consider the first exponential only, and the small difference observed

---

[4] In SHAKER these values refer, respectively, to the pion m_t spectrum and to the kaon and proton p_t spectra.

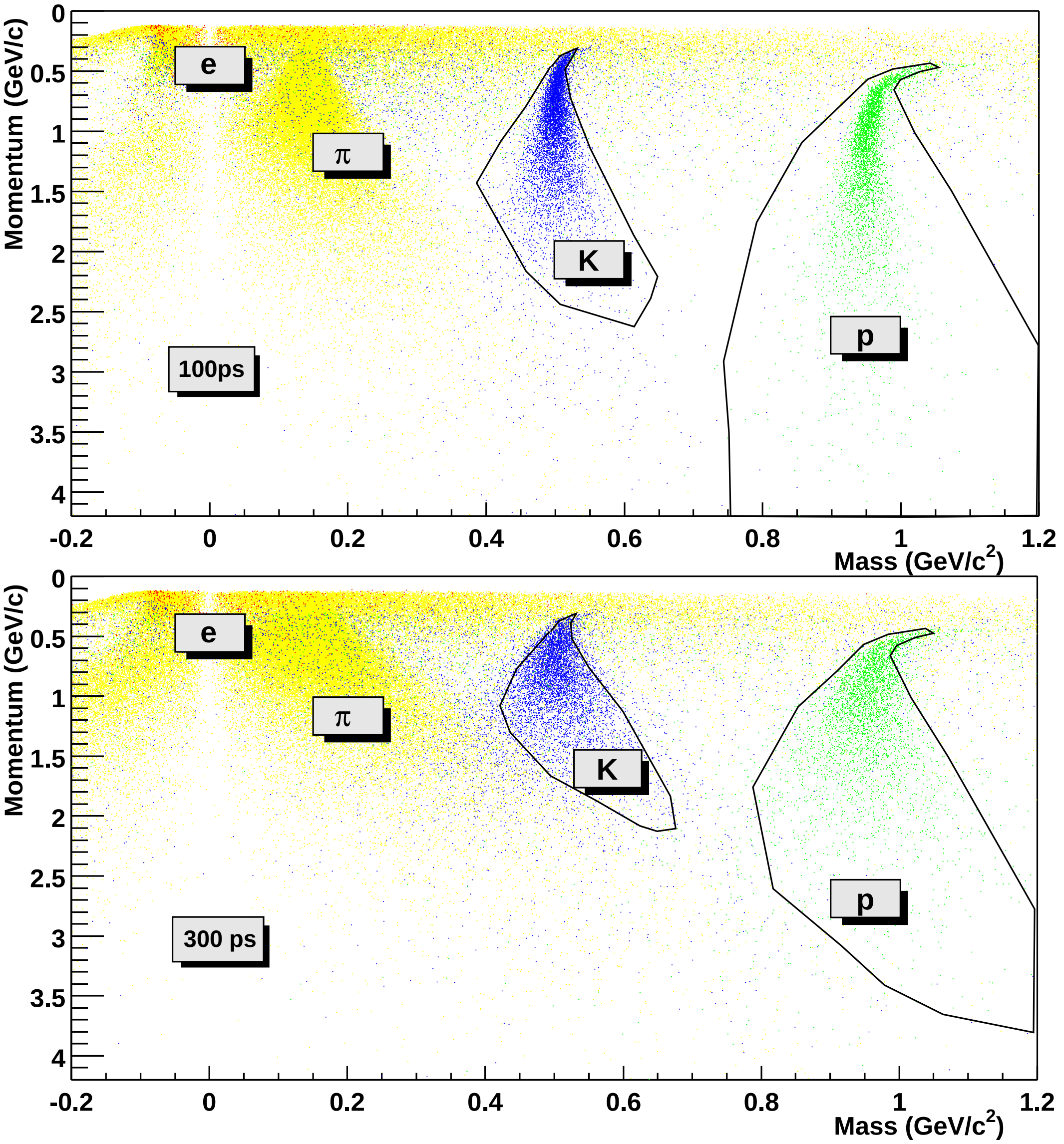

Figure 4.31: Same as Fig. 4.27 for different time resolutions, as indicated.

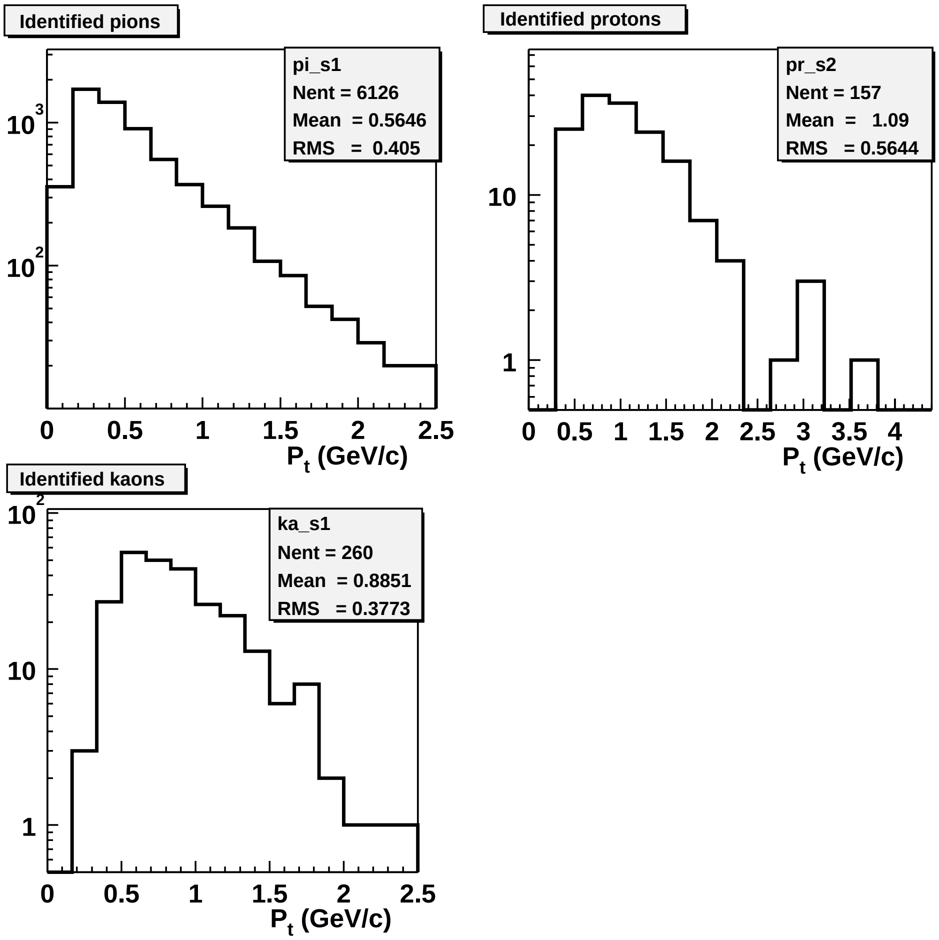

Figure 4.32: Single event p_t spectra of π, K and p hadrons identified by the TOF system (SHAKER).

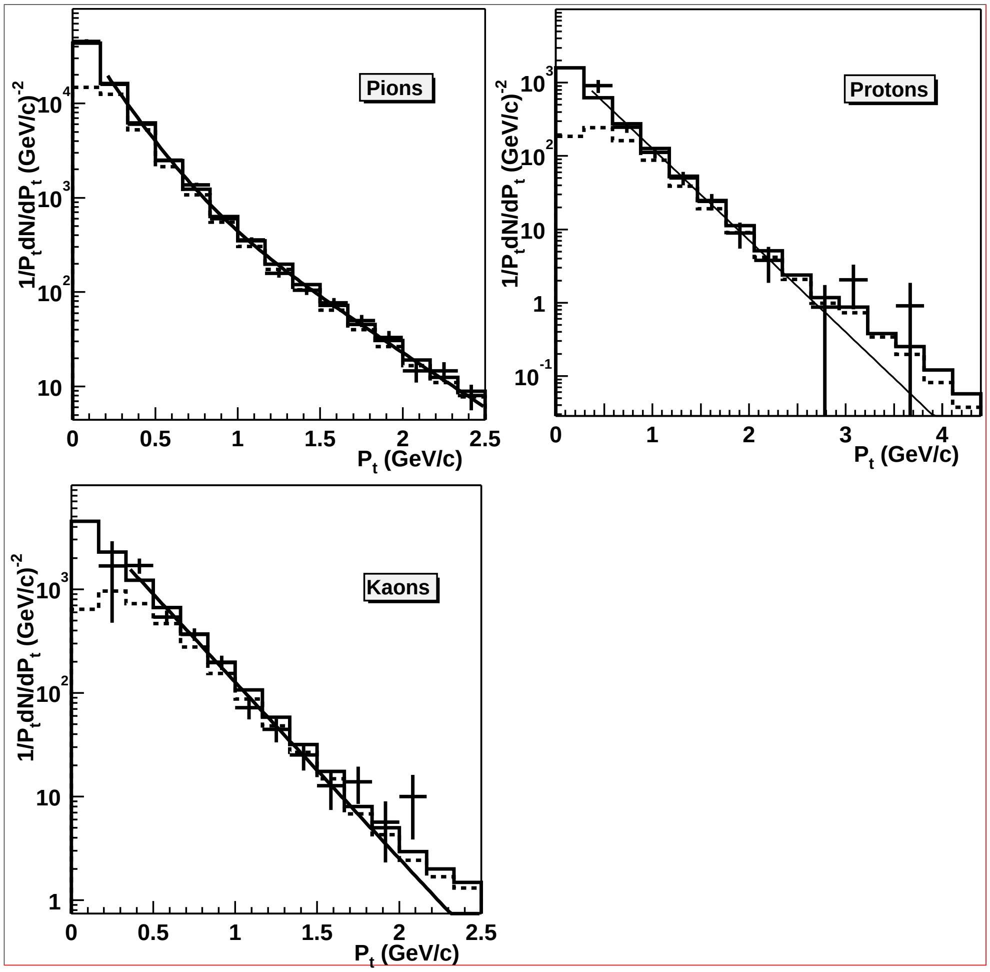

Figure 4.33: Reconstructed invariant p_t spectra (points with error bars) and fits for π, K and p in a single SHAKER event; also shown the originally generated spectra in the regions $|y| < 0.9$ (solid-line histograms) and $|\theta - 90°| < 45°$ (dashed-line histograms).

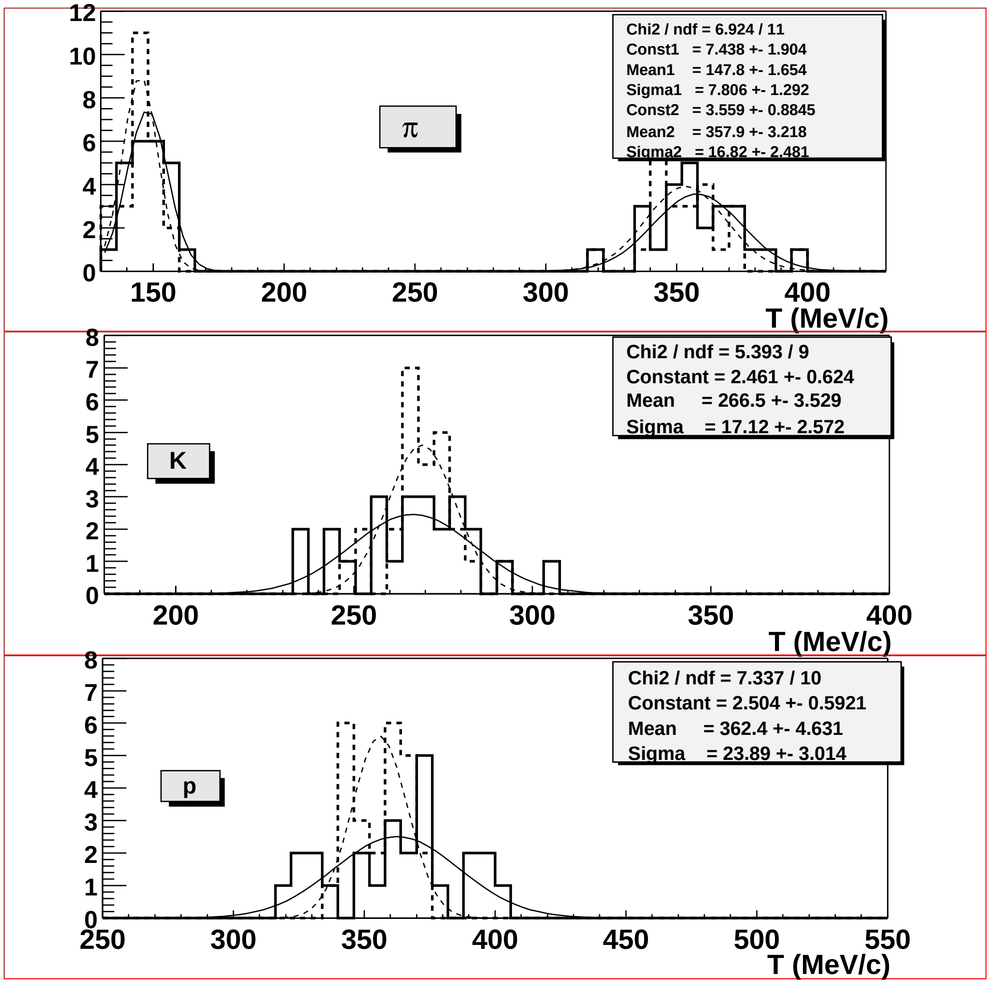

Figure 4.34: Inverse slope distributions for π, K and p in 25 SHAKER events from the fits of: TOF reconstructed p_t spectra (solid-line histograms) and original p_t spectra with lower cutoffs (dashed-line histograms). The Gaussian (solid- and dashed-line) curves superimposed are fits to the corresponding distributions and the fit parameters reported refer to the TOF reconstructed data (solid-line curves).

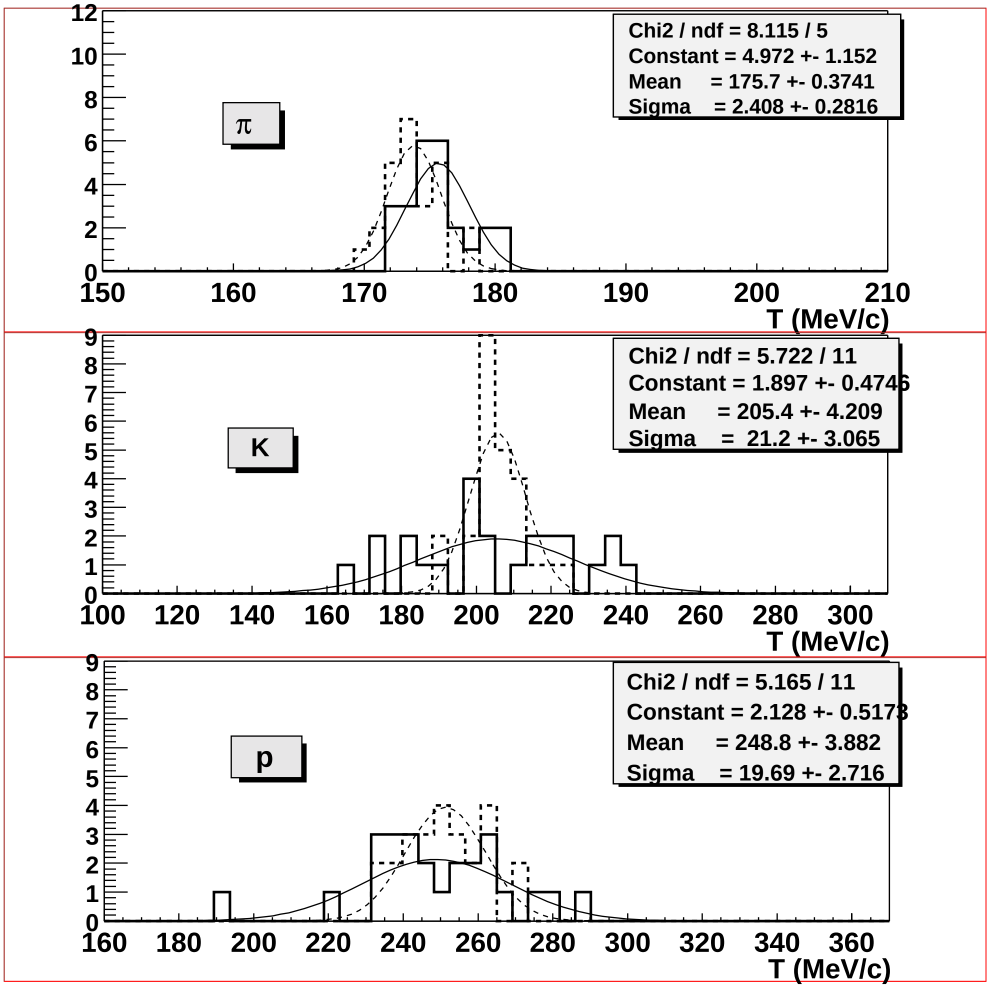

Figure 4.35: Same as Fig. 4.34 for 25 HIJING events.

with respect to the above input value is connected to the fact that pions are actually generated using the m_t variable [11]. Moreover, their original m_t distribution does not strictly follow a double exponential.

The inverse slope parameters reconstructed from the TOF measurements in SHAKER events have less than 10 MeV/c dispersion for pions (first exponential), as for the originally generated spectra, while for kaons and protons the dispersions are larger. However, one can see that the mean values of the inverse slope distributions obtained with reconstructed and original spectra are very close to each other. If the dispersions are due to statistics, the mean values of the inverse slope fit errors should be equal to the standard deviations of the (Gaussian) distributions in Fig. 4.34. We have checked that this is indeed true. Our results clearly indicate that the procedure of identification is correct and that the main source of fluctuations is the number of identified particles. Since a large number of particles falls below the lower cutoff values, the statistics could be improved in the low momentum region, especially for kaons, taking advantage of particle identification in the TPC.

The inverse slope distributions similarly obtained with 25 HIJING events are shown in Fig. 4.35. Comparing these distributions for HIJING and SHAKER events, one sees that the results are qualitatively the same as discussed above. But the differences among the two generators (in momentum spectra, particle multiplicities, event to event fluctuations, etc.) are clearly evident.

The results are summarized in Table 4.4. Any observed deviation from the expected E-by-E inverse slope distributions would signal a possible new physics effect in terms of QCD thermodynamics, namely a possible temperature fluctuation during phase transition.

Table 4.4: Inverse slope parameters (MeV/c) for single events, obtained as mean values over 25 events (TOF refers to the reconstructed data, as explained in the text).

Event generator	$\pi^{\pm}$	$K^{\pm}$	$p(\bar{p})$
SHAKER	152 ± 5	268 ± 7	353 ± 9
SHAKER (lower cutoff)	145 ± 7	269 ± 10	356 ± 11
SHAKER (TOF)	148 ± 8	266 ± 17	362 ± 24
HIJING (lower cutoff)	174 ± 2	204 ± 11	251 ± 11
HIJING (TOF)	176 ± 2	205 ± 21	249 ± 20

4.7.2 K/π ratio measurements

Another important event feature is the K/π ratio. With a procedure similar to the one described in the previous section for the inverse slope measurements, two samples of 25 events each, generated with SHAKER and HIJING, have been analysed on an E-by-E basis in terms of their multiplicity content of TOF reconstructed and identified pions and kaons. The pion and kaon PID efficiencies and contaminations were duly taken into account. The resulting K/π ratio distributions are shown in Fig. 4.36. In the same figure, the distributions relative to the originally generated pions and kaons falling within the TOF geometrical acceptance are also shown for comparison. Let us recall that in SHAKER and HIJING events, the original K/π ratios (over the full phase space) are different, namely $K/\pi = 0.2$ in SHAKER and $K/\pi = 0.13$ in HIJING (see Section 4.3). The K/π ratio values of Fig. 4.36 are smaller since the TOF acceptance for kaons is lower than for pions (see Section 4.4.2). However the difference between SHAKER and HIJING results remains, as it should. One can see that, similar to the inverse slope measurements, the "experimental" distributions are wider than the "theoretical" ones but that they are in agreement within statistics limits.

The results are summarized in Table 4.5. Here, as in the previous section, similar considerations hold true as far as the observation of possible deviations from the expected E-by-E K/π ratio is concerned.

Table 4.5: K/π ratios for single events, obtained as mean values over 25 events (TOF refers to the reconstructed data, as explained in the text).

Event generator	$K^{\pm}/\pi^{\pm}$
SHAKER	0.145 ± 0.004
SHAKER (TOF)	0.14 ± 0.01
HIJING	0.089 ± 0.006
HIJING (TOF)	0.09 ± 0.01

4.8 Discussion of the results and conclusion

The overall PID efficiencies and contaminations (see Section 4.6.2) for π, K and p primaries produced in the $|\theta - 90^{\circ}| < 45^{\circ}$ central region are summarized in Table 4.6. Different momentum ranges are considered, as suggested by the momentum dependence of these quantities (see Fig. 4.29). The numbers in Table 4.6 actually represent the overall PID power of the TOF detector with respect to all primaries produced within its geometrical acceptance in given p intervals, as specified.

Let us recall that the above PID results were obtained using the planar geometry version of the TOF

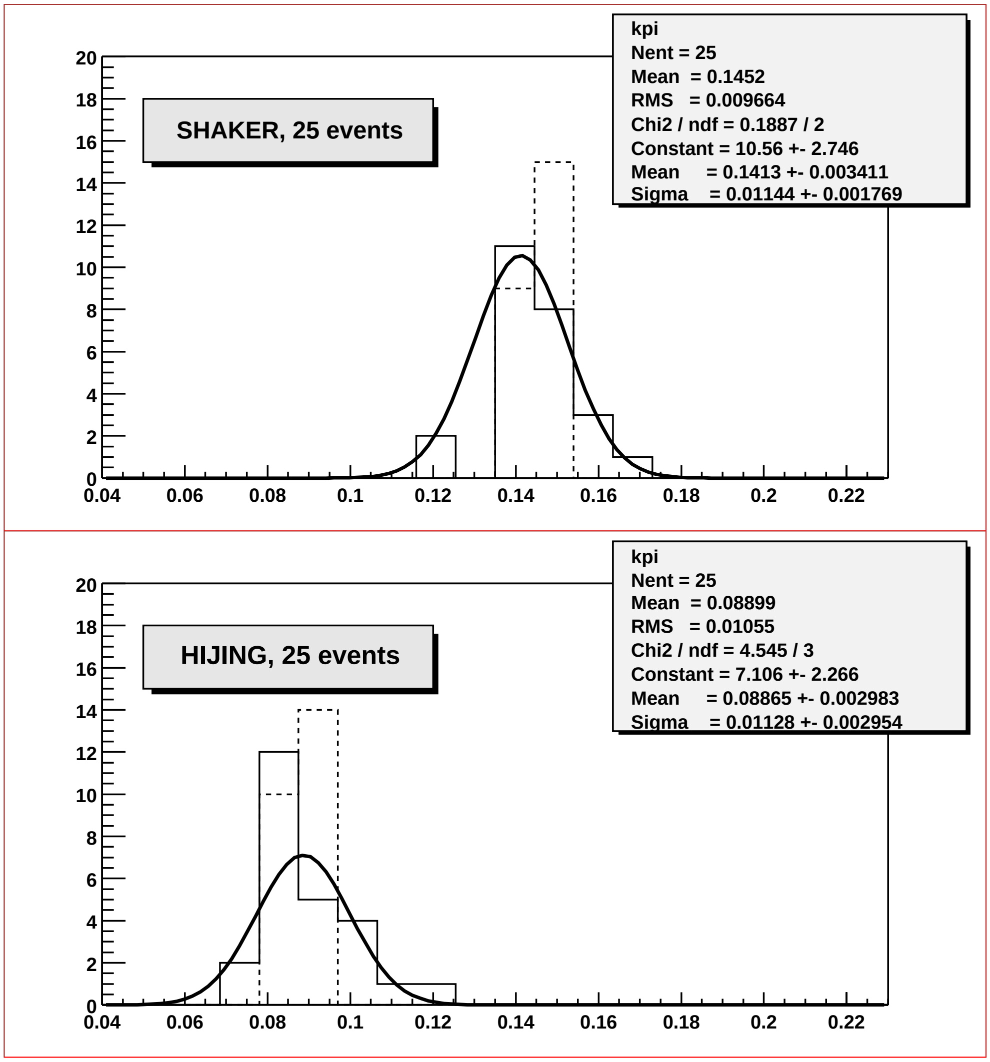

Figure 4.36: K/π ratio distributions for 25 SHAKER and HIJING events for TOF reconstructed and identified particles (solid-line histograms) and for originally generated particles (dashed-line histograms). The Gaussian (solid-line) curves superimposed are fits to the corresponding distributions and the reported fit parameters refer to these curves.

Table 4.6: Overall PID efficiencies and contaminations (%) for primary hadrons in the $|\theta - 90^\circ| < 45^\circ$ region (25 SHAKER events), relative to the planar TOF version with holes for the HMPID and PHOS.

Primary hadron	Momentum range	Efficiency	Contamination
$\pi^{\pm}$	$0.15 \lesssim p < 2.5\ GeV/c$	56	8
$K^{\pm}$	$0.3 \lesssim p < 2.5\ GeV/c$	16	8
$p(\bar{p})$	$0.4 \lesssim p < 4.5\ GeV/c$	33	7
$\pi^{\pm}$	$0.5 < p < 2\ GeV/c$	66	11
$K^{\pm}$	$0.5 < p < 2\ GeV/c$	23	6
$p(\bar{p})$	$0.5 < p < 2\ GeV/c$	39	7

detector with holes for the HMPID and PHOS. The Monte Carlo simulations were performed with a detector occupancy level of 13% (for $dN_{ch}/dy = 8000$, $r_{TOF} = 3.72\ m$ and $3 \times 3\ cm^2$ pads) and a time resolution of 150 *ps*. In these conditions, event-by-event physics studies could be achieved (see Section 4.7) with $\sim$ 6000, 250 and 150 identified pions, kaons and protons per (SHAKER) event.

However, the track finding and reconstruction inefficiency in the TPC, which should be of the order of 10% [3], and the spatial tracking errors at the outer wall of the TPC, which would imply a few percent loss in the TPC-TOF matching efficiency (see Section 4.5.3), were not taken into account. Possible edge effects which would affect the occupancy, hence the TPC-TOF matching algorithm, were not considered either.

When using the realistic tilted-strip design presented in Chapter 3, with holes for the HMPID and PHOS, the TOF acceptance for TPC tracks would increase by 5% (see Section 4.2.2) but a 5% loss would be caused by the envisaged shortening of the TOF barrel (see Section 4.4.2). On the other hand, if a full coverage TOF detector is considered, this acceptance would increase by 20% (see Section 4.5.2), while the occupancy would be the same (see Section 4.4.4).

Hence, our conclusion is that a full coverage TOF detector could be indeed foreseen in order to keep the PID power, in particular for kaons, at the above level. In addition, the tracking capability of the TDR detector, which could sizeably improve the TPC-TOF matching efficiency, should be seriously investigated.

Finally, the need for a tilted-strip layout, to enhance the detector performances by minimizing the particle traversal path through the strips (see Section 4.4.3), has been clearly shown.

5 Installation and organization

5.1 Implementation and infrastructure

5.1.1 ALICE experimental area

The ALICE detector will be installed at Point 2 of the LHC accelerator. The Point 2 experimental area was designed for the L3 experiment. The main access shaft, 23 m in diameter, provides a 15 × 7.2 m^2 installation passage and space for counting rooms. The counting rooms are separated from the experimental area by a concrete shielding plug (see Fig. 5.1). The experimental cavern is 21.4 m in diameter and will be re–equipped with 2 × 20 t cranes having a clearance of about 3 m over the L3 magnet.

The L3 magnet provides a 11.6 m long and 11.2 m diameter solenoidal field of up to 0.5 T. The end–caps have a door–like construction. The door frames will support large beams traversing the L3 magnet, from which the ALICE central detectors will be supported.

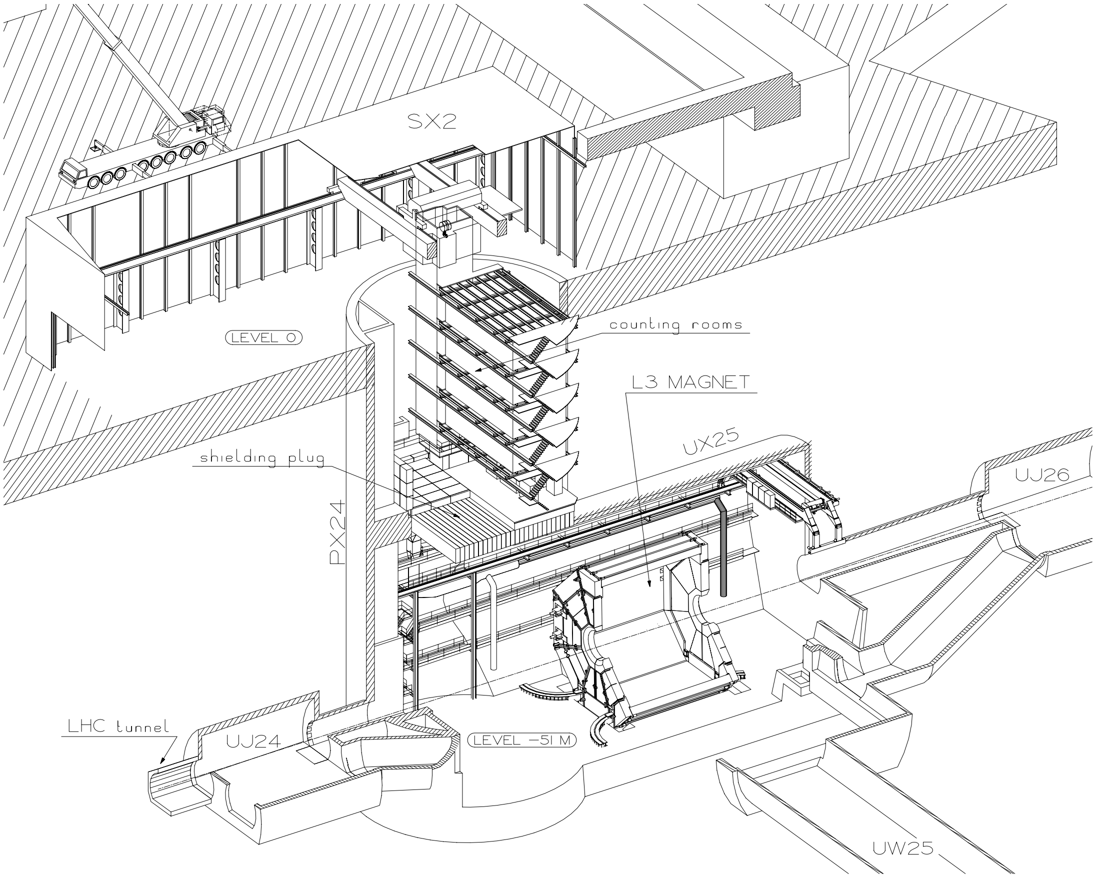

Figure 5.1: General layout of the basic underground structures at Point 2, showing the L3 magnet and the counting rooms.

5.1.2 Implementation of the TOF detector

5.1.2.1 General integration considerations

The TOF detector is supported by a cylindrical space frame construction (see Fig. 5.2), which also serves as a support for all the central detector units. The space frame is placed on large support beams straddling the coil section of the L3 magnet. This allows for the complete assembly of the central detector units to take place outside the L3 magnet. The TOF modules can be handled independently of the other detectors supported by the space frame and are supported by rails fixed to the support structure. These rails can be prolonged outside the space frame to allow the modules to be inserted as successive ”drawers” into the space frame.

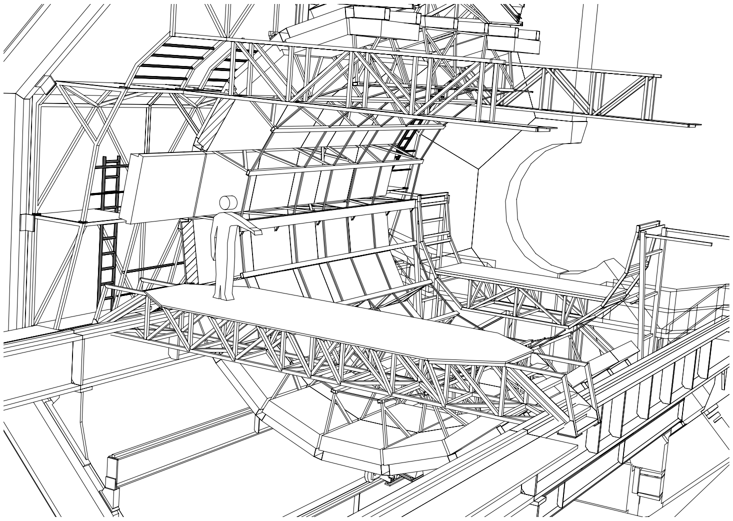

Figure 5.2: General view of the TOF detector and the space frame inside the L3 magnet.

5.1.2.2 The space frame

The space frame is divided into 18 sectors of 20° following the agreed sectorisation of the central detectors. All material has been concentrated at the sector boundaries and at two concentrically placed support rings, as indicated in Fig. 5.3.

The frame is supported on two support beams. There are two support points on each beam, which assures the same vertical displacement of the frame and the beams at all support points. The horizontal displacement of the frame is blocked on one side and free to move on the other side. The support beams are 12.1 m long and supported at their extremities by the L3 door structure.

The combined space frame and support beam structure has been calculated for a total load of 50 t [1]. The calculations were based on keeping the deformation between any two points on the space frame within a few mm and to limit the overall vertical displacement to less than 5 mm. The calculations show that the movements of the TOF support rails can be limited to less than 1 mm if the rails are attached to the outer support frame.

This position of the support rails would interfere with the *in situ* access to the modules and therefore the preferred fixation of the support rails would be to the radial ”webs” in the space frame. This would, however, result in a much larger relative movement of the support rails (typically 3 to 4 mm).

5.1.2.3 Pre–assembly phase

The present surface zone at Point 2 includes sufficient assembly hall space to meet the ALICE requirements and no new hall construction will be necessary for the detector assembly. The overall ALICE

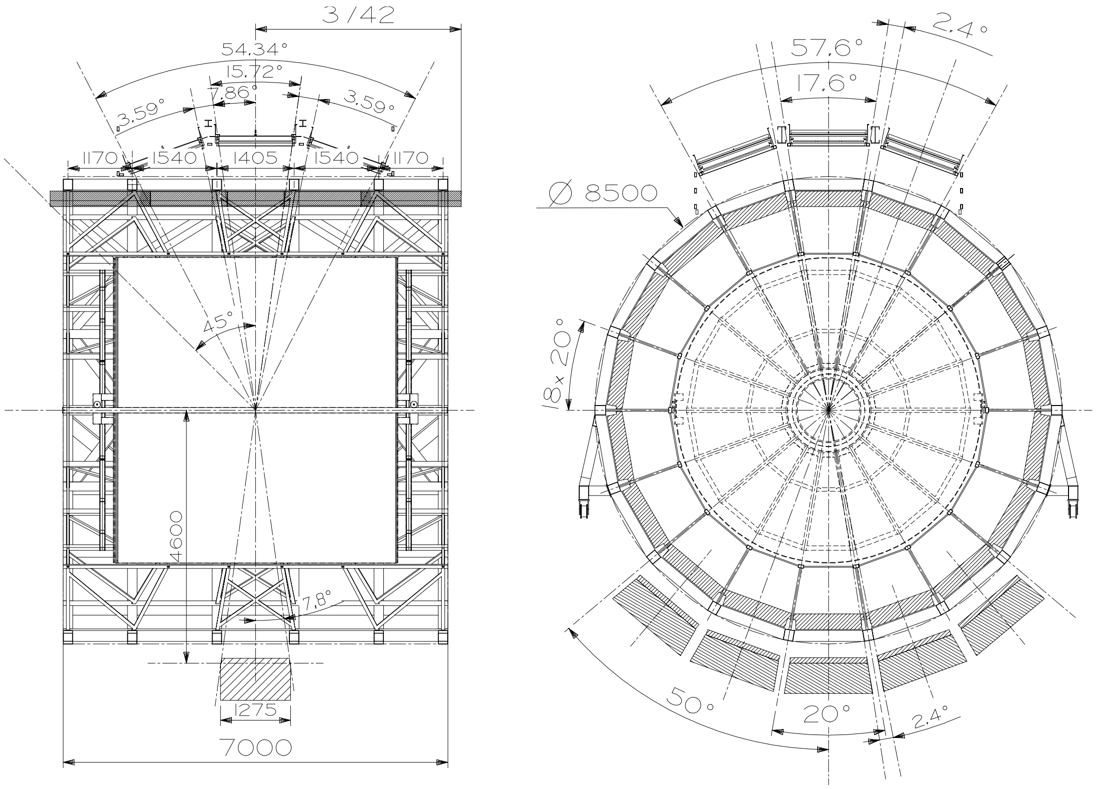

Figure 5.3: General layout of the space frame showing the position of the TOF modules.

planning foresees a pre–assembly phase for the TOF detector to take place in the SXL2 hall, prior to its installation in the underground area, as indicated in Fig. 5.4. The detector will be assembled inside the space frame structure. This will allow an early preparation of the various detector services and permit the installation and access scenarios to be analyzed and corrected before lowering the space frame into the experimental cavern.

5.1.2.4 Installation in the underground cavern

It is conceivable that the complete space frame, with the TOF detector installed, is lowered down as one unit into the experimental area (see Fig. 5.5), however, the present overall width of the TOF detector (7.5 m) exceeds the space available in the installation shaft. This implies that at least 18 TOF modules would have to be installed into the space frame, inside the experimental area, before it is moved into the final position inside the L3 magnet.

5.1.3 Access, maintenance and services

5.1.3.1 Access for maintenance and repair

Access for maintenance to the various parts of the TOF detector is relatively straightforward. The ”backside” of each module is in principle accessible. Clearly, the areas covered by the HMPID or the PHOS are not accessible but, by removing one or two modules, the hidden modules can be moved to an accessible region.

Both end–planes of the space frame are easily accessible from the platforms placed at several levels on both sides of the space frame. The access platforms will be equipped with support points for the chamber extraction tools. The installation or removal of TOF modules towards the absorber side must however be regarded as relatively complicated and time-consuming. It is therefore expected that all

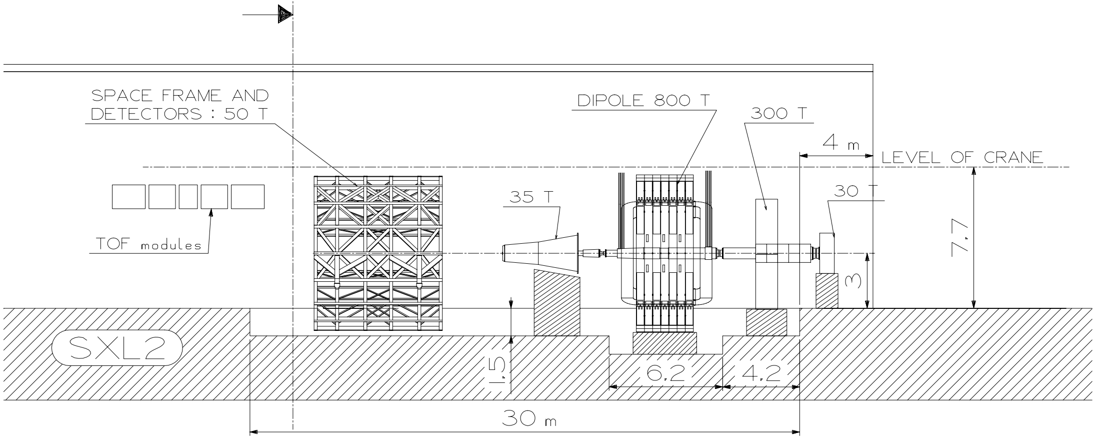

Figure 5.4: Pre–assembly of the ALICE detectors in the SXL assembly hall at Point 2. The left part of the figure indicates how the TOF modules can be mounted into the space frame.

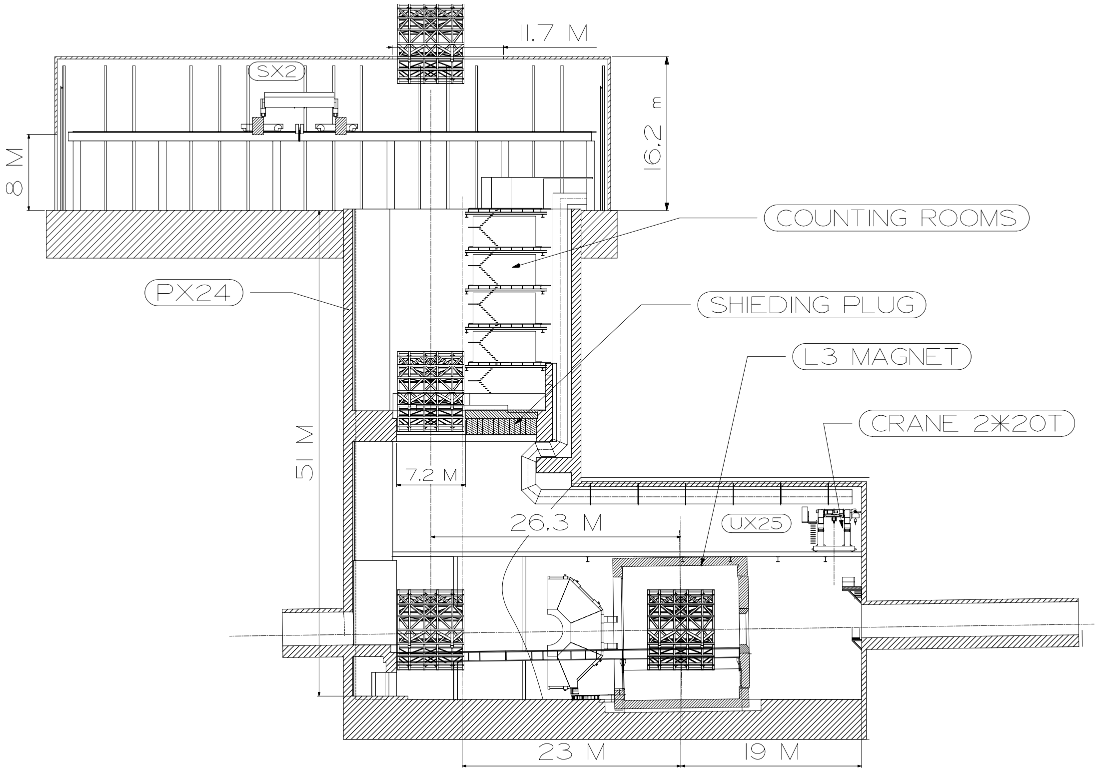

Figure 5.5: Lowering of the space frame and the TOF detector into the experimental area.

modules would be handled from the PX24 side (towards the access shaft).

5.1.3.2 Services

The TOF services will have to pass through the narrow chicane–shaped clearance (100 mm) between the magnet doors and the door frames (see Fig. 5.6). In order to install the services the door will have to be opened, which prohibits any further service installations on the absorber side once the Muon spectrometer is installed.

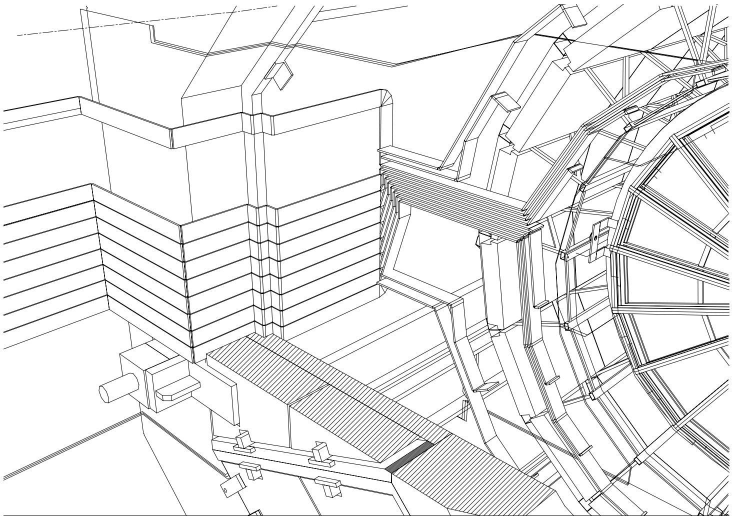

Figure 5.6: Routing of cables from the central detectors through the gap in the L3 magnet doors.

The gas supply will come from the existing surface building, and the distribution units will be located on the shielding plug in PX24.

In order to keep the loss and cable installation costs as low as possible, the racks for the power supplies will be installed as close as possible to the L3 magnet. They will be located on both sides of the L3 magnet, at floor level. Monitoring of the power supplies will be carried out remotely from the control room, since access to the power supplies will not be possible during LHC operation.

In the event of a displacement of the complete space frame or individual modules of the TOF detector all services will have to be disconnected. This is facilitated by the installation of ”patch panels” close to the end–planes of the space frame.

5.1.4 Safety aspects

The TOF detector has been the subject of a recent Initial Safety Discussion [2]. The outcome of this ISD was that the concept of the TOF detector does not present any major safety risk.

The TOF detector uses non–flammable gas mixtures, however all efforts will be made in order to further reduce the Isobutane component in the gas mixture. The absence of toxic, corrosive or flammable components makes the TOF an intrinsically safe detector.

The relatively high voltage applied to the detector (12 KV) could constitute a safety hazard during tests and stand–alone operations. The limited current used by the detector modules (less than 50 μA) will assure a safe final installation. An appropriate outer protection layer for the high voltage cables will be however included in the final design.

The handling of the TOF will always rely on the mechanical stability of the space frame or special transport frames, which will reduce the probability of any mechanical failure.

The closed volume inside the dipole magnet and the part of the Muon spectrometer that penetrates into the L3 magnet will be separately monitored for flammable gas and oxygen deficiency. The access to the inside of the L3 magnet will be restricted and regarded as a confined volume.

All construction materials and electronics printed circuit boards will conform to the CERN safety Instruction TIS IS41 and IS23 concerning the use of plastic and other non–metallic materials at CERN with respect to fire safety and radiation resistance.

5.2 General schedule and milestones

During 2000 and the first half of 2001, the design and prototyping of the TOF will be completed. Mass production of the most defined components could start at the end of 2001. The installation of the TOF detector is integrated with the general planning for the ALICE experiment. The pre–assembly phase will start at the end of year 2003 in the assembly hall SXL2 at Point 2. Figure 5.7 shows the general planning for the design, construction, testing and installation of the TOF.

The following technical milestones are to be fulfilled :

- Middle 2000 : Pilot high–resolution TDC chip preproduction and test
- Middle/End 2000 : Pilot FE ASIC design
- End 2000 : Small (about 1.3 m^2) detector module assembly and test
- End 2000/Beginning 2001 : Second generation TDC chip preproduction and test
- End 2000/Beginning 2001 : Pilot FE ASIC preproduction and test
- Middle 2001 : Second generation FE ASIC preproduction and test
- End 2001/Beginning 2002 : TDC and FE ASIC production, start MRPC production
- Middle 2002 : FEE cards assembly
- End 2002 : Start detector modules production and assembly

5.3 Organization

5.3.1 TOF organization

The ALICE TOF project has the following internal organization:

ALICE TOF Board

Chairperson	Antonino Zichichi
Deputy Chairperson	Luisa Cifarelli
Project Leader	Maurizio Basile
Deputy Project Leader	Giovanni Valenti
Director of MRPC R&D	Crispin Williams
Technical and Scientific Coordinators :	
Luisa Cifarelli	(M.C. Simulation)
Federico Cindolo	(DAQ)
Giuliano Laurenti	(Mechanics)
Giovanni Valenti	(Electronics)
Crispin Williams	(MRPC)

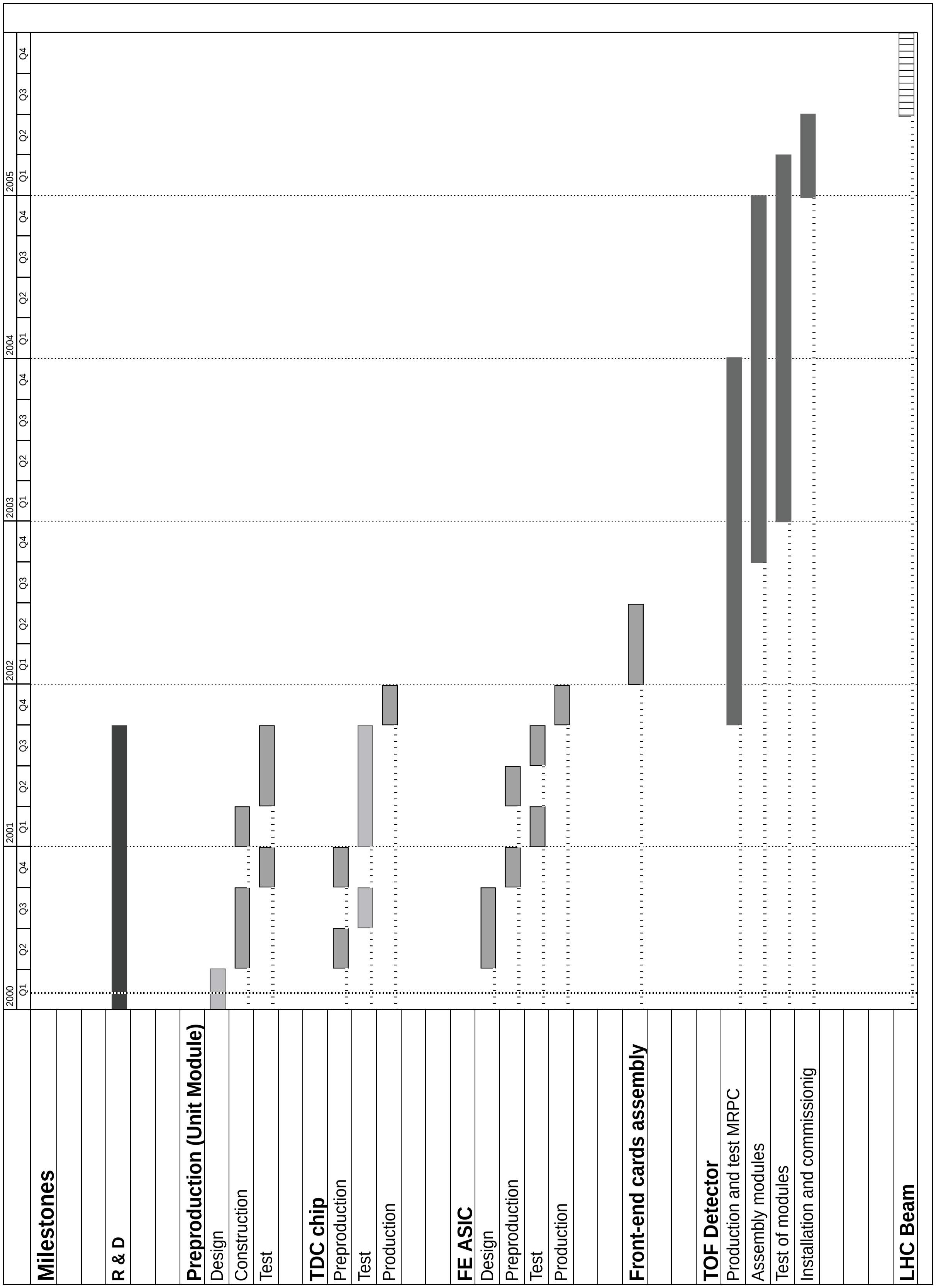

Figure 5.7: Schedule for construction, test and installation of the TOF detector.

5.3.2 Responsibilities

The following institutions will be involved in the construction, testing and commissioning of the TOF detector :

- Italy: INFN and Universities of Bologna, Salerno

The proposed sharing of the responsibilities in the construction and operation of the TOF detector is shown in Table 5.1.

Table 5.1: Sharing of responsibilities

Item	Bologna	Salerno
MRPCs construction	X	
Mechanical supports	X	
Assembly	X	
Power and gas distribution	X	
Front–end electronics	X	
Read–out Electronics	X	X
DAQ and slow control	X	X
Off–line software	X	X

According to the MoU signed at the end of 1999, between ITEP (Moscow) and the Bologna–Salerno group, it is agreed that ITEP will participate in the following parts of the TOF project, under the full Bologna–Salerno group responsibility :

- Finalisation of the TOF design and construction of full–scale prototypes of the TOF detector.
- Software development and Monte Carlo simulations.

A detailed program of the collaboration with ITEP is already defined in the Addendum to the above mentioned MoU; it refers to the first phase of implementation of the ALICE TOF project. In the future, detailed programs of the collaboration will be determined by other addendums.

5.3.3 Manpower

The manpower needed for construction of the TOF detector is estimated to be 180 man years and will be provided by the participating institutions. Some specific items and operations (e.g. part production for MRPCs and module assembly) will be performed by industrial firms.

5.3.4 Cost estimate and resources

The total cost of the TOF detector was estimated using realistic extrapolations and, whenever possible, industrial quotations. Nevertheless, a certain degree of uncertainty still exists for some items; for these, we have quoted lower and upper limits. Table 5.2 shows the cost estimates of the detector.

The resources of the participating institutions will cover the total cost of the TOF detector.

Table 5.2: Cost estimates

Item		Cost [kCHF]	
	Low		High
Detector	1904		2304
Assembly and tools		1450	
Gas system		300	
TDC design and prototypes	94		178
FE ASIC design and prototypes	208		416
Front–end electronics	4760		6886
Read–out Electronics		1151	
Slow control, Data transfer		224	
Power supplies	477		497
Cables and connectors	975		1174
Cooling, installation tools and transport		150	
TOTAL	11693		14730

References

Chapter 1

[1] ALICE Collaboration, Technical Proposal, CERN/LHCC/95–71.
[2] ALICE Collaboration, Alice TDR4, ALICE/ITS 99-12
[3] ALICE Collaboration, Alice TDR7, ALICE/TPC 2000-001
[4] ALICE Collaboration, Alice TDR2, ALICE/PHOS 99-4
[5] ALICE Collaboration, Alice TDR1, ALICE/HMPID 99-19
[6] ALICE Collaboration, Alice TDR5, ALICE/FMU 99-22
[7] ALICE Collaboration, Alice TDR6, ALICE/PMD 99-32
[8] ALICE Collaboration, Alice TDR3, ALICE/ZDC 99-5

Chapter 2

[1] Yu.N. Pestov,Proc. 4th San Miniato Topical Seminar, World Scientific,1991,156.
[2] YV.V. Parchomchuck, Yu.N. Pestov and N.V. Petrovykh, Nucl. Instr. Meth.**93** (1971)269
[3] I.V. Vasserman, P.M. Ivanov, Yu.N. Pestov et al. Jadernaja Fisica, **28** (1978)968; Jadernaja Fisica, 33(1981)709.
[4] Glenn F. Knoll, Radiation detection and measurement, John Wiley & Sons, 1979, 210.
[5] Yu.N. Pestov, Nucl. Instr. Meth. **A265** (1988) 150.
[6] L. Alunni et al., Nucl. Instr. Meth., **A348** (1994)344.
[7] J. Pastrnak and A.N. Trukhin, Czech.J.Phys. **B27** (1997).
[8] U. Frankenfeld et al. GSI-Preprint-98, 1998, in print.
[9] A.R. Frolov, Yu.N. Pestov and V.V. Primachek, Nucl. Instr. Meth. **A307** (1991)497.
[10] A.R. Frolov, T.V. Oslopova, Yu.N. Pestov, Nucl. Instr. Meth. **A356** (1995)447.
[11] PesTOF collaboration, GSI-Preprint-98-14, 1998.
[12] V.D. Laptev and Yu.N. Pestov, Pribori i Tekhnika Eksperimenta **N6** (1975)41.
[13] A. Devismes, J. Eschke, U. Frankenfeld et al., GSI Scientific Report (1998)178.
[14] U.Frankenfeld, GSI, DISS. 99-17, November 1999
[15] M. Mota, J. Christiansen. Proc. IEEE ICECS98, Vol. 1, 409.
[16] J. Christiansen and Z. Augewandte, Phys. **4** (1956)46.
[17] R. Bouclier, G. Charpak and F. Sauli, CERN NP Internal Report 71-12 (1971).
[18] A. Peisert and F. Sauli, Nucl. Instr. Meth. **A247** (1983)229.
[19] Yu. Galaktionov *et al.*, Nucl. Instr. Meth. **A317** (1992)116.
[20] A. Arefiev *et al.*, Preprint DFF 173/10/1992.
[21] V. Akimov *et al.*, Nucl. Instr. Meth. **A344** (1994)120.
[22] K. Voloshin, Thesis for Master of Physics degree, MIPT, Russia, 1994.
[23] R. D'Alessandro et al. Preprint ITEP 51-95, 1995
A. Martemianov, Proc. of the 1st workshop on electronics for LHC experiments, Lisbon, 11-15 Sept., 1995.
[24] A. Arefiev *et al.*, CMS IN/95-0730.
[25] ALICE Collaboration, Technical Proposal,CERN/LHCC/95–71.
[26] R. Santonico and R. Cardarelli, Nucl. Instr. Meth. **187** (1981)377.
[27] "Glass RPC Module for BELLE Endcap $KL_{L/\mu}$ Detector", K. Abe et al., Scientifica Acta Vol XIII, Anno XIII, Numero 2, May 1998, page 281. Proceedings of 4th International Workshop on Resistive Plate Chambers and Related Detectors.

[28] E. Cerron-Zeballos, I. Crotty, D. Hatzifotiadou, J. Lamas-Valverde, S. Neupane, V. Peskov, S. Singh, M.C.S. Williams and A. Zichichi, Nucl. Instr. and Meth. **A373** (1996)35.

[29] E. Cerron-Zeballos, I. Crotty, D. Hatzifotiadou, J. Lamas-Valverde, S. Neupane, M.C.S. Williams and A. Zichichi, Nucl. Instr. Meth. **A374** (1996)132.

[30] E. Cerron-Zeballos, J. Lamas-Valverde, S.C. Lee, D.W. Kim, D. Hatzifotiadou, E. Platner, J. Roberts, M.C.S. Williams and A. Zichichi, Nucl. Instr. Meth. **A434** (1999)362.

[31] E. Cerron-Zeballos, I. Crotty, D. Hatzifotiadou, J. Lamas-Valverde, R.J. Veenhof, M.C.S. Williams and A. Zichichi, Nucl. Instr. Meth. **A381** (1996)569.

[32] A. Akindinov, P. Fonte, F. Formenti, V. Golovinel, W. Klempt, A. Kluge, A. Martemiyanov, P. Martinengo, J. Pinhao, A. Smirnitski, M. Spegel, P. Szymanski, J. Zalipska, “A four gap glass RPC time-of-flight array with 90 ps time resolution”, ALICE-PUB-99-34 and submitted to IEEE transactions on Nuclear Science.

[33] V. Radeka, Ann. Rev. Part. Sci **38** (1988).

[34] E. Cerron-Zeballos, I. Crotty, D. Hatzifotiadou, J. Lamas-Valverde, M.C.S. Williams and A. Zichichi, Nucl. Instr. Meth. **A396** (1997)93.

Chapter 3

[1] ALICE Collaboration, Technical Proposal, CERN/LHCC/95–71.

[2] CERN/LHCC 98-19 ALICE TDR 1. 14 August 1998.

[3] G. Rubin, ALICE Detector Data Link (DDL) - DDL Physical and Signalling Layer Specification (PhI), ALICE/97-04, Internal Note DAQ.

[4] G. Rubin, ALICE Detector Data Link (DDL) - Hardware Guide for the Front-end Designers, ALICE/98-21, Internal Note DAQ.

[5] CERN ALICE DAQ group, ALICE Detector Data Link - Users’ Guide for the SIU Simulator ALICE/99-03, Internal Note DAQ.

[6] CERN ALICE DAQ group, ALICE Detector Data Link - Users’ Guide for the SIU Extender ALICE/99-04, Internal Note DAQ.

[7] G. Rubin and J. Sulyan, The Read-out Receiver Card (RORC) hardware user’s guide, ALICE/97-14, Internal Note DAQ.

[8] O.Villalobos et al., Data Acquisition, Control and Trigger: Common Report for the preparation of the ALICE Technical Design Reports, ALICE/98-23, Internal Note DAQ/DCS/Trigger. New updated version in preparation.

[9] CERN ALICE DAQ group, ALICE DATE User’s Guide - DATE V3.5, ALICE/99-46, Internal Note DAQ.

[10] B. G. Taylor, TTC Distribution, First Workshop in Electronics for LHC Experiments, CERN/LHCC/95-56, p. 180, October 1, 1995. RD12, Timing, Trigger and Control System for LHC Detectors, CERN/LHCC 97-29, LEB Status Report, RD12, April 30, 1997.

[11] J. Christiansen, 32 channel TDC with on-chip buffering and trigger-matching, Proceedings of the 3rd. Workshop on Electronics for LHC Experiments, London, UK, Sep. 1997.

[12] M. Mota, J. Christiansen, A four channel, self-calibrating, high resolution Time to Digital Converter, Proceedings of the 5th. IEEE International Conference on Electronics, Circuits and Systems (ICECS’98), Lisboa, Portugal, Sep. 1998.

[13] M. Mota, J. Christiansen. A high resolution time interpolator based on a Delay Locked Loop and an RC delay line, IEEE Journal of Solid-State Circuits, vol. 34, no. 10, pp. 1360-1366, Oct. 1999.

[14] P. Moreira et al., A 1.25Gbit/s Serializer for LHC Data and Trigger Optical Links, Proceedings of the 5th. Workshop on Electronics for LHC Experiments, Snowmass, CO, USA, Sep. 1999.

[15] J. Christiansen, High performance general purpose TDC specification, EP/MIC note, available at ”http://pcvlsi5.cern.ch:80/MicDig/hptdc.htm”

Chapter 4

[1] N. Ahmad *et al.*, ALICE Technical Proposal, CERN/LHCC 95-71, LHCC/P3, 15 December 1995.

[2] N. Ahmad *et al.*, ITS Technical Design Report, ALICE TDR 4, CERN/LHCC 99-12, 18 June 1999.

[3] N. Ahmad *et al.*, TPC Technical Design Report, ALICE TDR 7, CERN/LHCC 2000-001, 7 January 2000.

[4] N. Ahmad *et al.*, HMPID Technical Design Report, ALICE TDR 1, CERN/LHCC 98-19, 14 August 1998.

[5] http://www.cern.ch/ALICE/Projects/offline/aliroot/Welcome.html.

[6] R. Brun *et al.*, http://root.cern.ch.

[7] R. Brun *et al.*, GEANT3, CERN program library Q123.

[8] T. Sjöstrand, Comp. Phys. Commun. **39** (1986) 347.

[9] H.-U. Bengtsson and T. Sjöstrand, Comp. Phys. Commun. **46** (1987) 43.

[10] X. N. Wang and M. Gyulassy, Phys. Rev. **D44**(1991) 3501;
X. N. Wang and M. Gyulassy, Phys. Rev. **D45** (1992) 844;
X. N. Wang and M. Gyulassy, Comp. Phys. Comm. **83**(1994) 307.

[11] F. Antinori, Internal Note ALICE/SIM 93-9, 1993;
N. van Eijndhoven *et al.*, Internal Note ALICE 95-32.

[12] N. Ahmad *et al.*, PHOS Technical Design Report, ALICE TDR 2, CERN/LHCC 99-4, 5 March 1999.

[13] A. Morsch, http://home.cern.ch/ morsch/AliGenerator/AliGenerator.html
and http://home.cern.ch/ morsch/generator.html.

[14] A. Capella *et al.*, Z. Phys. **C3** (1980) 329;
J. Ranft, Phys. Lett. **188B** (1987) 379;
J. Ranft, Phys. Rev. **D37** (1988) 1842;
A. Capella *et al.*, Phys. Rep. **236** (1994) 64.

[15] B. Andersson *et al.*, Nucl. Phys. **B281** (1987) 289;
B. Nilsson-Almqvist and E. Stenlund, Comp. Phys. Comm. **43** (1987) 387.

[16] T. Alexopoulos *et al.*, Phys. Rev. Lett. **64** (1990) 991.

[17] M. Bourquin and J.M. Gaillard, Nucl. Phys. **B114** (1976) 334.

[18] N. Ahmad *et al.*, Muon Spectrometer Technical Design Report, ALICE TDR 5, CERN/LHCC 99-22, 13 August 1999.

[19] S. Kiselev, G. Paić, J. Schukraft, A. Smirnitsky and B. Zagreev, Internal Note ALICE/SIM 97-09, 1997.

[20] S. Kiselev, G. Paić, J. Schukraft, A. Smirnitsky and B. Zagreev, Internal Note ALICE/SIM 96-17, 1996.

[21] J. Belikov, Private Communication, November 1999.

[22] B. Batyunya, S. Kiselev, G. Paić, K. Safarik, A. Smirnitsky and B. Zagreev, Internal Note ALICE/SIM 98-08, 1998.

[23] S. Kiselev, G. Paić, J. Schukraft, A. Smirnitsky and B. Zagreev, Internal Note ALICE/SIM 97-08, 1997.

Chapter 5

[1] The mechanical properties of the ALICE space frame supporting structure, J. Bielski, Internal Note ALICE/97–32, November 1997 (updated with an annex in July 1999).

[2] Initial Safety Discussion for the ALICE TOF Detector, TIS/GS/WW/2000–002.